Casing Effusion Cooling

Matthew C.J. Collins
Hertford College
University of Oxford

A thesis submitted for the degree of
Doctor of Philosophy
Trinity Term 2014

Acknowledgements

This page is not large enough to thank and acknowledge all those who have helped me complete this chapter of my life. First and foremost I must offer my upmost thanks to my supervisor Tom Povey. His enthusiasm and support of my work has been most inspiring and I have relished in the freedom to develop my own ideas. A special thanks also goes to Kam Chana who played a significant role in getting my project off the ground and offered his continual advice on the experimental side of the project. My experiments would not have occurred without the excellent help and patience of David Cardwell and Sunny Chana who helped run my experiments on the OTRF. The work and friendship of Trevor Godfrey, who helped develop the new instrumentation, must also get special mention.

Next I must offer special thanks to my partner in crime in the office, my desk buddy Ben Kirollos. He has had to suffer with my continual questions and rants but is always ready to offer some fantastic advice along with a slightly inappropriate one liner.

My time at the Osney lab would not have been as fun or as enjoyable without the friends I have acquired along the way, both within the lab and within Hertford College. For fear of this sounding like an Oscars acceptance speech I will not list them but I would like to thank all of you.

Finally I would like to thank my parents and family who have always been there for me and I dedicate my thesis to them. I find it rather poetic that I ended up in the field of turbomachinery, an area whose heritage lies partly in the work of my late grandfather, who worked with Frank Whittle during the development and testing of the first British jet aircraft, the Gloster E.28/39.

Abstract

Casing Effusion Cooling

A thesis submitted for the degree of

Doctor of Philosophy

Matthew C.J. Collins, Hertford College, Trinity Term 2014

The design, modelling and testing of a film cooling system intended for the casing of an unshrouded HP turbine rotor is described in this thesis. Due to the dense network of small film cooling holes employed in such a system, this is often referred to as a *casing effusion cooling* scheme. Though there are patent references to such systems, there is as yet very limited published material on the aero thermal performance of such film cooling schemes. The casing of an unshrouded HP rotor is an incredibly hostile environment, witnessing the periodic passing of the HP rotor tips within close proximity at a frequency of ~10 kHz. These blade passing events subject the casing to extremely large amplitude fluctuations of pressure and heat load, which may at first seem to preclude the use of a film cooling scheme.

This thesis details many theoretical, computational and experimental advancements related to the research topic. Highlights include:

The introduction of a new fundamental mechanism to the field of film cooling, the propagation and reflection of pressure waves within film cooling holes and the impact on film cooling performance.

The development of new miniature thin film heat flux gauges manufactured using a new process. Sensor resolution is improved by a factor of seven.

The first published computational model reporting heat transfer data on a film cooled rotor casing.

Improvements to heat transfer data processing techniques and theory. These are applied to experimental work to produce the highest resolution heat transfer data obtained on the casing of a scaled rotating transonic HP rotor for both uncooled and cooled geometries.

Computational models are used to demonstrate that coolant injection on the rotor casing reduces the over-tip leakage mass flow, offsetting the spoiling and mixing losses that film cooling schemes introduce.

Much of the work in this thesis is based on papers that have been submitted to or are pending submission. To date three papers have been presented at conference with two published in journals and the third recommended and pending journal publication. Two other papers are pending submission. A patent has also been filed with the European and American patent office regarding novel film cooling hole shapes designed to make use of acoustic effects.

Contents

Chapter 1: Introduction

Since its development in the 20th century, the gas turbine engine has been used in many applications where efficiency and high power to weight are important design considerations. Applications include power generation and propulsion, but it is the application to the aviation industry where the impact has been most evident.

With the ever increasing financial and environmental pressures faced by aircraft operators (caused by rising oil prices and the increased awareness of global warming), research into improvements in gas turbine efficiency has become ever more important in order to lower operating costs and reduce aviation's environmental impact.

1.1 Research Motivation

Cycle efficiency can be improved by increasing the engine's pressure ratio and bypass ratio. Operation at increased pressure ratios increases the temperature of the gas entering the combustor. To maintain the specific thrust, the turbine entry temperature (TET) must also be increased. The maximum TET of an engine is primarily limited by metallurgical constraints, which dictate the maximum metal temperature and stress on the part to ensure sufficient component life. Active cooling allows the TET of a modern gas turbine to far exceed the maximum permitted metal temperature.

The current series of Rolls-Royce Trent engines use a shrouded HP rotor design, the rotor blading being enclosed by a rotating annular casing. This design eliminates rotor tip-gap losses inherent in un-shrouded rotors but adds a significant rotating mass. Future engine designs look to increase bypass ratio by both increasing the fan diameter and reducing the core diameter. In order to extract similar power levels from a smaller core, the engine operating speed must increase. When coupled with the additional cooling requirements due to increases in TET, the

reduced tip losses of the shroud are offset by structural and shroud cooling requirements. Future Rolls-Royce engines such as the next XWB engine will utilise an unshrouded rotor design.

The casing of an unshrouded rotor is subjected to large temporal variations in both static pressure and heat load. Increasing turbine entry temperatures necessitate that the casing be cooled. One such cooling strategy would utilise film cooling. As yet, there has been only one published pair of papers describing a casing film cooling scheme by Chana and Haller (2009). There are also a number of patents relating to the implementation of such a scheme, for example Liotta and Acquaviva (1999), Lee and Durgin (2001), White and Lee (2002), Lowe et al. (2003), Shapiro (2007) and Lee et al. (2012), indicating probable use in an engine.

This project aims to increase the understanding of a film cooling scheme employed on the casing of an HP rotor using computational models and experiments. This information will allow cooling designers to assess the applicability of such a design for future engine applications.

1.2 Historical Context

The modern gas turbine was developed at the turn of the 20th century. Frank Whittle is credited with the invention of the modern gas turbine, running the first modern jet engine design in April 1937. This initial engine, the Power Jets W.1 developed by Whittle and a small team, was later installed into the Gloster E.28/39 which first flew at RAF Cranwell on 15 May 1941. The airframe was later fitted with an upgraded W2.B developed with the assistance of Rover. Development was soon transferred to Rolls-Royce who cooperated with Whittle and his team at Power Jets to develop the Rolls-Royce Welland and later Derwent engines, which powered Britain's first operational jet aircraft, the meteor and many future aircraft.

Figure 1.1. Gloster E.28/39.

At this time, parallel work was being conducted in Germany by Hans van Ohain. The first of his designs ran in September 1937, with the design being rapidly and improved to be installed in the world's first gas turbine powered aircraft, the Heinkel He 178, first flown on 27 August 1939.

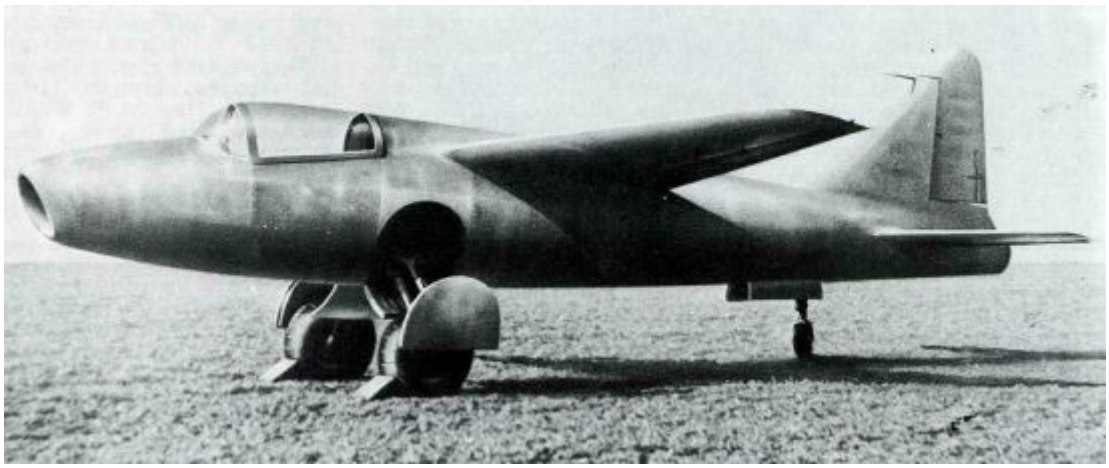

Figure 1.2. Heinkel He 178, the world's first gas turbine powered aircraft.

Both Whittle's and Ohain's engines utilised centrifugal compressors and turbines, which were well understood at the time from their application as superchargers and turbochargers on contemporary internal combustion engines. Though simple and lightweight, this design required a large frontal area to generate sufficient power, which was not suited to installation in an airframe. Austrian Anselm Franz, working within Junkers' engine division developed the axial flow compressor, common on aircraft engines today. This significantly reduced the frontal

area of the engine, though at the expense of significant extra complexity. Despite this, the engine was developed into the Jumo 004, which powered the first operational jet-fighter, the Me 262. Parallel work in Britain resulted in a similar axial flow design, the Metrovick F.2, first run in 1941 and later developed into the Armstrong Siddeley Sapphire (also built in the US as the J65), powering many 1950s aircraft including the Hawker Hunter.

Advances in gas turbine engines continued apace after the end of World War II, with De Havilland rapidly developing the world's first jet airliner, the Comet, which first flew on 27 July 1949. The aircraft demonstrated the advantages of the gas turbine engine for commercial aviation, and though plagued by structural problems, inspired the design of future aircraft.

Over the years, advances in materials, manufacturing, computer power and understanding of fluid mechanics has enabled the pressure ratios, bypass ratios and Turbine Entry Temperatures (TET) to rise significantly, all with the aim of reducing specific fuel consumption (sfc). The maximum pressure ratios achieved in the 1940s were around 5:1 whereas the latest Trent 1000, powering the Boeing 787 Dreamliner, operates at up to 52:1. Turbine entry temperatures have similarly increased from around 900 °C in the 1940s to in excess of 1800 °C in the Trent 1000, as shown in fig. 1.3.

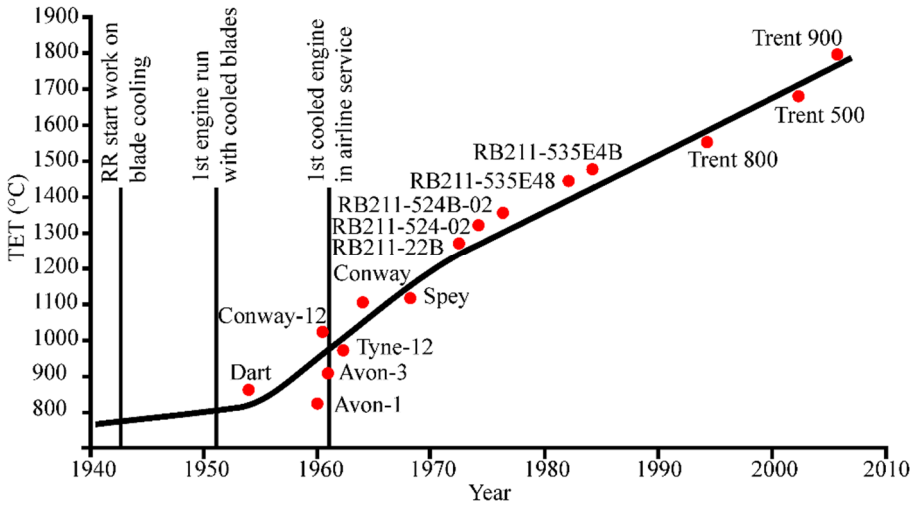

Figure 1.3. Historical evolution of turbine entry temperatures in Rolls-Royce civil engines, adapted from Friedrichs (2008).

1.3 The Gas Turbine Cycle

The full cycle of a modern gas turbine is very complex, with many secondary flows utilised for cooling components and providing bleed air for auxiliary systems. The process of combustion is highly complex and the large temperature changes within the engine means that the air and air/fuel mix cannot be considered as ideal gases for accurate evaluations. However, a simplified air standard cycle does offer an insight into the direction a designer may wish to push the TET and pressure ratio to achieve higher efficiency.

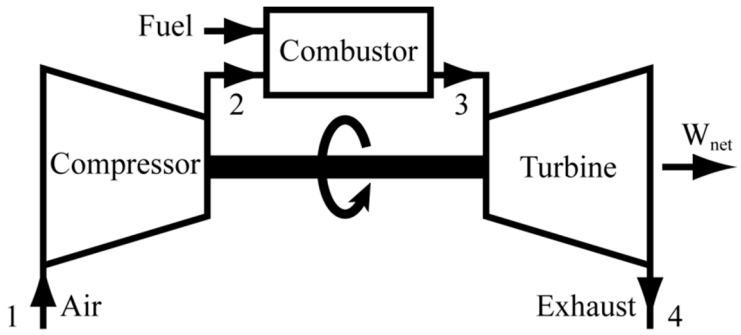

Figure 1.4. Joule cycle.

The Joule cycle represents an idealised cycle representation of the gas turbine engine which enables a simplified thermodynamics analysis. It can be thought of as a closed cycle if we consider that the inlet and exhaust are both connected to an infinitely large volume at constant temperature and pressure, the atmosphere.

In the following analysis it is assumed that for the idealised cycle the working fluid can be treated as an ideal gas and the following assumptions are made about the processes:

1 → 2. Adiabatic and reversible (isentropic) compression.

2 → 3. Combustion is equivalent to heat addition at constant pressure.
The additional mass of the fuel is neglected
Products of combustion are considered to be air.

3 → 4. Adiabatic and reversible (isentropic) expansion.

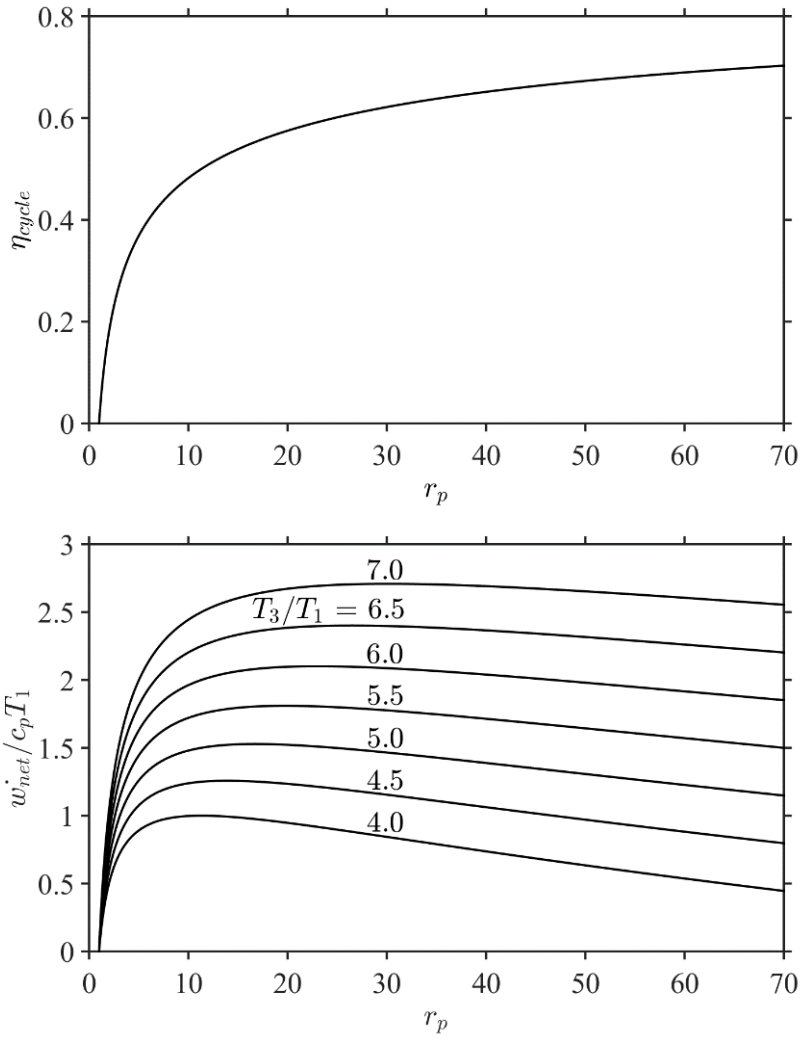

Figure 1.5. Idealised Joule cycle efficiency and non-dimensional specific work output.

$$\eta_{comp.} = \eta_{turb.} = 1.0.$$

With application of the 1st law of thermodynamics, it can be shown that the efficiency of this idealised cycle can be given by

$$\eta_{cycle} = 1 - \frac{1}{r_p^{\frac{\gamma-1}{\gamma}}} \tag{1.1}$$

The non-dimensional specific work output can be defined as

$$\frac{\dot{w}_{net}}{c_p T_1} = 1 + \eta \frac{T_3}{T_1} - r_p^{\frac{\gamma-1}{\gamma}} \tag{1.2}$$

These are both plotted in fig. 1.5 as a function of pressure ratio r_p. It is evident that though the idealised efficiency is only a function of pressure ratio, to maintain the same specific power output from the engine requires an increase in temperature ratio.

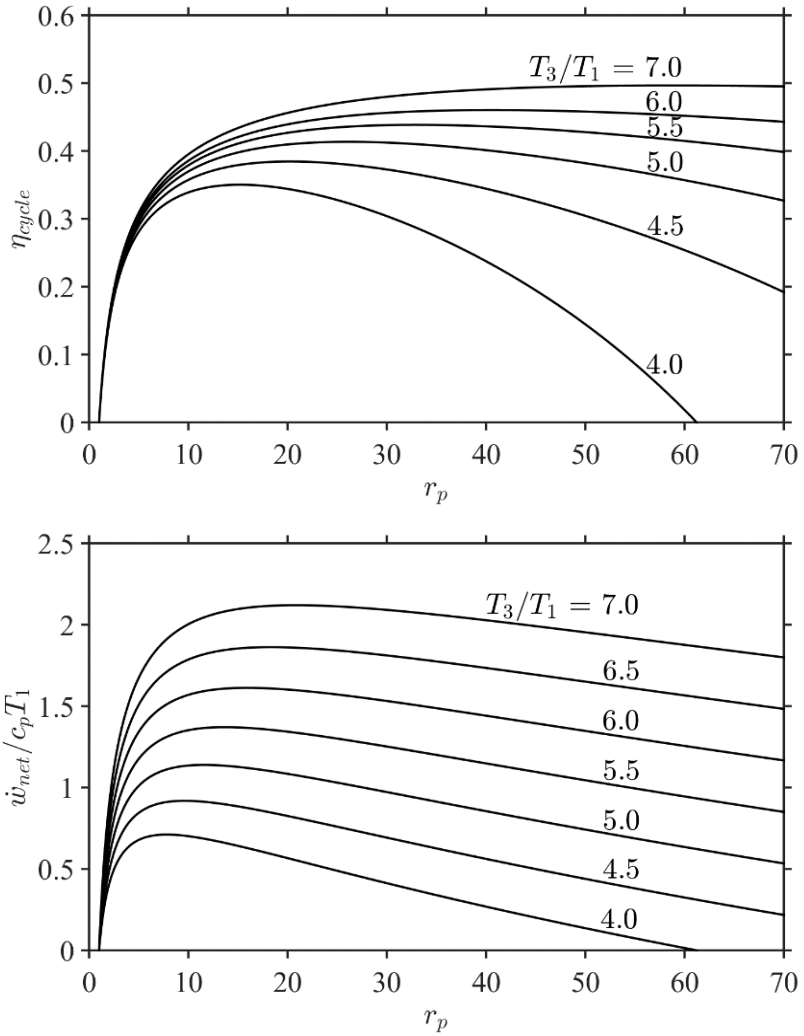

Figure 1.6. Joule cycle efficiency and non-dimensional specific work output.

$$\eta_{comp.} = \eta_{turb.} = 0.9.$$

If we now consider that the compressor and turbine stage are not isentropic, with their efficiency defined as follows

$$\eta_{comp.} = \frac{T_{2s} - T_1}{T_2 - T_1} \qquad \eta_{turb.} = \frac{T_3 - T_4}{T_3 - T_{4s}} \tag{1.3}$$

The non-dimensional specific work is now defined as

$$\frac{\dot{w}_{net}}{c_p T_1} = \eta_{turb.} \frac{T_3}{T_1}\left(1 - \frac{1}{r_p^{\frac{\gamma-1}{\gamma}}}\right) - \frac{1}{\eta_{comp.}}\left(r_p^{\frac{\gamma-1}{\gamma}} - 1\right) \tag{1.4}$$

A typical turbine and compressor efficiency in a modern gas turbine engine design is approximately 0.9. Figure 1.6 re-plots the data in fig. 1.5 using this value.

With a non-ideal compressor and turbine stage, the cycle efficiency becomes a function of the temperature ratio. Without the complexities of the cooling streams, the highest efficiencies are observed to occur at the largest bypass ratio and temperature ratios.

The parameter of most interest to the airline operator is the specific fuel consumption (sfc) of the engine. This is defined as the fuel consumption over the specific work output, and as defined by Saravanamuttoo et al. (2001), is related to the cycle efficiency by

$$\eta_{cycle} = \frac{\dot{w}_{net}}{fL} = \frac{1}{sfc\ L} \tag{1.5}$$

Thus improvements in cycle efficiency directly translate to improvements in sfc.

We now consider one further design parameter, the bypass ratio of the engine. A turbofan engine utilises a large fan, typically located at the front of the engine and driven by the LP turbine, which consumes more air than the core of the engine. We define the bypass ratio in terms of the mass flow rate through the core of the engine $\dot{m}_{core}$ and the amount of air consumed by the fan which bypasses the core $\dot{m}_b$

$$bypass\ ratio = \dot{m}_b\ /\dot{m}_{core} \tag{1.6}$$

Figure 1.7 plots the gross thrust, net thrust and sfc of a representative engine at a range of bypass ratios, using the same core. The gross thrust is that produced by the fan and core, whilst the net

thrust subtracts the aerodynamic drag encountered at cruise which increases with a larger diameter fan. The gross thrust is of most interest at take-off conditions when airspeed is low and thrust demands are high, whilst net thrust is most relevant at cruise conditions where thrust requirements are substantially lower and the airspeeds higher. The gross thrust of the engine increases almost linearly with bypass ratio, whilst the net thrust increases as the square root of bypass ratio. An engine with a large bypass ratio will thus have a higher amount of thrust available at take-off compared to cruise which is a desirable characteristic for a commercial jet airliner. Critically, it is most evident that the sfc decreases with increasing bypass ratio

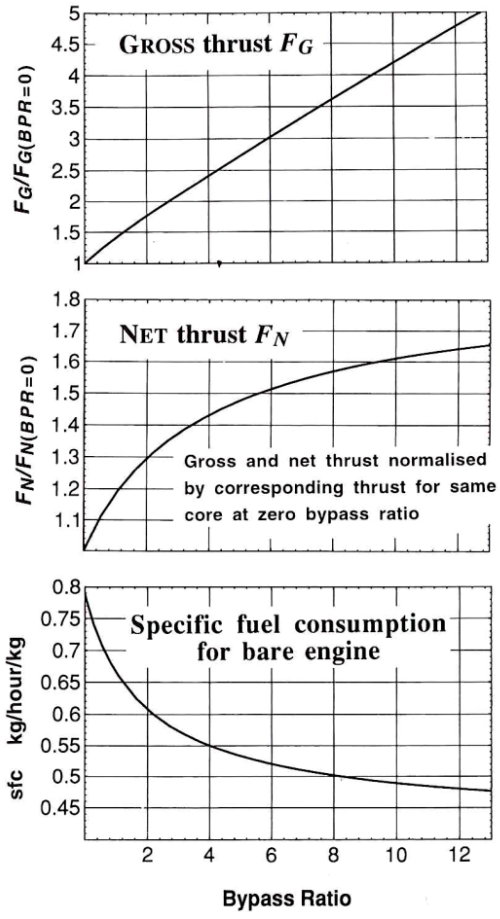

Figure 1.7. Thrust and sfc as a function of bypass ratio for a typical engine. Cumpstey (2003).

One method of increasing the bypass ratio is to increase the size of the fan. Indeed this has been the trend in the last 30 years. However, increasing the fan diameter has practical drawbacks, weight is increased and aerodynamic drag is increased. Engines also begin to begin to become

impracticably large beyond a certain point, necessitating radical airframe redesign. There is now increasing focus on increasing the bypass ratio by reducing the size of the core. To do this the non-dimensionalised specific work output must be increased to maintain a similar output power for a lower core mass flow rate. Referring back to fig. 1.6, it is clear that to achieve this objective the temperature ratio and thus TET of the engine must be increased to maintain similar efficiencies.

This continual rise in TET necessitates improvements to the materials and cooling of the turbine stage. Components which in the past required only modest cooling are now looking to be life limiting without improvements to the cooling system. One such component is the HP rotor casing and this project investigates the use of film cooling on this part.

1.4 Thesis Overview

The current generation of civil aircraft engines are highly complex machines. This thesis considers only one small component, the HP rotor casing, as highlighted in fig. 1.8.

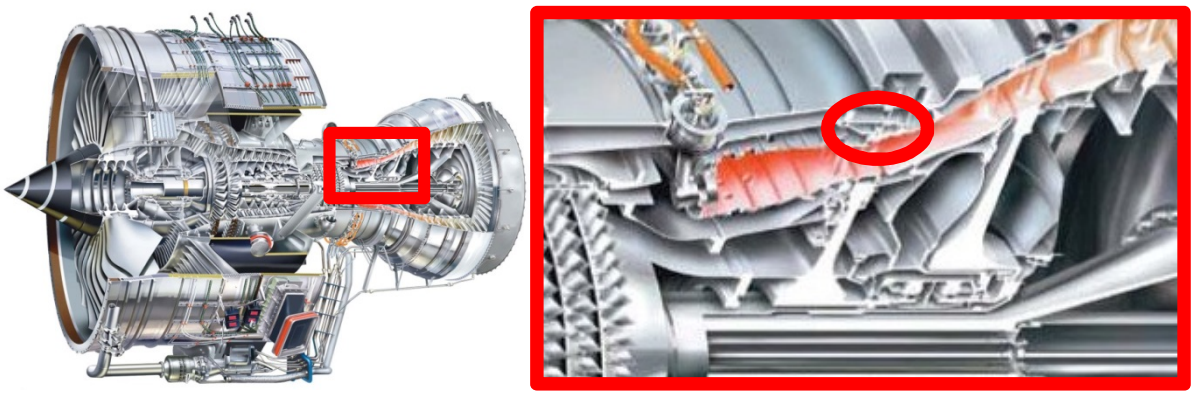

Figure 1.8. Location of HP rotor casing on Trent 900 engine, Rolls Royce (2015).

The research presented in this thesis covers a broad range of topics, as such each chapter is quite distinct and contains its own literature review and nomenclature. All work was focussed on the key objectives of the project and each chapter is outlined below.

Chapter 2: Exploitation of Acoustic Effects in Film Cooling

Until now, it has been assumed that cooling holes subject to temporal changes in exit static pressure have behaved in a pseudo-steady way. Numerical investigation discovered this was not the case. This chapter discusses the fundamental mechanism of pressure wave propagation through cooling holes, and describes systems in which holes which have been acoustically shaped have led to a direct improvement in cooling hole performance. The mechanism relies on sequential pressure wave reflection within an acoustically shaped hole, and is therefore applicable in regions where the external surface is subject to large pressure wave fluctuations at high frequency. The principle is developed analytically, and then demonstrated with a number of CFD simulations. It is demonstrated that a desired temporal mass flow rate profile can be achieved by appropriate acoustic shaping of the cooling hole.

The purpose of this chapter is to describe the fundamental design considerations relevant to acoustic shaping. The discussion is developed with reference to a film cooling system for the over-tip region of an un-shrouded rotor. The performance benefit of the system, in terms of modulation of unsteady mass flux and ingestion characteristics is quantified. It is believed that this is the first time this significant effect has been exploited in film cooling design.

Chapter 3: Computational Investigation of a Film Cooling Scheme Employed on the Over-Tip Casing of an Unshrouded Transonic Gas Turbine

This chapter describes an unsteady rotor stage CFD model used to model a film cooling scheme employed on an HP rotor casing. This is the first published model of its type. For the first time, heat transfer results are presented for the casing and the interaction of the coolant with the rotating rotor tip is described. Results highlight that the acoustic effects described in the previous chapter are evident in a full 3D computational model.

Chapter 4: Impact of Casing Coolant Injection on Rotor Efficiency

This chapter quantifies the impact of casing coolant ejection on the blade row efficiency. A number of cooled turbine efficiency models are described and data taken from the previous chapters CFD model is used to compare them. It is seen that certain cooling schemes can improve blade row efficiency. The cause of this improvement is investigated and it is shown that the coolant ejection reduces the over-tip leakage mass flow rate by up to 12%. This reduces the magnitude of the tip leakage vortex and subsequently the losses incurred in this region. The chapter also expands on the transportation of coolant within the passage using detailed CFD analysis.

Chapter 5: Development of new TFHFGs

This chapter details the improvements made to the design and fabrication of thin-film heat flux gauges at Oxford. These improvements have been driven by the desire to improve measurement accuracy and resolution in short duration wind-tunnel experiments.

A thin film heat flux gauge (TFHFG) measures heat flux by recording the temperature history of thin film resistive temperature sensors sputtered onto an insulating substrate. The heat flux can then be calculated using Fourier's law of heat conduction.

A new fabrication process utilising technology from the manufacture of flexible printed circuit boards is outlined, which enables the production of significantly smaller and more robust gauges than those previously used. A new automated calibration facility is described and used to compare old and new gauges.

Chapter 6: Experimental Investigation of Uncooled Rotor Casing Heat Transfer and Improved Data Processing Techniques

In this chapter improvements to data processing routines and instrumentation are described using experimental data taken on an instrumented uncooled rotor casing. The measurements

were taken in the Oxford Turbine Research Facility (OTRF), an engine-scale rotating turbine facility which replicates engine-representative conditions of Mach number, Reynolds number, and gas-to-wall temperature ratio. High density arrays of miniature thin-film heat-flux gauges were used with a spatial resolution of 0.8 mm and temporal resolution of ~120 kHz. The small size of the gauges, the high frequency response, and the improved processing methods allowed very detailed measurements of the heat transfer in this region. Time-resolved measurements of T_{AW} and Nu are presented for the casing region (-30% to +125% C_{AX}) and compared to other results in the literature. The results provide an almost unique data set for calibrating CFD tools for heat transfer prediction in this highly unsteady environment dominated by the rotor over-tip flow.

Chapter 7: Experimental Investigation of a Film Cooling Scheme Employed on the Over-Tip Casing of an Unshrouded Transonic Gas Turbine

Two sets of experimental studies are described in this chapter which were conducted on the OTRF. An initial study which did not yield acceptable results is first described and used to highlight areas of improvement. A second study is then presented which makes use of the data processing improvements described in the previous chapter as well as incorporating the lessons learnt from the initial experimental campaign. For the first time, time-resolved measurements of T_{AW} and η' are presented for the casing region (-30% to +125% C_{AX}) of a film cooled casing. The results are discussed and compared to the earlier CFD analysis.

1.5 Chapter Nomenclature

c_p	Specific heat capacity	$\dot{m}$	Mass flow rate
C_{AX}	Rotor tip axial chord	Nu	Nusselt number
γ	Ratio of specific heats	p	Pressure
η	Efficiency	$\dot{q}$	Heat flux
η'	Film cooling effectiveness	r_p	Pressure ratio (p_3/p_1)
f	Fuel to air ratio	T	Temperature
F	Thrust	$\dot{w}$	Work
L	Lower calorific value of fuel		

Subscripts

1	Compressor inlet	b	Bypass
2	Compressor outlet	*core*	Core
3	Turbine inlet	G	Gross
4	Turbine outlet	N	Net
AW	Adiabatic wall	s	Isentropic

Chapter 2: Exploitation of Acoustic Effects in Film Cooling

2.1 Abstract

There have been numerous studies of the behaviour of shaped film cooling holes for turbine applications. It is known that the introduction of coolant is an unsteady process, and a handful of studies have described and characterised the unsteadiness. To the author's knowledge there are no studies in which unsteady acoustic effects have been actively exploited such that they have led to novel designs with improved cooling performance.

This chapter discusses the fundamental mechanism of pressure wave propagation through cooling holes, and describes systems in which holes which have been acoustically shaped have led to a direct improvement in film cooling hole performance. The mechanism relies on sequential pressure wave reflection within an acoustically shaped hole, and is therefore applicable in regions where the external surface is subject to large pressure wave fluctuations at high frequency. The principle is developed analytically, and then demonstrated with a number of computational fluid dynamics (CFD) simulations. It is demonstrated that a desired temporal mass flow rate profile can be achieved by appropriate acoustic shaping of the cooling hole.

The purpose of this chapter is to describe the fundamental design considerations relevant to acoustic shaping. The discussion is developed with reference to a film cooling system for the over-tip region of an un-shrouded rotor. The performance benefit of the system in terms of modulation of unsteady mass flux and ingestion characteristics is quantified. It is believed that this is the first time this significant effect has been exploited in film cooling design.

2.2 Introduction

In most turbine cooling applications, film cooling holes and slots operate with relatively steady inlet and outlet conditions. There have been a few studies in which unsteady effects have been described and characterised: here we refer to flapping of the exit flow if two metastable states exist, and the unsteady kidney vortex entrainment process, etc. No studies have yet reported fundamental mechanisms which can be directly used to benefit performance by improved unsteady design. In this sense, there has so far been no *exploitation* of unsteady acoustic effects in film cooling.

In this chapter we explore fundamental acoustic mechanisms that can be exploited in some film cooling applications, leading to significant improvement in cooling hole performance by correct acoustic design. By *acoustic design* we mean holes shaped so as to maximize the benefit of pressure wave propagation within cooling holes. The methods are most applicable in regions where there is a significant driving pressure wave at a period similar to the transit time of sound through a cooling hole. These effects have long been utilised in the design of internal combustion engine inlet manifolds and exhausts (Winterbone and Pearson (2000)). In turbo-machinery operating at transonic conditions, much of the compressor and turbine are exposed to strong periodic pressure waves. Here we focus on the over-tip casing of a high pressure unshrouded rotor: an example in which the pressure variation is significant. This location is interesting because film cooling is both challenging and becoming an increasing priority.

The challenge lies in designing a film cooling system which can deliver good film performance whilst subject to large high frequency excursions in external pressure caused by the passing rotor blade. As the suction side approaches the quasi-steady coolant-to-mainstream pressure ratio will be high, and we risk film lift-off. As the pressure side approaches the pressure-ratio will be low or below unity and we risk ingestion. With a steady design philosophy it seems difficult to balance these contradictory requirements.

There is one published study by Chana and Haller (2009) and a number of patents, for example Lowe et al. (2003), which present proposed cooling schemes for the casing over-tip region. None of these designs appear to consider the unsteady impact of the rotor potential field. Previous publications by Chana and Haller (2009) on casing cooling systems have assumed that the cooling holes operate in a quasi-steady state manner. In this chapter we show that the unsteady effects are highly significant from a design perspective, allowing pressure wave reflection effects to be directly exploited by correct acoustic shaping of the holes.

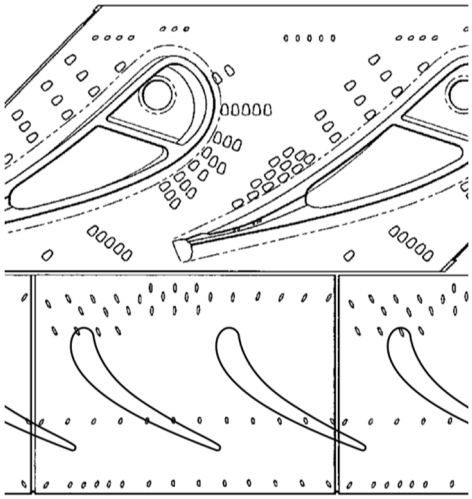

Figure 2.1. HP rotor casing film cooled segments, Lowe et al. (2003).

2.3 Rotor Casing Over-Tip Environment

To frame the discussion around a particular application we now describe the rotor casing over-tip flow environment, before turning to unsteady mechanisms that could be exploited in this region.

The rotor casing over-tip region (stationary frame of reference) is subject to large temporal variations in both static pressure and heat load. Previous studies have shown experimentally and computationally that the heat load on the casing is highest as the rotor tip and pressure side (PS) pass over the surface, El-Gabry and Ameri (2010), Chana and Jones (2003), Thorpe et al. (2004), Thorpe et al. (2007). The heat load reduces as the suction side (SS) approaches. The heat load is dominated by the local temperature, the gas on the suction side being lower in

temperature on account of having performed more work (higher deflection angle in the stationary frame). It has been postulated that the casing boundary layer is scraped off by the over-tip flow and entrained into the tip leakage vortex, Thorpe et al. (2007), Behr et al. (2007), which follows the SS of the rotor blade in the region between 100% and 80% span for most reported studies. Evidence for this includes higher heat transfer rates in the over-tip region and on the PS of the blade. On the PS of the blade velocities are lower, which supports the hypothesis of a re-establishing boundary layer, and attendant higher heat transfer coefficients. Where the boundary layer fluid is wrapped into the tip leakage vortex, the coolant film would also be removed from the surface.

Consider now a quasi-steady design approach in which we assume that films discharge approximately at the quasi-steady mass flow rate. In this approach the boundary conditions are defined by the inlet total pressure, which varies little, and the time-instantaneous external static pressure, which varies by a significant amount under the rotor blade. To avoid ingestion, we must design so there is a coolant-total-to-mainstream-static pressure ratio greater than unity as the PS of the blade approaches. For the same total pressure, for a typical rotor design, we would expect the coolant-to-mainstream pressure ratio to take a value of at least 2 when the suction side of the blade approaches. That is, choked, or near-choked flow through the hole. The result is that local to the SS, where heat transfer rates are lowest, we inject very high mass flow rates at pressure ratios that would cause film lift-off. The separated films are unlikely to reattach, because they are rolled into the tip leakage vortex. The attendant aerodynamic loss is high. On the PS, where heat transfer rates are highest, we inject very little flow. It is clear that a hole which behaves in a quasi-steady manner is ineffective at cooling the casing local to both the PS and SS of the passing rotor blade.

If we consider the heat load distribution on the casing surface, we require greatest cooling flow under the tip and local to the pressure side of the blade, where the external pressure is highest.

The requirement is in direct opposition to the temporal mass flow variation expected through a conventional hole using quasi-steady arguments.

We now explore the fundamental mechanisms of acoustic design (pressure wave reflection within holes) before demonstrating, as an example, how it can be applied to the rotor-casing over-tip environment to modify the temporal mass flux through a cooling hole.

2.4 Fundamental mechanisms

2.4.1 Pressure Wave Propagation

The equations describing pressure wave propagation can be derived by considering an isentropic compression wave moving along a duct of constant cross-sectional area A, Kentfield (1993). The validity of the isentropic assumption is discussed later.

Consider a pressure wave travelling between stations 2 and 1 of the duct shown in fig. 2.2. The wave travels at the speed of sound a with respect to the gas which is travelling at speed u. In a time increment δt the wave travels a distance δx. Assuming the flow is frictionless and adiabatic, applying continuity, the net mass inflow in period δt is equal to the mass accumulated in the same period

$$(u + \delta u)(\rho + \delta\rho)A\delta t - \rho u A\delta t = \delta\rho A\delta x \tag{2.1}$$

The wave travels at a with respect to the bulk flow which travels at u, so

$$\delta x = (a + u)\delta t \tag{2.2}$$

Combining and neglecting δ^2 terms

$$\delta u = a\frac{\delta\rho}{\rho} \tag{2.3}$$

This relates the difference between the inflow and outflow velocities to the proportional density change and the sonic velocity.

Assuming wave is isentropic

$$\left(\frac{a}{a_{ref}}\right)^{\frac{2}{\gamma-1}} = \frac{\rho}{\rho_{ref}} \tag{2.4}$$

Differentiating and combining

$$\delta u = \left(\frac{2}{\gamma - 1}\right)\delta a \tag{2.5}$$

Finally integrating

$$a - \left(\frac{\gamma - 1}{2}\right)u = constant = J_{+} \tag{2.6}$$

A similar analysis can be performed for an expansion wave and the resulting governing equations are summarised in fig. 2.3, these equations define the Riemann invariants, Courant (1948). These equations can also be derived using the method of characteristics, whereby the 1D wave equation is solved along characteristics, in this case corresponding to lines of constant J_{+} and J_{-} Anderson (2004).

The above derivation assumes a discontinuous pressure wave, which is unrealistic as waves either fan out or thicken as they travel, due to the crest and foot moving at different velocities.

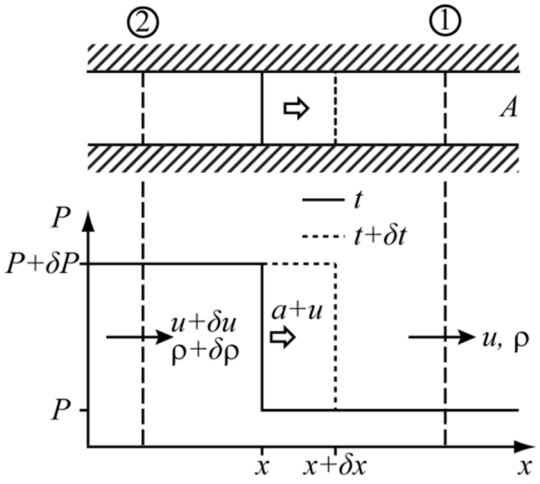

Figure 2.2. Propagation of an infinitesimally weak compression wave along a duct of uniform area.

Compression Wave	Expansion Wave
$J_+ = a - \left(\frac{\gamma-1}{2}\right)u = c$	$J_+ = a - \left(\frac{\gamma-1}{2}\right)u = c$
$c = constant$ $+u \longrightarrow$	
$J_- = a + \left(\frac{\gamma-1}{2}\right)u = c$	$J_- = a + \left(\frac{\gamma-1}{2}\right)u = c$

Figure 2.3. Summary of Riemann invariant equations governing pressure wave propagation.

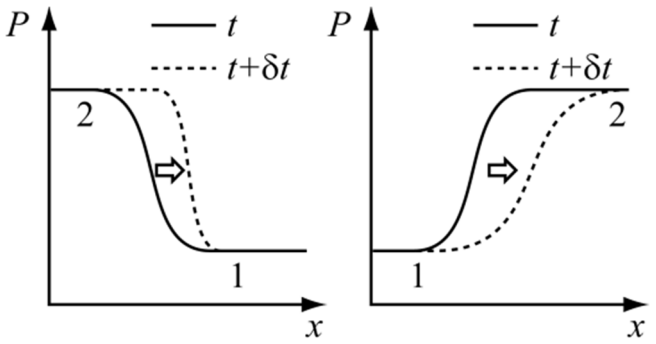

Figure 2.4. Steepening of a compression wave (left) and fanning of an expansion wave (right).

Consider an expansion wave as illustrated in fig. 2.4. The isentropic relationship applies between the crest and the foot

$$\frac{a_2}{a_1} = \left(\frac{P_2}{P_1}\right)^{\frac{\gamma-1}{2\gamma}} \tag{2.7}$$

Combining with eqn. 2.6 it is clear that the local velocity at the crest of the wave is greater than at the foot

$$a_2 + u_2 > a_1 + u_1 \tag{2.8}$$

The crest of the wave propagates more rapidly than the foot leading to a fanning out of the wave.

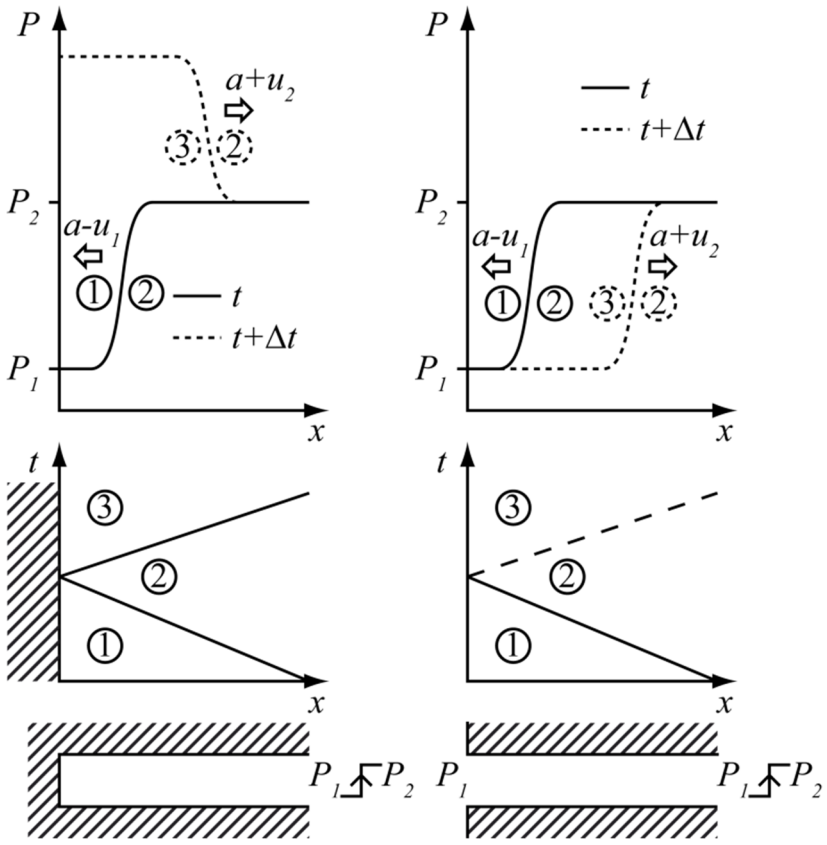

Figure 2.5. Pressure wave interactions with a closed end (left) and an open ended (right).

The same treatment can be applied to a compression wave yielding the result that the crest again propagates faster than the foot, leading to a steepening of the wave with time. If a compression wave is allowed to propagate for sufficient time, it becomes apparent that the wave will become a discontinuity, or a normal shock wave. In this limit, heat transfer processes across the shock

make the process non-isentropic. For pressure ratios lower than 2:1, however, the approximation yields negligible errors, Kentfield (1993).

2.4.2 Interactions with Boundaries

A cooling hole can be represented by a duct with a constant total pressure at the inlet and (at an instant in time, at least) a given static pressure at the outlet. We are interested in the situation where the pressure is suddenly changed at the outlet, by, for example, the passing of a rotor blade. In analysing the interaction of the pressure wave with the boundary conditions, there are three situations of interest. The interaction of a pressure wave with: a) a closed inlet (this represents a forward facing step); b) an open outlet; c) an open inlet.

Closed Inlet

Consider the interaction of a compression wave with the closed end of a duct, as illustrated in fig. 2.5. The fluid in the duct is initially at rest. At $t = 0$ we impose a step in pressure from P_1 to P_2 at the outlet. The wave propagates to the left increasing the pressure in the duct. The wave travels at the speed of sound a with respect to the initially stagnant fluid. This is represented by a line on the x, t chart partitioning a region demarcated 1. The mass contained within the duct increases as the pressure rises, requiring an inflow at the open end. Applying eqn. 2.6 and eqn. 2.7 to the crest and foot of the wave as it propagates from the open end to the closed end

$$a_2 = a_1 \left(\frac{P_2}{P_1}\right)^{\frac{\gamma-1}{2\gamma}} \tag{2.9}$$

$$u_2 = \frac{2a_1}{\gamma - 1}\left(1 - \left(\frac{P_2}{P_1}\right)^{\frac{\gamma-1}{2\gamma}}\right) \tag{2.10}$$

At the wall, the bulk flow velocity is zero ($u_3 = 0$), thus from continuity a wave must be reflected. Evaluating eqn. 2.6 and eqn. 2.7 for this reflected compression wave as it propagates through region 2

$$a_3 = a_2 + \left(\frac{\gamma - 1}{2}\right) u_2 \tag{2.11}$$

$$P_3 = P_2 \left(1 + \frac{u_2(\gamma - 1)}{2a_2}\right)^{\frac{2\gamma}{\gamma - 1}} \tag{2.12}$$

A similar analysis can be conducted for a reflected expansion wave. For both cases a wave of equal sign is reflected creating a region of higher or lower pressure than that incident in the region behind the reflected wave.

Open Outlet

It can be assumed that at an open ended outlet the static pressure remains constant during an interaction with a pressure wave. If the interaction is considered isentropic then eqn. 2.7 holds at the inlet and

$$a_1 = a_3 \tag{2.13}$$

To conserve momentum and satisfy continuity a wave is reflected. Hence applying eqn. 2.6 across a reflected expansion wave

$$u_3 = 2u_2 \tag{2.14}$$

A similar analysis of a reflected expansion wave yields the same result, that a wave of negative sign is reflected. The fluid in region 3 has double the bulk flow velocity as that in region 2 (given by eqn. 2.10).

Open Inlet

An open ended inlet can be considered to have a constant total pressure during an interaction with a pressure wave. Applying the steady flow energy equation at the boundary (assuming quasi-steady flow conditions)

$$c_p T_0 = c_p T + \frac{u^2}{2} \tag{2.15}$$

Hence for an ideal gas at the boundary

$$a_0{}^2 = a^2 + \left(\frac{\gamma - 1}{2}\right) u^2 \tag{2.16}$$

Applying eqn. 2.7 it is clear that a constant value of P_0 corresponds to a constant value of a_0. Considering momentum and continuity then it is also apparent that a wave must be reflected. Thus applying eqn. 2.6 and eqn. 2.16 across the reflected wave it is possible to determine the values of u_3, a_3 and P_3 in region 3. When a pressure wave interacts with an open inlet, a pressure wave of opposite sign to that incident is reflected.

Tapered Ducts

The elementary theory discussed in this section cannot directly deal with tapered ducts however the concepts can be extended to offer an insight into their behaviour. For instance, a tapered duct can be considered as a series of expanding stepped inlets or converging outlets. Each infinitesimal step will generate an infinitely small reflection, the result being a gradual reflected wave. This property opens the possibility of shaping the reflected pressure waves by modifying the duct geometry.

Using the method of characteristics it can be shown that the losses associated with reflections from a tapered section are less than those from open inlet duct reflection, Kentfield (1993).

2.4.3 Reduced Frequency Effects

So far the analytical discussion has focused on pressure wave effects. Another factor that will cause the cooling hole to behave in a non-quasi-steady manner is the inertial effects of the fluid within the hole. As discussed by R. J. Miller (personal communication, 29 July, 2015), the momentum stored within the cooling hole can be evaluated by considering the unsteady momentum equation on a control volume enveloping the fluid within the hole. If we neglect the viscous and gravitational effects and take the *x* axis to be along the centreline of the cooling hole, the 1D momentum equation can be defined along a hole as follows

$$\frac{d\rho V_x}{dt} + \frac{d\rho V_x V_x}{dx} + \frac{dp}{dx} = 0 \tag{2.17}$$

Integrating along the hole and assuming that the hole is of constant cross section and compressibility effects are small ($\Delta(\rho V_x V_x) \approx 0$)

$$\Delta p = L_1 \frac{d\rho V_x}{dt} \tag{2.18}$$

Here we have ignored the momentum of the inlet and outlet flow.

This unsteady momentum flux term will cause the hole to exhibit non-quasi steady behaviour For a hole to exhibit quasi-steady behaviour. We can non-dimensionalise this term by dividing through by the momentum flux through the hole

$$\frac{L_1\, d\rho V_x/dt}{\rho V_x V_x} = \frac{L_1\, d/dt}{V_x} = \frac{L_1 f}{V_x} \cong \frac{L_1}{\lambda}\frac{a_{0C}}{\overline{V_x}} = St \tag{2.19}$$

This defines the Strouhal number in terms of the overall length L_1, the rotor passing frequency f (dominant frequency) and the average velocity u_x. We can also substitute in the non-dimensional hole length to further define this parameter.

Typically, these unsteady momentum terms are considered important at a $St > 0.1$. For a hole of length 0.055 λ, the corresponding $\overline{V_x}/a_{0c}$ required to exceed $St > 0.1$ is 0.55, above a hole length of 0.1 λ, the $St > 0.1$ for all flow rates. Clearly these unsteady momentum effect will have some effect on the hole outlet mass flow rate, causing it to differ from the quasi-steady results. This must be considered during the analysis of the results.

2.5 Numerical Model

The commercial URANS CFD solver, Fluent, was used to generate quantitative data for the interaction of pressure waves with a number of shaped holes. The simulations were run at scaled engine realistic conditions relevant to a transonic turbine test facility in which demonstration experiments have been performed (the Oxford Turbine Research Facility, Anderson (2004)). An engine realistic temporal static pressure profile (measured in a transonic turbine facility) was imposed at the outlet of the holes.

2.5.1 Geometry and Mesh

A 2D axisymmetric model was used to investigate cylindrical and shaped holes of different lengths. All holes had an outlet diameter of 0.5 mm. The hole total axial length (L_1) can be expressed in terms of λ, the path-length of a pressure wave propagating at the speed sound, a_{0c}, in stagnant gas at the coolant total temperature, T_{0c}, for a duration equal to one rotor passing event, where the passing frequency is f.

$$\lambda = \frac{a_{0c}}{f} \tag{2.20}$$

A structured quadrilateral grid was used, with $y^+ \sim 1$ local to the walls and further refinement located at changes in area, to capture the unsteady pressure wave reflection. An example of the mesh is shown in fig. 2.6. Small inlet and outlet plena were included to capture pressure wave processes in the immediate vicinity of the hole. There is no entirely satisfactory way of

imposing the outlet boundary in a simplified study of this type. Full unsteady HP stage simulations with embedded cooling holes in a casing wall under a sliding interface have been performed by the author, in which the exit pressure boundary condition is imposed by a moving rotor. The same effects were demonstrated in the more sophisticated simulations, but a discussion is beyond the scope of this study, the primary purpose of which is to introduce the basic mechanisms. The geometry of the outlet plenum was selected to minimise its volume and to locate the boundary condition defining the unsteady pressure profile close to the hole exit.

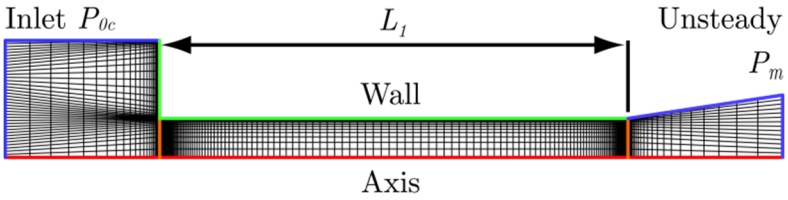

Figure 2.6. Structured mesh of a typical 2D axisymmetric hole.

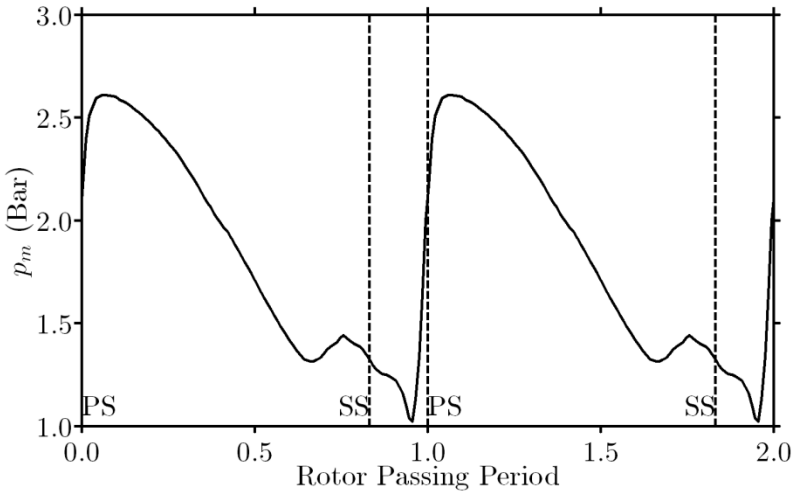

Figure 2.7. Unsteady outlet temporal pressure profile $P_m(t)$.

2.5.2 Boundary Conditions

The outlet boundary conditions are taken from CFD simulations and measurements conducted in the Oxford Turbine Research Facility by Chana and Jones (2003) and Qureshi et al. (2011)). The facility was operated as an engine-scaled rotating transonic HP turbine stage, in which Re, M, T_g/T_w and non-dimensional speed were all matched to engine conditions (NGV $Re = 2.54E6$, NGV exit $M = 1.054$, $T_g/T_w = 1.54$), Chana et al. (2013). The unsteady pressure

profile on the rotor over-tip casing was measured using fast response pressure transducers embedded in the casing wall. Good agreement with an unsteady HP-stage simulation run by Qureshi et al. (2011) of the same geometry was obtained. Time averaged results from a single stage CFD simulation of the rotor casing static pressure at 70% of rotor tip axial chord are presented in fig. 2.7. The rotor passing frequency was approximately 10 kHz. The large excursions in static pressure and the high frequency content of the signal are evident: the maximum and minimum static pressures were approximately 2.6 bar and 1 bar.

It is worth noting that for a transonic rotor, the passing speed at the mainstream temperature is close to the magnitude of the sonic velocity at that temperature. For a coolant-to-mainstream temperature ratio of approximately 2, therefore, the passing speed of the rotor (and therefore the pressure wave) exceeds the speed of sound at the coolant flow temperature by a factor equal to approximately $\sqrt{2}$.

The locations of the inlet and outlet boundaries for the 2D axisymmetric CFD simulations were chosen to minimise pressure wave reflections at the timescales of interest. The temporal static pressure distribution in fig. 2.7 was used as the outlet boundary condition (to represent the exit of a cooling hole located on the casing at 70% rotor tip axial chord). The inlet boundary condition was defined with a constant T_{0c} and P_{0c}. P_{0c} was set to a range of values between $1.05 < P_{0c}/\overline{P_m} < 1.47$ where $\overline{P_m}$ is the time mean hole-exit static pressure. A coolant temperature of $T_{0c} = 290$ K was used, corresponding to the correct engine-representative non-dimensional condition for the tunnel, for a temperature ratio of $T_{0m}/T_{0c} \sim 2$. For a rotor passing frequency of approximately 10 kHz, we obtain λ = 36.4mm.

2.5.3 Solver Setup

Fluent was run with the pressure-based coupled algorithm and the realizable k-ε turbulence model with standard wall functions. All equations were set to second order formulation. The

solution was demonstrated to be independent of time step at 150 time steps per rotor passing period. The model was run for a large number of passing events until a periodic solution was obtained. Post-processing was performed in Matlab.

2.6 CFD analysis

2.6.1 Effect of Hole Shape on Acoustic Behaviour: Long Cylindrical Hole

To visualise the pressure reflections within a hole, results from the unsteady CFD solutions are presented on space-time diagrams coloured by local static pressure or mass flow. The *x*-axis denotes normalised hole length (x/L_1), and the *y*-axis non-dimensionalised time expressed in terms of rotor passing period (ft). The intensity represents the variable of interest.

The local static pressure within a cylindrical cooling hole of length $L_1 = 0.25\lambda$ (9.1 mm) is shown in fig. 2.8. The rapid rise in pressure at the hole outlet ($x/L_1 = 1$) at $ft = 0$ generated by arrival of the rotor blade pressure surface sends a compression wave (marked by solid line) from the outlet to the inlet of the cooling hole. The wave travels at the speed of sound relative to the gas. Because the velocity of the gas is in opposition to the propagating wave, the pressure wave arrives at the hole inlet significantly later than $ft = 0.25$: if the gas in the hole were stagnant we would expect the wave to arrive at inlet at $ft = 0.25$ for a hole of length $L_1 = 0.25\lambda$. The pressure wave and the potential field of the hole (due to net mass flow through it) are superimposed, so there is an increase in both static and total pressure following the wave from outlet to inlet (along the solid line).

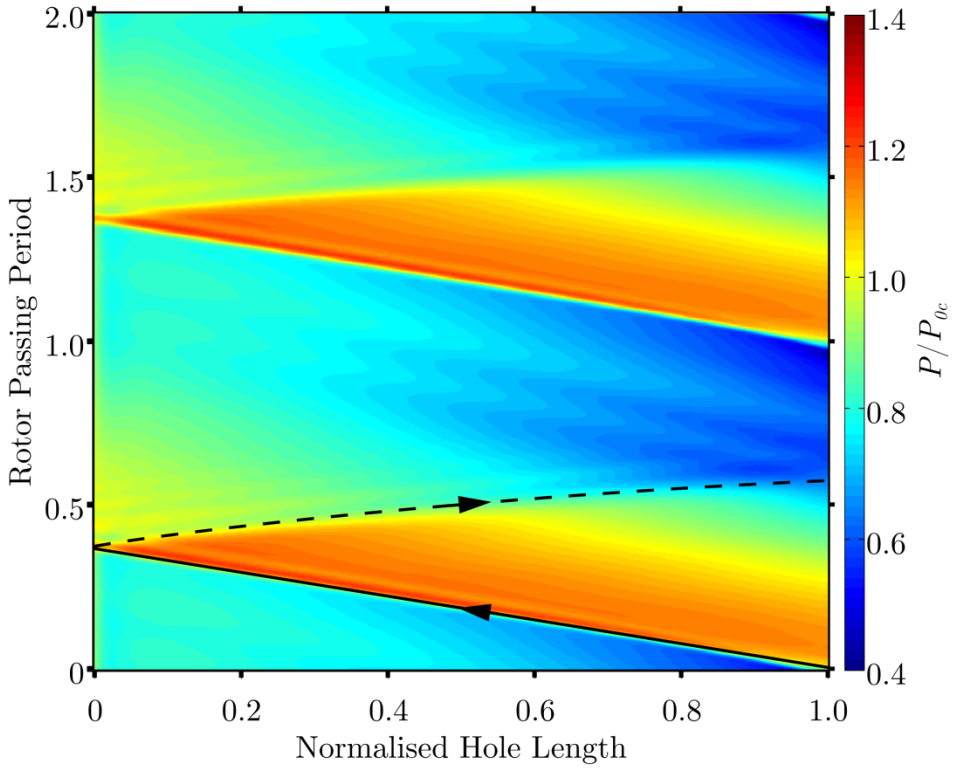

Figure 2.8. Plot of unsteady P within cylindrical hole.

$L_1 = 0.25\lambda$, $P_{0c}/\overline{P_m} = 1.25$.

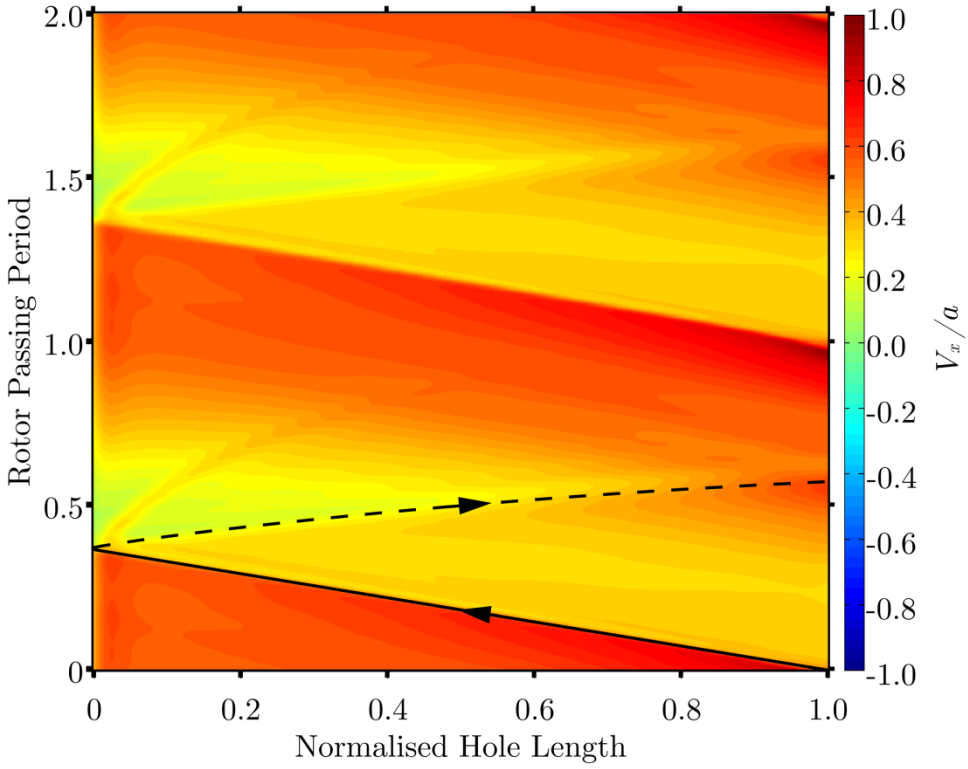

Figure 2.9. Plot of unsteady V_x/a within cylindrical hole.

$L_1 = 0.25\lambda$, $P_{0c}/\overline{P_m} = 1.25$.

When the pressure wave reaches the hole inlet ($ft = 0.35$) an expansion wave of similar strength is reflected back down the hole (dashed line). This acts to cancel the increase in pressure caused by the compression wave. The expansion wave travels in the same direction as the bulk velocity of the coolant gas, so the transit time to the hole exit is lower than $\Delta(ft) = 0.25$. The expansion wave arrives at the hole exit at approximately $ft = 0.60$. The expansion wave is reflected as a weak compression wave back up the hole (fig. 2.8).

The corresponding axial Mach number distribution (V_x/a) is presented in fig. 2.9. This is closely related to the mass flow rate distribution within the hole (temporally and spatially). We can see that neither the inlet nor our outlet Mach number is particularly uniform in time. Neither does the Mach number distribution follow the quasi-steady model, in which we expect temporal variation but no spatial variation (horizontal banding on an *x*-*t* plot). The temporal variation at both locations is strongly influenced by the propagation of pressure waves through the bulk flow.

Also evident in fig. 2.9 is an entropy wave generated at the reflection of the pressure wave with the hole inlet. Figure 2.10 plots the unsteady entropy within the hole and shows this more clearly. Entropy is generated due to non-reversible processes, for a cooling hole operating under steady conditions this would typically be due to frictional losses and heat transfer. Within the unsteady example, small amounts of entropy are generated across the propagating compression wave, indicating a slightly non-isentropic compression (a weak shock). Further entropy is generated in regions corresponding to rapid acceleration and high Mach number, indicating non-isentropic expansion and frictional losses.

Entropy waves are typically observed at the interaction of a pressure wave with a change in area, in this case the hole inlet. The reflection of the pressure wave with the hole inlet perturbs the hole inlet flow field by imposing what can be thought of as a temporary blockage. These

changes to the flow field generate entropy in the vicinity of the hole inlet, resulting in a rise in the total temperature of this fluid. This higher temperature fluid then propagates down the hole at the bulk flow velocity, generating the characteristic entropy wave observed in fig. 2.10.

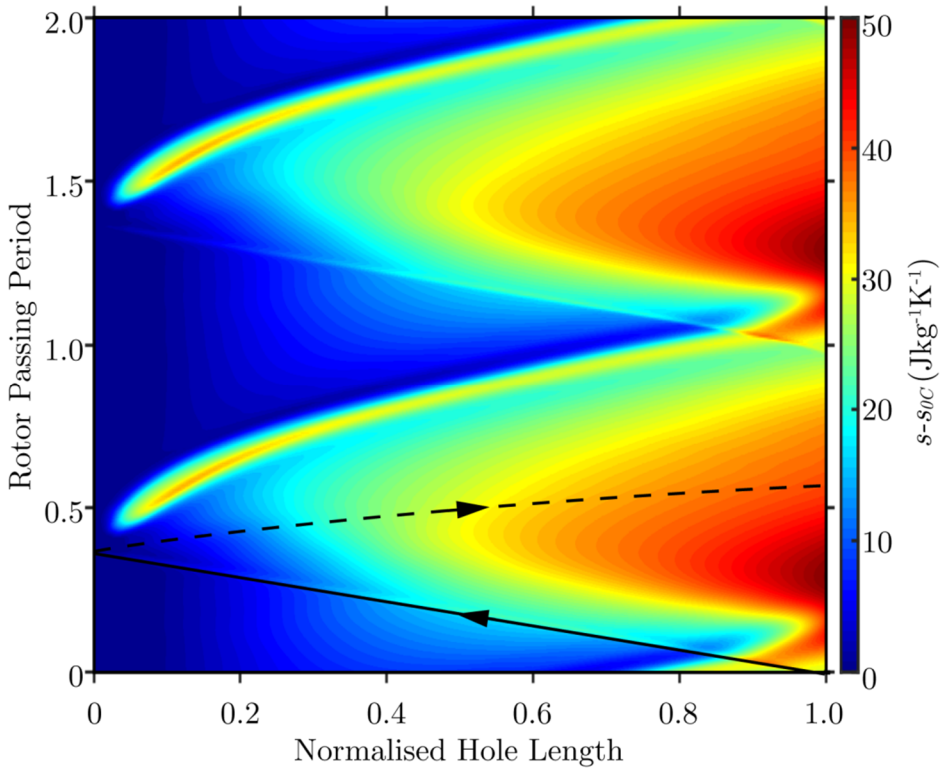

Figure 2.10. Plot of unsteady entropy within cylindrical hole.
$L_1 = 0.25\lambda$, $P_{0c}/\overline{P_m} = 1.25$.

In the time period $0.0 \leq ft \leq 0.6$, during which the pressure wave is travelling up and down the hole, the static pressure in the hole is elevated, and the mass flow rate is higher than a quasi-steady model would predict. In the time period immediately following $ft = 0.60$, there is a reduction in static pressure and the mass flow is reduced. The mass flow recovers only when the next pressure wave arrives. We can use this principle to *tune* the temporal mass flow rate distribution.

A key design parameter is the time taken between the compression wave being transmitted up the hole and the reflected expansion wave returning to the hole exit. We have discussed this in general terms, but formally we integrate as follows:

$$t_r = \int_0^{L_1} \left(\frac{1}{a_{0c} - u_1} + \frac{1}{a_{0c} + u_2} \right) dx \tag{2.21}$$

If $u < a$ and we assume that $\overline{u_1} \cong \overline{u_2}$ then this collapses to

$$t_r \cong \frac{2L_1}{a_{0c}} \tag{2.22}$$

For the hole fig. 2.8, taking our assumption, we expect the expansion wave to arrive at $ft = 0.50$. In fact, as discussed, the wave arrives at $ft = 0.60$. The explanation lies in the fact that $\overline{u_1} > \overline{u_2}$. This is illustrated by fig. 2.9.

2.6.2 Effect of Hole Shape on Acoustic Behaviour: Short Cylindrical Hole

Consider now the acoustic behaviour of a very short hole. We consider a hole with length $L_1 = 0.055\lambda$ (2.0 mm).

The *x-t* plot of static pressure is shown in fig. 2.11. Because the transit time is so short, we see several reflections of compression (solid) and expansion (dashed) waves within the hole. The static pressure field immediately at the hole exit is significantly modified by these reflections. The Mach number distribution within the hole is also affected (fig. 2.12) although here only the first compression and expansion waves can easily be seen. It is clear that shortening the hole has the effect of reducing the non-dimensional time (fraction of rotor passing period) at which the expansion wave returns. We will discuss the effect on temporal mass flow rate distribution subsequently.

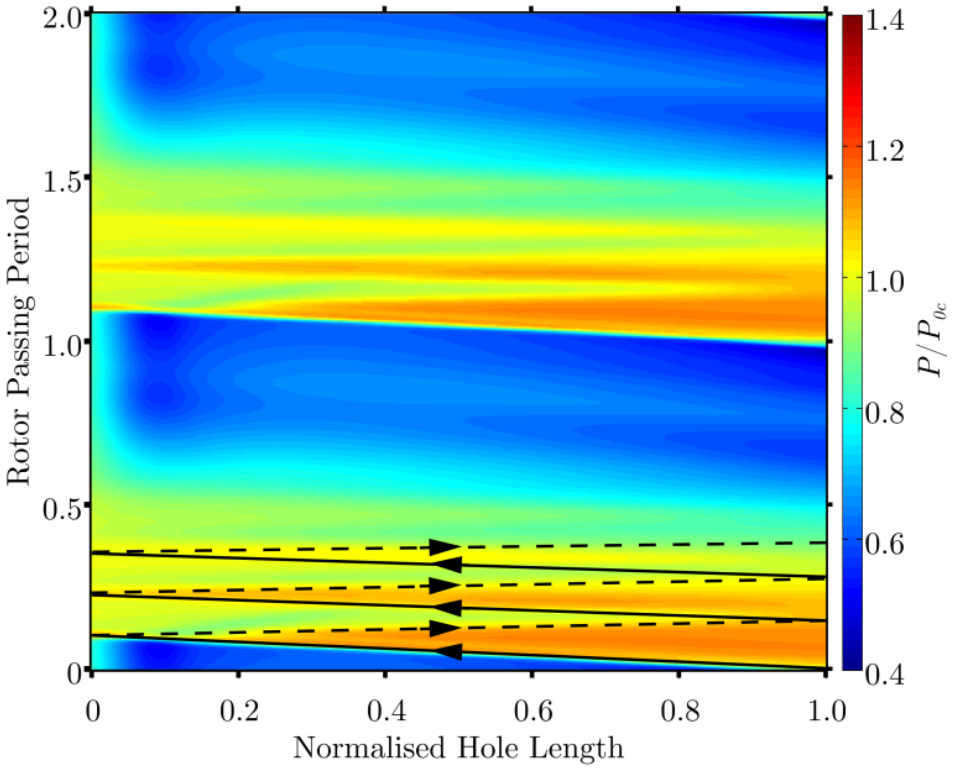

Figure 2.11. Plot of unsteady P within cylindrical hole.

$L_1 = 0.055\lambda$, $P_{0c}/\overline{P_m} = 1.25$.

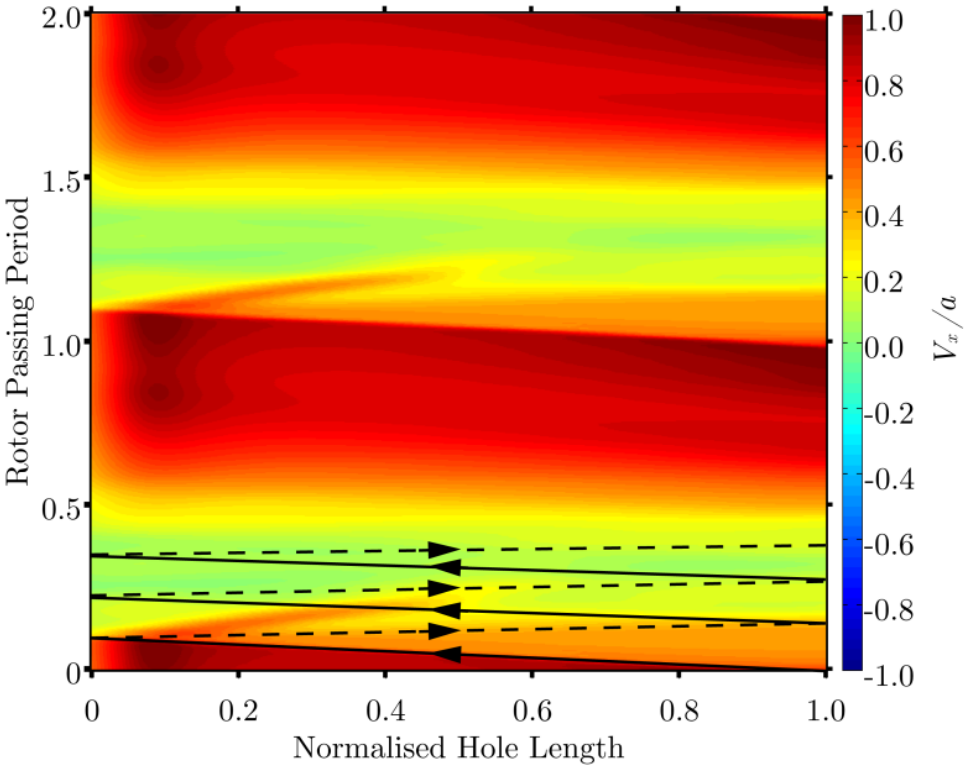

Figure 2.12. Plot of unsteady V_x/a within cylindrical hole.

$L_1 = 0.055\lambda$, $P_{0c}/\overline{P_m} = 1.25$.

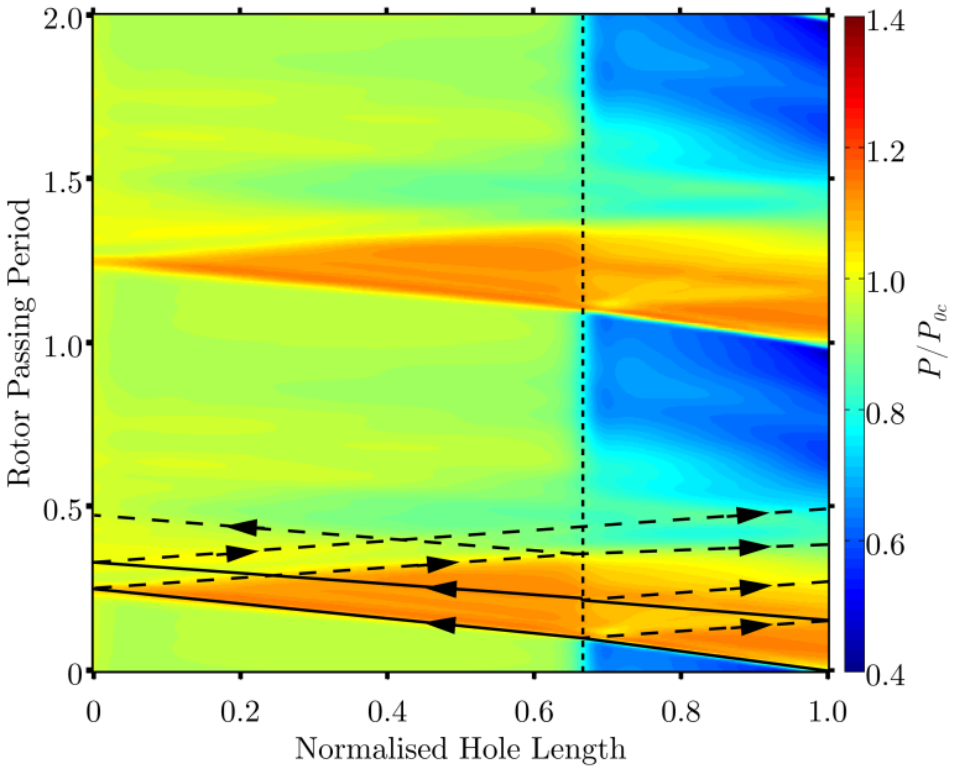

Figure 2.13. Plot of unsteady P within compound cylindrical hole.

$L_1 = 0.17\lambda$, $L_2 = 0.055\lambda$, $P_{0c}/\overline{P_m} = 1.25$.

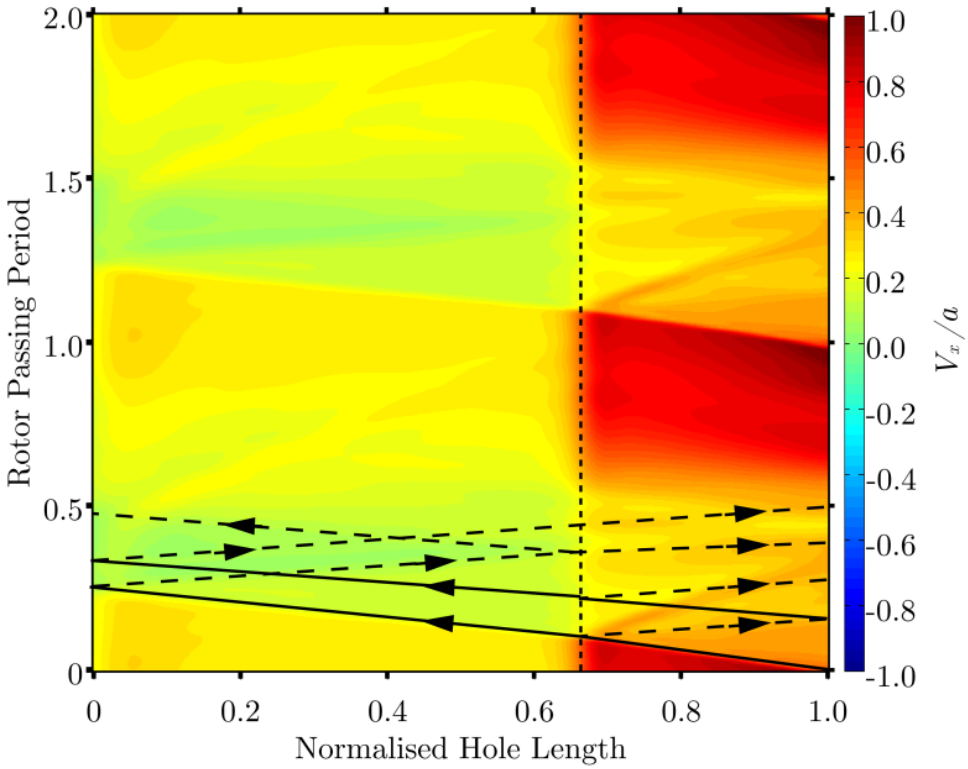

Figure 2.14. Plot of unsteady V_x/a within compound cylindrical hole.

$L_1 = 0.17\lambda$, $L_2 = 0.055\lambda$, $P_{0c}/\overline{P_m} = 1.25$.

2.6.3 Effect of Hole Shape on Acoustic Behaviour: Compound Cylindrical Hole

In analogy to the reflection coefficient of 1 for a hole with a closed inlet (reflected wave of same magnitude and sign), and a reflection coefficient of -1 for an open inlet (reflected wave of same magnitude but opposite sign), it can be shown that forward and backward facing steps with finite area ratios provide reflections coefficients between -1 and 1.

We can use conical or stepped transitions in duct diameter to control the timing and sign of pressure reflections, to achieve a particular desired temporal modification to M at the hole outlet. We now provide a specific example.

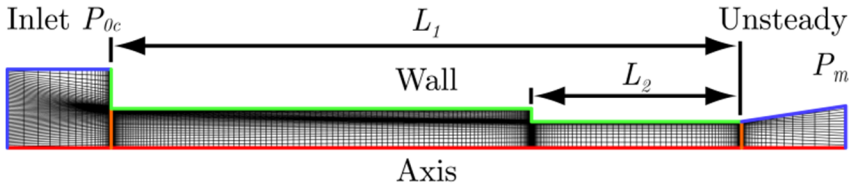

Figure 2.15. Compound hole geometry and mesh.

Consider the compound hole in fig. 2.15. The overall length is $L_1 = 0.17\lambda$. It is composed of an outlet section of length $L_2 = 0.055\lambda$ and diameter 0.5 mm, and an inlet of length $L_1 - L_2 = 0.115\lambda$ and diameter 0.75 mm. For a more complex hole of this type, which has one discreet step in area, we expect a series of compression and expansion reflections. Where a pressure pulse meets a finite increase in area it is partially reflected with opposite sign, and partially transmitted with the same sign. Where a pressure pulse meets a finite decrease in area it is partially reflected with same sign, and partially transmitted with the opposite sign. Let us now consider the example in hand.

The static pressure within the hole is shown in fig. 2.13. The primary compression wave travels up the hole from $ft = 0.0$, $x/L_1 = 1.0$ to $ft = 0.1$, $x/L_1 = 0.68$ where a step increase in hole area is encountered. At the change in area, an expansion wave is propagated in the reverse direction towards the exit ($x/L_1 = 1.0$), and a compression wave is propagated forwards

towards the inlet ($x/L_1 = 0.0$). Both waves have diminished strength. The forward running compression wave travels faster in the stationary frame after the step due to the change in area (change in carrier gas flow speed). Using area changes of this type allows the designer to take advantage of superposition effects and control the temporal pressure profile at the hole outlet. The effect on the Mach number distribution in the hole is shown in fig. 2.14 for completeness.

2.6.4 Effect of Hole Shape on Temporal Mass Flow Rate Profile

In the introduction we discussed the problems associated with introducing coolant into a region with significant temporal variation in static pressure: coolant lift-off at low hole-outlet static pressure and mainstream ingestion at high hole-outlet static pressure. Both these effects degrade the film cooling performance. A designer might desire to reduce the temporal variation in coolant mass flow through the cycle, or to control the point in the cycle at which most coolant is ejected. Whatever the aim, the temporal variation of mass flow rate (and attendant momentum flux ratios) is the parameter the designer might most wish to exercise control over through correct acoustic design.

To illustrate the importance of acoustic effects on the temporal variation of mass flow rate, quasi-steady mass flow rates were calculated for each geometry and flow condition. The quasi-steady mass flow rates were calculated utilising the steady state capacity characteristics and the time instantaneous pressure ratio across the holes. The steady state capacity characteristics for each hole geometry were calculated by running the CFD at steady conditions for 20 pressure ratios between $0.3 < P_m/P_{0c} < 1$. The mass flow has been normalised by the mass flow rate when the hole is fully choked.

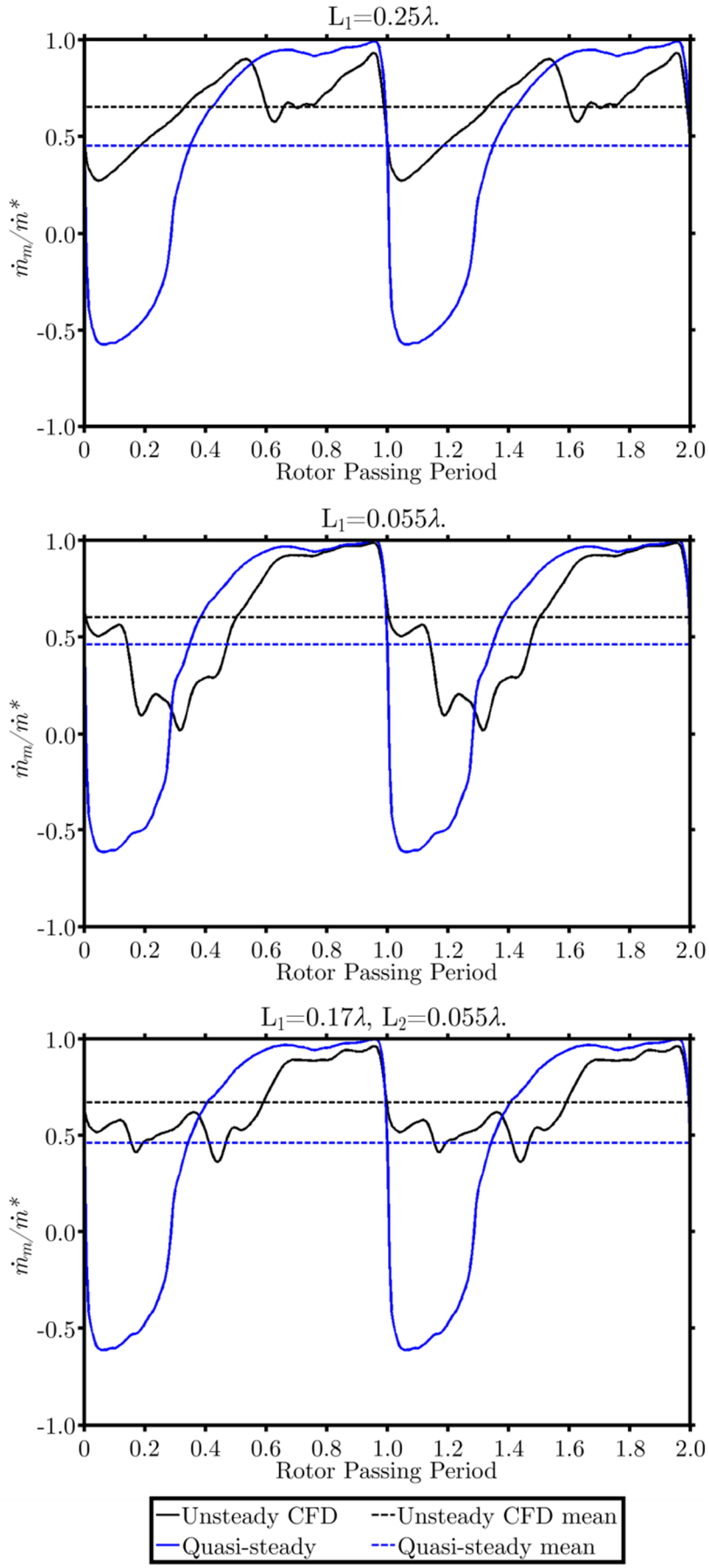

Figure 2.16. Plot of $\dot{m}_m$ *across exit plane of holes.* $P_{0c}/\overline{P_m} = 1.25$.

The results are presented in fig. 2.16 (solid blue lines). The normalised quasi-steady temporal mass flow rate distributions are similar for all three designs, demonstrating that the steady state capacity characteristics with pressure ratio are similar for all hole shapes.

The unsteady mass flow rates (computed using the method described previously, and relating to the *x-t* plots discussed) are also presented in fig. 2.16. The unsteady mass flow rates are very different from the quasi-steady trends, illustrating the importance of correct acoustic design. The mean mass flow rates through the cycle for the unsteady and quasi-steady methods are shown by dashed lines. For the three designs presented here, the unsteady CFD prediction yields a time averaged mass flow rate which is 30% to 45% higher than the quasi-steady solutions at a pressure ratio of $P_{0c}/\overline{P_m} = 1.25$. It is worth noting that for a hole

of length $L_1 = 0.5\lambda$ (not discussed here) unsteady CFD predicts an average mass flow rate which is lower than the quasi-steady result at $P_{0c}/\overline{P_m} < 1.25$: acoustic design is clearly important.

In the period in which the ingested compression wave elevates the pressure within the hole (during the transit to and from the hole inlet), the exit mass flow rate is increased in the unsteady simulation. This is simplest to see for the cylindrical hole with $L_1 = 0.25\lambda$. In the period $0.0 \leq ft \leq 0.6$ the pressure within the hole is elevated by the passage of the compression wave, and the mass flow is increased over the quasi-steady level (fig. 2.8 and fig. 2.16). Following the arrival of the reflected expansion wave at the hole exit ($ft \cong 0.60$) the pressure in the hole is reduced and the mass flow is below the quasi-steady level (fig. 2.8 and fig. 2.16). The overall effect is to moderate the temporal variation in mass flow rate

The maximum (outflow) and minimum (outflow or ingestion) mass flow rates for the quasi-steady and unsteady simulation are presented in Table 2.1 for each of the three designs. In the quasi-steady simulations the variation in time of the normalised mass flow rate ($\dot{m}_m/\dot{m}^*$) is

significant for all three designs. The hole operates between fully choked in the outflowing direction to a mass flow rate corresponding to between 57 and 61% of the fully choked condition during ingestion. It is clear that based on quasi-steady design an operating pressure ratio of $P_{0c}/\overline{P_m} = 1.25$ would be insufficient to ensure there was no ingestion.

Consider now the unsteady CFD prediction results. For all three hole geometries the variation in time of the normalised mass flow rate is substantially reduced (over the quasi-steady simulations). At an operating pressure ratio of $P_{0c}/\overline{P_m} = 1.25$ none of the holes ingest mass flow. There are now significant differences between the three designs due to pressure wave reflections with clear evidence of superposition effects for the compound cylindrical hole.

Table 2.1. Quasi-steady and unsteady CFD computed mass flow rates for $P_{0c}/\overline{P_m} = 1.25$.

	$L_1 = 0.25\lambda$	$L_1 = 0.055\lambda$	$L_1 = 0.17\lambda\ L_2 = 0.055\lambda$
Quasi-steady: $\dot{m}_m/\dot{m}^*$ mean	0.452	0.462	0.462
Quasi-steady: $\dot{m}_m/\dot{m}^*$ max	0.991	0.996	0.996
Quasi-steady: $\dot{m}_m/\dot{m}^*$ min	-0.572	-0.614	-0.613
Quasi-steady $\dot{m}_m/\dot{m}^*$ delta	**1.563**	**1.610**	**1.609**
Unsteady: $\dot{m}_m/\dot{m}^*$ mean	0.651	0.602	0.671
Unsteady: $\dot{m}_m/\dot{m}^*$ max	0.931	0.986	0.960
Unsteady: $\dot{m}_m/\dot{m}^*$ min	0.272	0.019	0.363
Unsteady: $\dot{m}_m/\dot{m}^*$ delta	**0.659**	**0.967**	**0.597**

The conclusion is that the temporal mass flow rate variation can be substantially reduced by better acoustic design. The compound cylindrical hole design has a relatively flat temporal mass flow rate distribution compared to the short and long hole designs. The effects associated with acoustic shaping are significant and can be employed by designers seeking to modify the temporal mass flux variation to achieve particular design objectives.

2.6.5 Effect of Hole Length on Ingestion Characteristics

In addition to temporal *shaping* of the outlet mass flow rate profile, an important design consideration in most cooling systems is to prevent ingestion of flow from the hot gas path. It is clear from fig. 2.16 that the hole geometry has a significant impact on ingestion (defined as negative mass flux across the hole exit plane) characteristics. A study of the effect of hole length on ingestion characteristics for cylindrical holes is now presented.

Cylindrical holes with lengths in the range $0.025\lambda \leq L_1 \leq 0.50\lambda$ (0.91 – 18.2 mm) were run for mean pressure ratios in the range $1.05 \leq P_{0c}/\overline{P_m} < 1.45$. To achieve these pressure ratios, the outlet temporal pressure distribution was unchanged, and the inlet total pressure was modified. The results are presented in fig. 2.17. The ordinate shows the mean pressure ratio $P_{0c}/\overline{P_m}$ and the abscissa shows the hole length as a fraction of λ. The solid line shows minimum (temporal) mean pressure ratio $P_{0c}/\overline{P_m}$ required to avoid ingestion for the particular (engine realistic) temporal variation in pressure presented in fig. 2.7. The strong variation in the minimum value of $P_{0c}/\overline{P_m}$ (between 1.4 and 1.1) demonstrates the importance of correct acoustic design. A cylindrical hole of length 0.25λ requires the lowest value, $P_{0c}/\overline{P_m} = 1.1$ to avoid ingestion. As discussed in the context of fig. 2.8, fig. 2.9 and fig. 2.16, for an acoustic length equal to ¼ of the rotor passing period, reflected waves arrive at an interval equal to ½ the rotor passing period and act to suppress the dominant rotor passing frequency. With correct acoustic design, only a very small pressure margin is required to avoid ingestion.

By the same argument poor performance would be expected for a hole length of 0.5λ, which one would expect to reinforce the dominate frequency. Indeed, a peak of $P_{0c}/\overline{P_m} = 1.4$ at $L_1 = 0.45\lambda$ is observed. At this highly non-optimal design point, very high pressure margins are required to avoid ingestion.

The standard deviation of the hole outlet mass flow rate is also shown in Fig 16. as a carpet plot (colour scale on RHS) as a function of mean pressure ratio $P_{0c}/\overline{P_m}$ and hole length. For very short holes ($L_1 \leq 0.10\lambda$) and for holes approaching the length for reinforcing resonance ($L_1 = 0.50\lambda$) there is large temporal variation in mass flow rate, particularly at low values of $P_{0c}/\overline{P_m}$. The effect is reduced for high values of $P_{0c}/\overline{P_m}$, for which the hole is choked for a larger fraction of the cycle. For values of L_1 close to $L_1 = 0.25\lambda$, acoustic effects suppress the temporal variation in outlet mass flow rate.

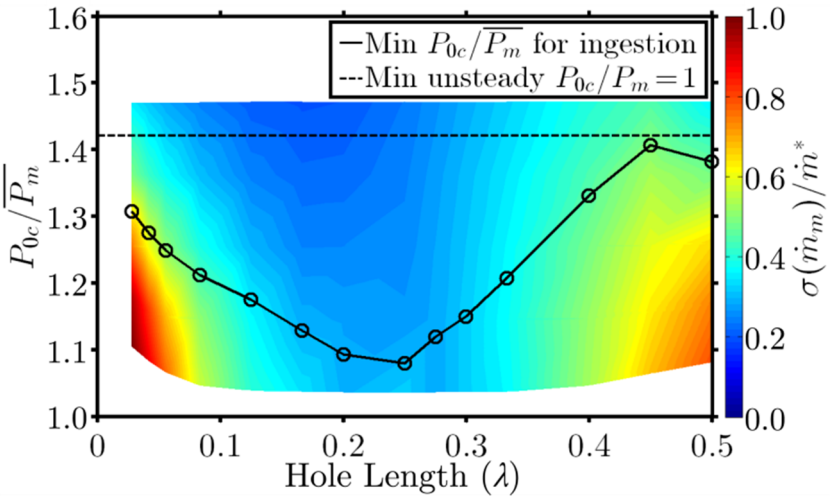

Figure 2.17. Plot of minimum pressure ratio for ingestion and normalised standard deviation of $\dot{m}_m$ across exit plane of cylindrical holes of different lengths.

The conclusion is that for most applications, where there is a desire to reduce temporal fluctuations in mass flow rate, the range $0.15\lambda \leq L_1 \leq 0.35\lambda$ might be considered optimum for designers.

2.7 Scaling to Engine Conditions

The results presented in this chapter are for non-dimensional conditions relevant to a particular engine-scaled test turbine for which λ = 36.4 mm. This value was chosen for the CFD investigation to complement a parallel experimental invesgitation in the Oxford Turbine Research Facility.

A typical value of λ for a current civil engine is approximately 45 mm resulting in a desired hole length of $6.75 \leq L_1 \leq 15.75$ mm. When considering a typical lay-angle of 20 –30 ° in the wall of an effusion cooling system corresponding to a desired wall thickness of 2.5 to 8.3 mm, it is clear that the implementation of optimum lengths is practicable in real engine systems. If more advanced manufacturing technologies such as metal laser sintering are employed, then the use of shaped hole geometries can yield further benefits in terms of moderation of the temporal mass flow rate variation.

2.8 Conclusions

Pressure wave propagation within cooling holes subject to large unsteady static pressure variations has been discussed from a simple analytical standpoint, to gain insight into the basic physical mechanisms. A computational study of the effect of hole shape and length on the acoustic behaviour of cooling holes has been described. Several hole geometries were modelled computationally at scaled engine-realistic conditions. The pressure and mass flow rate fluctuations were broadly in line with those predicted by a simple analytical treatment developed for ducts with relatively low bulk mass flow rates.

We have demonstrated that unsteady effects due to pressure wave reflections within holes have a highly significant effect on the performance of film cooling holes in terms of ingestion characteristics, mean and temporal modulation of mass flux. All these factors are likely to have a strong bearing on the film cooling effectiveness of the system. It is necessary to be aware of these effects during the design stage, and to acoustically tune holes to achieve the optimum performance.

The application of superposition effects within cooling holes was simulated with a compound cylindrical hole geometry. This proved that changes in cooling hole diameter could be utilised to tailor the cooling hole unsteady mass flux to a desired response. For the particular application

of a cooling hole located on a rotor over-tip casing, this could be utilised to significantly enhance the relative coolant mass flux in the period of time following the passing of the pressure surface (when the hole outlet pressure is high) of the blade tip. In other applications the same effects could be used to moderate the temporal variation in mass flow rate.

Quantitative results were as follows:

1) Holes of near-optimum acoustic design have been demonstrated to resist ingestion down to relatively low mean pressure ratios ($P_{0c}/\overline{P_m} = 1.08$) compared with the pressure ratios predicted by quasi-steady analysis ($P_{0c}/\overline{P_m} = 1.42$). Holes of poor acoustic design have similar performance to that predicted by quasi-steady analysis ($P_{0c}/\overline{P_m} = 1.40$). See fig. 2.17.
2) The normalised temporal mass flow rate variation ($\dot{m}_m/\dot{m}^*$) was reduced from 0.967 to 0.597 for holes of similar length by better acoustic shaping of the hole (Table 2.1).
3) The normalised temporal mass flow rate variation ($\dot{m}_m/\dot{m}^*$) has been shown to be a strong function of non-dimensional hole length, varying between 1 and 0.3 for hole lengths in the range $0.025\lambda \leq L_1 \leq 0.50\lambda$ (0.91 – 18.2 mm) for a mean pressure ratio of $P_{0c}/\overline{P_m} = 1.20$ (fig. 2.17).
4) For values of L_1 close to $L_1 = 0.25\lambda$, acoustic effects suppress the temporal variation in outlet mass flow rate. For very low L_1 and values of L_1 close to $L_1 = 0.5\lambda$, acoustic effects enhance the temporal variation in outlet mass flow rate (fig. 2.17)

Acoustic design of film cooling holes has a significant effect on film cooling performance for holes subject to large unsteady static pressure variations. By considering the acoustic behaviour of film holes it is possible to implement practical designs with considerably improved performance. It is believed this is the first time this important mechanism has been discussed in the literature of turbine cooling, and possibly the first example of the direct *exploitation*

(through design) of unsteady effects to control how the film is beneficially modulated on a surface through temporal mass flow rate control (and therefore momentum flux ratio control).

2.9 Chapter Nomenclature

A	Duct area
a	Sonic velocity
a_i	Sonic velocity in region i
a_{0c}	Sonic velocity at hole inlet
γ	Ratio of specific heats
D_1	Hole inlet diameter
D_2	Hole exit diameter
f	Rotor passing frequency
$J_{+/-}$	Riemann invariants
λ	Wavelength of pressure wave propagated in coolant
L_1	Total hole length
L_2	Length of outlet hole section
M	Mach number
$\dot{m}^*$	Choked hole mass flow rate
$\dot{m}_m$	Hole exit plane mass flow rate
P	Static pressure
P_i	Static pressure in region i
P_{0c}	Inlet plenum total pressure
P_m	Hole exit static pressure
$\overline{P_m}$	Mean hole exit static pressure
ρ	Density
Re	Reynolds number
T_{0c}	Inlet plenum total temperature
T_{0m}	Mainstream total temperature
T	Static temperature
T_g	Mainstream static temperature
T_i	Static temperature in region i
T_w	Wall temperature
t	Time
t_r	Duration of pressure wave propagation and reflection
u	Bulk flow velocity
u_i	Bulk flow velocity in region i
V_x	Axial flow velocity
x	Flow aligned location
y^+	Dimensionless wall distance

Chapter 3: Computational Investigation of a Film Cooling Scheme Employed on the Over-Tip Casing of an Unshrouded Transonic Gas Turbine

3.1 Abstract

The casing of an unshrouded HP rotor is subjected to high thermal loads at both low and high frequency resulting from the rotor's potential field and the high heat loads imposed by over-tip leakage flows. Increasing turbine entry temperatures necessitate that this component be cooled to ensure satisfactory service life and performance. Film cooling is commonly utilised on the turbine stages of a modern gas turbine, yet there are very few published studies investigating its use on an unshrouded casing.

In this chapter we describe the design and modelling of a film cooled casing. Specifically:

1. Outline the challenges faced in the design of a casing film cooling scheme and how the seemingly hostile film cooling environment can be managed with the use of holes shaped to utilise acoustic pressure wave reflections.
2. Describe an unsteady rotor stage CFD model utilising a sliding interface in the tip gap to model a film cooled casing.
3. Present time resolved and time averaged predictions of adiabatic film effectiveness on the rotor casing. Mechanisms for interaction of the coolant with the rotor tip are proposed and discussed.
4. Acoustic effects due to the passing of the rotor are demonstrated on a 3D CFD geometry, supporting conclusions drawn in the previous chapter on the importance of this effect in a casing film cooling system.

3.2 Introduction

The casing of an unshrouded rotor is subjected to large temporal variations in both static pressure and heat load. Increasing turbine entry temperatures necessitate that the casing be cooled. One such cooling strategy would utilise film cooling. As yet, there has been only one published pair of papers describing a casing film cooling scheme by Chana and Haller (2009). There are also a number of patents relating to the implementation of such a scheme, for example Liotta and Acquaviva (1999), Lee and Durgin (2001), White and Lee (2002), Lowe et al. (2003), Shapiro (2007) and Lee et al. (2012), indicating probable use in an engine.

A novel CFD model of a cooled rotor casing is presented utilising a sliding mesh interface in the tip gap. This is the first published model of a casing film cooling scheme incorporating casing relative motion and provides a unique insight into the complex environment such a scheme is subjected to.

3.2.1 Previous Work

Chana and Haller (2009) present a pair of papers which outline a design methodology for a casing film cooling scheme in conjunction with experimental measurements taken on the OTRF. The design was created with the assistance of a steady state CFD simulation of the rotor passage coupled with a 1D boundary layer code. The influence of the motion of the holes relative to the blade was not modelled. Holes were angled to the time mean flow angle for the entire passage and holes were fed from two plenums. Measurements were made on the OTRF with 7 Thin Film Heat Flux Gauges (THFHGs) with data presented as a time mean heat flux and time mean Nu. The study concluded that there was up to a 44% reduction in casing heat load with $\dot{m}_C/\dot{m}_{12} = 1.85\%$. Values of T_{AW} were not presented, nor was the data decomposed into time-resolved measurements of Nu or T_{AW}.

The previous chapter discusses the challenges faced by a casing film cooling designer and considers the influence of the unsteady rotor potential field on cooling holes located on the rotor casing using a 2D axisymmetric CFD study. Conclusions were that the unsteady mass flux from the hole, along with the ingestion characteristics, are directly linked to pressure wave propagations within the cooling holes. A hole length of $0.15\lambda \leq L_1 \leq 0.35\lambda$ was found to be optimal in modulating the unsteady coolant mass flux in addition to improving the ingestion characteristics.

Mischo et al. (2007) and Behr et al. (2008) discuss the use of casing coolant injection to reduce over-tip leakage flows and improve blade row efficiency using computational and experimental measurements. The computational study of Mischo et al. (2007) utilised an immersed boundary method to model cooling holes on the rotor casing. This extracts local conditions at the hole exit at each time step to separately calculated hole exit conditions which are applied as source functions to the appropriate rotor mesh nodes. This approach is limited in that it does not fully model the cooling hole (acoustic effects not captured) and assumes that the near hole flow field operates in a quasi-steady manner. Further, the number of nodes to which the source terms are applied are restricted due to the source terms having to move at each time step. Hole locations were covered by 4 – 7 nodes in the axial direction and 7 – 11 nodes in the circumferential direction. Despite these limitations this work highlighted that casing coolant injection can be used to reduce the over-tip leakage mass flow rate through blockage effects of the cooling holes and consequently reduce the magnitude of the tip leakage vortex. These results were confirmed by the experimental work of Behr et al. (2008) undertaken on a 1.5 stage rotating facility. Time resolved measurements indicated a reduction in the magnitude of the tip leakage vortex and computed an increase in the blade row efficiency of 0.55% for an injection $\dot{m}_C/\dot{m}_{12}$ = 1%. Neither of these studies considered heat transfer nor transport of coolant in the casing frame of

reference. However, it was observed that the casing boundary layer was scraped off by the rotor tip and entrained into the tip passage vortex.

3.3 CFD Study

To fully incorporate a casing cooling system into a rotor stage CFD model requires the use of a sliding mesh interface located within the rotor tip gap. This was accomplished with ANSYS® Fluent. A rotor only model was chosen to reduce computational time with boundary conditions derived from a full stage CFD model.

3.3.1 Cooling Geometry

Four cooling geometries are investigated in this study. All geometries have cooling holes inclined at 20° to the casing surface. Due to the pressure drop through the rotor passage in the casing frame of reference, it is desirable to feed each cooling hole row with its own plenum. It is also desirable to align the hole exit angle with the time mean flow direction of the flow on the casing. These two requirements, coupled with the close proximity of each cooling hole row necessitate that compromises be made. All cooling geometries utilise four plenums and are outlined in more detail below.

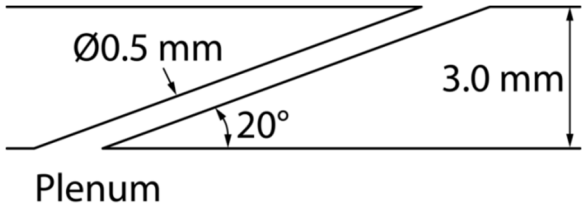

Figure 3.1. Geometry A and B hole geometry.

Geometry A

This is the baseline Rolls Royce design, consisting of 9 rows of 0.5 mm diameter cylindrical holes fed by four plenums. The cooling hole orientations are a compromise between matching the time mean whirl angle on the casing and achieving a geometrically even hole distribution which can be fed by four discrete plenums. This compromise is clearly evident in the selection

of hole orientation angles with some of the rows having an exit angle quite different from the time mean flow angle. The design parameters are given in table 3.1.

Table 3.1. Geometry A, C and D design parameters.

Row	Feed Plenum	Row Exit Location (% C_{AX})	Hole Spacing (°)	Hole Orientation (Angle to axis of rotation) (°)
1	P1	-36.0	1	83
2	P1	-21.3	1	59
3	P1	-3.2	1	39
4	P2	12.4	1	53
5	P2	32.2	1	39
6	P3	52.1	1	52
7	P3	71.5	2	39
8	P4	91.8	1	52
9	P4	111.7	2	39

Geometry B

Geometry B differs from geometry A in its circumferential hole spacing, which is 0.5° for all rows.

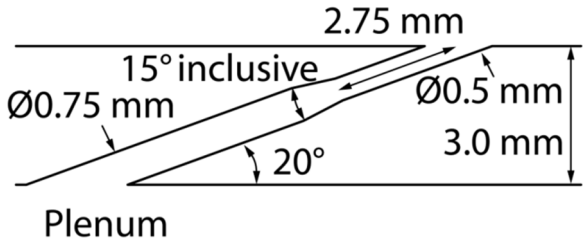

Figure 3.2. Geometry C hole geometry.

Geometry C

Geometry C differs from geometry A in its cooling hole design, which is an acoustically optimised design with geometry given in fig. 3.2. A typical cooling hole mesh is illustrated in fig. 3.3.

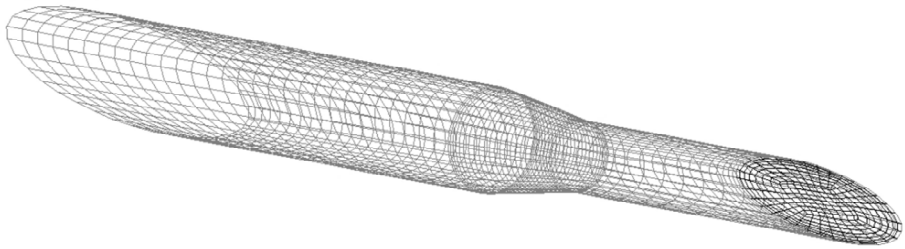

Figure 3.3. Geometry C acoustically optimised cooling hole mesh.

Geometry D

Geometry D is another Rolls-Royce design. It differs from geometry A in its hole design which is given in fig. 3.4. It was conceived as a hole geometry designed to resist rubbing by the rotor tip. This can occur during transient operation of the engine and the fan exit shape was aimed at preventing blockages. From an acoustic perspective this is a very bad design. The expansion at exit acts to magnify the pressure waves within the hole and increases the unsteadiness of the hole exit mass flux.

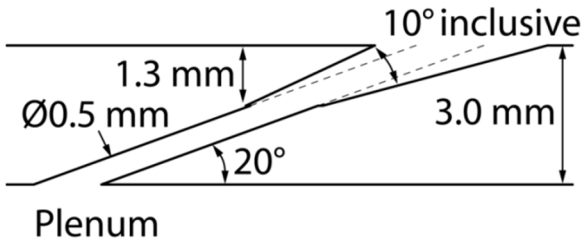

Figure 3.4. Geometry D hole geometry.

3.3.2 Meshing Strategy

The location of the sliding interface is difficult to define due to the small size of the tip gap (0.5 mm). Though sliding meshes are well documented for use in mixing tanks (ANSYS® Fluent 12.0, User manual), where it is possible to define the mesh interface at a location relatively remote from the complex tip leakage flows, the author is not aware of any previous studies using a sliding mesh for flow fields similar to a highly loaded unshrouded rotor.

The non-conformal sliding interface in Fluent uses the virtual polygon approach to calculate fluxes (ANSYS® Fluent 12.0, User manual). This adds diffusion to the solution as the solution is interpolated across the interface. It is desirable to place the interface such that the numerical diffusion will not lead to significant errors, in this case locating it outside of the boundary layer. The sliding mesh interface location was selected such that it captured most of the boundary layer thickness on the rotor casing, corresponding to a distance of 0.4 mm from the casing surface (80% of tip gap). A sliding mesh with an interface 0.1 mm from the casing surface was also tested and the results were very similar.

Rotor Mesh

The area of interest for this study is the region about the rotor tip and the region in close proximity to the casing. The rest of the mesh only needed to capture the aerodynamic flow field of the blade. Due to the large disparities in mesh densities these requirements impose, an unstructured tetrahedral mesh with prism boundary layers was selected over a structured hexahedral mesh. This scheme allowed a very fine mesh to be employed local to the rotor tip and casing whilst a coarse grid was used elsewhere.

Meshing was undertaken in ANSYS® ICEM 12.1 with a number of meshes ranging in size from 1-9 million cells evaluated. Mesh independence for the casing region was observed with 3 million cells. Local to the tip and casing $y+ < 1$, with 33 cells spanning the tip gap.

Casing Mesh

Cooling geometries were meshed using a hybrid meshing approach in ANSYS® ICEM 12.1. A structured mesh was used for both the cooling holes and adjacent to the casing wall, with an unstructured mesh within the plenums. A typical cooling hole contains 10,000 cells in order to capture acoustic effects. The resulting casing region meshes ranged from 3 – 7 million cells

depending on the cooling hole geometry with a y+ < 1 adjacent to the casing wall and within the cooling holes.

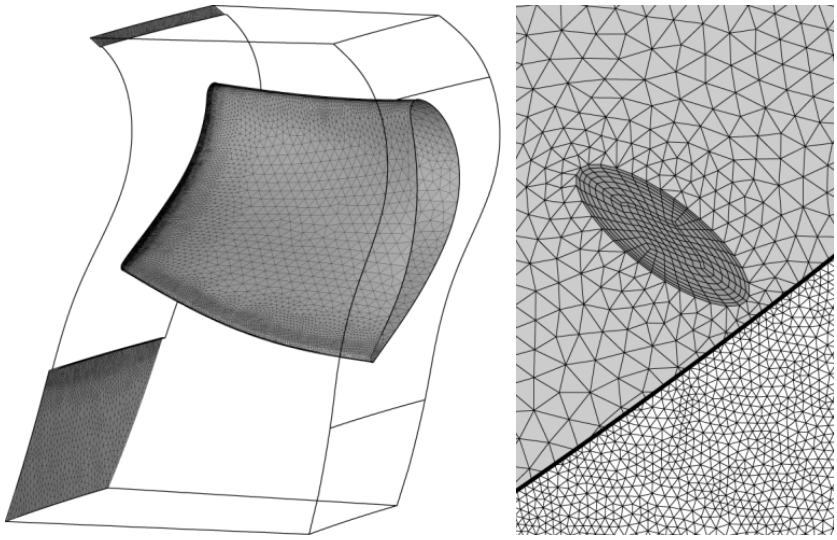

Figure 3.5. Rotor mesh (left) and mesh of cooling hole on casing local to rotor tip (right).

3.3.3 Fluent Set Up

The CFD study utilised the commercial solver ANSYS® Fluent 12.1 which was run on a 64 bit Redhat Linux machine with two 8 core Intel Xeon processors and 64 GB of RAM. A summary of the model set up is presented in table 3.2.

Table 3.2. CFD model set up.

Parameter (unit)	Nominal value
Elements	10 million
Turbulence Model	Spalart-Allmaras
Solver	Pressure-based coupled (2nd Order)
p_{01} (bar)	4.4
T_{01} (K)	436.4
T_{0C} (K)	297
ω (rpm)	9500
p_{01rel} (bar)	2.77
τ (ns)	702

Boundary conditions at the passage inlet and outlet were defined using radial pressure, velocity, temperature and turbulence profiles extracted from a previous HYDRA CFD model run at Rolls-Royce. For this chapter, the coolant plenum total pressures were set such that the time instantaneous pressure ratio across each hole never dropped below unity. The time mean pressure ratios across each hole are given in table. 3.3.

Table 3.3. Row time mean pressure ratios and resulting mass fluxes for geometry A.

Row	$p_{0c}/\overline{p_e}$	T_{0c} (K)	Geom. A $\dot{m}_C/\dot{m}_{12}$
1	1.047	297	0.059%
2	1.057	297	0.061%
3	1.064	297	0.064%
4	1.158	297	0.115%
5	1.226	297	0.137%
6	1.286	297	0.134%
7	1.570	297	0.085%
8	1.196	297	0.076%
9	1.211	297	0.043%

The model is initialized with interpolated results from previous solutions (greatly reducing solution times) and is then run for a number of rotor passing events (typically 10) until a time periodic solution is obtained. A time step of 702 ns was used to obtain the results, corresponding to 150 time steps per rotor passing event, selected to capture acoustic effects within the cooling holes. Solution time was approximately 300 – 400 hours on six cores.

3.3.4 Defining Film Cooling Effectiveness

Through the passage, work is extracted in the casing frame of reference. This reduces the driving temperature on the casing wall. Thus, the classical definition of film cooling effectiveness based on inlet total temperature (eqn. 3.1) cannot be used.

$$\eta = \frac{T_{01} - T_{AW}}{T_{01} - T_{0C}} \tag{3.1}$$

A new definition for film cooling effectiveness, termed the local film cooling effectiveness (η'), is introduced. The local driving temperature is obtained from a second uncooled solution, using the same mesh as the cooled solution.

$$\eta' = \frac{T_{AW,uncooled} - T_{AW,cooled}}{T_{AW,uncooled} - T_{0C}} \tag{3.2}$$

This definition does not account for changes in the total temperature of the coolant due to expansion through the rotor. Thus further from the holes, where there is greater work extraction from the coolant, the parallel between η' and coolant concentration breaks down.

3.3.5 Film Cooling Effectiveness Results

Data was extracted from Fluent at each time step and analysed in Matlab. Using both cooled and uncooled solutions of the same mesh (cooling hole exits closed for uncooled cases) unsteady and time averaged plots of η' could be generated.

Plots of time instantaneous and time averaged η' are plotted in fig. 3.6 – 3.9. Geometry A had a coolant to mainstream mass flow rate of $\dot{m}_C/\dot{m}_{12}$= 0.77%, geometry B $\dot{m}_C/\dot{m}_{12}$ = 1.73%, geometry C $\dot{m}_C/\dot{m}_{12}$ = 0.89% geometry D $\dot{m}_C/\dot{m}_{12}$ = 0.97%.

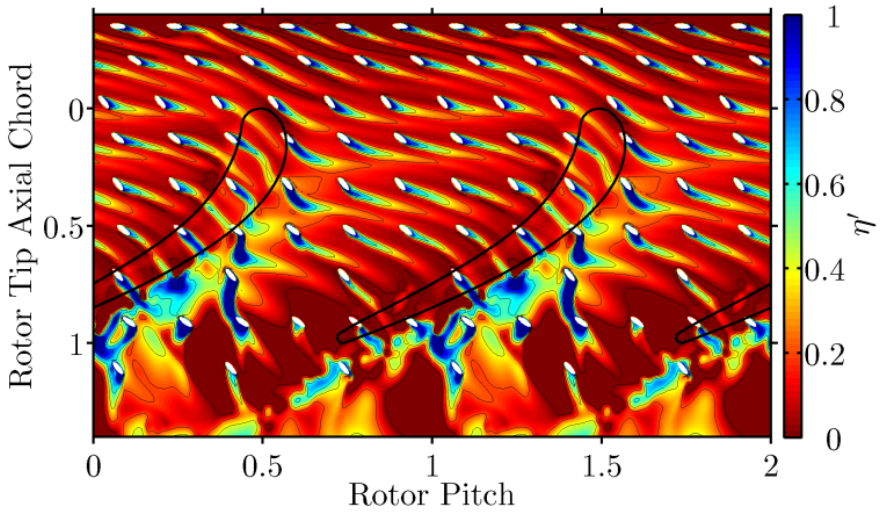

Figure 3.6. Geometry A time instantaneous η'. $\dot{m}_C/\dot{m}_{12}$ = 0.77%.

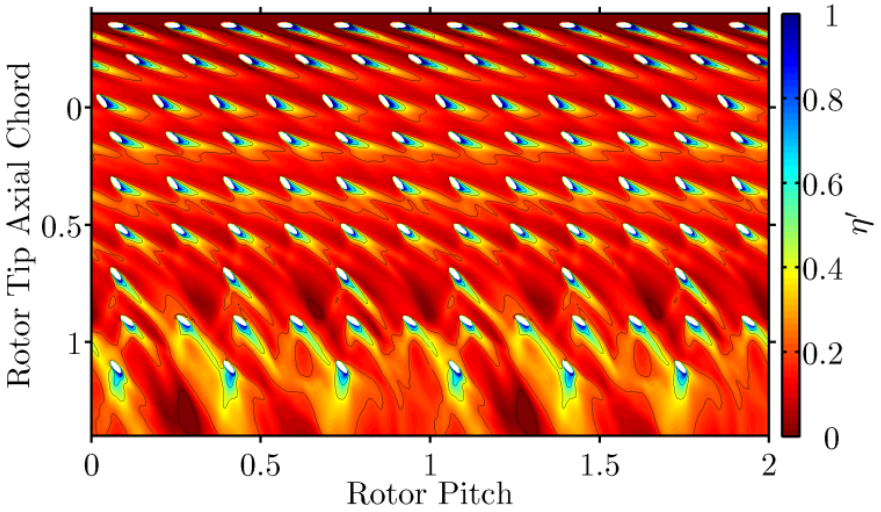

Figure 3.7. Geometry A time averaged η'. $\dot{m}_C/\dot{m}_{12}$ = 0.77%.

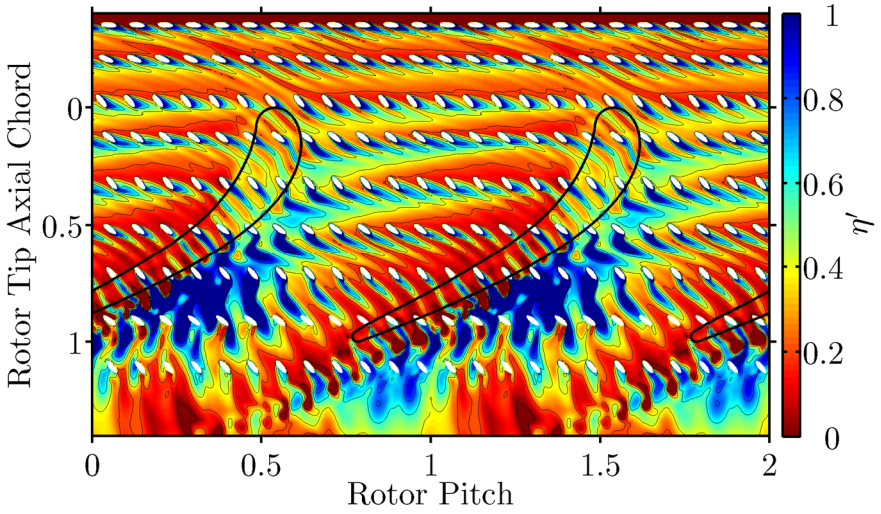

Figure 3.8. Geometry B time instantaneous η'. $\dot{m}_C/\dot{m}_{12}$ = 1.73%.

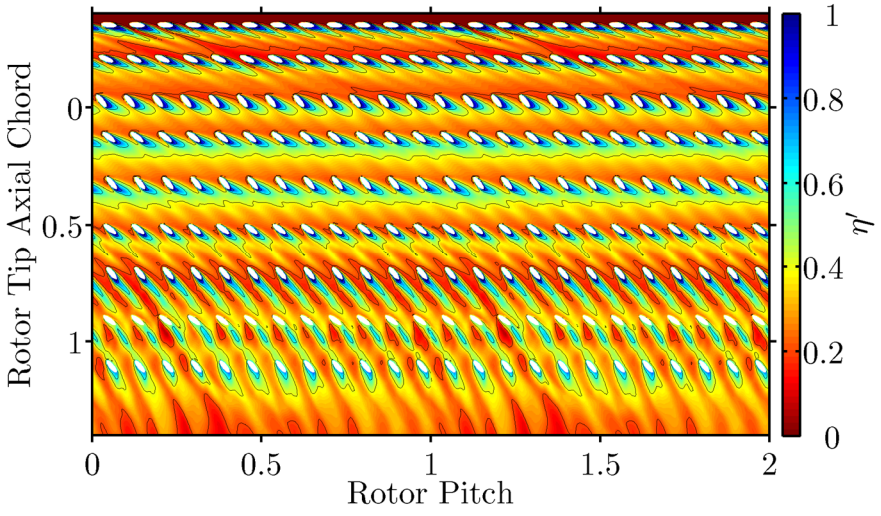

Figure 3.9. Geometry B time averaged η'. $\dot{m}_C/\dot{m}_{12}$ = 1.73%.

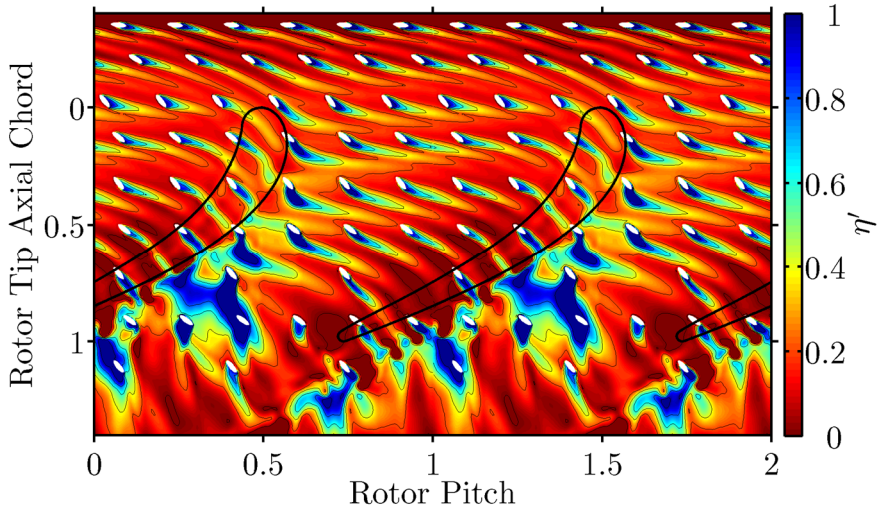

Figure 3.10. Geometry C time instantaneous η'. $\dot{m}_C/\dot{m}_{12}$ = 0.89%.

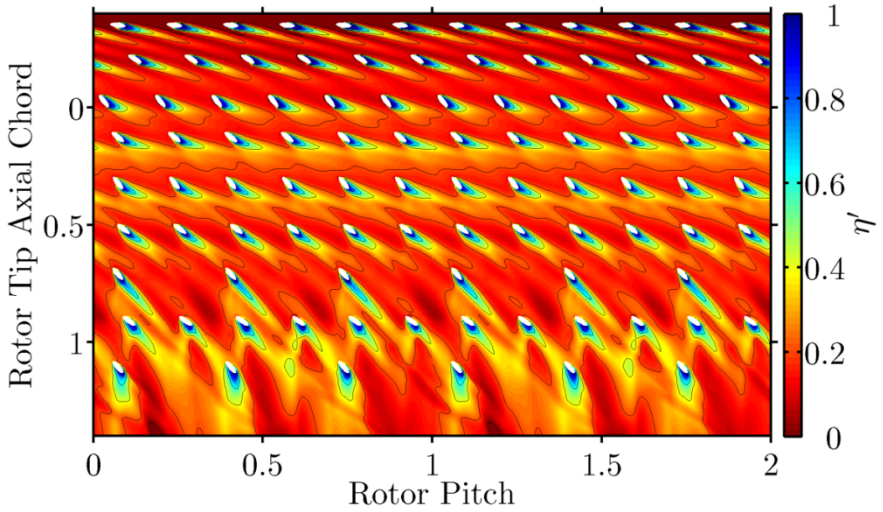

Figure 3.11. Geometry C time averaged η'. $\dot{m}_C/\dot{m}_{12}$ = 0.89%.

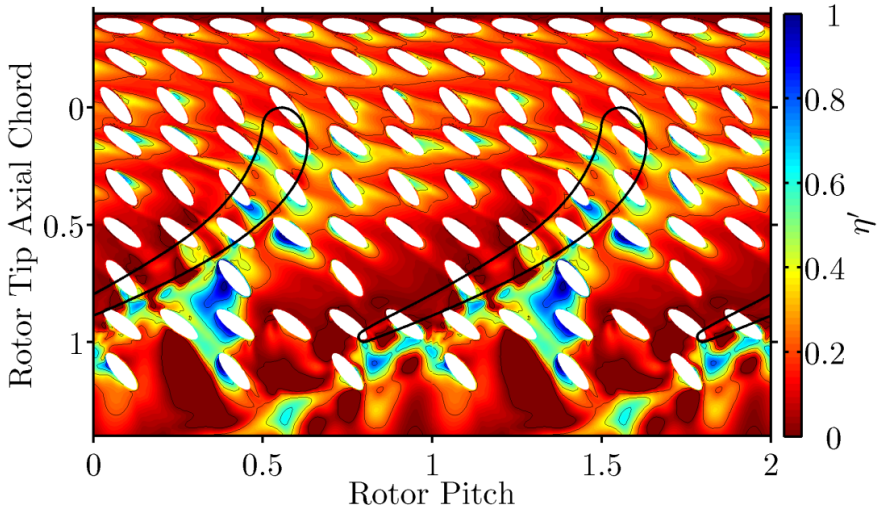

Figure 3.12. Geometry D time instantaneous η'. $\dot{m}_C/\dot{m}_{12}$ = 0.97%.

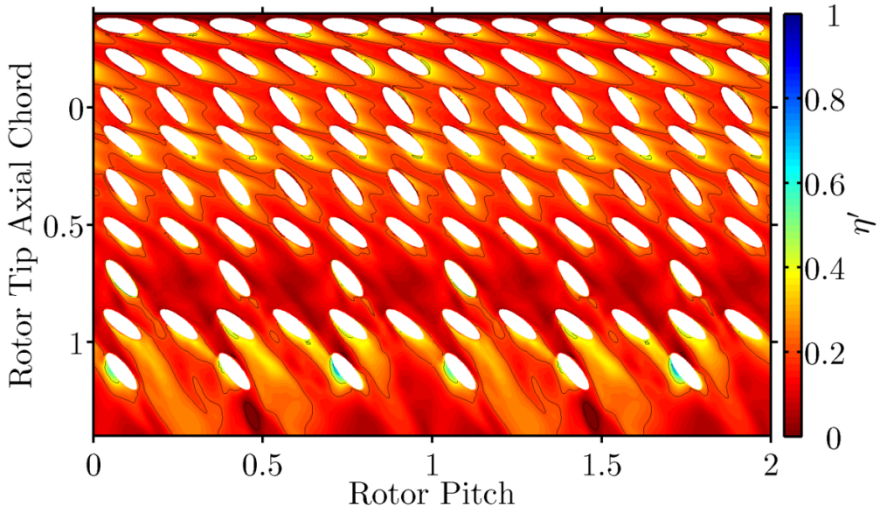

Figure 3.13. Geometry D time averaged η'. $\dot{m}_C/\dot{m}_{12}$ = 0.97%.

3.3.6 Film Cooling Effectiveness Discussion

Figures 3.6 and 3.8 clearly illustrate the interaction of the coolant and rotor. For most of the passage, coolant propagates along the time instantaneous flow direction. This is particularly evident between 20 – 70% C_{AX}, where there is a large temporal change in flow direction caused by the passing of the rotor. This is evident as a more scattered film cooling distribution downstream of the holes in the time averaged plots of fig. 3.7 and 3.9.

As the first reported CFD model of a film cooled rotor casing, the interaction of the coolant film with the rotor tip is of particular interest.

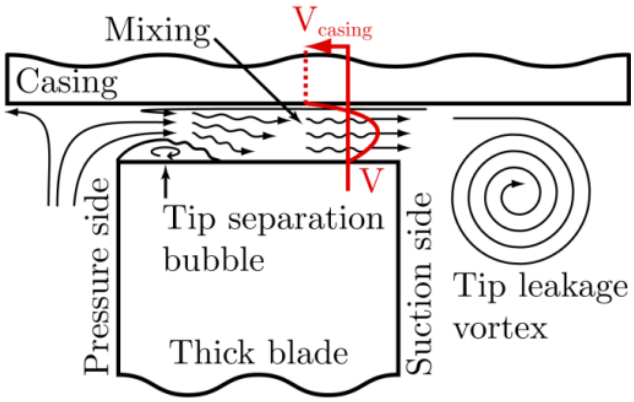

Figure 3.14. Over-tip leakage flow relative to the rotor over a thick blade, adapted from Denton (1993).

Interaction with Rotor Tip

The aerodynamics of tip leakage flow over flat tips with stationary uncooled casings has been extensively studied with detailed measurements taken by Bindon (1989), Moore and Tilton (1988), Heyes and Hodson (1992) and Yaras and Sjolander (1992). These surmise that tip leakage flow is predominantly driven by the static pressure difference across the tip gap. The flow structures over the tip are discussed by Denton (1993) and summarised in fig.3.14. Yaras and Sjolander (1991) conclude that relative casing motion has a significant effect on the magnitude of the tip leakage flow. The relative casing motion influences the velocities in the tip gap as described in the later uncooled casing heat transfer chapter, and highlighted in fig. 3.14. It also illustrates that there will be an impingement of the flow entering the tip gap onto the casing ahead of the tip gap. This acts to scrape off the casing boundary layer local to the pressure side corner.

These previous uncooled studies have all considered flow relative to the rotor. However for the discussion of a casing film cooling scheme, it is necessary to consider results in the absolute frame of reference. We now consider the flow environment from the perspective of a casing film cooling hole with reference to fig. 3.6 and 3.8.

- As the tip suction side approaches, the time instantaneous pressure ratio and subsequently mass flux from the hole increases.
- Beyond 50% C_{AX}, the tip leakage vortex located local to the suction side corner scrapes off much of the casing boundary layer and transports it into the passage vortex. In some locations, coolant jets are observed to detach from the surface and jet directly into the tip leakage vortex.
- Under the tip, cooling holes are in a near choked condition and coolant jets are squeezed close to the casing surface by the over tip leakage flow, resulting in large values of η'. Due to the relative velocity of leakage flow to the rotor tip, coolant ejected in the tip gap

will be transported out of the tip gap and into the tip leakage vortex. Upstream of 50% C_{AX} much of the casing films persist into the tip gap, resulting in large effectiveness values under the tip in this region.

- The arrival of the pressure side corner triggers a rapid rise in the pressure at the hole exit, reducing the mass flux from the holes. This markedly reduces the coolant being fed into the tip gap, with remaining coolant in the tip gap accelerated to the suction side.
- The impingement of the mainstream flow local to the pressure side corner is evident in these plots as a significant reduction in film effectiveness local to the pressure side corner. Coolant ejected after this impingement line does not enter the tip gap and is eventually swept off the casing surface by the tip leakage vortex.

To observe the interaction between the coolant and the secondary flows in the tip region, we can define a coolant concentration ψ within the rotor passage, using total temperatures calculated relative to the rotor.

$$\psi = \frac{T_{0rel,uncooled} - T_{0rel,cooled}}{T_{0\mathrm{rel},uncooled} - T_{0\mathrm{rel}C}} \tag{3.3}$$

Figure 3.15 plots iso-surfaces of coolant concentration within the rotor passage. These illustrate how the coolant film grows as the suction side approaches. Beyond 50% C_{AX}, the tip leakage vortex is evident and is seen to scrape off the coolant films from the casing, transporting the coolant into the passage vortex.

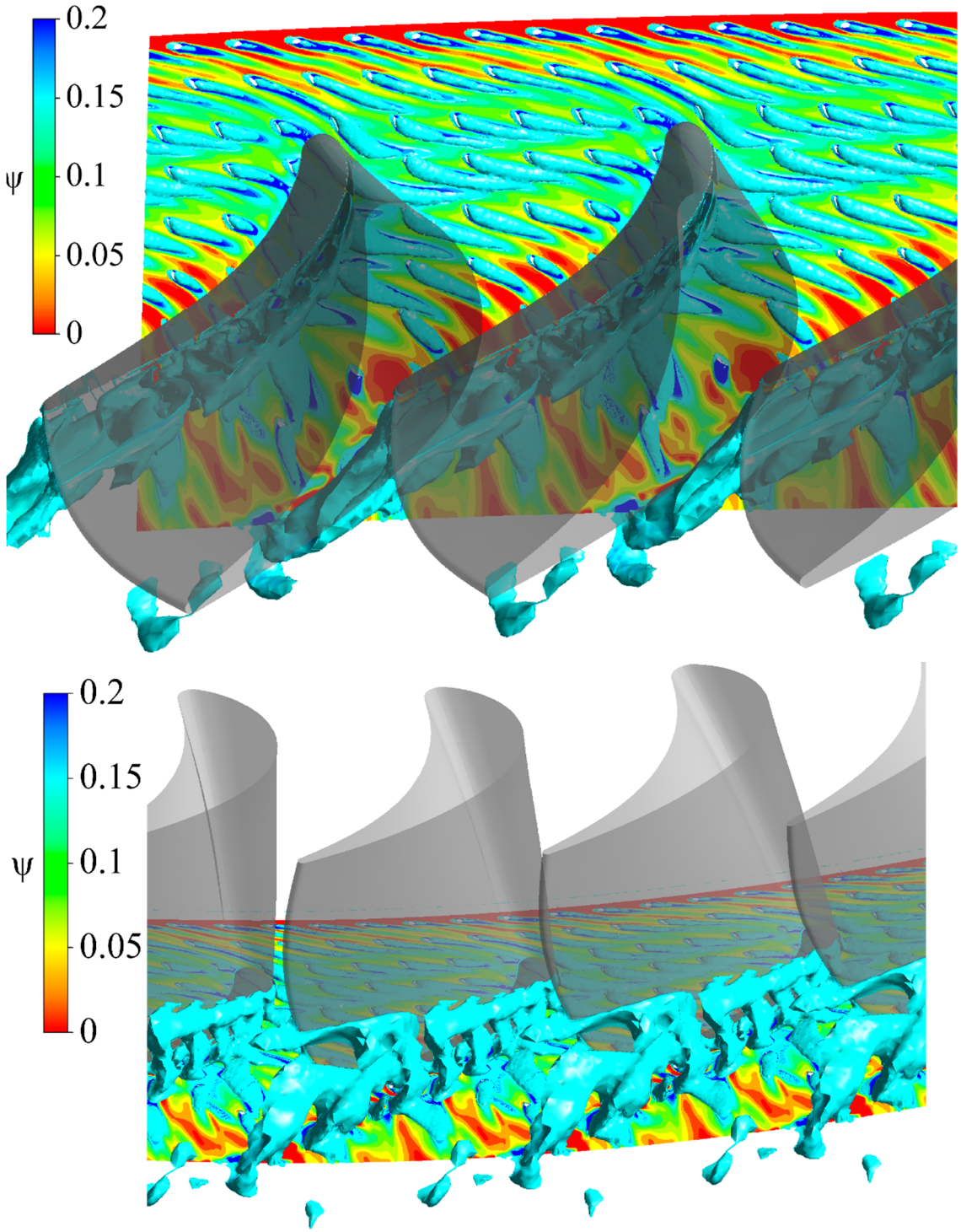

Figure 3.15. Iso-surfaces of coolant concentration (ψ=0.15) in rotor passage of geometry C.

Figure 3.16 plots pitch and time averaged values of ψ and provides a very useful insight into the transport of casing coolant throughout the rotor passage. This provides further evidence that the coolant is entrained into the casing passage vortex, with a lesser amount entrained into the tip leakage vortex. These conclusions are very similar to those drawn by Behr et al. (2008).

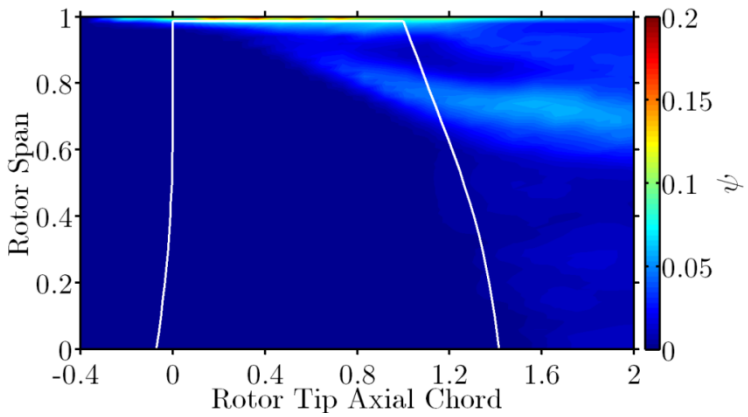

Figure 3.16. Pitch and time wise averaged plots of coolant concentration in geometry B.

These conclusions also agree with Mischo et al. (2007) who used numerical analysis to show that the over-tip leakage flow feeds the passage vortex upstream of 30% C_{AX}, and downstream feeds the tip leakage vortex. The over-tip leakage flow for a rotor with a film cooled casing contains a relatively low concentration of coolant. We would therefore not expect to see large concentrations of coolant in these vortices at these locations. Instead, we observe that downstream of 30% C_{AX}, the tip leakage vortex scrapes off the casing boundary layer and transports it into the passage vortex. This is evidenced by a significant increase in the coolant concentration within the passage vortex from 30 – 150% C_{AX}.

Scaling of η'

The cooling geometries A and B allow us to study the scaling of η' with coolant mass flow rate. For low values of η', η' is analogous to coolant concentration which scales linearly with $\dot{m}_C/\dot{m}_{12}$. Figure 3.17 plots the time and pitch-wise averaged values of η' in addition to geometry A scaled to a nominal $\dot{m}_C/\dot{m}_{12}$= 1%. Geometry B is then scaled such that the mass flux from rows 1 – 6 and 8 equals that of the scaled geometry A. As there are four times as many cooling holes in rows 7 and 9 of geometry B the scaling is not correct for these rows.

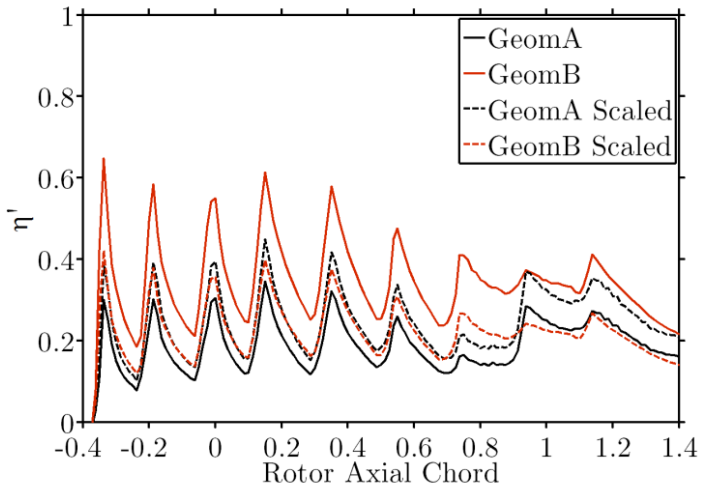

Figure 3.17. Computed and linearly scaled (to $\dot{m}_C/\dot{m}_{12}$= 1%) time and pitch-wise averaged η' for geometries A and B.

Rows 1 – 6, η' scale very well with $\dot{m}_C/\dot{m}_{12}$ however rows 7 – 9 do not, with geometry B performing relatively poorly. Much of the coolant in these rows is directly ingested into the tip leakage vortex without performing much cooling which explains this behaviour. We may therefore conclude that coolant injected downstream of 70% C_{AX} is less effective at cooling the rotor casing.

3.4 Acoustic Effects

A previous study by Collins and Povey (2014) highlighted the significance of acoustic effects in cooling holes subjected to large temporal variations in outlet static variations, such as those employed in a casing film cooling scheme.

To observe whether these effects were present in a full CFD model, mass flux and pressure data was taken from the outlet planes of cooling holes at each time step in the present study.

The steady state capacity characteristics of the modelled cooling holes were calculated using CFD. A mesh of a single cooling hole was operated over a wide range of steady state pressure ratios and the resulting mass flux recorded. Using this single hole capacity characteristic and the measured static pressure at the hole exit, it is possible to compute a quasi-steady mass flux

from the hole. This would be the expected result if unsteady acoustic effects were not present and the hole operated in a quasi-steady manner.

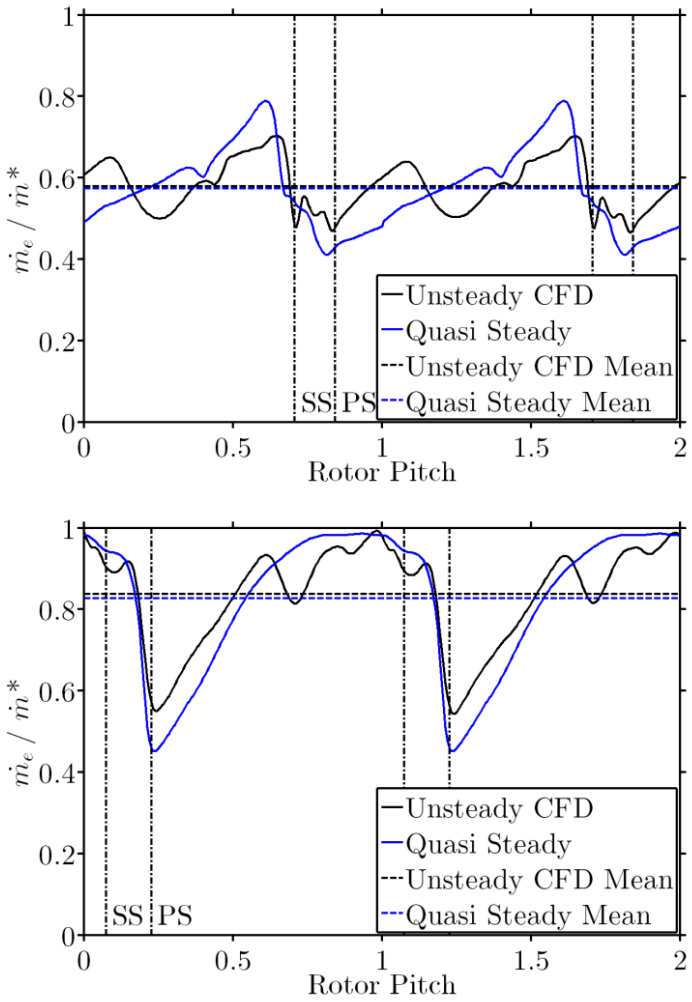

Figure 3.18. Plot of unsteady $\dot{m}_C$ across exit plane of holes located at 13% C_{AX} with $p_{0c}/\overline{p_e} = 1.14$ (top) and 72% C_{AX} with $p_{0c}/\overline{p_e} = 1.51$ (bottom).

The measured unsteady and computed quasi-steady results are plotted for holes located at 13% and 72% C_{AX} in fig. 3.18. This highlights that the mechanisms highlighted in the previous chapters 2D axisymmetric model are present for the 3D case. The work presented in the previous chapter indicated that the acoustic effects result in an increase in the hole exit mass flux vs. that predicted by a quasi-steady analysis in the time period after the passing of the pressure side corner. This is due to the propagation of a compression wave up the cooling hole. This compression wave is reflected at the hole inlet as an expansion wave which propagates

back towards the hole exit. Upon reaching the hole exit, the hole mass flux characteristically drops and reduces below the value predicted by the quasi-steady analysis. Simple theory predicts that the transmission time for the wave to propagate up and reflect is given by

$$t_r \cong \frac{2L_1}{a_{0c}} \tag{3.4}$$

The cooling holes for this study had a hole length of L_1=0.18λ, where λ defines the wavelength of the rotor passing frequency within the coolant. Thus we would expect to observe the interaction of the reflected expansion wave with the hole inlet 0.36 rotor periods after the passing of the pressure side corner (which propagates a compression wave up the hole). In fact we observe the reflected wave at approximately 0.375 rotor pitch. This is in good agreement with the 2D axisymmetric results which also exhibit a slightly longer transition time than simple theory due to reduction in the bulk flow velocity within the hole.

Only minor differences are observed between the 2D axisymmetric modelling and the results obtained from the full 3D model. In the tip gap, we observe a reduction in the hole exit mass flux and an increase in hole exit static pressure. This is due to blockage effects caused by the coolant being injected into the tip gap. This is not captured by the 2D axisymmetric model which simply used a hole exit static pressure profile derived from an uncooled casing, however the effect is relatively small and hence the 2D modelling approach offers a good way to assess the performance of different cooling hole designs. This is particularly important with regards to estimating the minimum operational pressure ratio before ingestion.

The chapter on acoustic effects highlighted that an acoustic hole geometry could improve performance of a film cooling scheme employed on the casing of an unshrouded rotor. The cylindrical hole design utilised in geometry A and B is within the optimal range identified in that chapter. A cooling hole design incorporating a change in area such as that used in geometry

C was shown to offer small additional benefits. The mesh of geometry A and C was identical aside from within the cooling holes (due to differing geometry). This allows a good comparison between the two designs. Since the cooling mass flow rates differed slightly, results of η' in geometry C were scaled down by the ratio of the two mass fluxes, using the scaling property identified previously. A time and pitch-wise averaged plot of the difference in η' between geometry A and C is given in fig. 3.19.

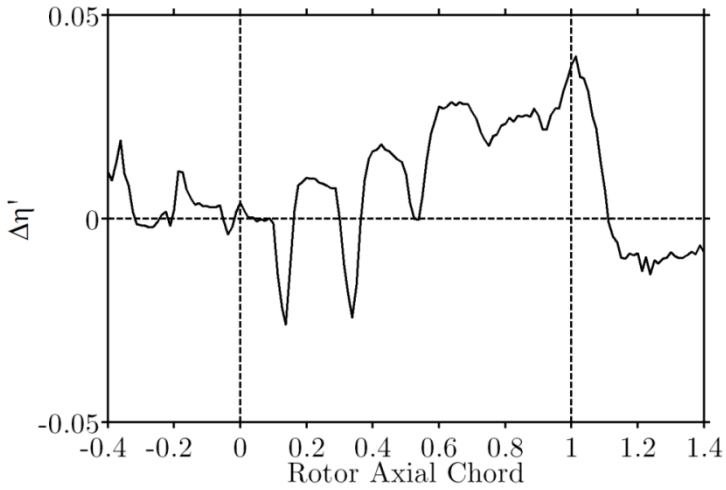

Figure 3.19. Time and pitch-wise averaged improvement of η' of geometry C over A.

The improvement in η' for geometry C is seen to increase with the blade loading, corresponding to an increased amplitude of the unsteady pressure experienced by the cooling hole. It must be stressed that the acoustically optimised hole is compared to an optimised cylindrical hole. Despite this, improvements of 15% are evident in the trailing edge region of the blade.

Figure 3.20 plots time and pitch-wise averaged η' for geometries A, C and D to compare the three different hole types. If we now consider geometry D, which is almost a worst case design in terms of acoustic design, we observe that cooling hole performance degrades in relation to blade loading. If we consider the surface plots of η' for geometry D in figs. 3.12 and 3.13, we observe that little coolant is ejected local to the blade suction surface, and large amounts are ejected local to the blade suction surface. Much of the coolant ejected local to the suction

surface is injected directly into the tip leakage vortex resulting in very low effectiveness values. These differences are much more significant compared to those between the cylindrical and acoustically optimised hole design. This highlights that acoustic effects can have a significant impact on the surface average η' in regions subjected to large amplitude pressure variations if they are not considered in the design process.

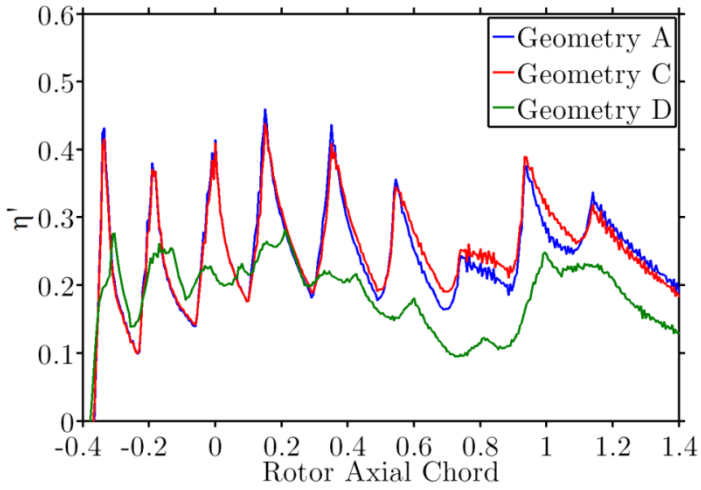

Figure 3.20. Comparison of geometries A, C and D scaled to $\dot{m}_C/\dot{m}_{12} = 1\%$.

3.5 Conclusions

The use of a full 3D CFD model of a casing film cooling scheme has been used to study the interaction of casing film cooling holes with an engine representative rotor. Analysis of a 3D CFD simulation incorporating cooling holes explains the interaction of the injected coolant with the rotor tip. The passing of the rotor tip leads to the following behaviour:

- Coolant films on the casing are scraped off by the tip leakage vortex and entrained into the passage vortex.
- Coolant ejected under the tip locally cools the casing under the tip but is then immediately entrained into the tip leakage vortex.
- Any coolant film created under the tip is stripped off by impingement of mainstream flow local to the pressure side corner.

- Coolant films quickly re-establish after the passing of the tip until it is then stripped off again by the tip leakage vortex.

Acoustic effects first observed and explained in the previous chapter and published by Collins and Povey (2014) are seen to have a significant impact on the unsteady hole mass flux for all holes located in the over-tip region. Results correlate very well with earlier work performed using 2D axisymmetric models. Comparison of different hole geometries yields that an acoustically optimised hole can yield a 15% improvement in casing η' when compared to an optimised cylindrical hole. Further an acoustically bad design is modelled and is evidenced to have significantly worse performance. This highlights the need to consider the acoustic effects when designing rotor casing film cooling scheme and indicate that a 2D axisymmetric modelling approach is a good option for predicting the behaviour of cooling holes on the casing of an unshrouded rotor.

3.6 Chapter Nomenclature

a	Sonic velocity
c_p	Specific heat capacity
C	Rotor true chord (OTRF = 36.6 mm)
C_{AX}	Rotor tip axial chord (OTRF = 21.39 mm)
η	Adiabatic film cooling effectiveness
η'	Local film cooling effectiveness
k	Gas conductivity
λ	Wavelength of pressure wave propagated in coolant
L_1	Total cooling hole length
$\dot{m}$	Mass flow rate
$\dot{m}^*$	Choked hole mass flow rate
M	Mach number
Nu	Nusselt number: $(htc \times C)/k_{01}$
p	Pressure
$\dot{q}$	Heat flux
Re	Reynolds number
t	Time
t_r	Pressure wave transmission time
τ	Time step
T	Temperature
T_{AW}	Adiabatic wall temperature
T_G	Gas static temperature
T_W	Wall temperature
T'_W	Corrected wall temperature
ψ	Coolant concentration
V	Flow velocity
ω	Rotor disc speed

Subscripts

01	Rotor inlet total
02	Rotor outlet total
12	Passage
2	Rotor outlet static
c	Coolant
e	Hole exit plane
g	Mainstream
rel	Rotor relative
tip	Over-tip

Chapter 4: Impact of Casing Coolant Injection on Rotor Efficiency

4.1 Motivation

The introduction of coolant into the mainstream flow of a gas turbine generates losses via mixing and spoiling effects. As reported by Denton (1993) these can have a significant effect on cycle efficiency, thus it is important to quantify these losses for a given cooling system. Typically these losses are calculated empirically with consideration given to the local main stream Mach number and local coolant blowing ratio. The study by Hartsel (1972), later expanded on by Köllen and Koschel (1985), describes the most commonly used method for loss calculation. However, injecting coolant into the over tip region of a highly loaded rotor will almost certainly have a significant effect on the rotor aerodynamics which is not considered by Köllen and Koschel (1985). This chapter quantifies and studies these effects, in particular focusing on the impact on rotor efficiency utilising a number of different methods.

4.2 Exergy Analysis

The treatment of thermodynamic loss from an analytical standpoint is developed in this section using the concept of exergy.

4.2.1 The Concept of Exergy

Applying the first law to a closed steady-state system, for which the changes in kinetic and potential energy are insignificant to the system presented in fig. 4.1

$$\dot{W} = \dot{m}(h_1 - h_2) + \dot{Q} \tag{4.1}$$

We can construct a theoretical reversible path connecting states 1 and 2 for the system presented in fig. 4.1. This consists of an isentropic expansion from states 1 to a, followed by an isothermal

heat addition at a temperature T_3 from states a to b and an isentropic expansion from states b to 2. The choice of T_3 and p_3 is dependent on application but for a typical system is equal to the dead state of the system surroundings.

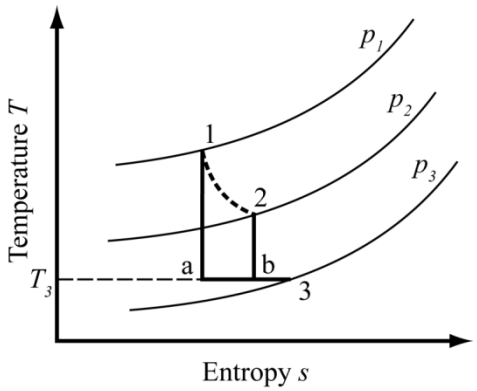

Figure 4.1. A T-s diagram illustrating reversible and irreversible processes between states 1 and 2.

We can calculate the theoretical reversible work from states 1 to 2 by summing the work of the reversible processes.

$$\dot{W}_{1a} = \dot{m}(h_1 - h_a)$$

$$\dot{Q}_{1a} = 0$$

$$\dot{W}_{ab} = \dot{m}(h_a - h_b) - \dot{Q}_{ab}$$

$$\dot{Q}_{ab} = \dot{m}T_3(s_2 - s_1) \tag{4.2}$$

$$\dot{W}_{b2} = \dot{m}(h_b - h_2)$$

$$\dot{Q}_{b2} = 0$$

Thus the reversible power is given by

$$\dot{W}_{rev} = \dot{W}_{1a} + \dot{W}_{ab} + \dot{W}_{b2}$$
$$\dot{W}_{rev} = \dot{m}(h_1 - h_2) - \dot{m}T_3(s_1 - s_2) \tag{4.3}$$

We can also calculate the maximum work if we were to simply expand from state 1 to the surroundings at state 3, this we term the exergy, φ

$$\dot{W}_{13} = \dot{W}_{1a} + \dot{W}_{a3}$$
$$\dot{W}_{a3} = \dot{m}(h_a - h_3) - \dot{Q}_{a3}$$
$$\dot{Q}_{a3} = \dot{m}T_3(s_3 - s_1) \tag{4.4}$$
$$\psi_1 = \dot{m}(h_1 - h_3) - \dot{m}T_3(s_1 - s_3)$$

We can substitute this into eqn. 4.3

$$\dot{W}_{rev} = \dot{m}(\psi_1 - \psi_2) \tag{4.5}$$

Thus if we can calculate the exergy of the two states we can formulate the $\dot{W}_{rev}$.

4.2.2 Application to Turbines

For a turbine, the outlet pressure is limited to the pressure p_2. Thus the maximum amount of work we can extract occurs when expanding isentropically to this pressure. Thus we take the conditions of T_{2s} and p_2 as our surrounding conditions (defined as $T_3$and p_3 previously). Thus eqn. 4.3 becomes

$$\dot{W}_{rev} = \dot{m}(\varphi_1 - \varphi_2) = \dot{m}(h_1 - h_2) - \dot{m}T_{2s}(s_1 - s_2) \tag{4.6}$$

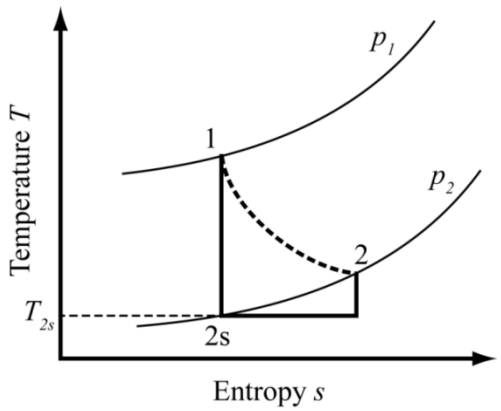

Figure 4.2. A T-s diagram for flow through an adiabatic turbine.

The actual work output from the turbine is given by

$$\dot{W} = \dot{m}(h_1 - h_2) \tag{4.7}$$

Thus the loss of work due to irreversibilities between states 1 and 2 is given by

$$\dot{W}_{lost} = -\dot{m}T_{2s}(s_1 - s_2) \tag{4.8}$$

We can define the second law (or rational) efficiency for a blade row as

$$\varepsilon_2 = \frac{\dot{w}_{sys}}{\dot{w}_{rev}} = \frac{h_1 - h_2}{h_1 - h_2 - T_{2s}(s_1 - s_2)} \tag{4.9}$$

More commonly for a turbine blade row we utilise the static to static isentropic efficiency

$$\varepsilon_{isen,\ SS} = \frac{\dot{w}_{sys}}{\dot{w}_{isen}} = \frac{h_1 - h_2}{h_1 - h_{2s}} \tag{4.10}$$

Another often used form is the total to static isentropic efficiency given by

$$\varepsilon_{isen,\ TS} = \frac{h_{01} - h_2}{h_{01} - h_{2s}} \tag{4.11}$$

The difference between the isentropic and second law efficiency formulations results by considering whether useful work could be done between states 2 and 2s. The exergy and hence useful work which could be utilised between states 2s and 2 is given by

$$\dot{W}_{2-2s} = \dot{m}(\varphi_2 - \varphi_{2s}) = \dot{m}(h_2 - h_{2s}) - \dot{m}T_{2s}(s_2 - s_{2s}) \tag{4.12}$$

Equations 4.6 and 4.12 are related by

$$\dot{W}_{isen,\ ss} = \dot{W}_{rev} + \dot{W}_{2-2s} \tag{4.13}$$

Comparing these, we can see that the amount of exergy (or reversible work between states 1 and 2) lost due to irreversible expansion in the turbine is given again by eqn. 4.8 given $s_{2s} = s_1$.

4.3 Cooled Turbine Efficiency

One of the most commonly referenced works on cooled turbine efficiency is by Hartsel (1972), latterly expanded on by Köllen and Koschel (1985). Young and Horlock (2008) review this work and suggest a number of improved models which better simulate the physical mixing processes.

4.3.1 Hartsel Mixing Model

The introduction of coolant introduces significant additional complications to the analysis. Hartsel (1972) proposed the following definition for the efficiency of a stationary blade row cooled by a single coolant stream

$$\varepsilon_{HART} = \frac{\text{Exit KE of actual mixed expansion}}{\text{Total exit KE of seperate unmixed isentropic expansions}} \tag{4.14}$$

The denominator is calculated assuming that the coolant and mainstream flows expand isentropically from their supply stagnation conditions to the exit static pressure without mixing. With reference to the notation in fig. 4.3, this gives the following formulation

$$\varepsilon_{HART} = \frac{(\dot{m}_g + \dot{m}_c)(h_{02} - h_2)}{\dot{m}_g(h_{01g} - h_{2sg}) + \dot{m}_c(h_{01c} - h_{2sc})} \tag{4.15}$$

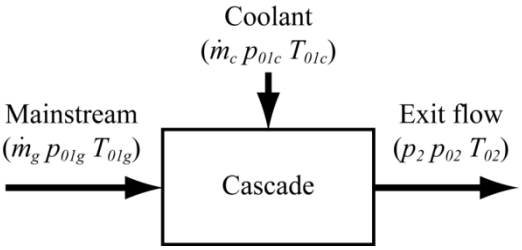

Figure 4.3. Notation for Hartsel's cooled cascade.

As the turbine is adiabatic, we can calculate h_{02} from the steady flow energy equation

$$(\dot{m}_g + \dot{m}_c)h_{02} = \dot{m}_g h_{01g} + \dot{m}_c h_{01c} \tag{4.16}$$

This separated expansion is clearly not realistic but as identified by Young and Horlock (2006), eqn. 4.15 can be applied to the case where the mainstream and coolant flows are mixed adiabatically to give total conditions of p_{0m} and T_{0m} with $p_{01g} = p_{01c} = p_{0m} = p_{01}$. The mixture can then be expanded isentropically to the exit pressure. However if differing values of c_p and γ are chosen for the mainstream and coolant then ε_{HART} can be shown to exceed unity. Young and Horlock (2006) propose alternative methods for calculating an ideal mixed expansion to replace the denominator in eqn. 4.15.

4.3.2 Mixed Expansion Model

In this analysis we assume that both the coolant and mainstream are ideal gasses and that there are *n* coolant streams each with exit conditions of p_{01ci}, T_{01ci} and of mass flow rate $\dot{m}_{ci}$. If we

define the mixing process as adiabatic, we can solve for T_{0m} by solving the steady flow energy equation

$$(1-\phi)\int_{T_{01g}}^{T_{0m}} c_{pg}(T')dT' + \sum_{i=1}^{n} \phi_i \int_{T_{01ci}}^{T_{0m}} c_{pc}(T')dT' = 0 \tag{4.17}$$

Where $\phi_i = \dot{m}_{ci}/(\dot{m}_g + \sum \dot{m}_{ci})$, $\phi = \sum \phi_i$.

The value of p_{0m} depends on the mixing process specified.

We now wish to define an ideal process for our coolant expansion. To that end it is useful to consider how entropy is generated in a mixing process. First we can define the entropy created per unit mass of the mixture as

$$\sigma = s_{0m} - [(1-\phi)s_{01g} + \sum_{i=1}^{n} \phi_i s_{01ci}] \tag{4.18}$$

Young and Horlock (2008) show that for a semi perfect gas, eqn. 4.18 may be written

$$\sigma = \sigma_T + \sigma_P + \sigma_C$$

$$\sigma_T = (1-\phi)\int_{T_{01g}}^{T_{0m}} \frac{c_{pg}(T')}{T'} dT' + \sum_{i=1}^{n} \phi_i \int_{T_{01ci}}^{T_{0m}} \frac{c_{pc}(T')}{T'} dT'$$

$$\sigma_P = (1-\phi)R_g \ln\left(\frac{p_{01g}}{p_{0m}}\right) + \sum_{i=1}^{n} \phi_i R_c \ln\left(\frac{p_{01ci}}{p_{0m}}\right) \tag{4.19}$$

$$\sigma_C = (1-\phi)R_g \ln(X_{gm}) + \phi R_c \ln(X_{cm})$$

Where X_{gm} and X_{cm} denote the mole fractions of the mainstream gas and coolant after mixing and R the specific gas constant.

The terms σ_T and σ_P refer to the entropy generation due to bringing the streams to the mixed temperature and pressure respectively. The term σ_C refers to the diffusional entropy generation due to change in composition. Without the use of semi permeable membranes this component of the mixing cannot be utilised to generate useful work, thus it makes sense to ignore it for the purpose of our ideal mixing analysis as it will occur for both the ideal and real processes.

We could now define an ideal process in which $\sigma_T + \sigma_P = 0$, which can be solved to evaluate p_{0m}, which for this idealised process we denote as p_{0f}

$$\frac{p_{0f}}{p_{01g}} = \exp\left(\frac{\sigma_T}{R}\right)\prod_{i=1}^{n}\left(\frac{p_{01ci}}{p_{01g}}\right)^{\phi_i R_c/R} \tag{4.20}$$

Where $R = (1-\phi)R_g + \phi R_c$

Young and Horlock (2008) refer to this as the fully reversible mixed efficiency. The conceptual cycle for this is given in fig. 4.4 and the T-s diagram in fig. 4.6. The blade row efficiency of this cycle is then defined as

$$\varepsilon_{FR} = \frac{h_{02} - h_2}{h_{0f} - h_{2sf}} \tag{4.21}$$

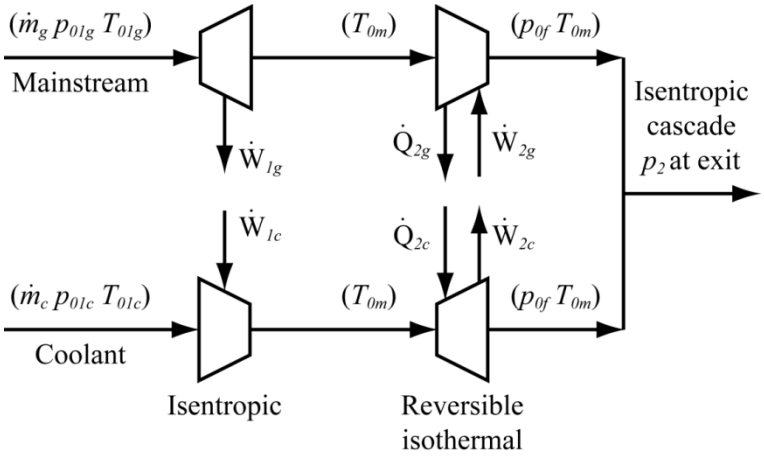

Figure 4.4. Conceptual fully reversible mixing process.

Although this measure of efficiency fulfils all the requirements of a cooled cascade efficiency, as the reference process represents a fully reversible process, it may not represent the true intent of the design. In practise the designer does not intend to recover work from bringing the two streams to the same temperature, but to ensure a large temperature difference between the mainstream gas and the wall temperature. This inevitably results in entropy generation from the resulting heat transfer, σ_T.

Another reference process which excludes the entropy generation due to thermal mixing is instead proposed, for which we calculate p_{0m}, referred to as p_{0w} for this process, by solving $\sigma_P = 0$.

$$\frac{p_{0w}}{p_{01g}} = \prod_{i=1}^{n} \left(\frac{p_{01ci}}{p_{01g}} \right)^{\phi_i R_c / R} \tag{4.22}$$

Young and Horlock (2008) refer to this as the *weighted pressure* efficiency. The conceptual cycle for this is given in fig. 4.5 and the T-s diagram in fig. 4.6. The blade row efficiency of this cycle is then defined as

$$\varepsilon_{WP} = \frac{h_{02} - h_2}{h_{0w} - h_{2sw}} \tag{4.23}$$

This definition of efficiency takes into account the usefulness of injecting the coolant to reduce temperatures local to the walls. In this idealised process, heat is exchanged between each stream in a lossless heat exchanger bringing both streams to T_{0m}. The two streams are then compressed/expanded in a reversible isothermal turbo-compressor, bringing each stream to a common p_{0w} and T_{0m}. The pressure p_{0w} being defined such that the entropy generation in the turbo-compressor is 0.

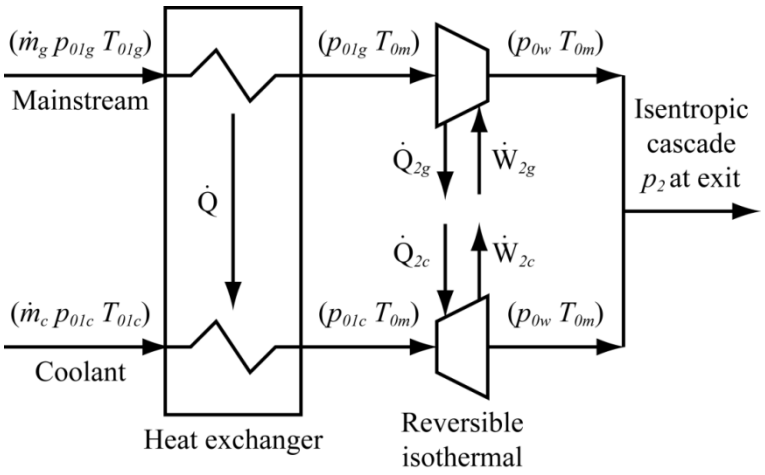

Figure 4.5. Conceptual weighted pressure mixing process proposed by Young and Horlock (2008).

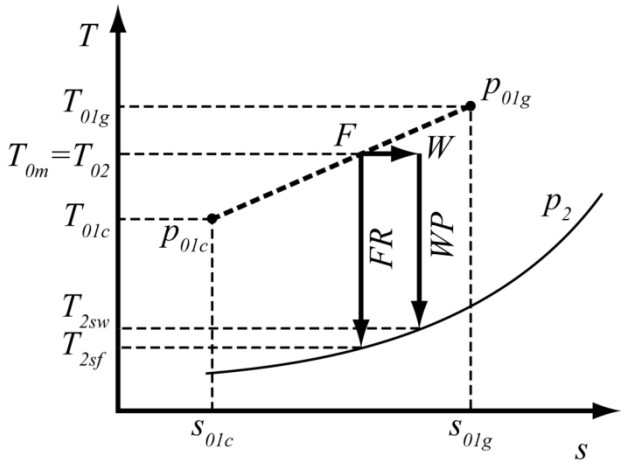

Figure 4.6. A T-s diagram of the weighted pressure (WP) and fully reversible mixed (FR) process for one coolant stream.

4.3.3 Comparison with an Uncooled Turbine

Returning to the Hartsel efficiency given in eqn. 4.15, it is evident that if $\dot{m}_c = 0$ then we can write the uncooled Hartsel blade row efficiency as

$$\varepsilon_{HART,Uncooled} = \frac{(h_{02} - h_2)}{(h_{01} - h_{2s})} \tag{4.24}$$

This can be directly compared to the fully reversible and weighted pressure efficiencies, which also collapse to this expression for an uncooled case.

Table 4.1. Comparison of blade row efficiencies.

	$\dot{m}_c/\dot{m}_{12}$	ε_2	$\varepsilon_{isen,TS}$	ε_{HART}	ε_{FR}	ε_{WP}
Uncooled	0	86.54%	88.12%	87.90%	87.90%	87.90%
Geom A	0.712%	86.84%	NA	88.14%	88.07%	88.10%
Geom B	1.726%	86.38%	NA	85.16%	85.33%	85.42%

4.4 Application to CFD Data

The cooled turbine efficiency models were compared with the use of time and mass averaged data extracted from the CFD model used in the earlier CFD chapter. Data was captured at the inlet and outlet planes of the rotor passage as well as at the exit plane of each cooling hole. To ensure consistency, the same mesh was utilised for all cases. The mesh of geometry B was used, with hole exit planes defined as walls to recreate the hole pattern of geometry A. For the uncooled case all hole exit planes were defined as walls. Each case was run until periodic convergence of all quantities was observed. Calculations of efficiency were made by extracting the mass flow rates and mass averaged quantities of enthalpy and entropy at each time step from the outlet plane of all cooling holes and the rotor inlet and outlet planes. The mass averaged quantities were then time averaged across a full rotor passing event. All calculations were performed in the rotor frame of reference. The results are summarised in table 4.1.

The introduction of coolant in geometry A leads to an increase in the rotor blade row efficiency for all models vs. the uncooled case. This indicates that the casing cooling scheme is able to reduce other losses occurred in the rotor passage. Geometry B causes a drop in efficiency, indicating that the introduction of extra coolant, in particular in the downstream region of the blade, introduces mixing losses that are not offset in the rest of the passage. This is perhaps unsurprising as geometry B contains proportionally more cooling holes in the downstream region of the passage, which in the rotor frame of reference, corresponds to a region of higher

Mach number. The mixing model presented by Köllen and Koschel (1985) predicts that mixing losses will be higher for injection into higher Mach number regions.

Comparison of the three models across both cases is interesting and hints at the predominant losses occurring in both systems. Geometry B has a proportionally larger difference between $\Delta\varepsilon_{HART}$ and $\Delta\varepsilon_{FR}$ than between $\Delta\varepsilon_{FR}$ and $\Delta\varepsilon_{WP}$ than geometry A. Again this indicates that the coolant injected in the downstream regions of the passage introduces higher mixing losses.

The uncooled stage efficiency of this geometry was measured in the OTRF by Beard et al. (2011) to be 88.63%. When the efficiency of the stator is accounted for (~94.93%, Beard (2010)) indicating a rotor blade row efficiency of 93.4%. This is significantly different to the value measured from the CFD model. It is thought that much of this error is due to the mesh used in the CFD study, which was highly optimised for heat transfer measurements in the over-tip region. The mesh was relatively coarse at the hub, mid-passage and trailing edge regions which most likely increased the errors in these regions. Since the same mesh was used for all studies, it is thought that these mesh errors have little to no effect on the relative results presented here.

4.4.1 Effect of Casing Coolant Ejection on Secondary Flows

We observe that mixing losses incurred by the introduction of coolant from the casing are to an extent offset by reduction in losses incurred elsewhere in the passage. Bindon (1989) states that most of the losses incurred in an unshrouded rotor result from tip secondary flows.

$$\psi = \frac{T_{0rel,uncooled} - T_{0rel,cooled}}{T_{0\mathrm{rel},uncooled} - T_{0\mathrm{rel}C}} \tag{4.25}$$

To observe the interaction between the coolant and the secondary flows in the tip region, we can define a coolant concentration ψ within the rotor passage, using total temperatures calculated relative to the rotor.

Figure 4.7 plots pitch and time averaged values of ψ and provides a very useful insight into the transport of casing coolant throughout the rotor passage. Most significantly it indicates that much of the coolant is entrained into the casing passage vortex, with a lesser amount entrained into the tip leakage vortex.

These conclusions are very similar to those drawn by Behr et al. (2008) and Mischo et al. (2007), who used numerical analysis to show that the over-tip leakage flow feeds the passage vortex upstream of 30% C_{AX}, and downstream feeds the tip leakage vortex. The over-tip leakage flow for a rotor with a film cooled casing contains a relatively low concentration of coolant. We would therefore not expect to see large concentrations of coolant in these vortices at these locations. Instead, we observe that downstream of 30% C_{AX}, the tip leakage vortex scrapes off the casing boundary layer and transports it into the passage vortex. This is evidenced by a significant increase in the coolant concentration within the passage vortex from 30 – 150% C_{AX}.

With an understanding of the location of coolant through the passage it is now possible to consider the impact on loss. As discussed in section 4.2.2, the change in entropy is a measure of loss and closely related to the efficiency of the blade row. Entropy is calculated relative to the mass averaged rotor inlet conditions using

$$s - s_{ref} = c_p \ln\left(\frac{T}{T_{ref}}\right) - R \ln\left(\frac{p}{p_{ref}}\right) \tag{4.26}$$

As is well discussed by Denton (1993), entropy is generated in boundary layers (by viscous effects and mixing processes), shock waves and heat transfer across temperature differences. These predominantly occur within the secondary flows of the blade passage and thus analysing the entropy generated in these secondary flows allows us to investigate the impact of casing coolant ejection on loss.

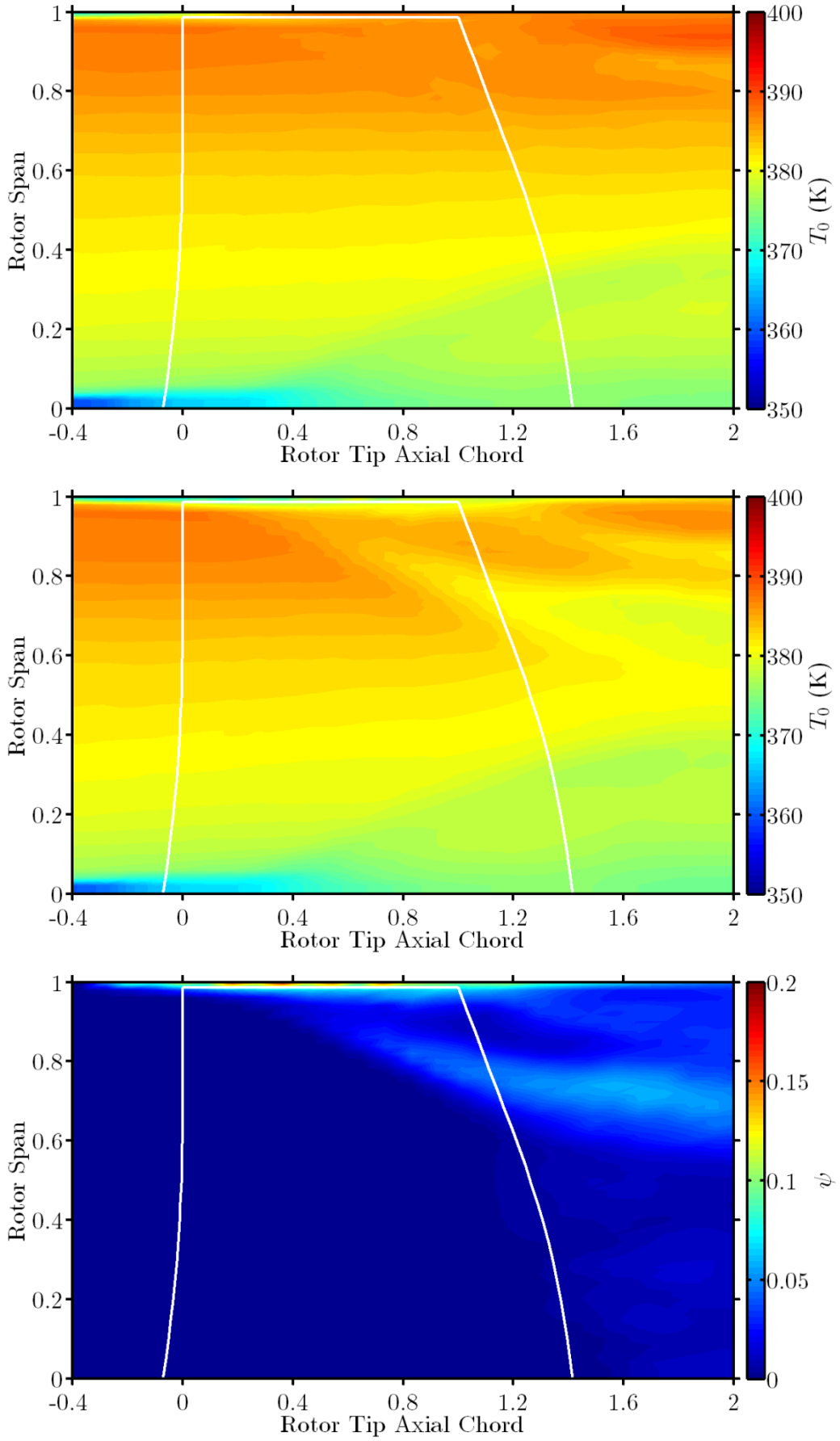

Figure 4.7. Pitch and time wise averaged plots of passage relative total temperature for uncooled case (top), cooled case (middle) and the derived coolant concentration (bottom).

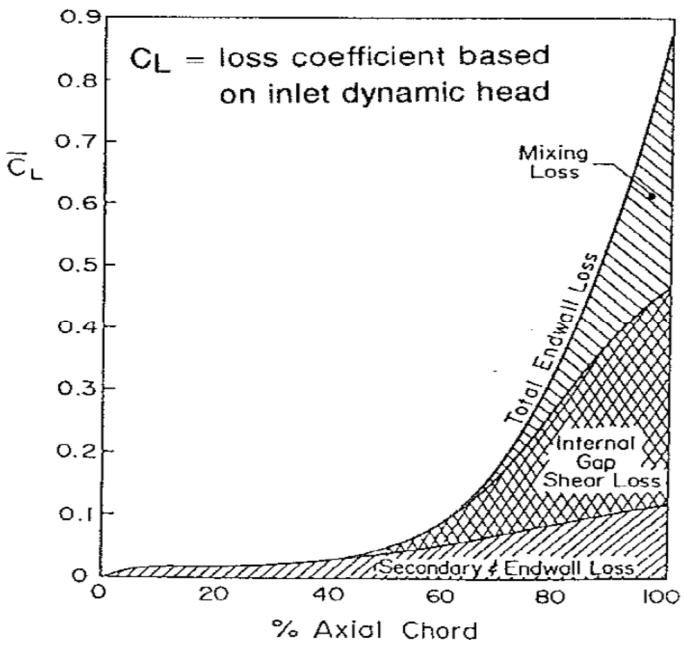

Figure 4.8. Losses in a turbine passage as presented by Bindon (1988).

Figure 4.9 shows contours of entropy as generated through the blade passage. It is evident that much of the entropy and therefore loss is generated in the tip region, most significantly in the tip leakage vortex. These conclusions are supported by the work of Bindon (1988) who analysed loss mechanisms in a low speed cascade. Figure 4.8 plots the loss coefficient as a function of axial chord. For Bindon's case, as the endwall was stationary, the loss was calculated based on total pressure loss

$$C_L = \frac{\Delta p_0}{\frac{1}{2}\rho {V_1}^2} \tag{4.27}$$

Again with reference to fig. 4.9, the entropy generated in the cooled case is notably less local to the blade tip suction surface, suggesting a reduction in the over tip leakage flow and the magnitude of the tip leakage vortex.

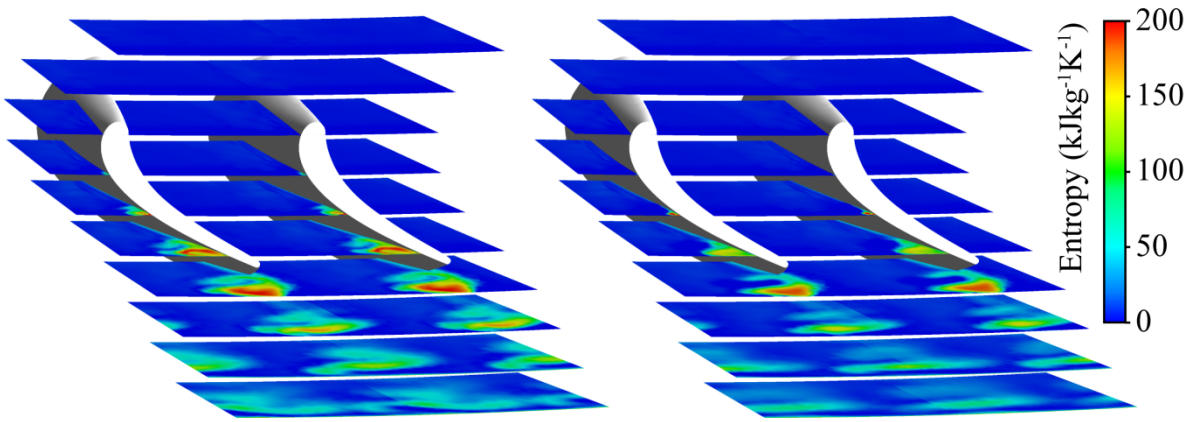

Figure 4.9. Contours of entropy in blade passage for uncooled casing (left) and cooled casing (right).

The changes in entropy generation are further highlighted in the following figures. Figure 4.10 plots circumferentially averaged data for a cooled and uncooled rotor casing. The increase in entropy generated by the coolant mixing with the mainstream is evident in the casing region between 0 – 40% C_{AX}. Downstream of 50% C_{AX} there is a reduction in entropy observed in the regions corresponding to the location of the casing passage vortex and the over-tip leakage flow. It is possible that some of this reduction is due to the flow in these vortices containing a greater proportion of coolant which enters the mainstream with a lower entropy value (due to its lower temperature) than the mainstream.

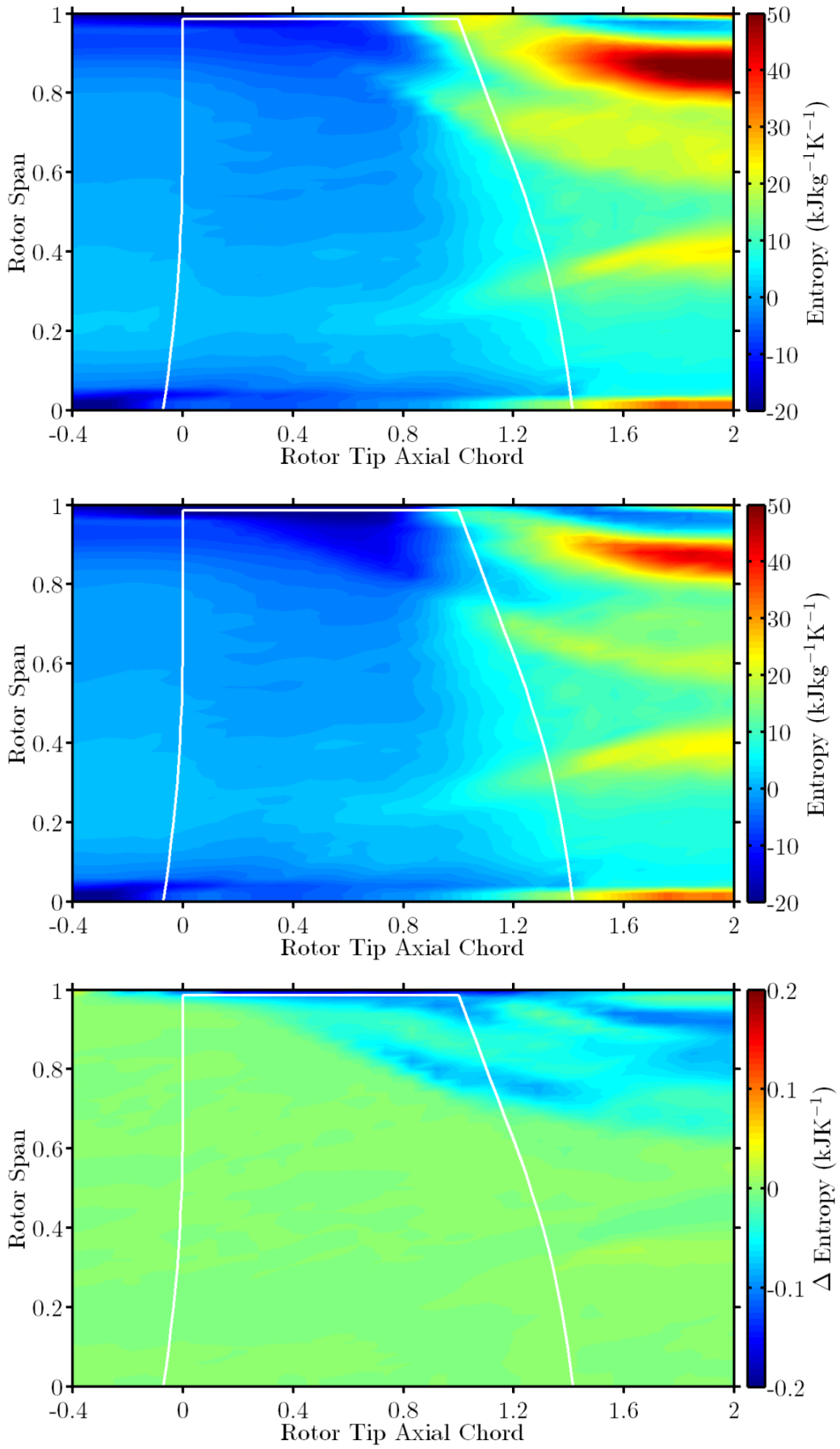

Figure 4.10. Pitch and time wise averaged plots of entropy in the rotor blade passage for uncooled (top), cooled (middle) and difference between cooled and uncooled (bottom).

The most notable reduction in entropy which does not correlate to coolant concentration is that in the tip vortex region. This is most significant beyond 70% C_{AX}, indicating a reduction in the magnitude of the tip leakage vortex, a similar conclusion to Behr et al. (2008). The reduction in entropy observed in the vicinity of the passage vortex is most likely due to the increased concentration of low entropy coolant.

Another often used parameter for defining loss is the total pressure loss in the passage. In the case of a moving endwall, the endwall will impart work on the fluid in the passage and so total pressure loss does not accurately account for all loss. However a comparison between both the cooled and uncooled cases proves interesting and is presented in fig. 4.11.

If we make the assumption that the work imparted on the casing is the same for both the cooled and uncooled cases then consideration of the difference in total pressure yields interesting results, though it must be considered that the coolant is injected at a slightly higher total pressure relative to the mainstream. It is observed that the total pressure loss is reduced in the tip leakage vortex and is confined to a smaller region. Since the tip leakage vortex contains a relatively low amount of coolant, this indicates the increase is due to a reduction in loss rather than presence of coolant. An increase in total pressure loss is observed in the passage vortex region. With an increase in coolant concentration in this region, an increase in total pressure would be expected if loss remained constant. This indicates that the loss in the passage vortex is increased by the introduction of coolant on the casing.

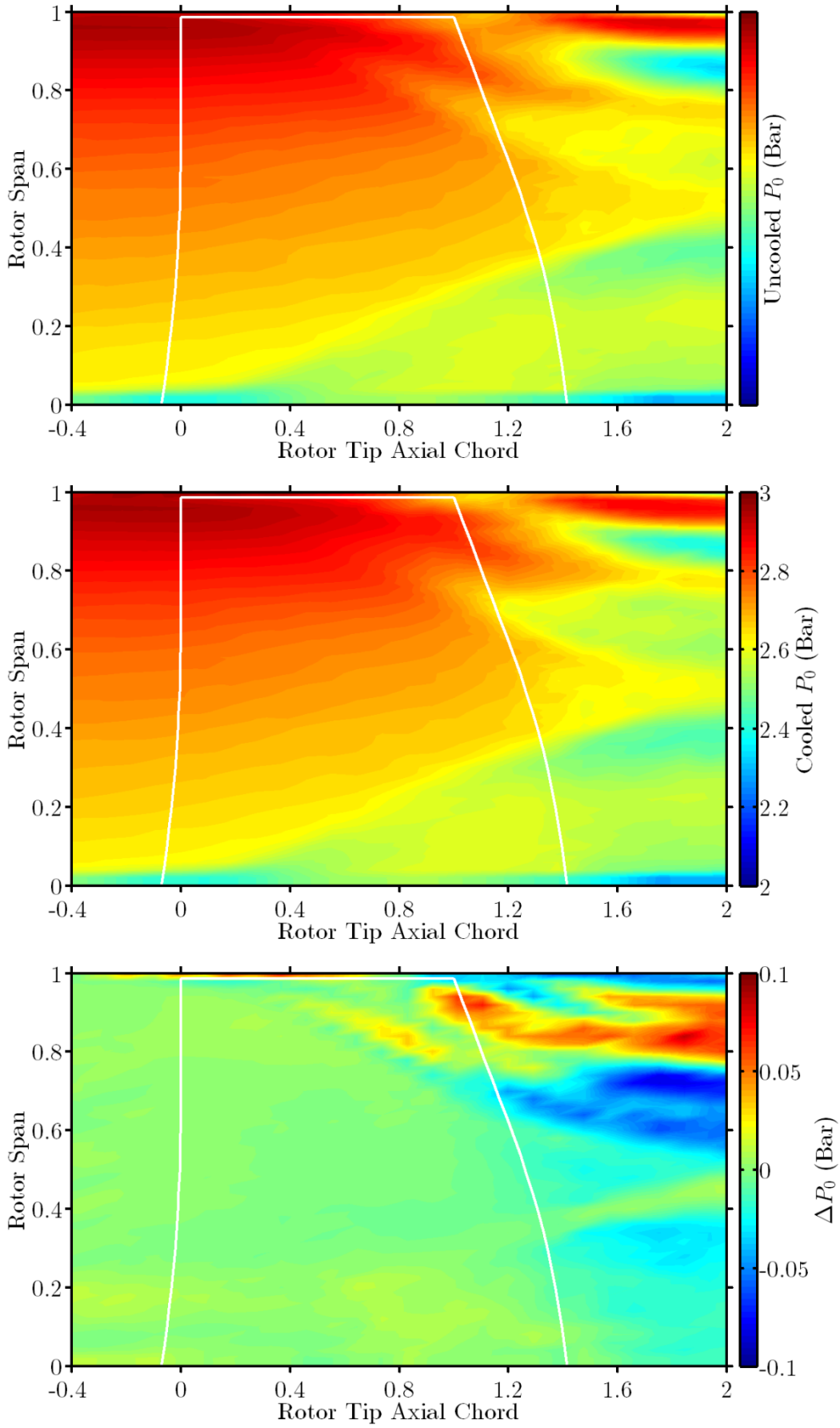

Figure 4.11. Pitch and time wise averaged plots of passage relative total pressure for uncooled case (top), cooled case (middle) and the difference (bottom).

To further investigate the losses in the passage and tip leakage vortices, iso-surfaces of swirling strength (helicity) were plotted to highlight the size and location of the vortices in the flow. Figures 4.12 and 4.13 show iso-contours of helicity coloured by entropy. Figures 4.14 and 4.15 show the same iso-contours of helicity but with streamlines coloured by entropy superimposed to show the direction of rotation.

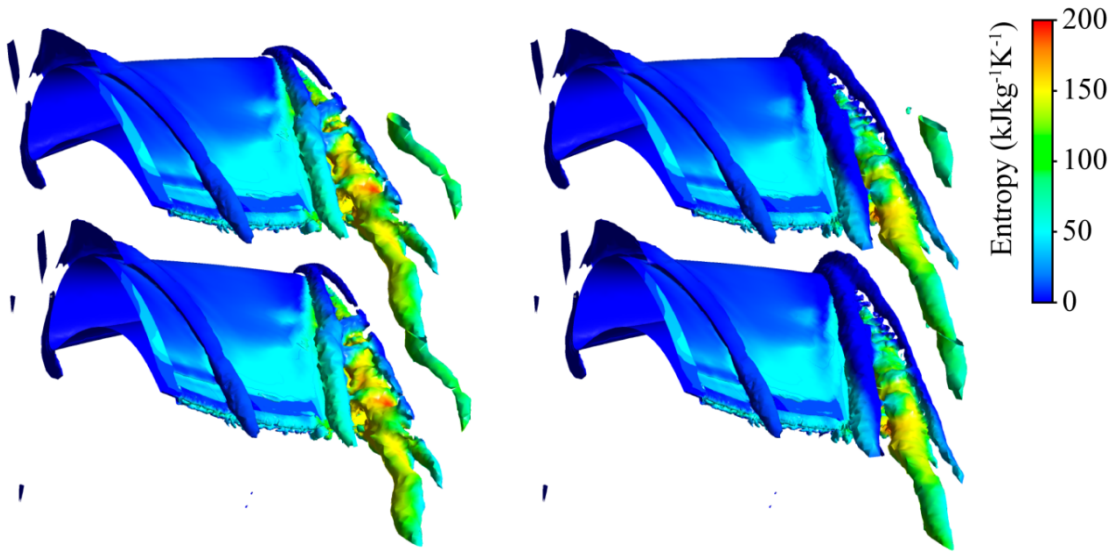

Figure 4.12. Iso-surfaces of vorticity (flow helicity) coloured by entropy for uncooled casing (left) and cooled casing (right).

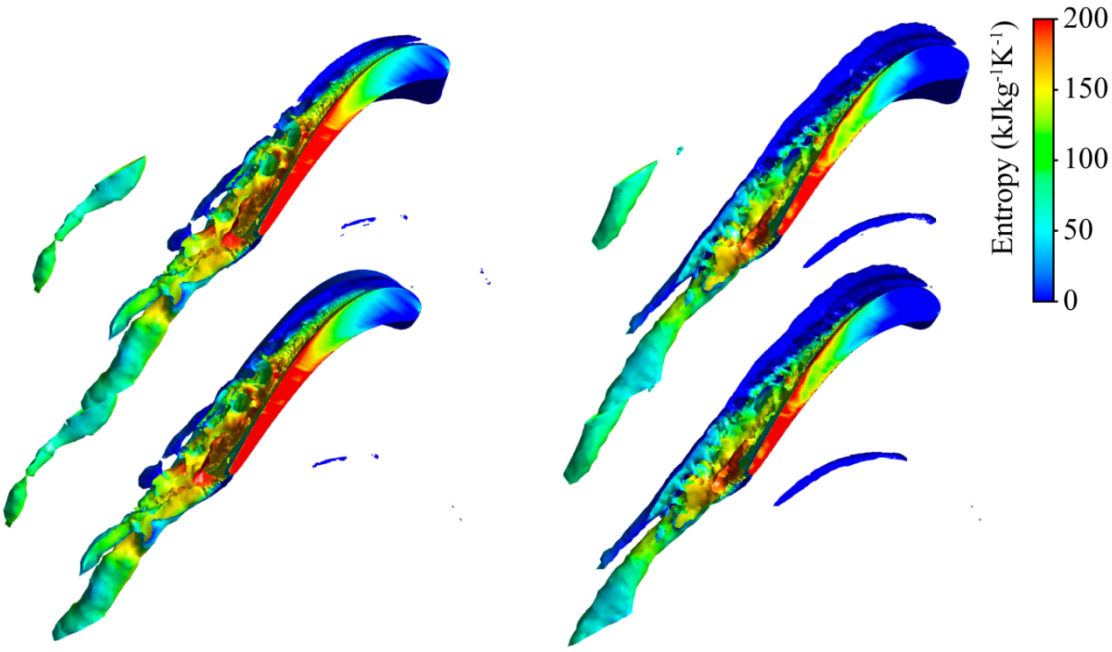

Figure 4.13. Iso-surfaces of vorticity (flow helicity) coloured by entropy for uncooled casing (left) and cooled casing (right).

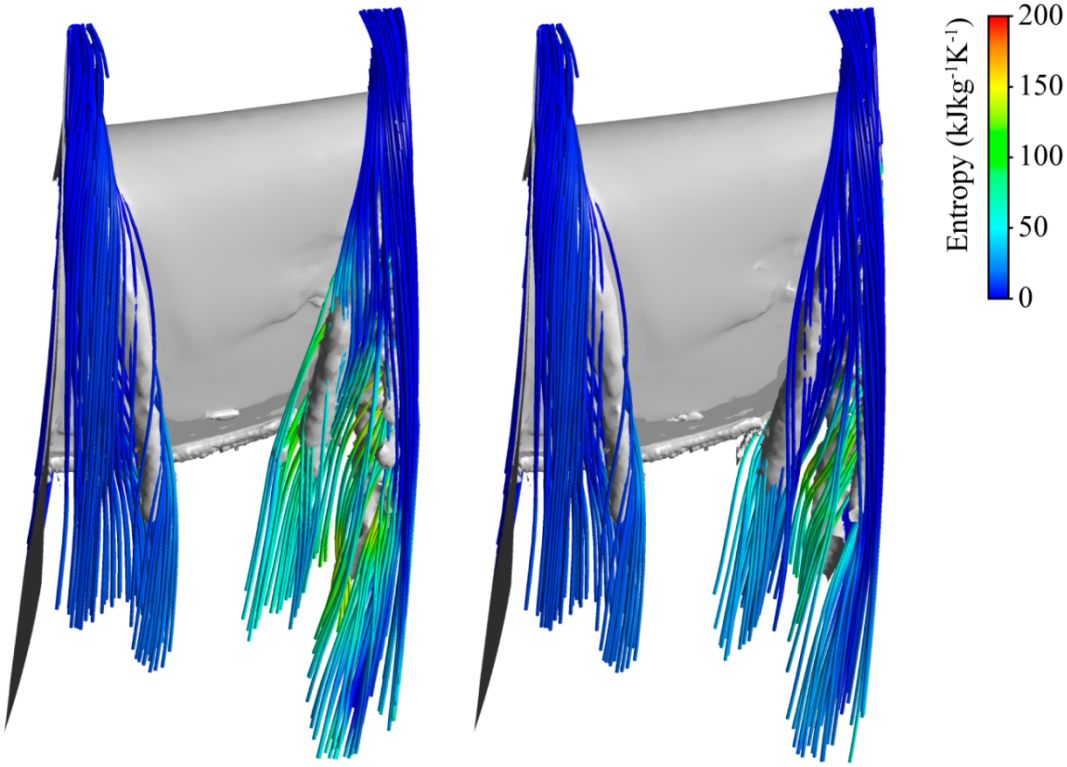

Figure 4.14. Iso-surfaces of vorticity (flow helicity) and streamlines coloured by entropy for uncooled casing (left) and cooled casing (right).

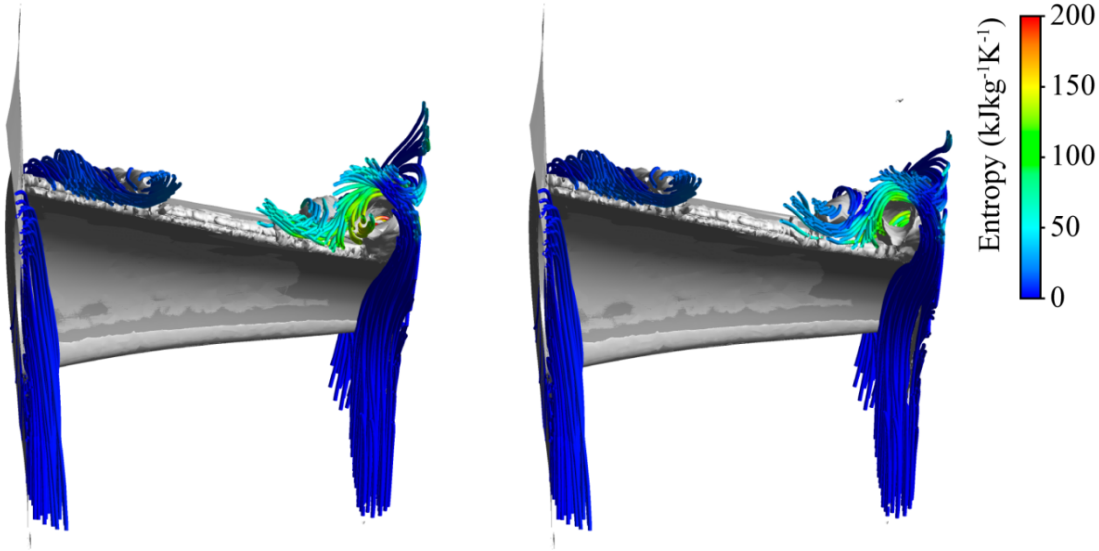

Figure 4.15. Iso-surfaces of vorticity (flow helicity) and streamlines coloured by entropy for uncooled casing (left) and cooled casing (right).

Passage Vortices

The hub and casing passage vortices are clearly evident in figures 4.12 – 4.15. The secondary flow features in a blade cascade are shown in fig. 4.16. and 4.17 are well summarised by

Sieverding (1985) and Wang (1997). The flow features described correlate well with the features observed in the CFD results presented here.

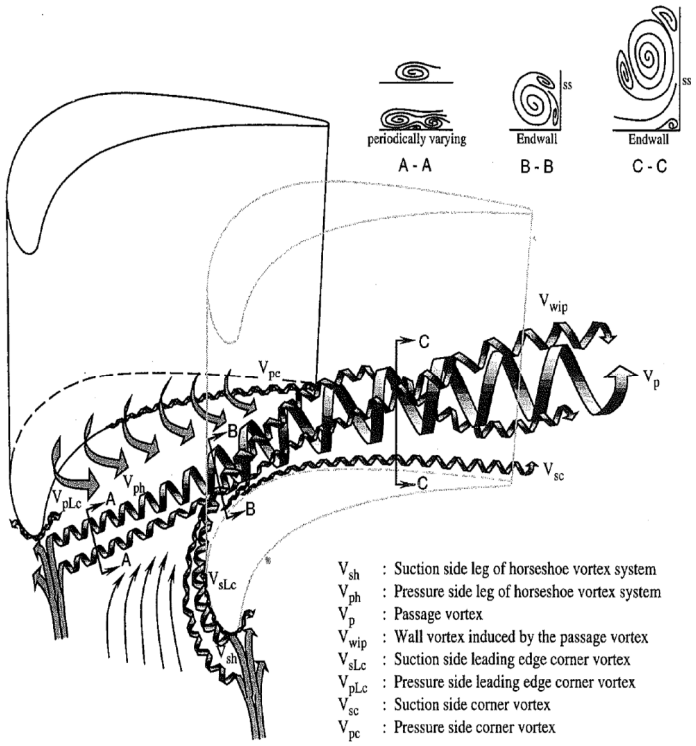

Figure 4.16. Secondary flow features as described by Wang et al. (1997).

The passage vortices form from the interaction of the endwall cross flow with the counter rotating horseshoe vortex legs from the pressure and suction side. The passage vortex remains in close proximity to the suction surface and is conducted away from the endwalls by the strong endwall crossflow. The counter rotating tip leakage vortex further assists in displacing the passage vortex away from the casing, as evident in fig. 4.9. Figure 4.9 also indicates an increase in the size of the casing passage vortex for the cooled case. This can be explained by an increase in the density of the casing boundary layer local to the blade leading edge due to the introduction of the coolant. This would act to increase the magnitude of the horseshoe vortices at the leading edge, which develop to form the passage vortex. Further coolant is conducted into the passage vortex by the tip leakage vortex, which scrapes off the casing boundary layer local to the suction side corner of the tip. The presence of coolant in the entrained flow also results in the casing passage vortex having slightly lower entropy contours.

Tip Leakage Flow

Tip leakage flow over flat tips has been extensively studied with detailed measurements taken by Bindon (1989), Moore and Tilton (1988), Heyes and Hodson (1993) and Yaras and Sjolander (1992). These surmise that tip leakage flow is predominantly driven by the static pressure difference across the tip gap. The flow structures over the tip are discussed by Denton (1993) and summarised in figures 4.17 and 4.18. Yaras and Sjolander (1991) conclude that relative casing motion has a significant effect on the magnitude of the tip leakage flow. The relative casing motion influences the velocities in the tip gap as described in the later uncooled casing heat transfer chapter and highlighted in fig. 4.18. It also illustrates that there will be an impingement of the flow entering the tip gap onto the casing ahead of the tip gap. This acts to scrape off the casing boundary layer local to the pressure side corner.

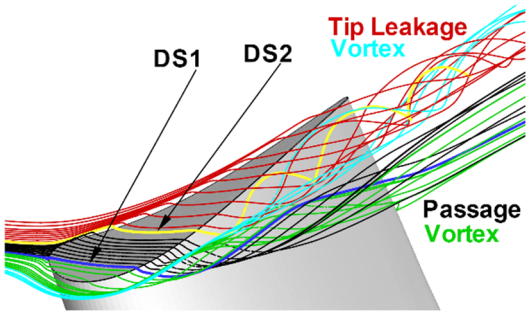

Figure 4.17 Tip leakage vortex development over flat tip, Mischo (2008).

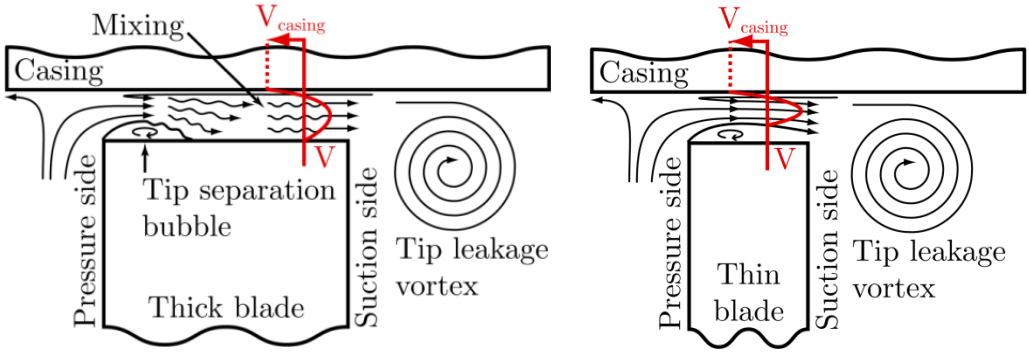

Figure 4.18 Over tip leakage flow over a thick blade (left) and thin blade (right), adapted from Denton (1993).

Along the exit of the tip gap a vortex sheet is formed, due to the differing magnitude of the mainstream and leakage flow velocities. This rolls up along the suction side corner to form the

concentrated tip leakage vortex. Wang et al. (1997) describes how this interacts with the counter rotating passage vortex, which is generated along the leading edge of the blade tip (fig. 4.17), and further entrains casing secondary flow from the passage endwall.

Figures 4.12 and 4.13 indicate a reduction in the magnitude of the tip leakage vortex for the cooled case and a reduction in entropy in the over tip flow. This is further evidenced in fig. 4.19, which is a circumferential slice taken at the radius of the blade tip. It is most likely that the 'unsteadiness' of the entropy in the tip leakage vortex for the cooled case results from localised concentrations of injected coolant being transported in the tip secondary flow. There is however an observed reduction in the magnitude of the tip leakage vortex at this location.

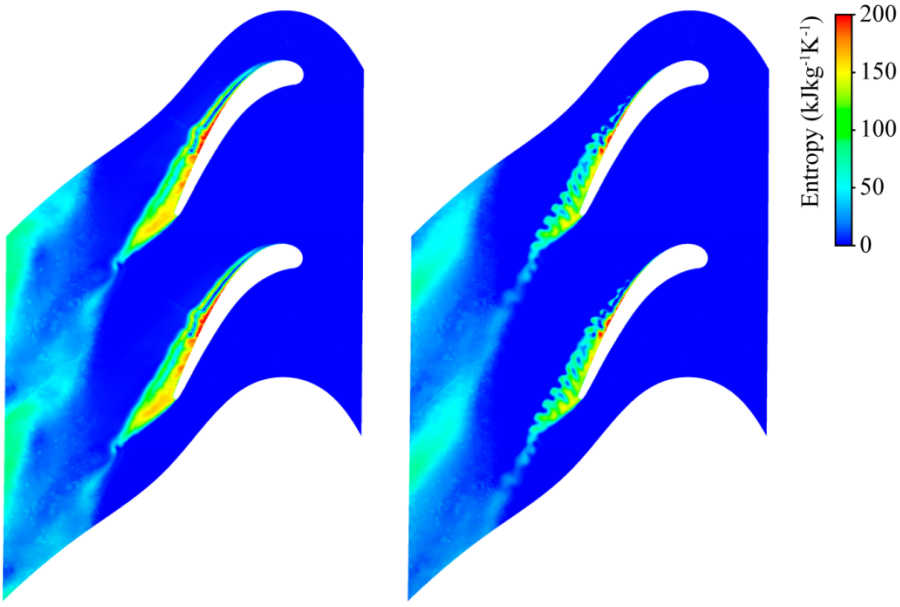

Figure 4.19 . Circumferential slice taken at 100% span of rotor (relative to tip) of entropy, uncooled (left) and cooled (right).

The flow over the tip is characterised by its contraction into a jet as it is accelerated about the pressure side corner, leading to the formation of a separation bubble. The separation bubble is clearly visible in fig. 4.20. There are some very notable differences between the cooled and uncooled tip surface streamlines.

- The size of the separation bubble is reduced between 0 – 10% axial chord.

- The size and location of the separation bubble is more irregular in the cooled case indicating unsteadiness in the size of the bubble.
- In the uncooled case, the flow does not reattach for a larger part of the trailing edge region.

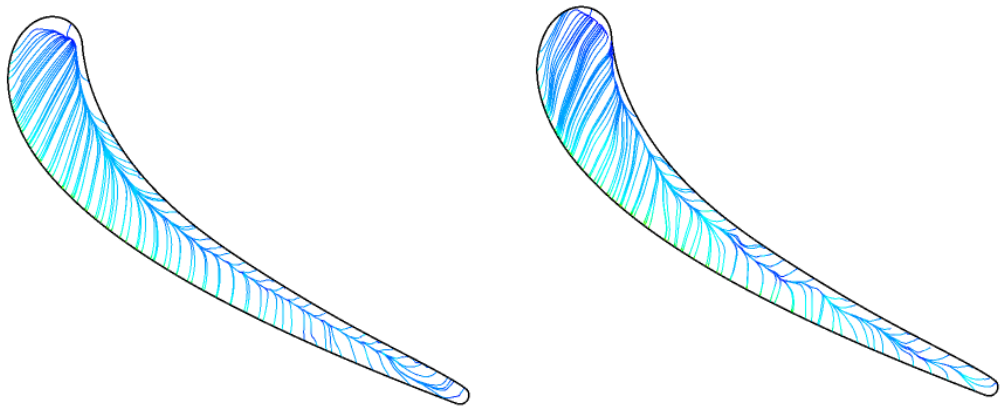

Figure 4.20. Surface streamlines on blade tip of uncooled casing (left) and cooled casing (right).

It is postulated that these differences result primarily from the blockage effects due to the injection coolant into the tip gap. It must be remembered that the cooling holes will be choked under the tip and thus the blowing ratio will be high despite the high tip gap flow velocity. The unsteadiness in the size of the separation bubble can be explained by the relative cooling hole motion to the blade tip.

The unsteadiness of the tip leakage vortex indicated in fig. 4.19 can be explained by the apparent unsteady appearance of the surface streamlines in fig. 4.20. This indicates that the velocity components of the tip flow are influenced by proximity to casing coolant holes. As these move relative to the rotor tip this will generate an unsteadiness in the flow exiting the tip gap.

To understand whether these blockage effects had any result on the mass flow rate through the tip gap, mass flow rates and Mach numbers across a surface along a blade mid-chord surface (fig. 4.21) were extracted from the CFD model.

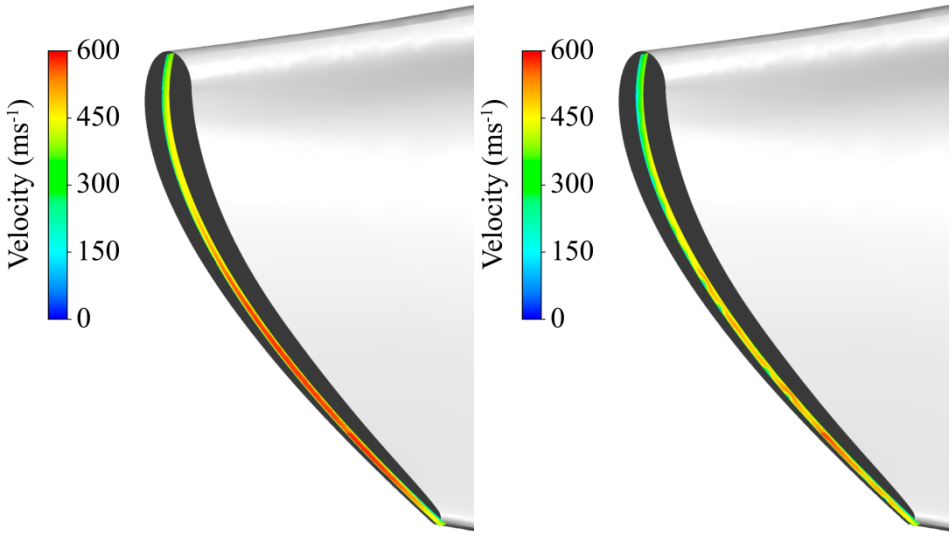

Figure 4.21. Mid-chord surface used to calculate leakage mass flow rate, coloured by flow velocity. Uncooled casing (left), cooled casing (right).

Table 4.2. Averaged values of tip leakage flow across mid-chord surface.

	$\dot{m}_c/\dot{m}_{12}$	$\dot{m}_{tip}/\dot{m}_{12}$	$\bar{M}_{tip}$	$\frac{\Delta\dot{m}_{tip}}{\dot{m}_{tip,uncooled}}$	$\frac{\Delta M_{tip}}{M_{tip,uncooled}}$
Uncooled	0%	2.49%	0.842	NA	NA
Geom. A	0.712%	2.35%	0.779	5.64%	6.46%
Geom. B	1.726%	2.19%	0.745	12.17%	11.53%

The surfaces in fig. 4.21 were exported at each time step and time averaged over one full rotor passing period, with data presented in table 4.2. Casing cooling geometries A and B respectively cause a 6% and 12% reduction of leakage mass flow rate and over tip Mach number. This is a significant reduction which scales with the number of cooling holes on the casing. The reduction results from the cooling holes on the casing introducing a blockage effect under the tip. Time-resolved reductions in leakage mass flow rate are observed as the rotor tip passes over cooling holes, very similar to those presented by Mischo et al. (2007).

The Mach number normal to the mid-chord surface as a function of rotor axial chord is presented in fig. 4.22. As would be expected, the Mach number increases with blade tip loading (fig. 4.23) and also with the reduction in thickness of the blade tip. The cooled case exhibits a

reduction in over tip Mach number for the entire axial chord of the tip. With reference to fig. 4.23, it is clear that this reduction is not due to a change in the static pressure field local to the tip, but instead due to the blockage effect of the coolant in the tip gap.

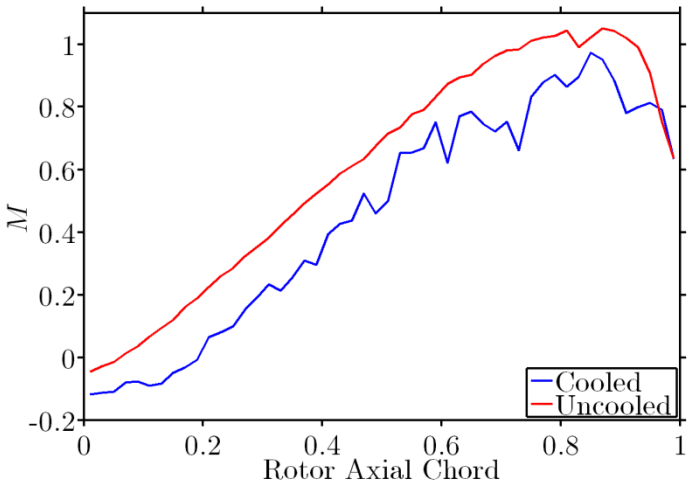

Figure 4.22 Tip leakage Mach number calculated normal to mid-chord surface.

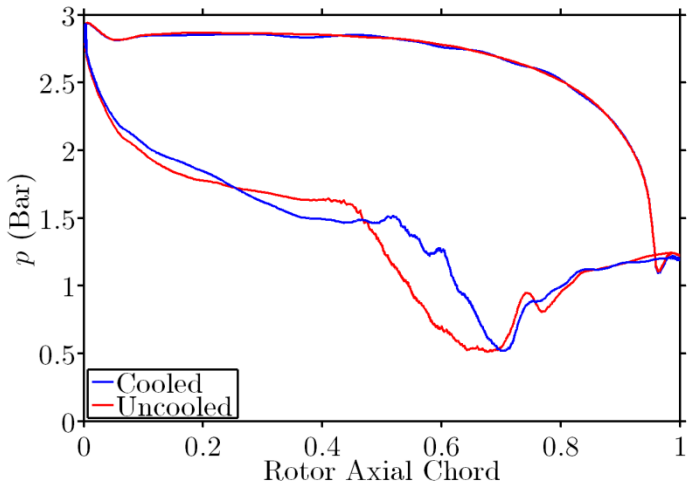

Figure 4.23. Plot of blade surface static pressure at 95% span.

These results give us reason to explain the reduction in entropy generation seen for the cooled example. As discussed by Denton (1993), much of the entropy produced in the tip gap is the result of viscous and mixing effects in the tip gap and tip leakage vortex. For the cooling geometry B, the over-tip mass flow rate is reduced by 12%, this consequently reduces the entropy generated by viscous effects and from mixing of the leakage jet and separation bubble

in the tip gap. The associated reduction in the tip leakage mass flow rate will reduce the size of the tip leakage vortex and the associated mixing losses as it mixes with the suction side flow.

4.5 Conclusions

The use of a full 3D CFD model of a casing film cooling scheme has been used to study the impacts of casing coolant injection on the blade row efficiency of an HP rotor. A number of cooled turbine efficiency models are discussed and used to show that coolant injection on the rotor casing can result in improvements of cooled rotor blade row efficiency. These improvements are shown to result from a reduction of over-tip leakage mass flow (12% reduction for $\dot{m}_c/\dot{m}_{12}$= 1.73%) via blockage effects in the tip gap. This reduction in over-tip leakage mass flow rate reduces the size of the tip leakage vortex, leading to a reduction of entropy generation and a reduction in total pressure loss. These reductions are partly offset by an increase in size of the tip passage vortex which entrains much of the injected casing coolant flow, with a subsequent increase in total pressure loss. The combined result of these effects helps offset the inevitable mixing losses associated with film cooling injection, resulting in improvements in rotor blade row efficiency for some cases. This is a key benefit of a casing film cooling scheme vs. a purely internally cooled casing. This suggests that a combined internally cooled and film cooled casing may well be the optimal solution when compared to a solely internally cooled scheme, which dumps used coolant downstream of the rotor passage, incurring significant mixing losses.

4.6 Chapter Nomenclature

c_p	Specific heat capacity
C	Rotor true chord (OTRF = 36.6 mm)
C_{AX}	Rotor tip axial chord (OTRF = 21.39 mm)
ε	Blade row efficiency
h	Enthalpy
k	Gas conductivity
$\dot{m}$	Mass flow rate
$\dot{m}^*$	Choked hole mass flow rate
M	Mach number
Nu	Nusselt number: $(htc \times C)/k_{01}$
p	Pressure
$\dot{q}$	Heat flux
ρ	Density
Re	Reynolds number
R	Specific gas constant
s	Entropy
σ	Entropy per unit mass of mixture
t	Time
t_r	Pressure wave transmission time
τ	Time step
T	Temperature
T_G	Gas static temperature
ϕ	Mass flux ratio
φ	Exergy
ψ	Coolant concentration
V	Flow velocity
X	Mole fraction

Subscripts

01	Rotor inlet total
02	Rotor outlet total
1	Rotor inlet static
12	Passage
2	Rotor outlet static
c	Coolant
f	Fully reversible mixed condition
g	Mainstream
m	Mixed
rel	Rotor relative
s	Isentropic
tip	Over-tip
w	Weighted pressure mixed condition

Chapter 5: New Technique for the Fabrication of Miniature Thin Film Heat Flux Gauges

5.1 Abstract

This chapter details the improvements made to the design and fabrication of thin-film heat flux gauges at Oxford. These improvements have been driven by the desire to improve measurement accuracy and resolution in short duration wind-tunnel experiments.

A thin-film heat flux gauge (TFHFG) measures heat flux by recording the temperature history of thin film resistive temperature sensors sputtered onto an insulating substrate. The heat flux can then be calculated using Fourier's law of heat conduction.

A new fabrication process utilising technology from the manufacture of flexible printed circuit boards is outlined, which enables the production of significantly smaller and more robust gauges than those previously used.

Improvements in data processing techniques are also briefly discussed and presented in the context of experimental data.

5.2 Introduction

The thin film heat flux gauge was first used to record heat transfer within a shock tunnel, Vidal (1956). The TFHFG was extensively developed at the Osney Laboratory, the history of which is described by Jones (1988), (1995). They are fabricated by sputtering a thin layer of platinum (< 0.04 μm) onto a polyimide substrate with copper tracks forming the connections.

5.2.1 Principal of Operation

The TFHFG operates on the principal that the heat flux into a surface can be calculated by measuring or calculating the temperature gradient within a material of known thermal properties using Fourier's law

$$\dot{q} = -\lambda \nabla T \tag{5.1}$$

The theory can be extended to an unsteady problem whereby the surface temperature history of a material can be used to calculate the heat flux by applying the heat-conduction equation

$$\frac{\partial^2 T}{\partial x^2} = \frac{1}{D}\frac{\partial T}{\partial t} \tag{5.2}$$

These equations can be solved analytically in the discrete time domain for a limited set of boundary conditions and the data processed numerically, Schultz and Jones (1973), Doorly and Oldfield (1986). Alternatively the data can be processed using a computationally more efficient impulse response method, Oldfield (2008).

There are two principal types of TFHFGs, single layered gauges and double layered gauges. A single layered gauge comprises of one thin film resistive sensor on an insulating substrate. Most commonly the substrate is thick enough such that for the experiments duration it is considered semi-infinite in depth. However Oldfield (2008) describes impulse response methods which can process data from gauges located on two layered substrates and those on an insulating layer atop an isothermal surface. These gauges are used when it is possible to assume isothermal conditions in a sufficiently thick insulating substrate at the start of the measurement.

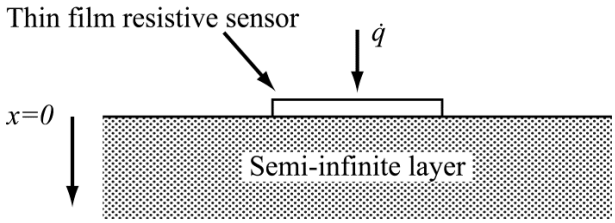

Figure 5.1. Single layer TFHFG.

5.3 Conventional Design and Fabrication Techniques

TFHFGs were first manufactured on ceramic substrates (or enamelled metal parts) using a firing process, Shultz and Jones (1973). The resistive element is typically platinum, though nickel has

also been used. The resistive sensor is connected via tracks of gold or copper to points at which wiring can be soldered. The platinum resistive sensor and copper tracks are painted on using a metallo-organic ink. The sample is then fired to leave behind conducting platinum and copper tracks. This method is still used in high temperature applications which are not subjected to large mechanical stresses. This technique is very labour intensive and the size of the sensors is usually quite large (typically 3000 x 300 μm).

The above method was improved upon by Thorpe et al. (2004). Rather than hand painting each gauge, the entire substrate is covered in a fired layer of metallo-organic ink. A laser is then used to ablate the unwanted conducting film to leave the desired gauges. With this method, gauges of dimensions of 1000 x 80 μm can be produced. The spatial resolution of this method is typically limited by the width of the gold/copper connecting tracks which are typically quite thin (< 0.5 μm). This method also requires a substantial amount of time and care to set up and program the laser when used on 3D surfaces.

Another approach developed by Epstein et al. (1986) and used extensively in Oxford since, is to manufacture TFHFGs on a flexible polyimide substrate. These flexible gauges can then be laminated to the test piece using a glue layer, Guo et al. (1998). The process utilises photolithography techniques which can create intricate features. The process can also be used to manufacture large volumes of gauges as the technique requires substantially fewer man hours than the firing processes.

From now on these flexible TFHFGs are referred to as the "conventional" type. The fabrication process subsequently developed at Oxford consists of sputtering a thin layer of platinum (< 0.04 μm) onto a polyimide substrate. Copper tracks are then deposited in a vacuum chamber by evaporation to a thickness of 0.5 μm. The process used at the Osney laboratory for a number of years has not been fully described in published literature and is illustrated in fig. 5.2 and outlined below

1. Sputter polyimide surface with a layer of copper. Apply photoresist, overlay phototool 1, expose and develop.
2. Etch copper, remove developed phototool and sputter a layer of platinum.
3. Etch away the copper underneath the unwanted platinum, leaving the platinum sensing elements. Deposit a new layer of copper over entire surface.
4. Apply photoresist, overlay phototool 2 and expose.
5. Etch away unwanted copper then remove developed phototool to leave completed gauges.

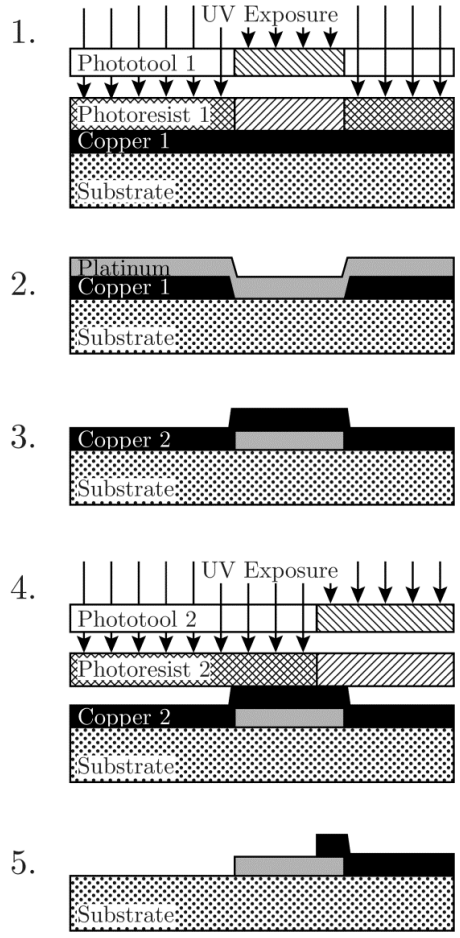

Figure 5.2. Conventional gauge manufacturing process.

This process is reasonably time consuming and the copper tracks are fragile, typically cracking and lifting off when bent around small radii. This imposes a limit of 0.5 μm on the thickness of the copper tracks for typical applications. To ensure that their resistance and corresponding

thermal resistance changes during an experiment are negligible the copper tracks must be made relatively wide (2000 μm).

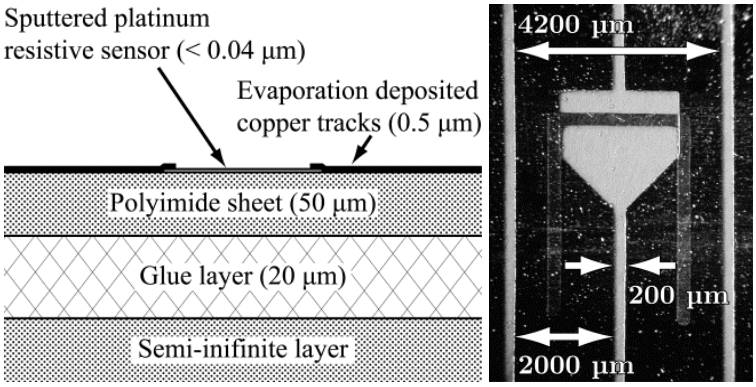

Figure 5.3. Conventional TFHFG typical dimensions.

Figure 5.3 shows the design of a typical conventional gauge manufactured using a 200 μm processing resolution. The platinum sensing element is 2000 x 200 μm giving a L/W ratio of 10. The lateral gauge spacing is 4.4 mm.

5.4 New Manufacturing Technique

The size of conventional TFHFGs is limited by the width of the copper connecting tracks. The tracks can be made narrower either by making them thicker or by moving to a four wire measurement system, with separate exciting and sensing tracks. The four wire approach is undesirable as it increases the complexity and number of connections, though the principal has been used to fabricate small high density TFHFG arrays, Anthony et al. (1999).

Since the manufacturing process of conventional TFHFGs was developed in the early 1990's at Oxford, there has been a huge increase in the development and manufacturing of Flexible Printed Circuits (FPCs). These circuits are manufactured by etching a pre-laminated sheet of copper and polyimide using a dry film photoresist. These pre-laminated materials are available without an adhesive between the copper and polyimide layer. The copper quality is such that the sheets can be repeatedly folded without delamination, despite having a copper thickness that can be in the hundreds of microns.

5.4.1 Manufacturing process

To make use of a pre laminated copper-polyimide laminate, a new manufacturing process has been devised. The metal lift off process previously used to fabricate the platinum sensors is replaced with a dry film photoresist lift off technique as described by Chew et al. (2009). The platinum film is now deposited over pre-etched copper tracks, manufactured in a dedicated FPC fabrication facility using the process illustrated in fig. 5.4 and outlined below.

1. Apply photoresist, overlay phototool 1, expose and develop.
2. Etch copper then remove developed photoresist.
3. Apply new photoresist, overlay phototool 2, expose and develop.
4. Sputter entire surface with platinum.
5. Remove developed photoresist taking away unwanted platinum.

Using this process, TFHFGs have been manufactured with the use of 18 μm thick copper connecting tracks (36 times thicker than conventional gauges). This permits connecting track widths of 100 μm, the fine line resolution of the etching process. This has substantially improved the achievable TFHFG density, now primarily limited by the footprint of the platinum sensor element rather than the connecting tracks. The new gauges have also proven to be much more resistant to bending and abrasion, easing installation and extending operating life.

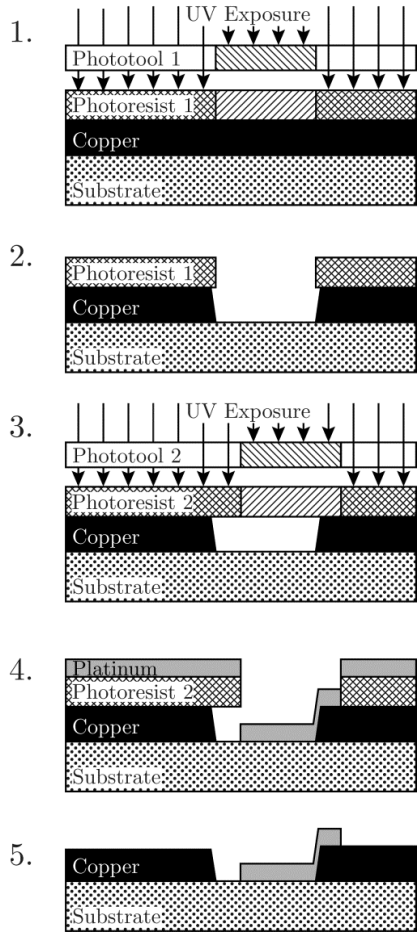

Figure 5.4. New TFHFG manufacturing process.

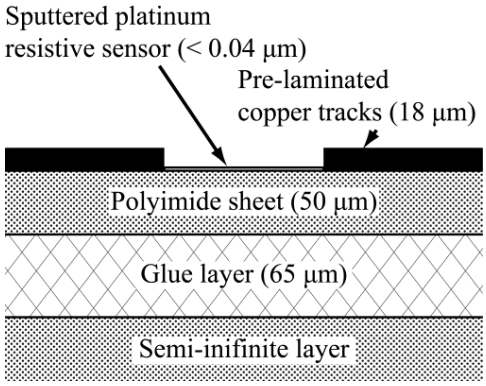

Figure 5.5. New TFHFG typical dimensions.

5.4.2 SEM Analysis

The new manufacturing process relies on a good bond being formed between the etched copper connecting tracks and the deposited platinum film. A Scanning Electron Microscope (SEM) was used to image the interface, as shown in fig. 5.6.

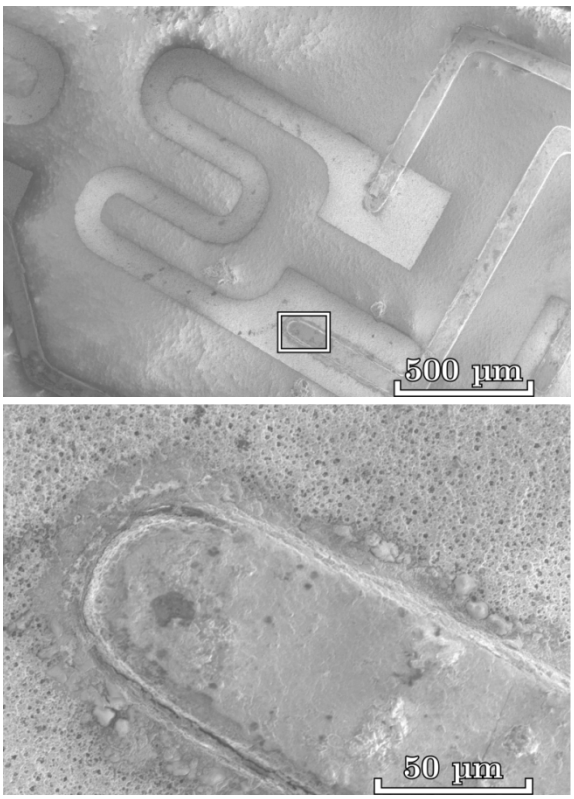

Figure 5.6. SEM images of TFHFG manufactured using new process.

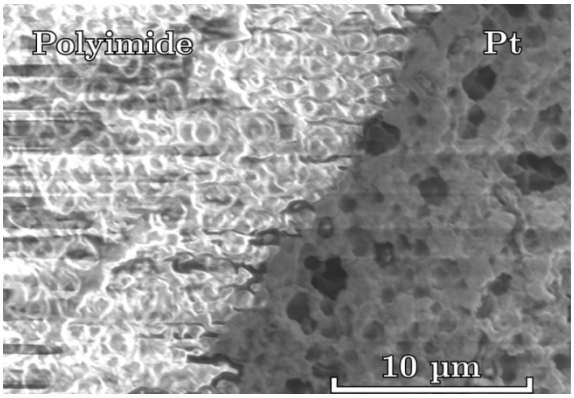

Figure 5.7. SEM image of platinum deposited on polyimide substrate.

A good copper/ platinum bond is evident along a substantial portion of the interface with a platinum meniscus formed. In places, cracks are visible along the interface. This is most likely due to differing thermal expansion of the copper and polyimide during platinum deposition or during calibration. The flaws signify the importance of maximising the length of the copper/platinum interface, which in this case is achieved by utilising a long thin connecting copper track at the interface.

Also visible in the SEM images is the porous nature of the deposited platinum. It is not clear what causes this porosity, but it could be due to the interaction between the deposited film and the surface topology of the polyimide substrate, as visible in fig. 5.7. During the laminate's manufacture, the polyimide's surface is roughened using an oxygen plasma as described by Yang et al. (2005), before bonding with copper. It is this roughness, of comparable length scale to the platinum's porosity, that is visible in fig. 5.7.

5.4.3 Finite Element Analysis

The increased thickness of the copper tracks substantially increases the thermal mass of the copper tracks local to the gauge. To investigate whether this has any impact on the measured wall surface temperature a finite element heat transfer model of a thin film heat flux gauge with connecting track was generated and solved in Abaqus CAE 6.12.

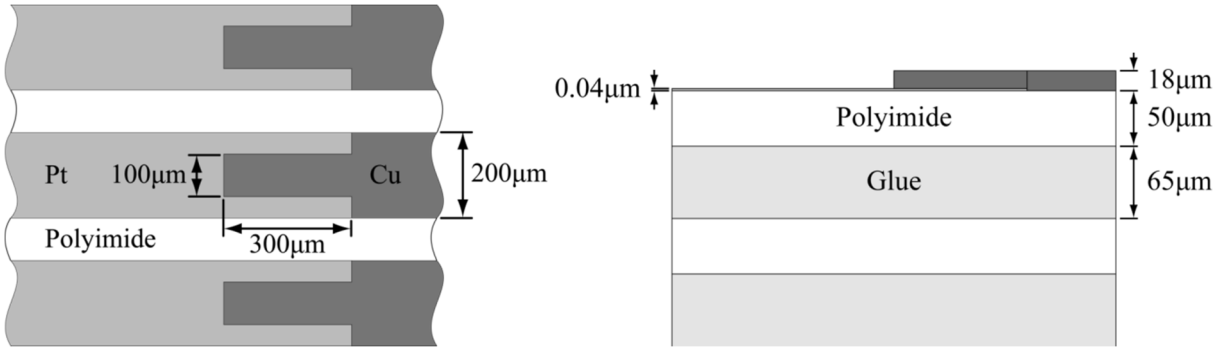

Figure 5.8. Thin film gauge heat transfer geometry

Geometry

A periodic 3D geometry of a thin film heat transfer gauge was modelled. The model included the copper connecting track and platinum sensing element. The geometry is given in fig. 5.8 and the structured mesh generated using Abaqus in fig. 5.9. The overall depth of the modelled substrate was 3.23 mm, chosen so that the thermal pulse does not propagate through the entire material during the test time.

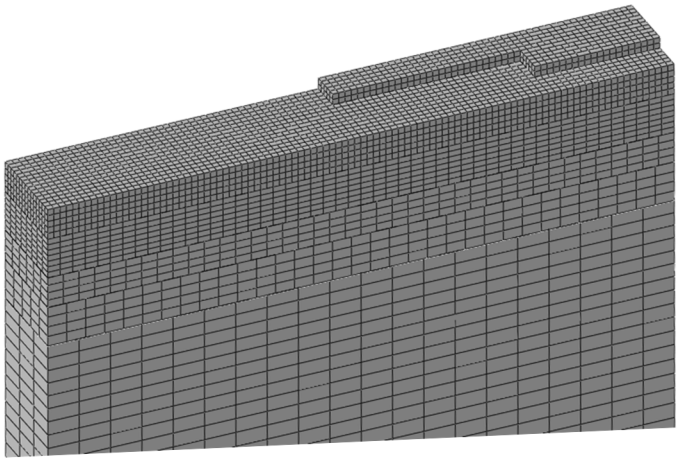

Figure 5.9. Abaqus CAE mesh.

Abaqus CAE Setup

The model was run as a heat transfer only problem (no mechanical equations) with the material properties given in table 5.1. All internal surfaces were specified as being fully insulated ($\dot{q} = 0$) to resemble a periodic interface.

The model was isothermally initialised with all volumes and surfaces set to 297 K. A step in heat flux equal to $\dot{q} = 100\ \mathrm{kWm^{-3}}$ was then applied to all external surfaces. A variable time stepping solution scheme was used which limited the maximum node temperature rise to 3 K per time step. The model was run for 0.8 s in total over 115 time steps.

Table 5.1. FEA model material parameters.

Material	$\boldsymbol{\rho}\ (\mathbf{kgm^{-3}})$	$\boldsymbol{c}\ (\mathbf{Jkg^{-1}K^{-1}})$	$\boldsymbol{\lambda}\ (\mathbf{Wm^{-1}K^{-1}})$	$\sqrt{\boldsymbol{\rho c \lambda}}$
Polyimide	1420	1090	0.155	490
Glue	1420	1090	0.155	490
Copper	8940	390	390	36875
Platinum	21450	130	69	13871

Results

The temperature rise on the external surfaces ($T_{Rise,S}$) was recorded at each time step and compared to the analytical 1D calculated value, evaluated using the following equation

$$T_{Rise,1D} = \frac{2\dot{q}\sqrt{t}}{\sqrt{\pi\rho c\lambda}} \tag{5.3}$$

For short time scales (i.e. high frequency signals), the surface temperature of the copper and surrounding polyimide is reduced relative to the 1D solution. This is due to the increased thermal mass and high thermal conductivity of the copper. At longer timescales, the increased surface area of the copper track (due to its 18 µm height) causes the copper track to act like a heat exchanger fin, raising the copper and surrounding polyimide surface temperatures above the 1D analytical value. The boundary conditions applied here are simplified (in reality you would expect a different heat flux on the sides of the copper tracks) however it is thought that the result still applies.

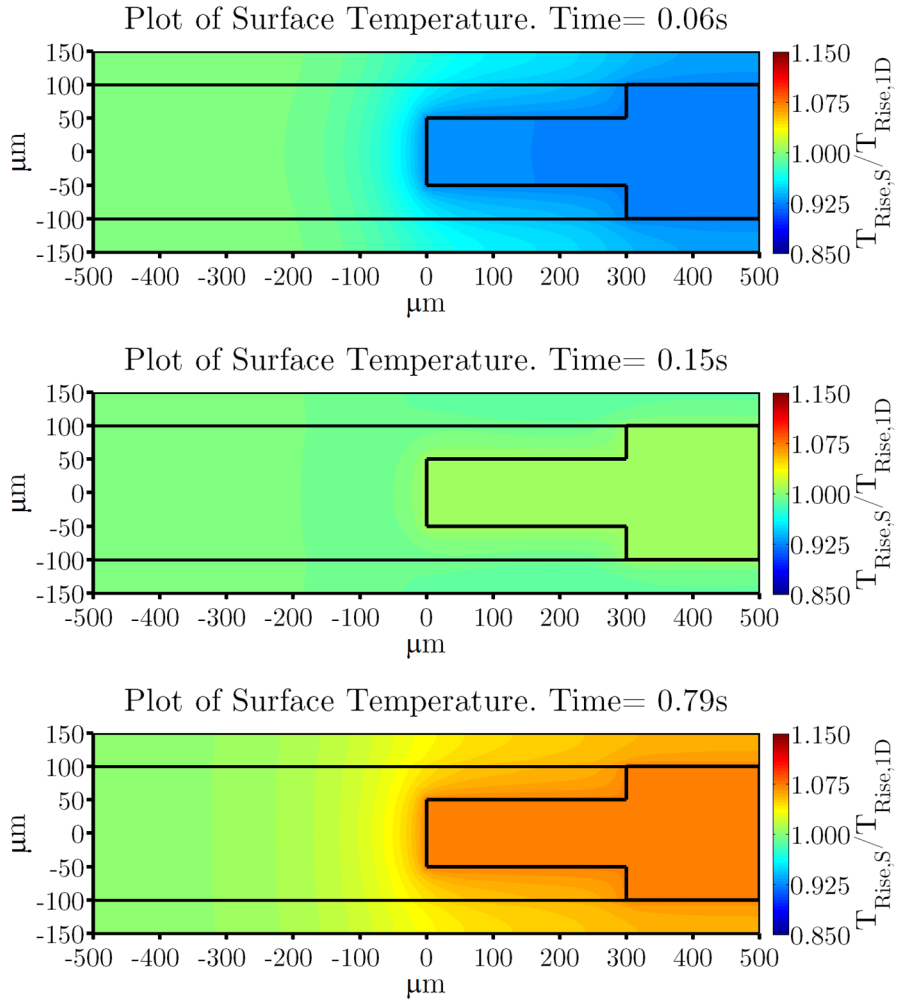

Figure 5.10. Recorded surface temperatures vs. 1D analytical solution.

The most significant result is that these effects are localised to the copper track and are relatively small in magnitude (maximum of 10% difference at 0.8 s). Beyond 300 μm from the copper track, the recorded surface temperature error is less than 1% at 0.6 s (the duration of an OTRF test). In practice the temperature error is likely to be smaller due to a constant driving T_{AW} and *htc* boundary condition rather than constant heat flux. It is recommended that the copper track be separated from the platinum sensing element by a wider platinum section to minimise these errors, this is incorporated into the improved sensor designs discussed in this chapter.

5.4.4 Optimised Design of Gauges

The parameter of most interest to the thin film gauge designer is the magnitude of the voltage signal generated across the element relative to the change in temperature.

$$\frac{\Delta V}{\Delta T} = I\ (\alpha_{Pt}\ R_{0,Gauge} + \alpha_{Cu}\ R_{0,Track}) \tag{5.4}$$

The platinum element will also generate heat due to resistive heating by the excitation current. This heat will be dissipated by 1D conduction and convection but must be small enough to not affect the measurement.

$$\dot{q}_{internal} = \frac{I^2\ \rho_e}{w^2 d} \tag{5.5}$$

These equations can be combined with the resistance defined in terms of the geometry to give an equation for the gauge sensitivity. Assuming that changes in the connecting track resistance are negligible

$$\frac{\Delta V}{\Delta T} = \alpha_{Pt}\ \mathrm{L} \sqrt{\frac{\dot{q}_{internal}\ \rho_e}{d}} \tag{5.6}$$

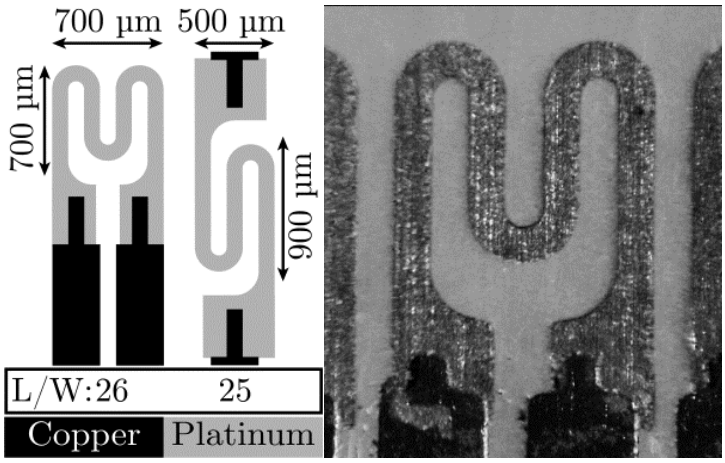

Figure 5.11. New Oxford TFHFG typical dimensions based on 100 µm processing resolution (left) and as manufactured (right).

The internal heat flux generation of the gauge is limited to an experimentally determined value which results in no measurable heating of the gauge. Sensitivity can then be increased by maximising the length L (and hence for a given gauge footprint, L/W) and reducing the platinum thickness (though this is the less dominant term). Using a material with a larger α value will also improve the sensitivity, however platinum is typically the material of choice due to the consistency of α over a large temperature range, significantly easing calibration.

Previous TFHFGs in use at Oxford utilise a linear platinum sensor element with L/W of 10. This design originated from the use of hand painted platinum sensors on ceramic and glass which were developed in the 1960s, Shultz and Jones (1973). New gauge designs have been created which maximise the L/W ratio for a given gauge footprint and are shown in fig. 5.11. Features were rounded to improve the structural rigidity of the photoresist layer during manufacture.

Figure 5.12 compares the new Oxford gauge to conventional gauges produced at Oxford and also to the laser ablated gauges utilised by Thorpe et al. (2004), which have hitherto had the highest published resolution. The new TFHFG designs published here offer a 7 fold improvement in gauge density vs. the conventional Oxford gauges and greater than double the resolution of the laser ablated gauges. The new Oxford gauges can offer even greater

improvements in resolution for applications where the number of gauges is constrained by the total width of the connecting tracks, due to the increased connecting track thickness (18 µm vs. 0.5 µm). An example is the rotor tip instrumentation shown in fig. 5.13, which places 25 TFHFGs on the blade tip. The width of the tip is only 4 mm and has a chord of 32 mm.

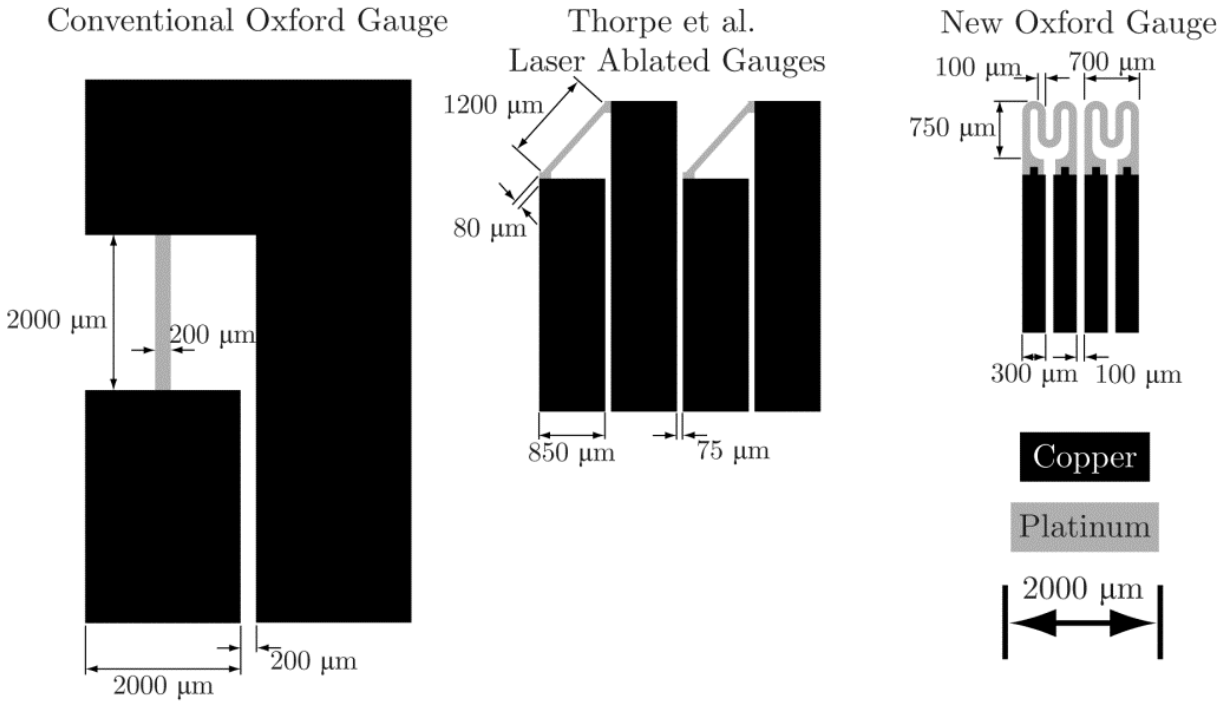

Figure 5.12. Comparison of gauge manufacturing technologies, conventional Oxford (left), Thorpe et al. (2004) laser ablated gauges (centre) and new Oxford gauge (right).

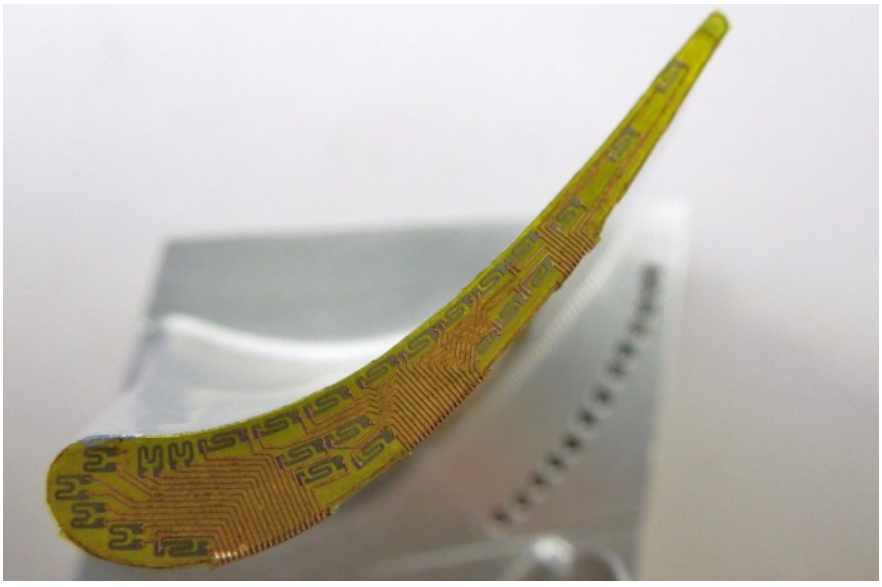

Figure 5.13. Rotor blade tip instrumented with 25TFHFGs. (Rotor chord = 32 mm).

5.5 Calibration of Conventional and New Gauges

5.5.1 Theory

The surface temperature of a TFHFG is measured by applying a constant current and recording the voltage across the sensor. Typically the temperature history is recorded by measuring the initial voltage (V_1) at a known isothermal condition (T_1) and then recording the change in voltage

$$T_W - T_1 = \frac{(V - V_1)(1 + \alpha\,(T_1 - T_0))}{\alpha\, V_1} \tag{5.7}$$

This removes the need to measure the connecting lead resistances or the current during the run. The assumption is that the resistance of the connecting tracks and leads between the calibration and experiment are kept similar. The only parameter for each gauge that need then be calibrated is α. This is calibrated by measuring the resistance using a digital multi meter (DMM) at a number of known temperatures then applying a linear regression to fit the following equation

$$R - R_0 = \alpha R_0\,(T_W - T_0) \tag{5.8}$$

The term R_0 is taken to be the resistance at T_0 which is typically taken to be 0 °C and includes the lead resistances. Thus α, which is a non-dimensionalised resistance/temperature gradient, incorporates the lead resistances into its definition and is given by

$$\alpha = \frac{1}{R_0}\frac{dR}{dT} \tag{5.9}$$

If the lead resistances cannot be kept constant from calibration to experiment then a four wire measurement approach can be used. This doubles the number of connecting leads which is undesirable, unless a TFHFG array as described by Anthony et al. (1999) is used. The array

approach is less robust as the failure of one TFHFG can cause failure of the entire instrumented region.

Alternatively changes in lead resistances can be corrected for by measuring the resistance of the gauge at a known temperature T_{Gauge} when installed in the experiment with a DMM. The α (for use in eqn. 5.7) can then be corrected as follows

$$\alpha_{Exp} = \frac{\alpha_{Cal} R_{0,Cal}}{R_{Gauge} - \alpha_{Cal} R_{0,Cal} (T_{Gauge} - T_0)} \tag{5.10}$$

Later work identified that the uncertainty in the value of R_0 is one of the most significant contributors of uncertainty in the computed T_{AW} and htc. This is due to observed drift in the value of R_0 over long time periods. Recalibration of gauges that had experienced this drift calibrated with very similar values of dR/dT_W. Hence the uncertainty is mostly confined in the estimation of the current through the gauge. This can be greatly reduced by instead measuring the current through each gauge, by recording the voltage (V_{Cal}) across a high precision resistor of known value (R_{Cal}) in place of the gauge before each run. T_W is then calculated using the following equation with dR/dT_W taken from the water bath calibration

$$T_W - T_1 = \frac{(V - V_1) R_{Cal}}{V_{Cal} dR/dT_W} \tag{5.11}$$

The HTA boxes have subsequently been modified with high precision calibrated resistors that can be connected instead of the gauges using a switch. Before a run the calibration switches of all channels would be enabled (connecting the calibration resistor across the channel input in place of the gauge) and a set of zeroes data taken using the same data acquisition system as that to record the experimental data. The switches would then be changed to reconnect the gauges and the experimental data taken. This approach also eliminates any changes in R_0 due to changes in the connecting wires between the calibration and the experiment.

To convert the measured surface temperature history to heat flux requires knowledge of the thermal properties of the substrate as described by Oldfield (2008). Piccini et al. (2000) describes the calibration of D and λ using a shuttered hot air gun to generate a step in surface heat flux, calibrated values are given in table. 5.2. It was found that the polyimide and glue layers were found to have indistinguishable thermal properties, to the extent that they can be regarded as being the same. The new TFHFGs are manufactured on the same polyimide substrate as that calibrated by Piccini et al. (2000) and these values were retained for use with the new gauges.

Table 5.2. Calibrated material properties measured by Piccini et al. (2000)

Material	$\boldsymbol{\lambda}\,(\mathbf{Wm^{-1}K^{-1}})$	$\boldsymbol{D}$	$\sqrt{\boldsymbol{\rho c \lambda}}$
Polyimide	0.169	1.190×10^{-7}	490

5.5.2 New TFHFG Calibration Facility

TFHFGs are calibrated using a new calibration facility at Oxford developed by the author, pictured in fig. 5.14. This is a National Instruments based PXI system consisting of a thermostatically controlled water bath (incorporating a heater and chiller and capable of attaining 5 – 95 °C with water) interfaced to a computer via a serial interface. Resistance measurements are made using a 22 bit National Instruments DMM (resolution of 1 mΩ) interfaced with a relay switch module, permitting the calibration of 96 TFHFGs simultaneously.

The calibration is automated and controlled with a Labview script. Two thermocouples monitor the temperature of the water in the water bath and multiple thermocouples are also attached to the sample to be calibrated. The script functions as follows:

- The Labview script first instructs the water bath to heat up or cool to a desired set point.
- The script then monitors both the water bath and sample temperatures and waits until these are all within a given tolerance of the set point temperature.

- The script then records these temperature over a given time period (usually 10 mins). If any of the measurements exceeds the initial value by another given tolerance (usually 0.2 °C) then the temperature monitoring period restarts.
- Once a time period has elapsed with all temperatures within tolerance, the NI switch cycles though all connected gauges to enable the NI DMM to record the gauge resistances. A thermocouple acquisition card records all the temperatures.
- The script then moves on to the next set point.

The script is also able to automatically anneal the sample at an elevated temperature for a set period (typically 6 hours at 80 °C before the calibration.

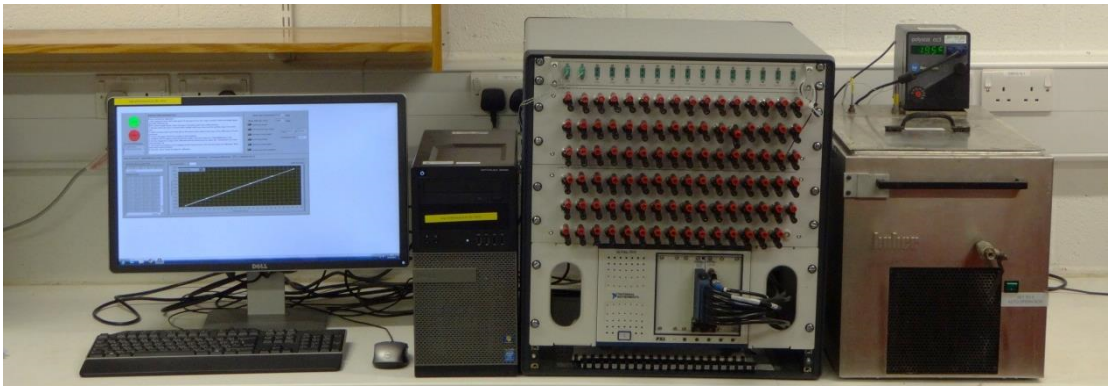

Figure 5.14. New TFHFG automated calibration facility. From left, control PC, PXI system, water bath.

Prior to the automated facility, calibrations were done manually, with a hand held DMM used to measure all the gauge resistances at a given temperature. This was an incredibly labour intensive process with many sources of error. These included:

- Lack of repeatability in the measurements due to changes in the DMM to gauge resistance due to manual reconnection at each measurement point.
- No method for monitoring the sample temperature convergence was provided for. This could mean measurement points were taken when the sample was not iso-thermal.
- Recording errors due to incorrect manual recording of the data points.

- The very long time scales resulted in relatively small numbers of data points being recorded, 5 – 10 vs 50 – 150 for the automated system.

5.5.3 Calibration Method

The TFHFGs are calibrated when mounted to the test piece using the same wiring as when installed in the experimental facility to minimise changes in lead resistances. The test piece is instrumented with thermocouples and placed inside a plastic bag to keep it dry. Resistances are recorded at a set number of temperature steps, with test piece and water bath thermocouples monitored to ensure isothermal conditions are attained at each step.

TFHFG's are sometimes witnessed experience a drift in the value of R_0 when subjected to sustained elevated temperatures. This is most likely due to stress relaxation in the platinum film and/or at the copper platinum interface. The prevalence of this effect can be reduced by depositing a thicker platinum film during the manufacturing process. Running an annealing cycle at a temperature above the calibration temperature range can also often assist with reducing this effect. The effect is observed to occur over time periods much longer than those of the experiment so is only a problem for the calibration. As the α of platinum varies very little with temperature, the TFHFG's are typically calibrated over a lower temperature range than those experienced during an experiment. This is assisted with the use of a water bath incorporating a chiller. The calibration calculations can also be modified to reduce the impact of this effect on the calibration. Rather than performing a linear regression on the entire data set simultaneously, regressions are performed on each pair of data points. 30% of the data outliers are then removed and the mean of the relevant parameters taken.

5.5.4 Typical Calibration Curves

The calibration curves of typical conventional and new gauges are plotted in fig. 5.15. Both of the calibrated α values are significantly less than the bulk platinum material value ($\alpha =$

3.279×10^{-3}). This is due to thin film effects as discussed by Neugebauer and Webb (1962), resulting from a reduction in the mean free path of the electrons within the film. This is supported by the observation that α reduces with decreasing platinum thickness.

The calibration curves evidence the repeatability and accuracy of the new automated water bath. The two calibrations shown in fig. 5.15 use 110 measurement points per calibration, 18 at each temperature step. The conventional gauge is only measured over a range of 0.7 Ω, yet the individual data points are almost indistinguishable (within 1mΩ).

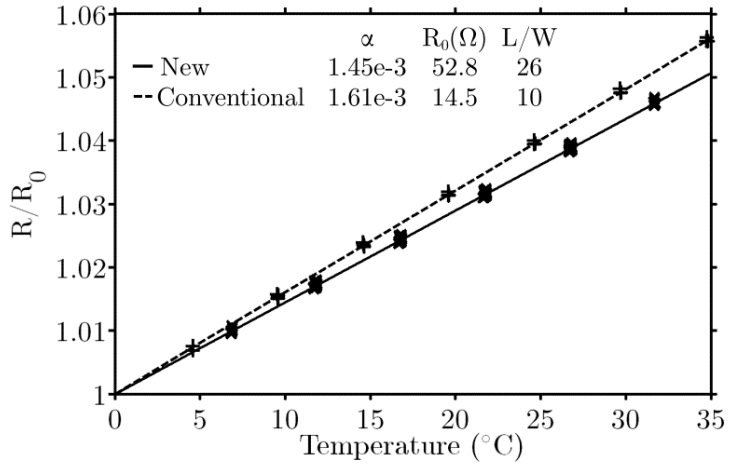

Figure 5.15. Calibration of conventional and new Oxford TFHFGs using 110 measurement points.

5.6 Demonstration in Test Facility

TFHFGs are typically employed for heat transfer measurements on short duration transient facilities. One such example is the Oxford Turbine Research Facility (OTRF), used to simulate the conditions in the high pressure stage of a typical civil aircraft gas turbine. As described by Chana et al. (2013), the facility is an engine-scale rotating turbine facility which replicates engine-representative conditions of Mach number, Reynolds number, and gas-to-wall temperature ratio.

The rotor casing is witness to the periodic passing of the rotor blade tips. This subjects the casing to large transient heat loads at a frequency of 10 kHz. This offers a good opportunity to demonstrate both the low and high speed capabilities of the gauges.

Heat transfer measurements have been made on the rotor casing of the OTRF by Chana and Jones (2003). As pictured in fig. 5.16, this study utilised an array of 7 TFHFGs placed on a Perspex block with a gauge to gauge spacing of 4.2 mm. Thorpe et al. (2004) presents comparable data on a different facility using laser ablated gauges with a gauge to gauge spacing of 1.85 mm. Gauges were placed on a macor block interfaced with a number of peltier heat pumps, used to alter the wall temperature at the start of the run.

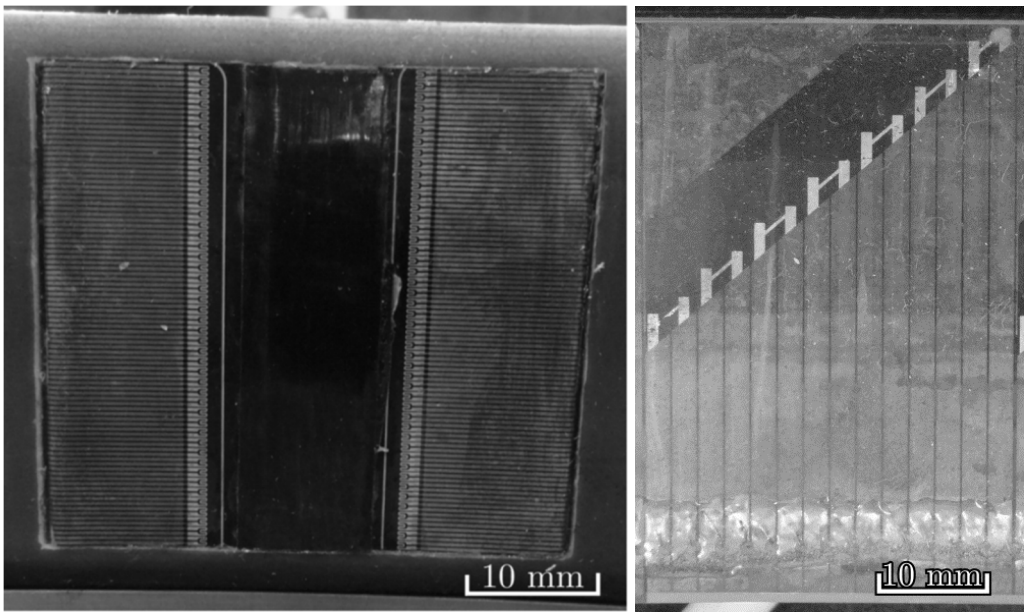

Figure 5.16. Casing instrumented with 88 TFHFGS as used in current study (left) and the 7 utilised by Chana and Jones (2003) (right).

This chapter summarises uncooled casing heat transfer measurements explained in a later chapter in more detail to demonstrate the capabilities of the new gauges. Measurements are made with a high density array of the new Oxford TFHFGs with a gauge to gauge spacing of 0.8 mm. This permits an array of 88 TFHFGs in two parallel axial strips 35 mm wide as pictured in fig. 5.16. Gauges were placed on an aluminium block incorporating a water circuit. Heated or cooled water is circulated to alter the wall temperature at the start of the run in a similar

fashion to Thorpe et al. (2004). This permits measurements over a wider range of measured wall temperatures which improves the regression to obtain the adiabatic wall temperature and heat transfer coefficient.

5.6.1 Experimental Setup

The surface temperature history from a TFHFG is recorded by supplying each gauge with a constant current and measuring the voltage across it. The frequency response of TFHFGs reduces at high heat flux frequencies (Anthony et al. (1999)) and for high speed measurements (> 1 kHz), a high-frequency amplifier is required to avoid digitisation errors in the high frequency part of the signal. At Oxford the TFHFG electronics and data acquisition systems have recently been upgraded. TFHFGs are now connected to a two break-point gain-shaping Heat Transfer Amplifier (HTA) to boost the high frequency components of the temperature signal. The boosted output from the HTA is recorded by a high speed Data Acquisition system (DAQ) at a 2 MHz sampling frequency. The recorded signal is de-boosted in Matlab (which has much greater resolution than the DAQ) with an impulse response filter to recover the measured temperature signal. This can then be converted to heat-flux using the impulse method as described by Oldfield (2008). This method enables the measurement of signals with a bandwidth of approximately 150 kHz (limited by the thermal properties of the gauge). The work process for measuring and processing heat transfer data is summarised in fig. 5.17.

The high speed boosted signal from the HTA is AC coupled, recording only the rise in wall temperature. To measure absolute temperatures, the initial wall temperature must be known. If the instrumentation can be assumed to be isothermal immediately before the experiment, this can be measured using thermocouples placed under the TFHFGs. This is often not the case and the low speed DC signal must also be recorded and referenced to an earlier point when the instrumented region can be assumed to be isothermal.

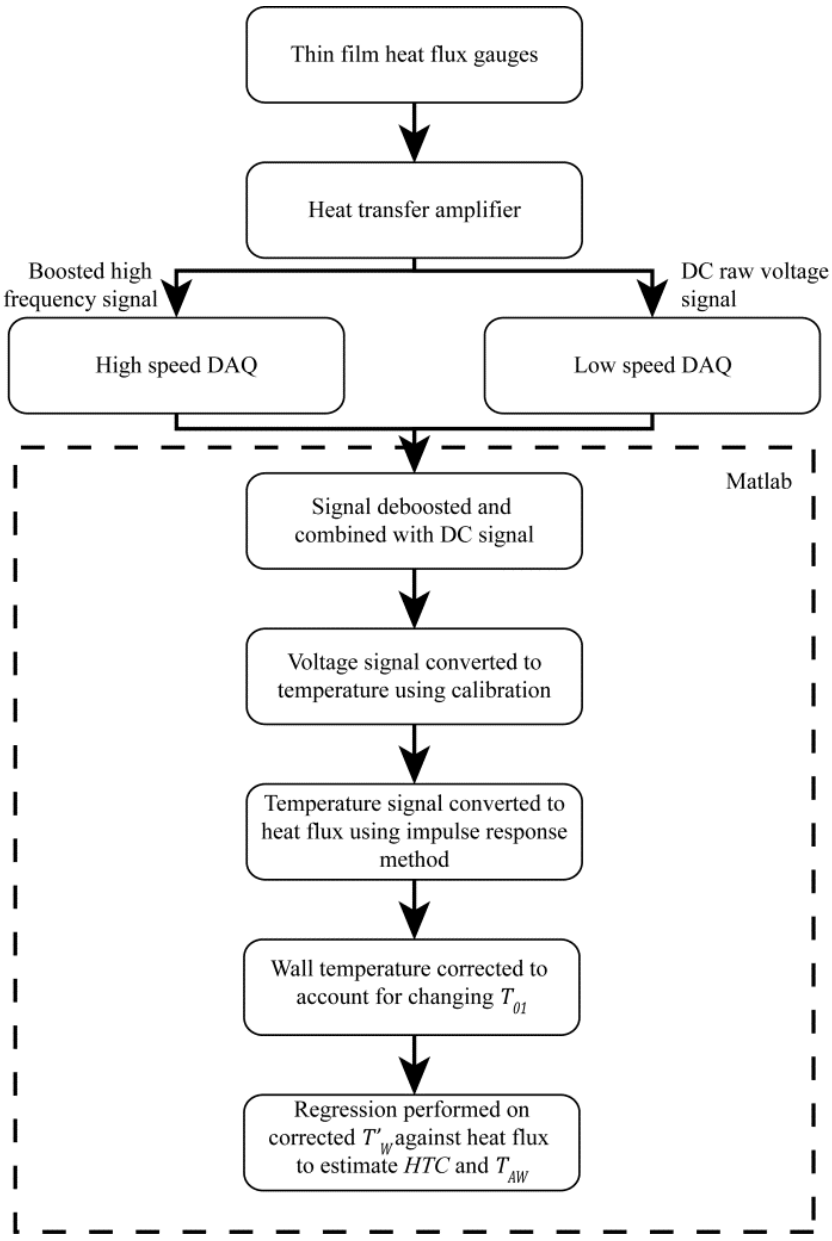

Figure 5.17. Work process for measuring, recording and processing heat transfer data.

The adiabatic wall temperature and heat transfer coefficient are found by performing a linear regression between the measured temperature (T_W) and computed heat flux ($\dot{q}$) to solve the convective heat flux equation, as described by Qureshi et al. (2012).

$$\dot{q} = h(T_W - T_{AW}) \tag{5.12}$$

The intercept with the temperature axis (zero heat flux) corresponds to the adiabatic wall temperature and the slope ($d\dot{q}/dT$) of the regression corresponds to the heat transfer coefficient.

Use of the linear regression technique assumes that the local driving temperature (T_{AW}) at the measurement location remains constant throughout the run. This would be the typical result if inlet T_{01} remained constant for the measurable part of the run. There are applications when this is not possible and a modified regression has been developed which can account for changes in the driving temperature. Assuming that the process between the inlet plane and the measurement point is polytropic, we can then state that T_{AW} is a linear function of the time varying inlet total temperature T_{01}

$$k = T_{AW}/T_{01} \tag{5.13}$$

We can then compute a corrected wall temperature T'_W to replace T_W in eqn. 5.12 and the heat transfer regression.

$$T'_W = T_W - k(T_{01} - \overline{T_{01}}) \tag{5.14}$$

5.6.2 Time Averaged Data

The OTRF presents several challenges to heat transfer processing. As evidenced in fig. 5.18, though the inlet total pressure in the working section is very stable for the aerodynamically stable portion of the run, the inlet total temperature varies quite substantially. There is also a peak in total temperature before the start of the run which has a very negative effect on heat transfer processing, as much of the surface temperature rise on the instrumented wall occurs during this period.

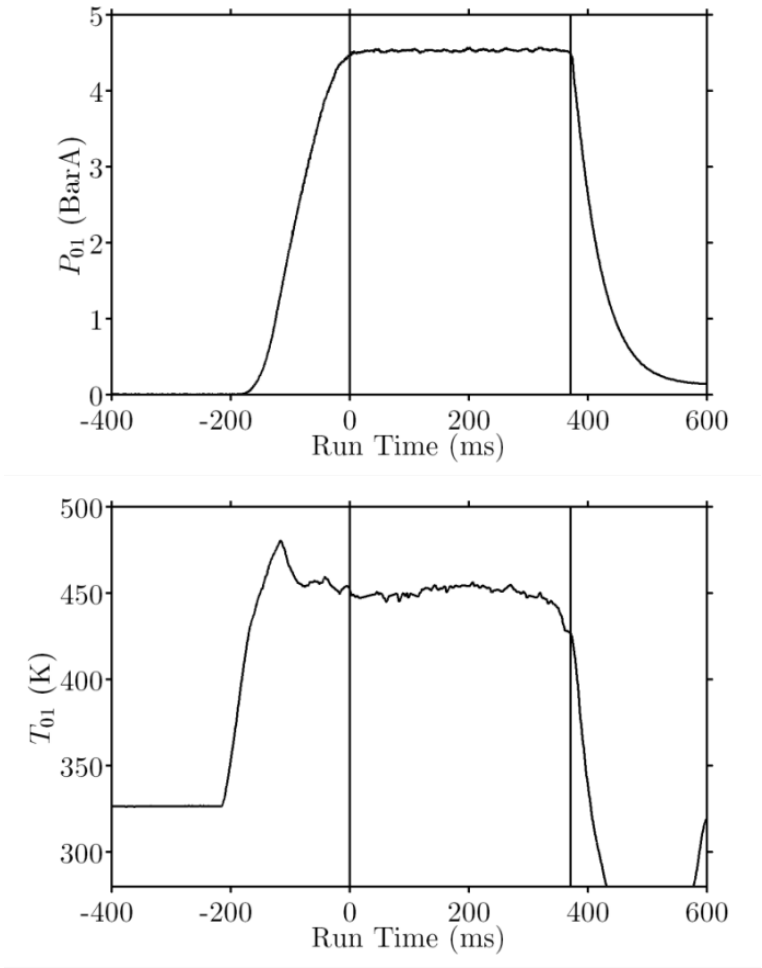

Figure 5.18. Plots of measured inlet total pressure (top) and inlet total temperature (bottom) for a typical OTRF run.

Figure 5.19 shows the measured wall temperature and derived heat flux from a single TFHFG located on the HP rotor casing during a run with a 500 Hz low pass filter applied. The aerodynamically stable portion of the run is marked. The effect of the peak in inlet total temperature before the aerodynamically stable part of the run is clearly evident, resulting in a ~70 K rise in wall temperature before the run starts.

The corresponding $\dot{q}$ vs. T'_W regression is shown in fig. 5.20. The data from the aerodynamically stable portion of the run is plotted in black, and it is to this that the regression is fitted using a least squares approach. The slope of the regression gives the heat transfer coefficient (HTC) and the intercept with the temperature axis the adiabatic wall temperature.

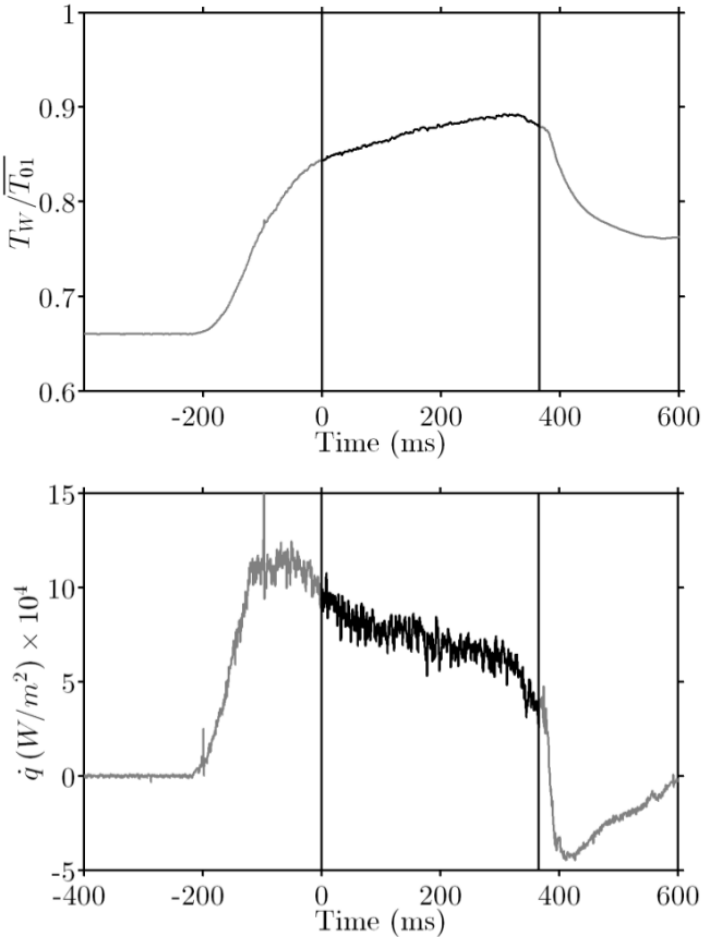

Figure 5.19. Plots of measured T_W (top) and $\dot{q}$ calculated using impulse response (botttom) from a TFHFG during a run.

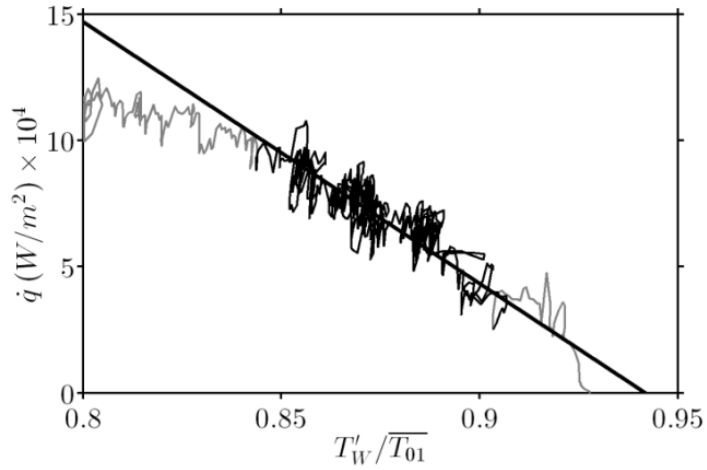

Figure 5.20. Regression performed on one TFHFG for one run.

5.6.3 Time Resolved Data

The large bandwidth (~ 150 kHz) of TFHFGs enables the measurement of high speed experimental data. The data processing techniques described previously can be modified to analyse time resolved periodic data. Gauges located on the over-tip casing observe the passing of the rotor blade at the rotor passing frequency. It is therefore possible to measure the heat transfer in the rotor frame of reference by analysing the time-resolved periodic signal.

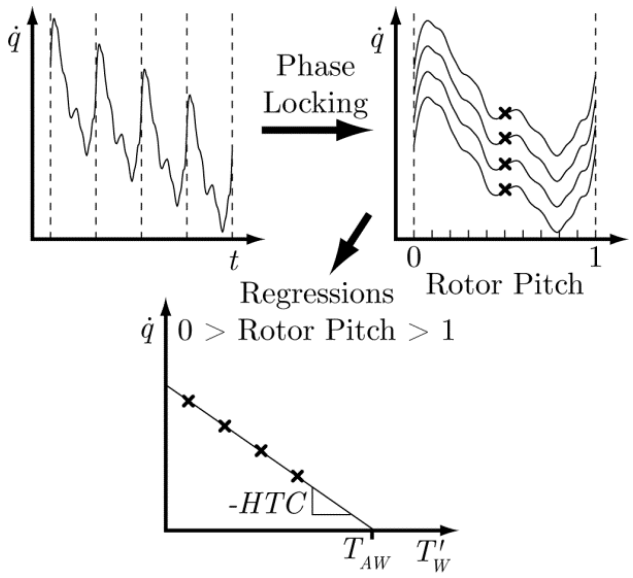

Figure 5.21. Schematic illustrating unsteady data processing to extract T_{AW} and HTC as functions of rotor pitch.

The time resolved data processing technique is summarised in fig. 5.21. The periodic signal is first phase locked using autocorrelation to group the passing events. A time history of the heat flux and surface temperature for a given rotor pitch can then be extracted for each gauge. Separate regressions are then conducted for a number of phase locked pitch points for each gauge.

Figure 5.22 shows the high pass filtered heat flux data obtained from the measured wall temperature using the impulse response method. The data from each gauge was then analysed at 100 temporal rotor pitch points (corresponding to 100 locations in the rotor frame of reference). The corresponding results of unsteady T_{AW} and Nu distributions are shown in fig.

5.22. Thirty nine TFHFGs span the axial ordinate with 100 time-resolved regressions per each rotor pitch. Figure 5.22 therefore presents the data of 3900 independent regressions. The data is not subjected to any smoothing though there is interpolation in the axial ordinate to enable the plotting of a smooth surface.

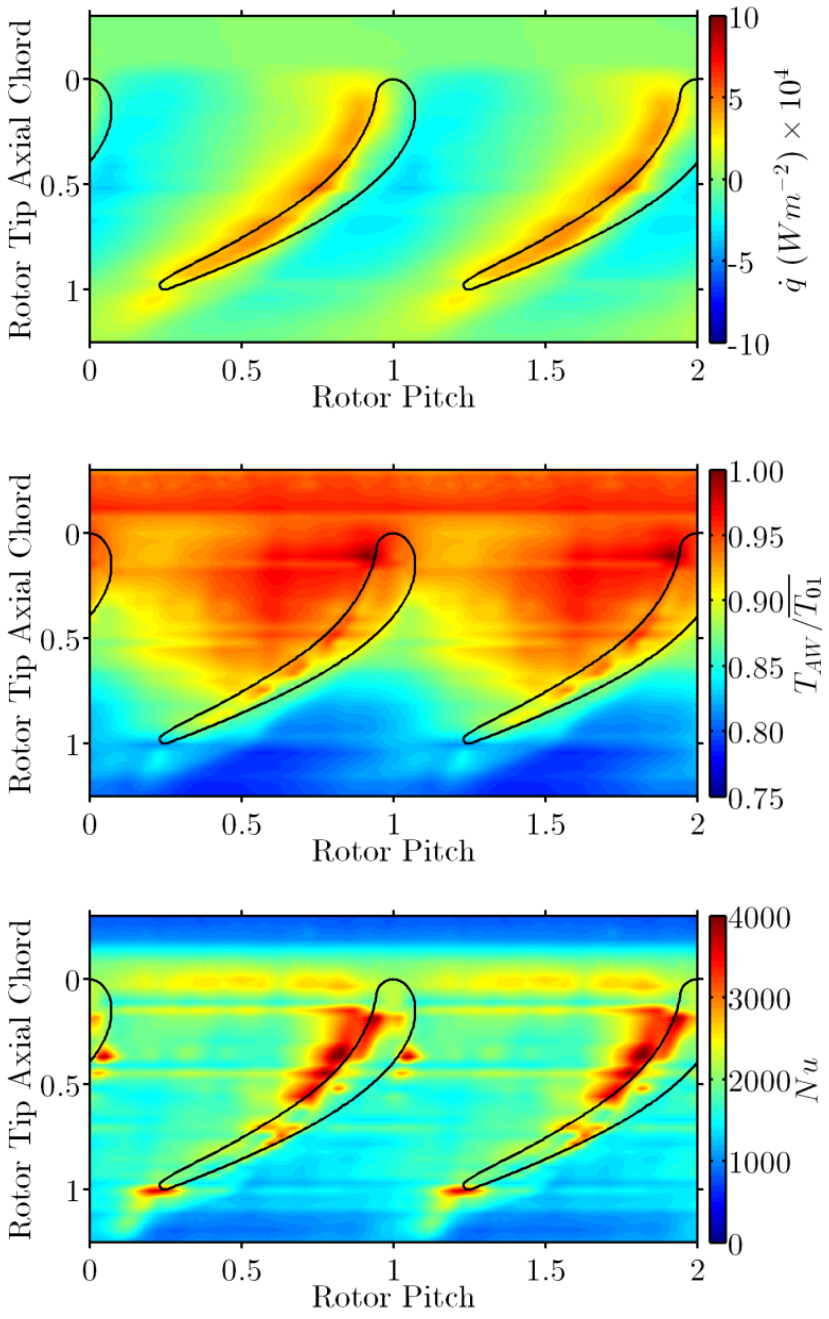

Figure 5.22. Time resolved experimental measurements of rotor casing unsteady heat flux (top), T_{AW} (center) and Nu (bottom).

A detailed discussion of the results in fig. 5.22 is beyond the scope of this chapter, though it is worth noting the large bandwidth of the gauges (~ 150 kHz) and the gauge to gauge consistency. With comparison to the previous results of Chana and Jones (2003) and Thorpe et al. (2004), there is a significant improvement in both the spatial and temporal resolution of the data. This is significant as it allows the detailed study of heat transfer and flow processes in the tip gap.

5.7 Conclusions

A new fabrication process for the manufacture of TFHFGs has been described and compared to previous methods. New gauge designs which improve the sensitivity for a given footprint are also introduced. The result is the ability to manufacture gauges which are both significantly smaller and more robust. Examples of TFHFGs which offer a 7 fold increase in gauge density are presented.

Methods for calibrating TFHFGs are discussed, with typical calibrations for both new and conventional TFHFGs compared. Calibrations performed in a new calibration facility are described and demonstrate that gauges manufactured using the conventional and new Oxford methods have comparable calibrations.

Improvements to the processing of TFHFG data are discussed and demonstrated on experimental data. These show that with a well-crafted experiment, TFHFGs can be used to obtain high spatial and temporal resolution heat transfer data in short duration transient tests. The improvements in temporal and spatial measurement resolution permit the study of flow processes which hitherto have not been measurable in experimental facilities.

5.8 Chapter Nomenclature

α	Temperature coefficient of resistance ($\sqrt{\rho c \lambda}$)
c	Specific heat
d	TFHFG platinum sensor thickness
D	Thermal diffusivity $\lambda/\rho c$
h	Heat transfer coefficient (HTC)
I	Excitation current
k	T_{AW}/T_{01}
ρ	Density
ρ_e	Material resistivity
λ	Thermal conductivity
L	TFHFG platinum sensor length
$\dot{q}$	Heat flux
W	TFHFG platinum sensor width
t	Time
T	Temperature
T_{01}	Inlet total temperature
$\overline{T_{01}}$	Time mean inlet total temperature
T_{AW}	Adiabatic wall temperature
T_W	Surface temperature
T'_W	Corrected wall temperature
V	Voltage
x	Depth from surface

Chapter 6: Improved Methodologies for Time Resolved Heat Transfer Measurements, Demonstrated on an Unshrouded Transonic Turbine Casing

6.1 Abstract

The HP rotor tip and over-tip casing are often life-limiting features in the turbine stages of current gas turbine engines. This is due to the high thermal load, and high temperature cycling at both low and high frequency. In the last few years there have been numerous studies of turbine tip heat transfer. Comparatively fewer studies have considered the over-tip casing heat transfer. This is in part, no doubt, due to the more onerous test facility requirements to validate computational simulations. Because the casing potential field is dominated by the passing rotor, to perform representative over-tip measurements a rotating experiment is an essential requirement.

This chapter details measurements taken on the Oxford Turbine Research Facility (OTRF), an engine-scale rotating turbine facility which replicates engine-representative conditions of Mach number, Reynolds number, and gas-to-wall temperature ratio. High density arrays of miniature thin-film heat-flux gauges were used with a spatial resolution of 0.8 mm and temporal resolution of ~120 kHz. The small size of the gauges, the high frequency response, and the improved processing methods allowed very detailed measurements of the heat transfer in this region. Time-resolved measurements of T_{AW} and Nu are presented for the casing region (-30% to +125% C_{AX}) and compared to other results in the literature. The results provide an almost unique data set for calibrating CFD tools for heat transfer prediction in this highly unsteady environment dominated by the rotor over-tip flow.

6.2 Introduction

The casing of an unshrouded rotor is subjected to large temporal variations in both static pressure and heat load. Increasing turbine entry temperatures require that the rotor casing heat load be well understood to develop cooling strategies, which may include the use of film cooling, Chana and Haller (2009). As discussed in the earlier acoustic chapter, a film cooling scheme employed on the rotor casing is a highly unsteady system which can be designed to make use of pressure wave reflections to modulate the unsteady mass flux from the holes. The design of such a system requires knowledge of not only the time mean casing heat load but also the unsteady heat load.

In this chapter we describe improved methodologies for time resolved heat transfer measurements. Specifically we show that:

1. Changes in driving temperature (within limits) can be accounted for in both time-resolved and steady heat transfer measurement processing. This allows useful data to be extracted even under varying inlet temperature.
2. Superposition of several runs with different starting wall temperatures can be used to improve the accuracy of time resolved regressions by extending the wall temperature range over which the unsteady regressions are conducted.
3. A new time-resolved data processing technique that can be applied to data sets involving changes in wall temperature has been developed and is applied to experimental measurements to compute time resolved T_{AW} and Nu.

These improvements are demonstrated using unsteady heat transfer measurements conducted on the stationary casing above an unshrouded transonic turbine. Experimental measurements of both T_{AW} and Nu in this flow regime are highly important as they permit results to be scaled to engine conditions.

6.2.1 Previous Work

Chana and Jones (2003) present the first published measurements in which heat flux is decomposed into T_{AW} and Nu. These results are further analysed and discussed by Qureshi et al. (2012). Both time averaged and time resolved results are published for the QinetiQ Isentropic Light Piston Facility which was moved to Oxford in 2010 and renamed the Oxford Turbine Research Facility (OTRF). This study used an array of 7 thin film heat flux gauges located on the rotor casing between 0 – 115% C_{AX}. The unsteady T_{AW} and Nu results presented contain a significant amount of experimental noise and many of the flow structures one would expect to see are not evident.

Thorpe et al. (2004) presents a more detailed study into casing heat transfer using the Oxford Rotor Facility. This facility was a precursor to the OTRF with a significantly shorter duration run time (~ 10 ms vs. 400 ms data acquisition time). As described by Ainsworth et al. (1988), the facility is unbraked which results in the speed of the turbine rotor increasing through the run. Hence the period at which the rig is running at design speed, when data can be collected, is approximately 13 ms (120 rotor passing events). The rotor casing was instrumented with 56 laser cut thin film heat flux gauges located on a macor block arranged in 7 columns with 8 gauges in the axial direction between -20 – 80% C_{AX}. To obtain T_{AW} and Nu from this facility, the initial wall temperature of the instrumented casing region was controlled with the use of integrated peltier elements. This chapter details the phase locking methods used to generate unsteady plots of T_{AW}. The influence of the upstream nozzle guide vane on casing heat load is also measured spatially and is observed to be very small.

A later paper by Thorpe et al. (2008) separates the measured unsteady heat flux into an unsteady T_{AW} and a normalised heat transfer coefficient. Heat flux is observed to be highest in the blade tip gap, with peak values observed local to the broadest parts of the blade at 30 – 60% C_{AX}. This is attributed to both a rise in heat transfer coefficient and adiabatic wall temperature.

Adiabatic wall temperature is shown to be highest local to the blade suction surface. In the passage, heat flux is highest local to the pressure surface, corresponding to high adiabatic wall temperatures and enhanced heat transfer coefficient. The high heat transfer coefficients measured in the tip gap are attributed to the high flow velocities in this region. Similarly, the heat transfer coefficient distribution in the passage is also linked to the absolute flow velocities local to the casing.

El-Gabry and Ameri (2010) reported the results of a CFD study on an unshrouded turbine rotor passage, including heat transfer on the casing. The results indicated that T_{AW} on the casing was enhanced above the inlet total temperature local to the leading edge stagnation region and local to the blade pressure surface. This was attributed to work processes in the near tip region. In the tip gap itself, adiabatic wall temperatures were similar to those local to the blade pressure surface. The Nu predictions also showed peaks local to the blade pressure surface, though little enhancement was evident under the tip itself. The results show good qualitative agreement to the numerical work presented by Qureshi et al. (2012).

6.2.2 Experimental Approach

This chapter seeks to build on the work and techniques of Thorpe et al. (2004) and makes use of advances in thin film heat flux gauges developed by the author at Oxford and described in an earlier chapter. This chapter also presents improvements to data processing techniques which can be applied to longer duration transient heat flux facilities to account for changes in inlet total temperature during the run.

6.3 Experimental Facility

Experiments were conducted on the Oxford Turbine Research Facility (OTRF), formerly named the Turbine Test Facility and prior to that the Isentropic Light Piston Facility. The facility is a short duration light piston driven facility operated as a 1½ stage engine-scaled

rotating transonic HP turbine stage with uniform inlet conditions as described by Chana et al. (2013). Re, M, T_G/T_W and non-dimensional speed were all matched to engine conditions and the operating conditions are summarised in table 6.1. The tip clearance is 0.56 mm, which corresponds to 1.4% of span at mid-chord.

Table 6.1. OTRF operating conditions.

Parameter (unit)	Nominal value	Allowable run-to-run variation (%)
p_{01} (bar)	4.6	± 1
T_{01} (K)	444	± 2
T_G/T_W	1.54	± 2
M_2^{hub}	1.054	± 1
M_2^{casing}	0.912	± 1
ω (rpm)	9500	± 1
p_{02rel} (bar)	2.697	± 1
Re_{NGV}	2.54E6	± 1

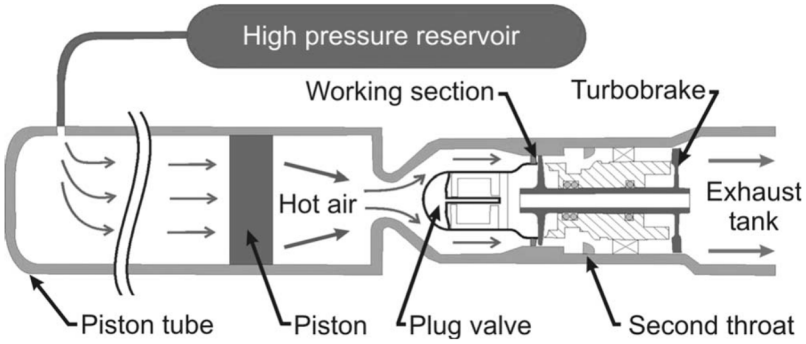

Figure 6.1. Schematic of OTRF.

A schematic of the OTRF is provided in fig. 6.1. Prior to an experimental run, the plug valve is closed and the working section is evacuated to near vacuum conditions. The rotor is spun up to design speed by an air motor. When up to speed, air from the high pressure reservoir is admitted to the piston tube behind the free piston. The free piston moves down the piston tube compressing and heating the test gas ahead of it. When the correct pressure in the test gas is achieved, the fast acting plug valve opens to admit air into the test section. The rotor's speed is maintained by a turbobrake situated downstream of the working section. Steady conditions are maintained for approximately 400 ms, ending when the free piston reaches the end of its travel.

6.4 Experimental Hardware

Experimental hardware was incorporated into a removable aluminium cassette in the over tip rotor casing of the OTRF. This held an ABS block and spacers manufactured with laser sintering, fig. 6.2. These were installed on a railed system which permitted clocking of the instrumented block relative to the upstream nozzle guide vanes. The ABS block incorporates an aluminium insert which was instrumented with 92 Thin Film Heat Flux Gauges (TFHFGs) in two columns of 46.

Figure 6.2. Experimental hardware installed in cassette.

6.4.1 Instrumentation

The TFHFGs are similar in construction to those developed in Oxford by Jones (1995), with a thin film platinum sensing element deposited onto a polyimide substrate. The gauges used for this study are of an improved construction developed by the author in Oxford. These TFHFGs utilise a new manufacturing process as described in an earlier chapter, which makes use of a pre-laminated copper and polyimide substrate. This enables the thickness of the copper connecting tracks to be increased from 0.5 μm to 18 μm. The width of the connecting tracks can then be shrunk considerably, which for this application offers a greater than fivefold improvement in lateral gauges density. The platinum sensor is also of a new serpentine design which increases the sensitivity for a given footprint. The result is a lateral gauge spacing of 0.8 mm vs. 4.4 mm used in similar previous studies, Chana and Jones (2003).

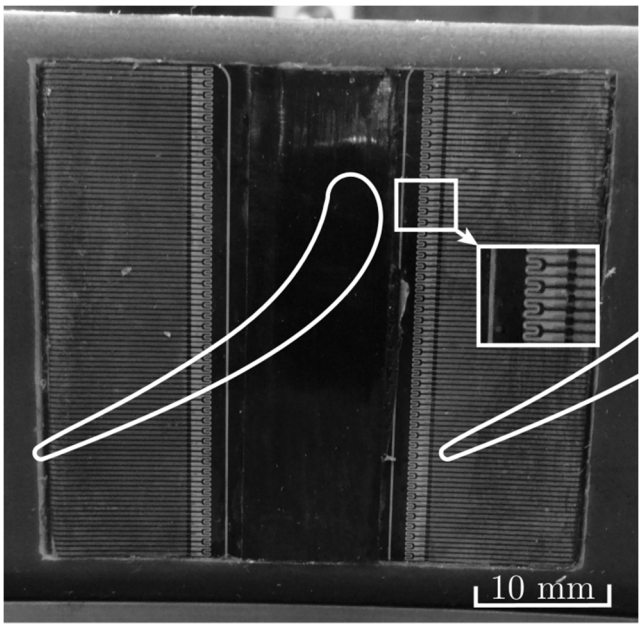

Figure 6.3. Instrumented casing region with 92 TFHFGS and superimposed tip.

The TFHFGs were connected to new amplifiers and a new Data Acquisition system (DAQ). For some time at Oxford, TFHFGs were connected to a Heat Transfer Amplifier (HTA) which made use of a transmission line analogue to convert the temperature signal from the gauge to a heat flux signal, Oldfield et al. (1978), Oldfield et al (1984). This heat flux signal was recorded by a DAQ which negated the need at the time for lengthy data processing techniques. The HTA assumed that the gauge was placed on a material that was thick enough to be assumed semi-infinite for the experiments duration. Advances in both computer power, and in particular the development of the impulse response processing technique, Oldfield (2008), have substantially reduced the time required to compute the heat flux from the measured temperature signal. In more recent years, it became common to apply a reverse transformation of the recorded heat flux signal from the HTA using a semi-infinite 1D impulse response function to return the measured but not recorded temperature signal, for example Chana and Jones (2003). It was then possible to account for a non-semi-inifinite substrate using further impulse response processing Oldfield (2008). The heat transfer analogue response from the HTA was still recorded as it was able to reduce digitization noise of the recorded high frequency signals, which were boosted by the original HTA design.

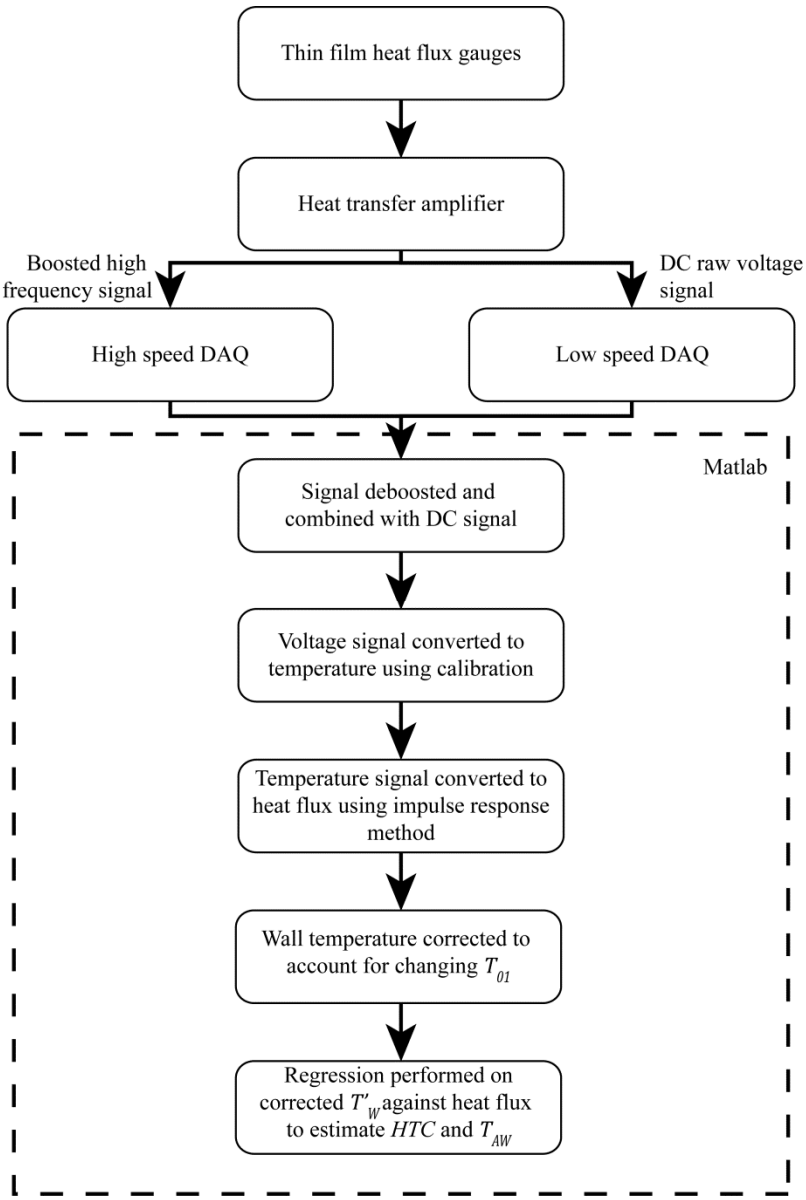

Figure 6.4. Work process for measuring, recording and processing heat transfer data using new HTA.

Appreciating that the original HTA transmission line analogue was now superfluous, a new HTA was designed by Oldfield and Beard (2012). This utilises a two break-point gain-shaping amplifier to boost the high frequency components of the temperature signal to avoid digitization errors at high frequencies due to the reduced frequency response of TFHFGs at high heat flux frequencies, Anthony et al. (1999). This is similar to the amplifiers used by Anthony et al. (2004). The boosted output from the new HTA is recorded by a high speed DAQ at a 2 MHz sampling frequency and then de-boosted in Matlab (which has much greater resolution than the DAQ) with an impulse response filter to recover the measured temperature signal. This can then

be converted to heat-flux using the impulse method as described by Oldfield (2008). This new HTA is able to resolve frequencies of 0 – 1 MHz vs. the previous HTA frequency range of 0 – 100 kHz, Oldfield et al. (1984).

The new work process for measuring and processing heat transfer data is presented in fig. 6.4.

6.4.2 Wall temperature control

The initial wall temperature of the instrumented aluminium insert is controlled using a water circuit, enabling measurements at a number of different gas/wall temperature ratios. A schematic of the custom built external hardware is illustrated in fig. 6.5 and pictured in fig. 6.6. Heating or cooling is achieved by passing water through a heat exchanger connected to a number of thermostatically controlled peltier elements, with a combined heating power of 250 W and cooling power of 72 W at room temperature. Water is passed from the heater/chiller unit to the sample to be heated through a pair of silicone tubes. This enables the initial wall temperature to be set between 8 – 60 °C.

The heater/chiller unit is controlled by a separate control panel. This incorporates a digital thermostat which monitors the temperature of the water side of the heat exchanger using a PT1000 RTD and controls the peltier elements through a series of relays. The control panel can also control the pump speed, which is useful for the initial priming of the system.

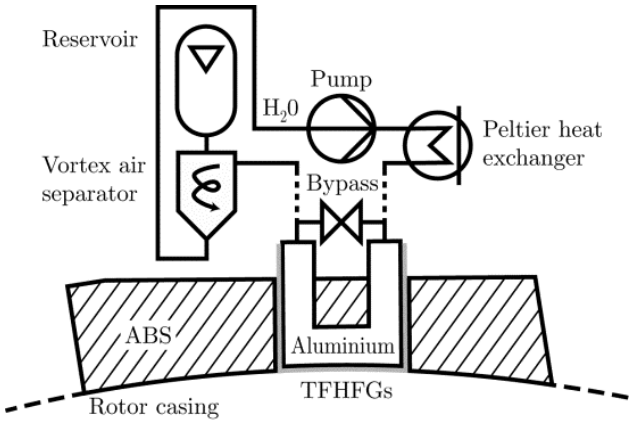

Figure 6.5. Schematic of wall heating/cooling hardware.

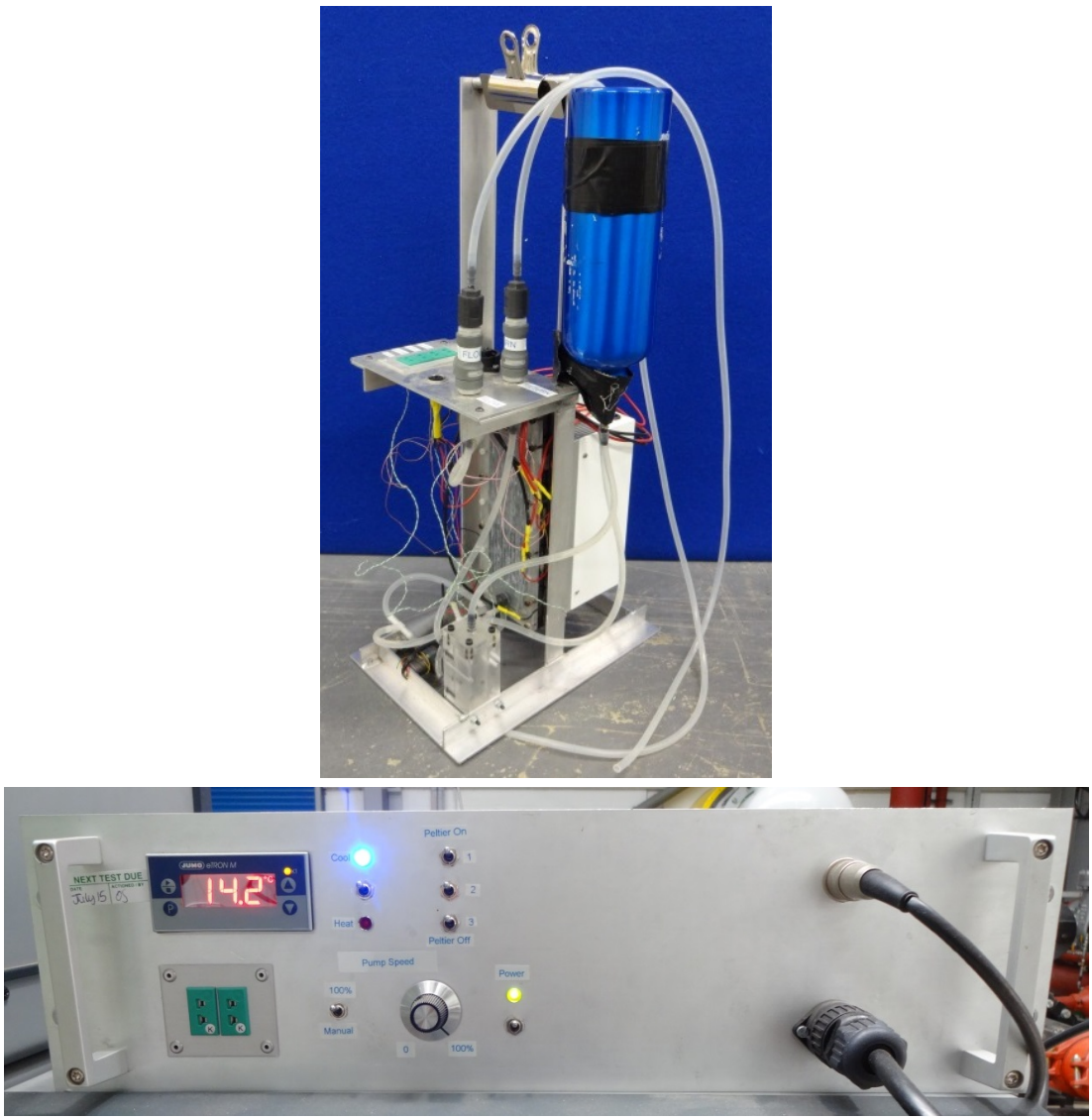

Figure 6.6. Wall heater/cooler hardware.

6.5 Time Averaged Experimental results

Each run recorded the output from 44 TFHFGs along with mainstream flow parameters. A total temperature probe was located at the leading edge of the instrumented block, offset by 1 rotor pitch to record the variation in total temperature. As discussed later, this plays an important part in improving the data-processing of the Nu and T_{AW} calculations.

The data presented in this section is taken from one clocked position relative to the vane, chosen to avoid the wake. A total of 4 different initial wall temperatures were set (14 °C, 24 °C, 43 °C and 59 °C) with a single repeat at each temperature, totalling 8 runs.

6.5.1 Data Processing Techniques

The high speed boosted temperature history and low speed DC temperature are recorded during each run. The high speed hardware boosted signal is deboosted in Matlab using an impulse response filter and combined with the low speed DC signal as described by Oldfield (2008). The spinning up of the OTRF in a near vacuum leads to localised heating of the gauges and this is measured by recording the low speed DC temperature history. Measured data is referenced to a time when the instrumented region can be considered iso-thermal and zeroes data can be taken using a number of thermocouples embedded beneath the TFHFGs. This data is taken before the wall heating system is enabled (coolant is circulated through a bypass valve rather than the instrumented block) and before the OTRF rotor is spun up. After this zeroes data is taken, the bypass valve is closed circulating pre-heated/cooled water through the block and the rig is spun up to speed.

The TFHFGs were located on seven layers of glue and polyimide corresponding to a composite thickness of 805 μm. This is less than the propagation distance of the thermal wave during the test duration, so a two-layered impulse response filter was used to calculate the heat flux from the temperature signal as described by Oldfield (2008).

The OTRF presents several challenges to heat transfer processing. As evidenced in fig. 6.7, though the inlet total pressure in the working section is very stable for the duration of the run, there are significant variations in the total temperature local to the rotor casing. The peak observed before the beginning of the aerodynamically stable portion of the run is caused by the compression of remaining gas in the evacuated working section upon opening of the fast acting inlet valve. The reduction in temperature observed towards the end of the aerodynamically stable portion of the run is due to the passage of test gas which had been in contact with the cooler piston surface.

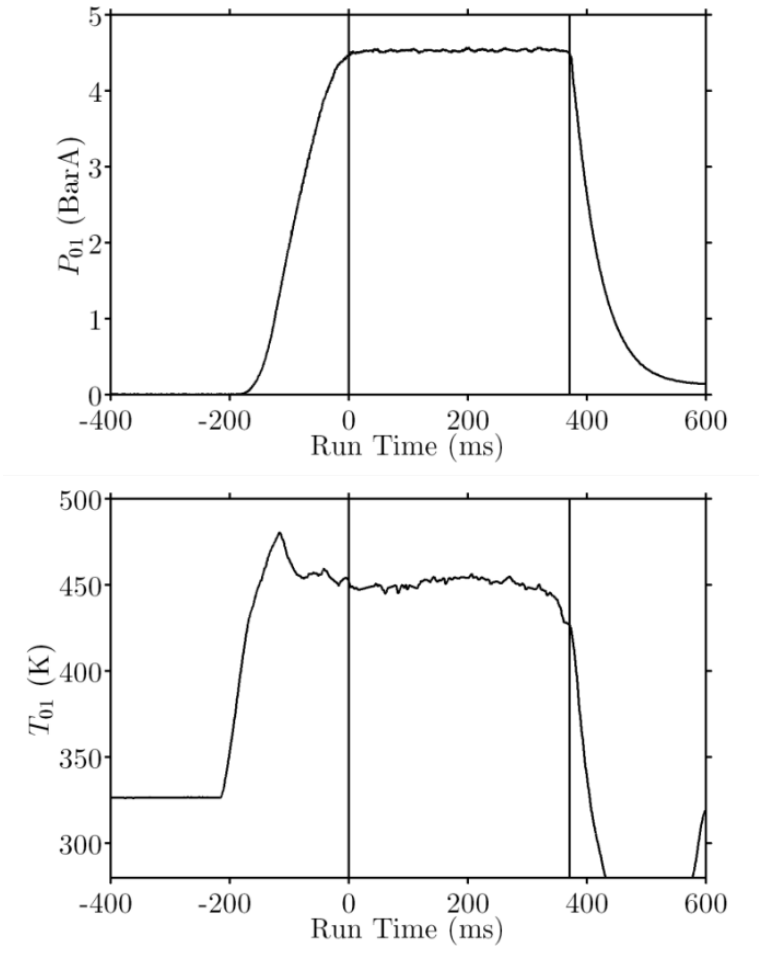

Figure 6.7. Plots of measured inlet total pressure (top) and total temperature measured local to the rotor casing (bottom).

The peak in total temperature before the start of the run has a very negative effect on heat transfer processing as much of the surface temperature rise on the instrumented wall occurs during this period. As there is no aerodynamic stability, this temperature rise cannot be utilised for the purpose of calculating heat transfer parameters.

The reduction in total temperature towards the end of the aerodynamically stable portion of the run can be recovered and used to significantly extend the run time available for processing. In the past this data was typically discarded since a simple $\dot{q}$ vs. T_W regression to find the adiabatic wall temperature assumes that the driving temperature of the mainstream remains constant.

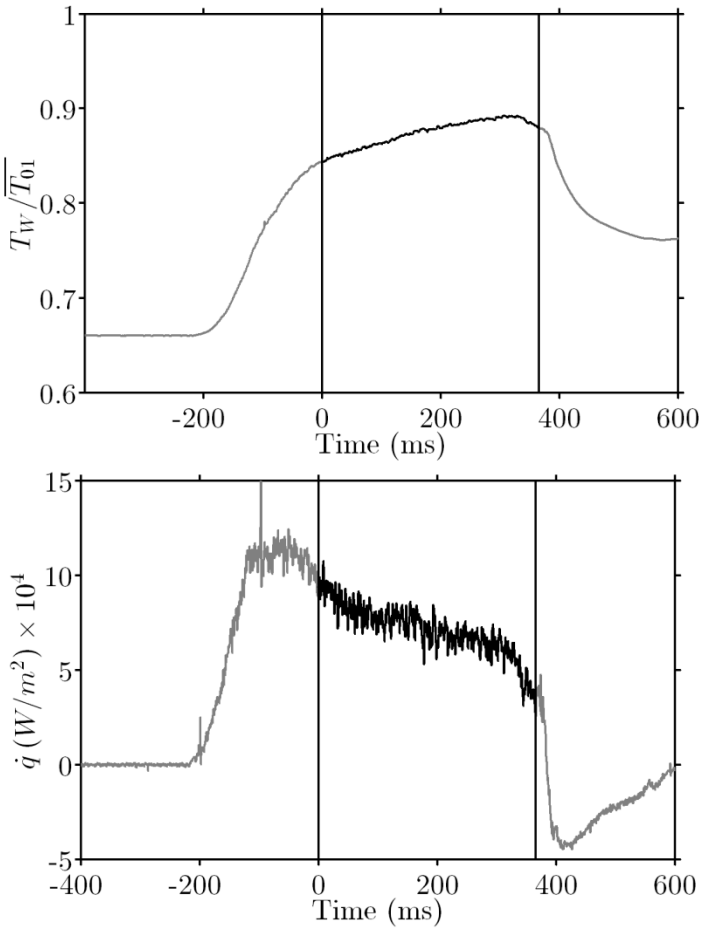

Figure 6.8. Plots of measured T_W (top) and $\dot{q}$ calculated using impulse response (botttom) from a TFHFG during a run.

Floating Regression

For many experimental arrangements it can be assumed that the mainstream total temperature remains constant between the inlet and the measurement location, with T_{AW} taken to be equivalent to the recovery temperature T_r at the measurement location (Gröber and Erk (1961)) given by

$$T_{0m} - T_r = \frac{(1-r)u^2}{2c_p} = T_d \tag{6.1}$$

We can assume that if the *Re* and *Pr* remain constant for the course of an experiment (constant p_{01} and T_{01} as per fig. 5.18), then T_d will also remain constant. We can then modify the convective heat flux equation to account for a time varying T_{0m}

$$\dot{q} = h(T_w - T_{0m} + T_d) \tag{6.2}$$

A linear regression can then be performed between the measured temperature minus the time varying mainstream total temperature ($T_W - T_{0m}$) and the computed heat flux ($\dot{q}$). The intercept with the *x*-axis denotes the T_d which can be used to calculate the T_{AW}.

If there is significant heat transfer or work is added or removed from the fluid between the inlet and the measurement location then T_{0m} is unknown at the measurement point. If the exact nature of this process is unknown we must derive a relationship between the inlet total temperature and the driving temperature at the measurement point. If we make the assumption that the process between the inlet plane and the measurement location is polytropic, then the total temperature local to the measurement location is

$$\frac{T_{0m}}{T_{01}} = \left(\frac{p_{0m}}{p_{01}}\right)^{(n-1)/n} \tag{6.3}$$

If we can assume that our run is aerodynamically stable, that is the ratio of inlet and local pressures remains constant, and that this polytropic process is more significant than those due to a recovery effects, then we can construct a linear relationship between T_{AW} and the inlet total temperature T_{01}

$$T_{AW} = kT_{01} \tag{6.4}$$

This can then be substituted into the convective heat flux equation.

$$\dot{q} = h(T_W - kT_{01}) \tag{6.5}$$

We can then express a corrected wall temperature T'_W which can be plotted against $\dot{q}$ for the purposes of a regression. T'_{AW} is defined as $k\overline{T_{01}}$ and is given by the intercept with the corrected temperature axis, where $\overline{T_{01}}$ is defined as the time averaged inlet total temperature.

$$T'_W = T_W - k(T_{01} - \overline{T_{01}}) \tag{6.6}$$

The value of k at each spatial and temporal (if performing a periodically unstable analysis) location is unknown so an iterative solution procedure must be undertaken. The updated value of k for each iteration is given by eqn. 6.7.

$$k_{(n)} = T'_{AW(n-1)}/\overline{T_{01}} \tag{6.7}$$

A further refinement to the regression was implemented by resampling the $\dot{q}$ data at regular intervals of T'_W. Consider a simple step change in heat flux applied to the surface of a semi-infinite substrate, the wall surface temperature history will exhibit a rise proportional to $t^{0.5}$. Thus for data sampled at regular values in time, there will be proportionally more values at higher temperatures. This weights the regression to the data in this region where there is a smaller change in temperature. Resampling at regular intervals of T'_W removes this bias and assigns equal weighting to the entire temperature rise.

A comparison between a regular $\dot{q}$ vs. T_W regression and a floating regression of $\dot{q}$ vs. T'_W is given in fig. 6.9. The comparison illustrates how much more of the run can usefully be utilised and the improvement to the robustness of fit. The Matlab code used to perform the regressions is included in the appendices.

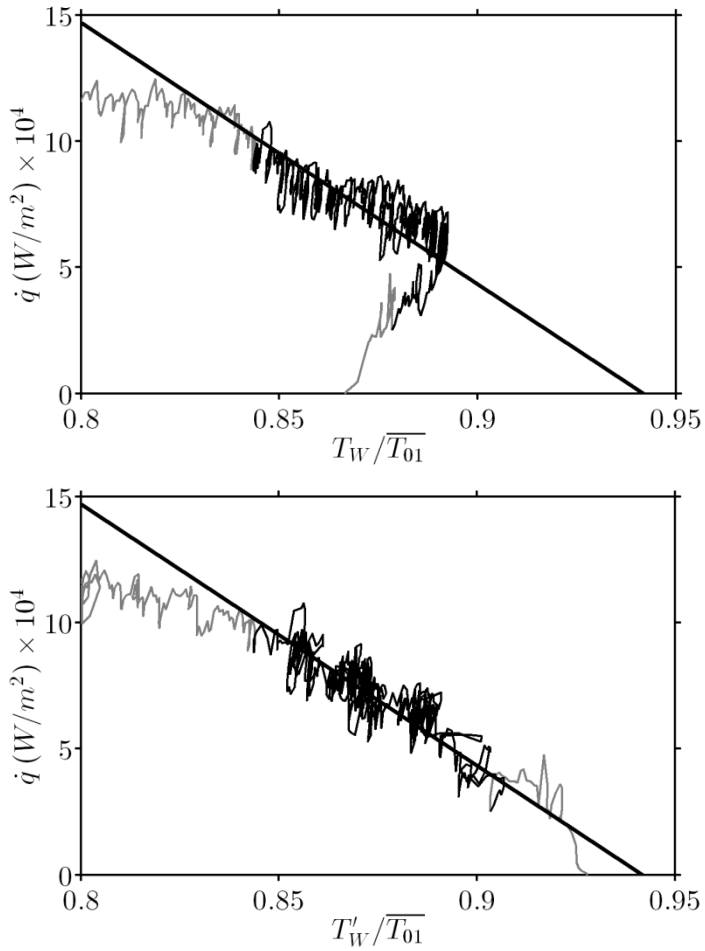

Figure 6.9. Regression performed on one TFHFG for one run, with a $\dot{q}$ vs. T_W regression (top) and a regression against corrected T'_W (bottom).

Multiple Wall Temperature Processing

Thorpe et al. (2004) discuss the use of a similar experimental set up on the Oxford Rotor facility. This facility was a precursor to the OTRF with a significantly shorter duration run time (~10 ms vs 400 ms data acquisition time). As described by Ainsworth et al. (1988), this facility is unbraked which results in the speed of the turbine rotor increasing through the run. Hence the period at which the rig is running at design speed and where data can be collected is a short period corresponding to approximately 13 ms (120 rotor passing events). As a result Thorpe et al. averaged the wall temperature data for this short duration. The experiments were performed at a range of wall temperatures from 35 – 60 °C which subsequently dictated the gas to wall temperature ratio. These data points were then subjected to a $\dot{q}$ vs. T_W regression to calculate a time averaged *HTC* and T_{AW}.

The OTRFs much longer on condition run time enables 3600 rotor passing events to be recorded per run. The longer duration also results in the wall temperature changing significantly during the run. In this study multiple initial wall temperatures were used to increase the temperature range for the regressions. Resampled $\dot{q}$ vs. T'_W for all of the runs was compiled into one data set and a regression performed on this entire data set simultaneously. This method highlights a supplementary benefit of the floating regression technique, which is that it also accounts for any change in run to run $\overline{T_{01}}$. A plot of a multiple wall temperature regression for one gauge is given in fig. 6.12.

6.5.2 Time Averaged Processed Data

Time averaged T_{AW} and Nu obtained using the afore mentioned data processing techniques are plotted in fig. 6.10. Each data point represents an independent regression for an individual gauge and the T_{AW} and Nu values are evaluated directly from the $\dot{q}$ vs. T'_W regression using the intercept and slope respectively. The consistency of the gauge to gauge results presented in fig. 6.10 highlights the robustness of the data processing techniques employed.

The T_{AW} results in fig. 6.10 are in qualitative agreement with those presented by Thorpe et al. (2004a) and in very good quantitative agreement with the numerical predictions and experimental data presented by Qureshi et al. (2012) on the same turbine geometry. As expected, the T_{AW} in the casing frame of reference reduces as work is extracted by the rotor.

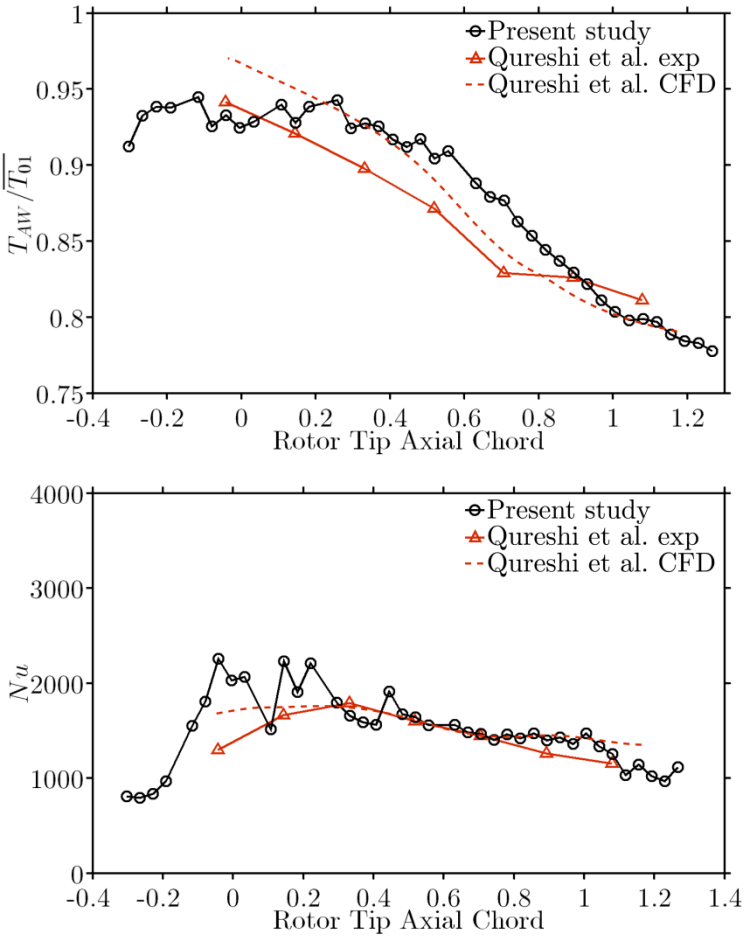

Figure 6.10. Time averaged plots of T_{AW} (top) and Nu (bottom) for 8 runs.

The Nu results also presented in fig. 6.10 are in good qualitative agreement with those presented by Thorpe et al. (2009a) for the over tip region. They are in very good quantitative agreement with the numerical predictions and experimental data presented by Qureshi et al. (2012) on the same turbine geometry in the over-tip regions. The data presented here shows a significant enhancement in Nu local to the blade leading edge, which conforms to the idea that the passing of the blade tip enhances Nu in the tip region. This effect is not observed in the results of Thorpe, and the Qureshi data does not extend upstream of the rotor tip.

6.6 Time Resolved Experimental results

A number of papers have looked at decomposing unsteady heat flux data into a time resolved T_{AW} and HTC. Pinilla et al. (2012) presents the most detailed description of a technique which attempts to capture both the time resolved T_{AW} and HTC. The technique relies on averaging the

unsteady component (high pass filtered) of both the $\dot{q}$ and T_W to create a characteristic unsteady variation. This is then superimposed onto the low pass filtered data to create a characteristic $\dot{q}$ and T_W signal with time. Regressions are then performed on this data at multiple phase locked points corresponding to different rotor pitches.

This technique is useful for short duration facilities where there is little change in wall temperature during the useful portion of the run and instead the wall temperature is set from run to run with the use of heaters or coolers. For experiments where there is a significant rise in wall temperature this approach runs into difficulties. The flaw can be identified by considering a periodic unsteady data set in which one portion of the phase of the signal is subjected to an enhanced HTC. As the mean wall temperature increases, one would anticipate that the magnitude of the unsteady heat flux at this phase location with enhanced HTC would reduce more rapidly relative to the rest of the phase. This is not accounted for if a characteristic unsteady signal is computed from the entire run.

6.6.1 Time Resolved Data Processing Techniques

An improved time-resolved data processing technique that can be applied to data sets involving changes in wall temperature has been developed.

The large bandwidth (~ 150 kHz) of TFHFGs enables the measurement of high speed experimental data. The data processing techniques described previously can be modified to analyse time resolved periodic data. Gauges located on the over-tip casing observe the passing of the rotor blade at the rotor passing frequency. It is therefore possible to measure the heat transfer in the rotor frame of reference by analysing the time-resolved periodic signal.

The time resolved data processing technique is summarised in fig. 6.11. The periodic signal is first phase locked using autocorrelation to group the passing events. A time history of the heat flux and surface temperature for a given rotor pitch can then be extracted for each gauge.

Separate regressions are then conducted for a number of phase locked pitch points for each gauge.

This technique does not rely on time averaging the unsteady signal. To minimise the effects of experimental noise, each passing event was correlated against all others to identify the most statistically significant events. Only 70% of the best correlated events were used for the unsteady analysis.

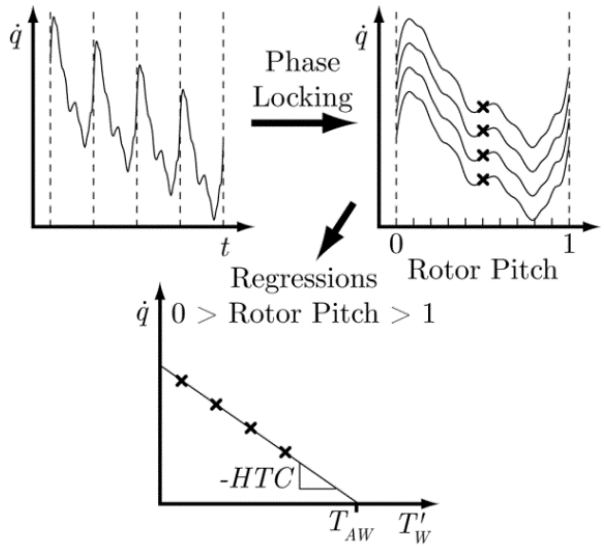

Figure 6.11. Schematic illustrating unsteady data processing to extract and T_{AW} and HTC as functions of rotor pitch.

The data from each gauge was then analysed at 100 temporal rotor pitch points (corresponding to 100 locations in the rotor frame of reference). Each location is an independent regression and not influenced by the surrounding data points. A typical regression for a number of runs at different wall temperatures is presented in fig. 6.12 for a gauge located at 29.5% C_{AX} at a given rotor pitch.

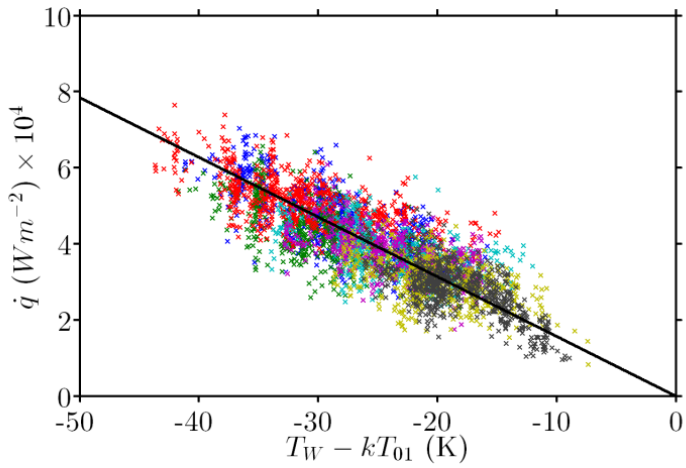

Figure 6.12. Plot of floating regression performed on multiple runs with different initial wall temperatures.

6.6.2 Time Resolved Processed Data

Processed unsteady results of high pass filtered unsteady heat flux, T_{AW} and Nu are presented in fig. 6.13. As with the time averaged data, the T_{AW} and Nu distributions are evaluated directly from the $\dot{q}$ vs. T'_W regression which is executed independently at 100 points per rotor passing event for each gauge. Thirty nine TFHFGs span the axial ordinate and with 100 time-resolved regressions per each rotor pitch, fig. 6.13 presents the data of 3900 independent regressions. The data is not subjected to any smoothing though there is interpolation in the axial ordinate to enable the plotting of a smooth surface.

The location of the rotor tip was inferred by cross correlating the heat flux signal at a number of gauge locations with a CFD solution of heat flux.

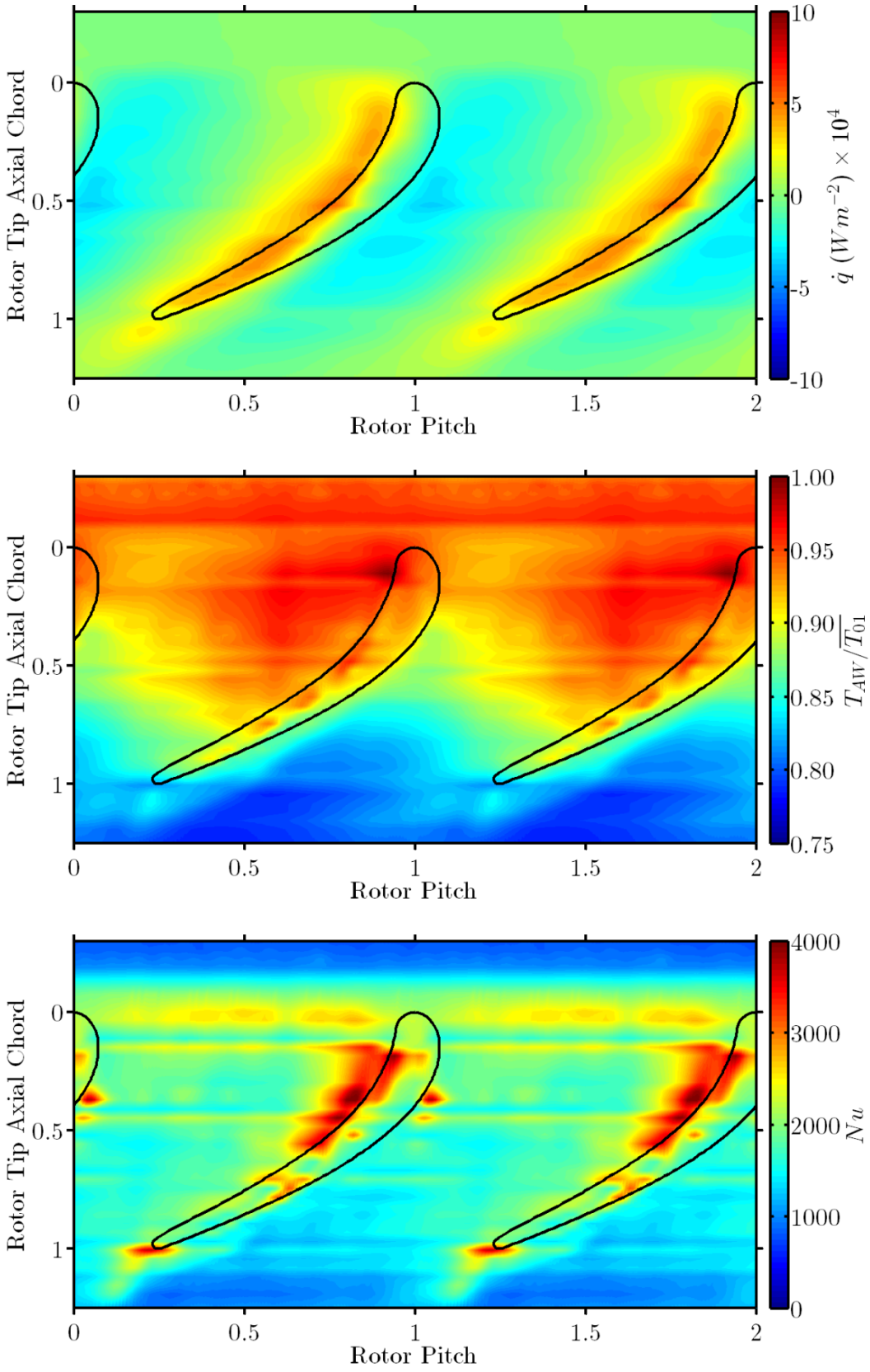

Figure 6.13. Time resolved experimental measurements of rotor casing unsteady heat flux (top), T_{AW} (center) and Nu (bottom).

6.6.3 Time Resolved Results Discussion

Aerodynamics

The aerodynamics of tip leakage flow over flat tips has been extensively studied with detailed measurements taken by Bindon (1989), Moore and Tilton (1988), Heyes et al. (1992) and Yaras and Sjolander (1992). These surmise that tip leakage flow is predominantly driven by the static pressure difference across the tip gap. The flow structures over the tip are discussed by Denton (1993) and summarised in fig. 6.14. The tip leakage flow is contracted into a jet as it is accelerated about the pressure side corner, resulting in a separation near the pressure side edge on the tip. For a thick blade, the jet reattaches forming a separation bubble. The flow then decelerates (increasing the static pressure) and mixes. For a thin blade there is insufficient space for the jet to reattach, resulting in higher flow velocities through the full width of the tip gap with subsequently little pressure recovery. Yaras and Sjolander (1991) conclude that relative casing motion has a significant effect on the magnitude of the tip leakage flow. Figure 6.14 highlights how the relative casing motion influences the velocities in the tip gap. It also illustrates that there will be an impingement of the flow entering the tip gap onto the casing ahead of the tip gap. This acts to scrape off the casing boundary layer local to the pressure side corner.

Along the exit of the tip gap a vortex sheet is formed, due to the differing mainstream and leakage flow velocities. This rolls up along the suction side corner to form the concentrated tip leakage vortex. Wang et al. (1997) describes how this interacts with the counter rotating passage vortex which is generated along the leading edge of the blade tip (fig. 6.15), and further entrains casing secondary flow from the passage endwall.

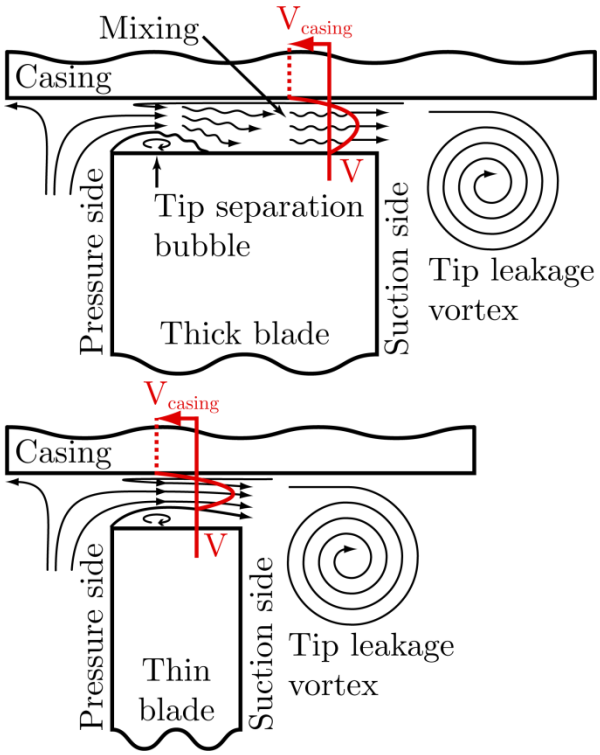

Figure 6.14. Over tip leakage flow relative to the rotor over a thick and thin blade.

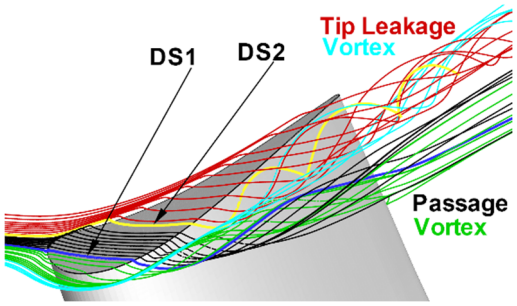

Figure 6.15. tip leakage vortex development over flat tip, Mischo et al.(2008).

Heat Transfer

In the tip gap, the regions of highest casing heat flux correspond to the location of the tip leakage jet adjacent to the flow separation over the tip. Between 0 – 70% C_{AX} a separation bubble forms, confining the region of highest over tip heat flux local to the pressure side corner. Beyond 70% C_{AX}, the flow does not reattach and the heat flux remains high across the full width of the tip. This corresponds to a blade thickness of 3.5 times the tip gap, which is slightly less than the value of 4 given by Denton (1993). If we now consider the T_{AW} and Nu components in the tip gap we see that the T_{AW} in fig. 6.13 shows only a moderate enhancement compared to the flow local to the pressure side and does not exceed T_{01}. This differs somewhat from the

measurements of Thorpe and Ainsworth (2008), who predict an enhanced T_{AW} over the entire tip. These results do agree well with the predictions of El-Gabry and Ameri (2010), though the predicted enhanced T_{AW} in the immediate vicinity of the pressure side corner is not captured well. It is possible that the bandwidth of the gauges is not sufficiently high to detect such a confined feature. Nu in the tip gap is measured to be significantly enhanced adjacent to the tip leakage jet. This is most likely the result of the acceleration and radial velocity component of over-tip leakage flow in this region thinning the boundary layer. Enhanced Nu under the tip is not observed so clearly between 60 – 100% C_{AX}, again this may be due to a limitation in the gauge bandwidth. This data indicates that the increase in heat flux in the tip gap is primarily driven by enhancements in Nu rather than increases in T_{AW}.

In the passage, we observe that the casing heat flux (which is highest local to the pressure side corner) decays as the suction side approaches. If we consider the T_{AW} and Nu components in fig. 6.13, we see that the heat flux distribution in the passage is predominantly driven by changes in T_{AW}. The T_{AW} distribution in the passage is mostly dictated by the work extraction of the rotor. As discussed by Thorpe and Ainsworth (2008), for much of the passage, the Nu distribution correlates well with absolute mainstream velocities local to the casing. Other features of note include:

- Enhancement of Nu upstream of the pressure side corner. Most likely the result of the over-tip leakage flow impinging on the casing as it enters the tip gap. This also acts to scrape off the casing boundary layer which further enhances Nu.
- Evidence of the tip leakage vortex local to the suction side corner downstream of 60% C_{AX}, indicated by an increase in T_{AW}.
- Enhancement in heat flux caused by an enhancement in Nu in the vicinity of the blade wake local to the blade trailing edge.

6.7 Uncertainty Analysis

The following discussion aims to quantify the uncertainty of the heat transfer measurements. These mostly arise from three sources, the surface temperature measurement, the conversion to heat flux and the regression to obtain T_{AW} and Nu.

6.7.1 Uncertainty of Surface Temperature Measurement

The thin film gauges used in this study utilise a platinum resistive temperature sensor. Platinum is used as it has a very linear resistance-temperature relationship over a wide temperature range. This significantly simplifies calibration as the sensor need only be over a smaller temperature range than that of the experiment. This is of benefit to TFHFGs as they often exhibit a drift in the value of R_0 when subjected to sustained elevated temperatures. TFHFGs are calibrated in an automated water bath facility. Using the calibration data, the typical 95% confidence interval dR/dT_w is calculated to be ± 0.25% and the 95% confidence interval of R_0 to be ± 3% of the calibrated value.

The wall temperature is calculated using the following equation, with α referenced to conditions of $T_0 = 0$°C. The temperature is referenced to an isothermal condition before the start of the run (T_1) when T_W can be measured with two thermocouples located under the gauges. These were calibrated in the water bath and estimated to have confidence interval of ± 0.4%.

$$T_W - T_1 = \frac{(V - V_1)(1 + \alpha\,(T_1 - T_0))}{\alpha\, V_1} \tag{6.8}$$

The uncertainty in R_0 can be eliminated by instead measuring the current through each gauge with the use of high precision resistor of known value (R_{Cal}) in place of the gauge before each run. This also eliminates any changes in R_0 due to changes in the connecting wires between the calibration and the experiment. The above equation can then be amended to the following.

$$T_W - T_1 = \frac{(V - V_1)R_{Cal}}{V_{Cal} dR/dT_W} \tag{6.10}$$

All amplifiers and data acquisition systems were calibrated before the experimental campaign and are assumed to introduce negligible uncertainty into the measurements.

6.7.2 Heat Flux Transformation Uncertainty

The measured wall temperature signal is converted to heat flux using the impulse response method for a two layered substrate developed by Oldfield (2008). This conversion requires knowledge of the material effusivity of the top and bottom layers in addition to the thermal conductivity and thickness of the upper insulating layer. The two-layered model is highly non-linear and analytical solutions are extremely lengthy (Doorly and Oldfield (1986)). To understand the effect of these variables on the uncertainty of the measurements at the typical values used in this study, each material property was perturbed in the range of ± 20% of the nominal value. Experimental data from the study was then reprocessed using the same processing routines to evaluate the sensitivity of T_{AW} and HTC to these permutations.

The thickness of the upper layer in this study is close to a value that may be considered semi-infinite. This is borne out in the results of the sensitivity study which indicates that a ± 20% permutation in the upper layer thickness, conductivity or the effusivity of the bottom layer had no measurable effect on the T_{AW} and HTC results (maximum ± 1e-3% difference observed). A ± 20% variation in these parameters is well within the known bounds for these parameters and thus these can be discounted from the uncertainty analysis. The transformation can thus be assumed to be that of a 1D semi-infinite substrate. The following equation describes the relationship between heat flux and surface temperature.

$$\dot{q} = \frac{dT_W}{d\sqrt{t}} \frac{\sqrt{\pi}}{2} \sqrt{\rho c \lambda} \tag{6.11}$$

The transformed heat flux is linearly dependent on the material effusivity of the top layer ($\sqrt{\rho c \lambda}$). This acts to linearly scale the processed HTC result but has no effect on the calculated T_{AW}. This is significant as the effusivity of the insulating layer is widely considered to be the largest source of uncertainty in heat transfer measurements. The effusivity for this study is taken to be 490 ± 4%, as calibrated by Piccini et. al. (2000).

6.7.3 Regression Uncertainty

The data processing scripts compute T_{AW} and Nu with a regression using the Matlab 'fit' function. The time-resolved 95% confidence intervals from this function are plotted in fig. 6.16.

Confidence intervals of T_{AW} increase in regions of higher T_{AW}. This is due to the measured data occurring at temperatures being significantly above T_{AW}, thus the intercept with the temperature axis is more sensitive to the slope of the regression.

Confidence intervals of Nu are largest in regions of low Nu, resulting from a smaller range of measured T_W in these regions from the experiments. Confidence intervals are also observed to increase for both parameters in regions subjected to highly unsteady flow processes, such as in the over-tip and wake regions.

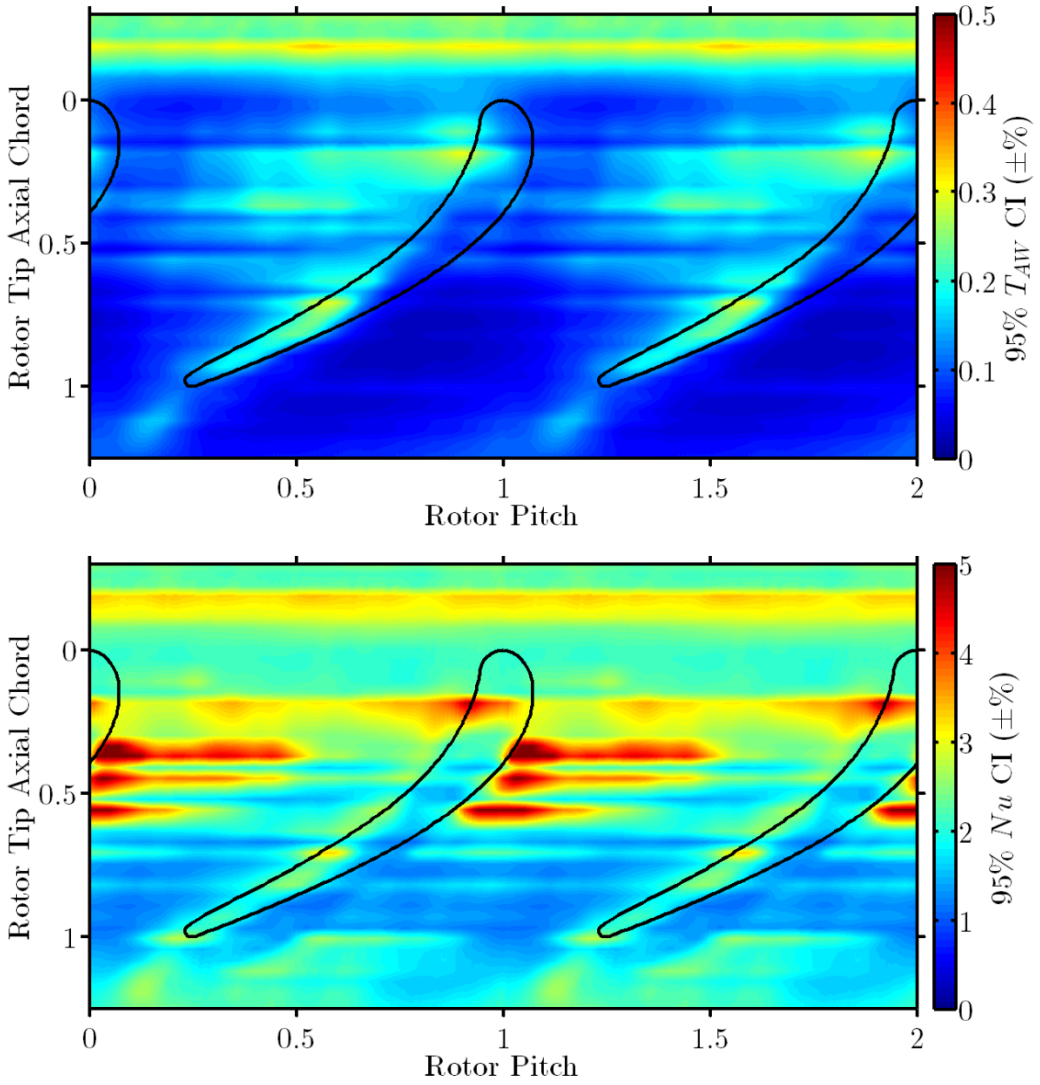

Figure 6.16. T_{AW} *(top) and* Nu *(bottom) 95% confidence intervals as a proportion of measured value obtained from regression.*

6.7.4 Overall Uncertainty

The most significant sources of uncertainty affecting heat transfer measurements are given in table 6.2. These can be combined to give an overall figure of uncertainty of ± 5% for T_{AW} and ± 10 – 13% for Nu. These figures are similar to those given by Thorpe et al. (2004b) for a similar measurement region.

It is suggested that future experiments make use of a modified heat transfer amplifier in which the input can be switched to a high precision resistor before each run to measure the current. This eliminates the relatively large uncertainty associated with the calibrated R_0.

Table 6.2. Heat transfer experimental uncertainty.

Variable	T_{AW} Uncertainty (%)	Nu Uncertainty (%)
dR/dT_w	± 0.25	± 0.25
R_0	± 3	± 3
T_1	± 0.4	0
$\sqrt{\rho c \lambda}$	0	± 4
Regression	± 0.1 – 0.4	± 2 – 5
Re	± 1	± 1
Total	**± 4.75 – 5.05**	**± 10.25 – 13.25**

6.8 Conclusions

Both time averaged and time resolved measurements of heat flux and the corresponding components of Nu number and T_{AW} have been measured on the casing of a high-speed fully scaled rotor casing. New data processing techniques and improved instrumentation has generated much improved measurements of time resolved Nu number and T_{AW} which are in good agreement with numerical predictions.

The time resolved heat transfer results highlight important features which have not been previously observed in a rotating facility, though have been well documented in cascade tests.

1. The presence of a separation bubble on the tip at locations with a blade thickness to tip gap ratio greater than 3.5. For ratios less than 3.5, the flow is not observed to reattach as indicated by high heat flux over the full blade width. Increases in heat flux are observed to be predominantly driven by an increase in Nu.
2. Increased heat flux ahead of the pressure side corner caused by impingement of the tip leakage flow on the casing. This scrapes off the casing boundary layer, increasing heat transfer in the passage adjacent to pressure side corner. Again these increases in heat flux are predominantly driven by an increase in Nu.
3. The presence of a tip leakage vortex adjacent to the suction side and local to the casing. This continues to propagate downstream of the blade. This enhances heat transfer,

predominantly by an increase of both T_{AW} due to entrainment of higher temperature tip leakage flow.

4. Elsewhere in the passage T_{AW} is dictated by work extraction by the rotor and Nu is well correlated to the absolute flow velocity local to the casing, as discussed by Thorpe and Ainsworth (2008).

6.9 Chapter Nomenclature

α	Temperature coefficient of resistance: $(dR/dT)/R_0$,
C	Rotor true chord (OTRF = 36.6 mm)
C_{AX}	Rotor tip axial chord (OTRF = 21.39 mm)
c	Specific heat
h	Heat Transfer Coefficient (*HTC*)
k	T_{AW}/T_{01}
λ	Thermal conductivity
M	Mach number
n	Polytropic index
Nu	Nusselt number: hC/λ_{01}
ρ	Density
p	Pressure
Pr	Prandtl number
$\dot{q}$	Heat flux
Re	Reynolds number
r	Recovery factor
R	Gauge resistance
t	Time
T	Temperature
T'	Corrected temperature
$\bar{T}$	Time mean temperature
T_d	$T_r - T_{0m}$
T_r	Recovery temperature
τ	Iteration number
u	Local free stream velocity
V	Velocity
ω	Rotor disc speed

Subscripts

01	Inlet total
02rel	Rotor inlet relative
0m	Total local to measurement location
AW	Adiabatic wall
Cal	Calibrated resistor
W	Wall

Chapter 7: Experimental Investigation of a Film Cooling Scheme Employed on the Over-Tip Casing of an Unshrouded Transonic Gas Turbine

7.1 Abstract

The casing of an unshrouded HP rotor is subjected to high aerodynamic and thermal loads at both low and high frequency resulting from the rotor potential field and over-tip leakage flows. Increasing turbine entry temperatures necessitate that this component be cooled to ensure satisfactory service life and performance. Film cooling is commonly utilised on the turbine stages of a modern gas turbine, yet there are very few published studies investigating its use on an unshrouded casing.

In this chapter we describe the experimental testing of a film cooled casing. Specifically:

1. Describe the experimental testing of such a film cooled rotor casing on the Oxford Turbine Research Facility (OTRF), an engine-scale short-duration (0.4 s run time) rotating transonic facility.
2. Present high resolution time resolved measurements of heat transfer using high density arrays of miniature thin-film heat-flux gauges with a spatial resolution of 0.8 mm and temporal resolution of ~120 kHz. The small size of the gauges, the high frequency response, coupled with recent improvements to data processing techniques allows very detailed measurements of the heat transfer in this region. Time-resolved measurements of T_{AW} and η' are presented for the casing region (-30% to +125% C_{AX}).

7.2 Introduction

The casing of an unshrouded rotor is subjected to large temporal variations in both static pressure and heat load. Increasing turbine entry temperatures necessitate that the casing be cooled. One such cooling strategy would utilise film cooling. As yet, there has been only one

published pair of papers describing a casing film cooling scheme by Chana and Haller (2009). There are also a number of patents relating to the implementation of such a scheme, for example Liotta and Acquaviva (1999), Lee and Durgin (2001), White and Lee (2002), Lowe et al. (2003), Shapiro (2007) and Lee et al. (2012), indicating probable use in an engine.

This study utilises recent improvements to instrumentation and data processing techniques to provide time resolved measurements of T_{AW} and η'.

7.2.1 Previous Work

There have been only two sets of studies which have looked at injecting coolant on the casing. Chana and Haller (2009) consider a design primarily intended to cool the rotor casing whilst Behr et al. (2008) considers the use of casing coolant injection to reduce tip leakage flow and subsequently improve the aerodynamic performance of an unshrouded rotor.

Chana and Haller (2009) present a pair of papers which outline a design methodology for a casing film cooling scheme in conjunction with experimental measurements taken on the OTRF. Holes were angled to the time mean flow angle of the passage and were fed from two plenums. Measurements were made on the OTRF with 7 Thin Film Heat Flux Gauges (THFHGs) with data presented as a time mean heat flux and time mean Nu. The study concluded that there was up to a 44% reduction in casing heat load with $\dot{m}_C/\dot{m}_{12} = 1.85\%$. Values of T_{AW} were not presented, nor was the data decomposed into time-resolved measurements of Nu or T_{AW}.

Behr et al. (2008) and Mischo et al. (2007) discuss the use of casing coolant injection to reduce over-tip leakage flows and improve blade row efficiency using computational and experimental measurements. Experiments were undertaken on a 1.5 stage rotating facility. Time resolved measurements indicated a reduction in the magnitude of the tip leakage vortex and computed

an increase in the blade row efficiency of 0.55% for an injection $\dot{m}_C/\dot{m}_{12}$ = 1%. Neither of these studies considered heat transfer nor transport of coolant in the casing frame of reference.

There is also a limited amount of published literature available for heat transfer on the casing of a rotating unshrouded rotor at high speed engine-representative conditions. A number of studies present measured heat flux data from the rotor casing of transient facilities, Guenette et al. (1985), Metzger et al. (1991), and Polanka et al. (2003). Collins et al. (2015) summarises this earlier work and presents improved time resolved heat transfer data (both Nu and T_{AW}) taken on the OTRF. Improvements to heat transfer processing are also presented and have been applied to the measurements in this study.

7.3 Experimental Facility

Experiments were conducted on the Oxford Turbine Research Facility (OTRF), formerly named the Turbine Test Facility and prior to that the Isentropic Light Piston Facility. The facility is a short duration light piston driven facility operated as a 1½ stage engine-scaled rotating transonic HP turbine stage with uniform inlet conditions as described by Chana et al. (2013). Re, M, T_G/T_W and non-dimensional speed were all matched to engine conditions and the operating conditions are summarised in table 7.1. The tip clearance is 0.56 mm, which corresponds to 1.4% of span at mid-chord.

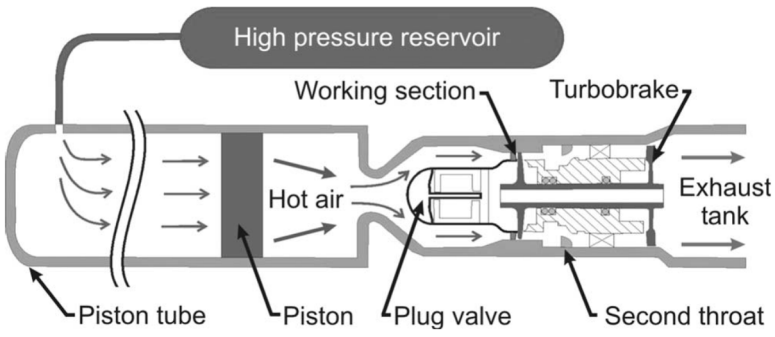

Figure 7.1. Schematic of OTRF.

Table 7.1. OTRF operating conditions.

Parameter (unit)	Nominal value	Allowable run-to-run variation (%)
p_{01} (bar)	4.6	± 1
T_{01} (K)	444	± 2
T_G/T_W	1.54	± 2
M_2^{hub}	1.054	± 1
M_2^{casing}	0.912	± 1
ω (rpm)	9500	± 1
p_{02rel} (bar)	2.697	± 1
Re_{NGV}	2.54E6	± 1
$T_{0C}/\overline{T_{01}}$	0.675	± 2

A schematic of the OTRF is provided in fig. 7.1. Prior to an experimental run, the plug valve is closed and the working section is evacuated to near vacuum conditions. The rotor is spun up to design speed by an air motor. When up to speed, air from the high pressure reservoir is admitted to the piston tube behind the free piston. The free piston moves down the piston tube compressing and heating the test gas ahead of it. When the correct pressure in the test gas is achieved, the fast acting plug valve opens to admit air into the test section. The rotors speed is maintained by a turbobrake situated downstream of the working section. Steady conditions are maintained for approximately 400 ms, ending when the free piston reaches the end of its travel.

7.4 Initial Experimental Study

Experimental testing was undertaken in two parts. This section details the first set of experiments undertaken on the OTRF.

7.4.1 Experimental Hardware

Experimental hardware was incorporated into an aluminium removable cassette in the over tip rotor casing of the OTRF, see fig. 7.2. This was CNC machined from 6000 series aluminium

and incorporated quite a complex sealing arrangement. The cassette contains a machined inset rail into which a film cooling module can be installed. The clocked location of the module is then set by installing appropriate spacer modules. Sealing was achieved with offset O-ring grooves in the rails and modules. This system permits the entire cooling system, instrumentation and feed system to be clocked relative to the vane, allowing measurements of the vane potential field using the same instrumentation and cooling module.

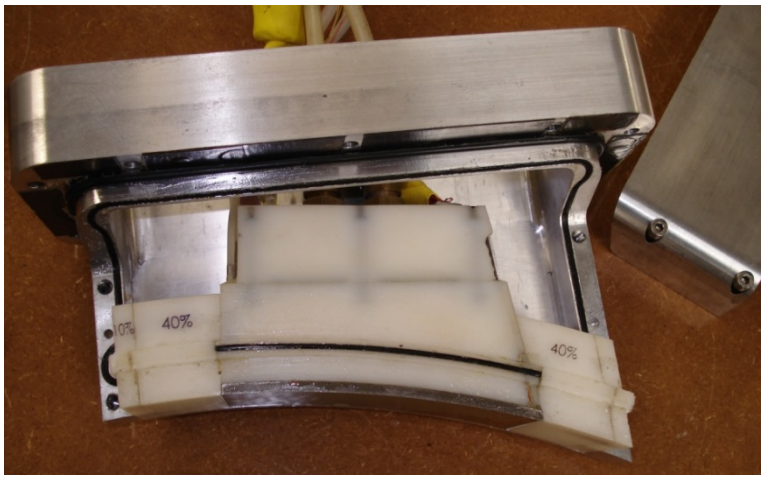

Figure 7.2. Disassembled aluminium cassette holding cooling module and spacer blocks.

The spacer blocks and cooling module plenums were manufactured using Stereolithography (SLA) in Protogen 18420 resin. The film cooling system itself was manufactured as a plate in titanium (Ti64 alloy) using metal laser sintering and bonded to the SLA plenums using screws and glue. Traditionally cooling holes are either machine drilled, electrical discharged machined (EDM) or laser drilled. Due to the small diameter and low lay angle of the holes machine drilling was not possible. The EDM and laser drilling processes are mostly used for large scale production runs and incur large set up costs on parts consisting of many holes at different angles. Laser sintering offers the entire part to be built in one process. This significantly reduces cost and lead time for this part. One problem with laser sintering, especially for large thin wall parts, is warping due to thermal stresses in the build process. To generate a cylindrical casing

surface, the outer surfaces of the plates were EDM wire cut after manufacture to the required casing radius. The laser sintered parts are specified as having zero porosity.

Table 7.2. Initial experimental testing hole geometry.

Row	Feed Plenum	Row Exit Location (% C_{AX})	Hole Spacing (°)	Hole Orientation (Angle to axis of rotation) (°)
1	P1	-35	1.225	83
2	P1	-25	1.225	59
3	P1	-3	1.225	39
4	P2	13	1.225	53
5	P2	33	1.225	39
6	P3	52	1.225	52
7	P3	72	2.45	39
8	P4	92	1.225	52
9	P4	112	2.45	39

7.4.2 Cooling System Geometry

The film cooling geometry investigated in this study was derived from an in house Rolls-Royce design, intended for testing on the Environmentally Friendly Engine (EFE) at Rolls-Royce. The EFE engine has a different casing diameter to the OTRF so the design had to be scaled. The scaling process is outlined in fig. 7.3 and the resulting design details are given in table 7.2. All cooling holes were designed to be ∅0.5 mm at a lay angle of 20° to the surface, though the as manufactured holes were measured to be smaller at ∅0.4 mm. The resulting design is very similar to geometry A in the CFD chapter. The CFD design only differs in circumferential hole spacing which is modified to 1° so that the holes form a periodic pattern across one blade passage.

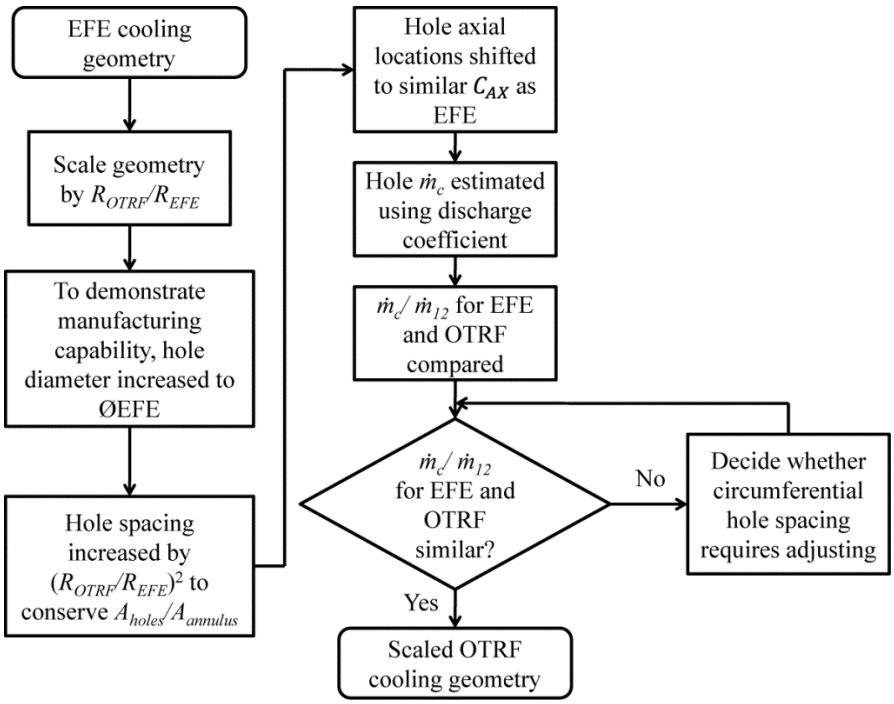

Figure 7.3. Process used to scale Rolls-Royce casing cooling geometry to the OTRF.

7.4.3 Coolant Feed System

Particular attention was paid to the coolant feed system in terms of regulating the mass flow rates to each plenum and optimizing for transient operation.

Due to the short duration of the experiments, it is critical that any coolant system is able to respond sufficiently quickly to changes in feed and outlet pressure. At the start of a run, the plenums will pressurise as the working section is brought from vacuum to operating pressure. If we consider this process to be isentropic, the gas contained within the plenums will be heated. To mitigate this effect, each coolant plenum is fed from a common manifold attached to the coolant module through a plate containing a series of choked holes. This allows the relative mass flow rate into each plenum to be set, whilst the total mass flow rate can be altered by changing the common manifold total pressure. Each plenum incorporates a distribution plate to disperse the feed jets and equalize the feed pressure within the plenum. Thermocouples are placed in each plenum to measure the coolant total temperature and pressure tappings measure the coolant total pressure. The entire cooling module including the coolant manifold and instrumentation measures only 100x70x44 mm and is shown in fig. 7.4.

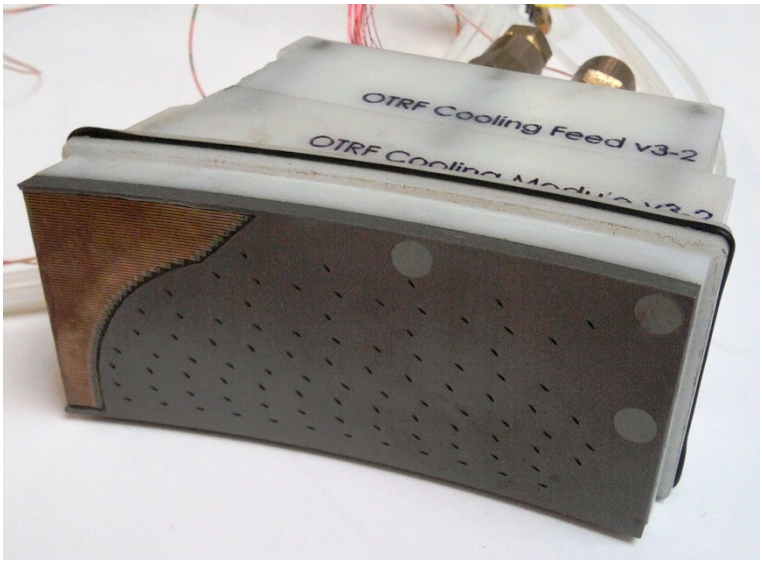

Figure 7.4. Cooling module of initial experimental hardware.

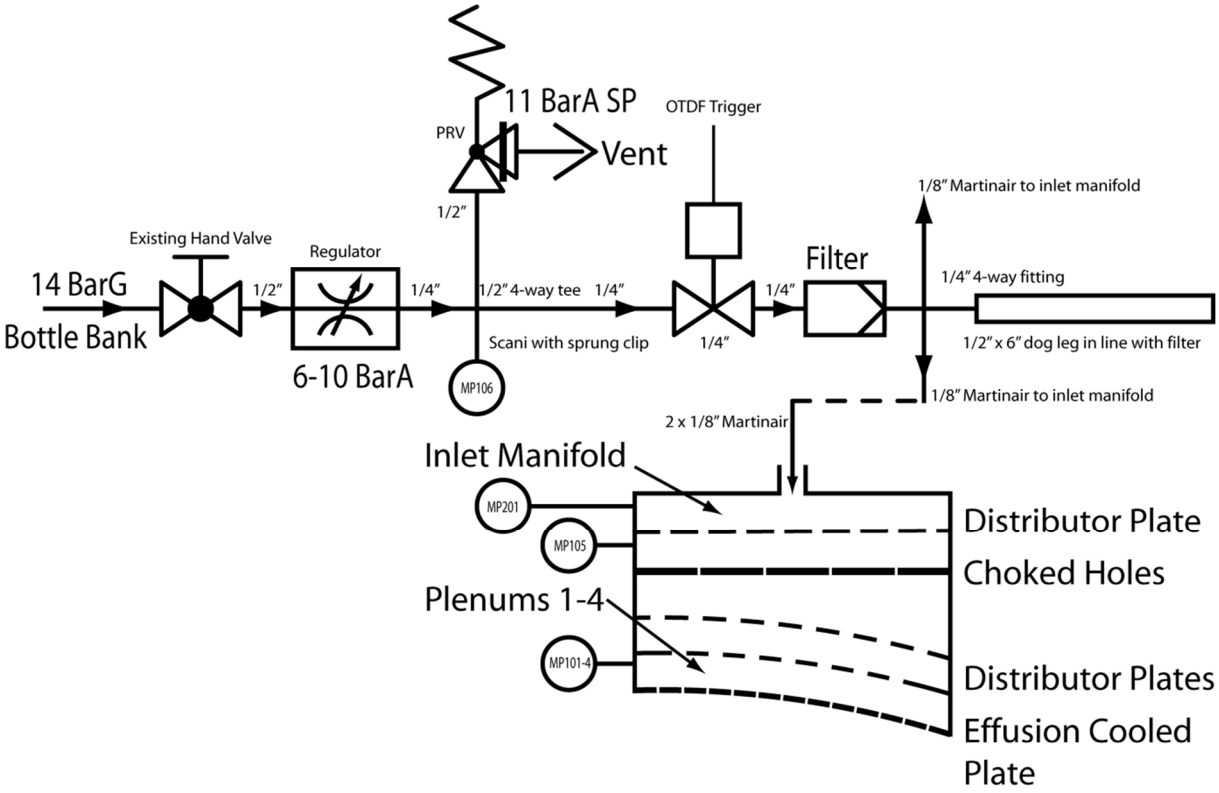

Figure 7.5. Diagram of the coolant supply as installed on the OTRF.

Coolant Supply System

The coolant supply valve can only be triggered approximately 1 s before the start of each run, as the addition of coolant into the evacuated working section slows the pre-spun up rotor. The arrangement of the coolant supply was therefore also optimised to minimise temperature spikes during the pressurisation of the system. The coolant supply to the module is initialised with the

opening of a pneumatic valve. This passes through a filter before a tee incorporating a dog leg. The dog leg is present to capture gas contained within the relatively large pneumatic valve, heated during the valve opening. The cooling module is then fed by flexible connections. The setup was successful with only a minimal temperature spike evident within the cooling inlet manifold at the opening of the pneumatic valve.

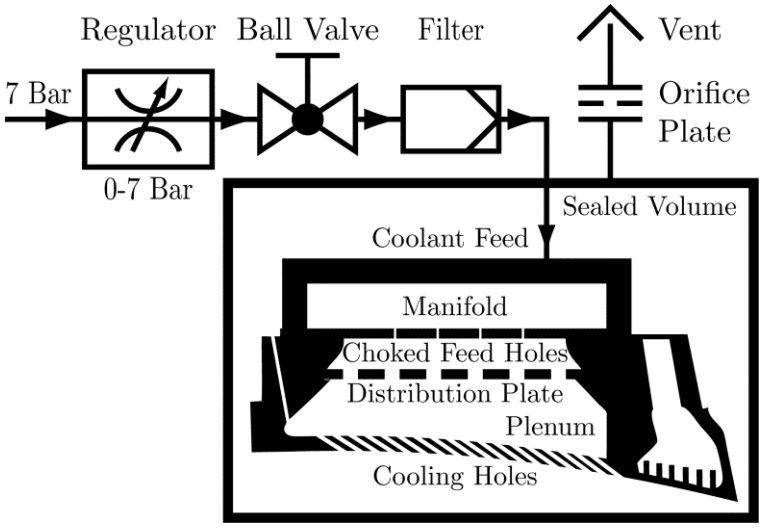

Figure 7.6. Cooling module flow calibration rig schematic.

Mass Flow Calibration

The capacity characteristics of the manufactured cooling holes and feed holes for each plenum were measured with a flow calibration rig illustrated 7.6 in fig. and pictured in fig. 7.7. This allows the mass flow rate into and out of each plenum to be calculated during the experiment using only measurements of the upstream and downstream pressures and temperatures. The holes to be calibrated are fed from a pressure regulator with the other holes in the system blanked off. The cooling module is placed inside a sealed volume with an outlet to atmosphere via a small orifice plate. The feed pressure is adjusted by hand and stepped over a large number of values. All relevant upstream and downstream pressures are recorded on a data acquisition system, including the pressure differential across the orifice plate. Each run is processed in Matlab with a script that can automatically identify each stable portion of experimental data. Mass flow rates are evaluated using a compressible orifice plate calculation and combined to

formulate a capacity curve, an example is given in fig. 7.8. Results are very repeatable and the automated nature of the processing enables a large number of pressure ratios to be measured.

Figure 7.7. Flow calibration and pressure testing rig.

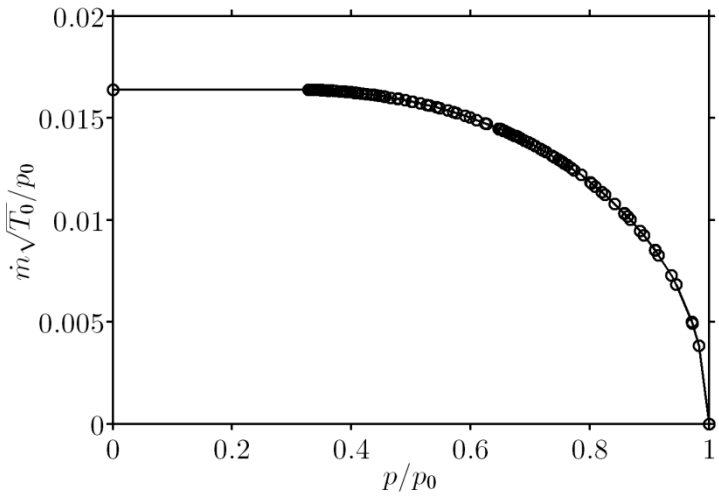

Figure 7.8. Measured capacity curve of cooling holes using flow calibration rig.

7.4.4 Instrumentation

The gauges used for this study are of an improved construction developed at Oxford by the author and detailed in an earlier chapter. These TFHFGs utilise a new manufacturing process which makes use of a pre-laminated copper and polyimide substrate. This enables the thickness

of the copper connecting tracks to be increased from 0.5 μm to 18 μm. This allows the width of the connecting tracks to be shrunk considerably, which for this application offers a greater than fivefold improvement in lateral gauges density. The platinum sensor is also of a new serpentine design which increases the sensitivity for a given footprint. The result is a lateral gauge spacing of 0.8 mm vs. 4.4 mm used in similar previous studies (2003).

Heat transfer instrumentation was located immediately downstream of the cooling system along a line of the computed time mean flow normal. The resulting instrumentation consisted of 52 TFHFGs and is pictured in fig. 7.9. The TFHFGs were located on five layers of glue and polyimide corresponding to a composite thickness of 575 μm. This is less than the propagation distance of the thermal wave during the test duration, so a two-layered impulse response filter was used to calculate the heat flux from the temperature signal as described by Oldfield (2008).

Gauges were calibrated in the automated calibration facility described in the TFHFG chapter.

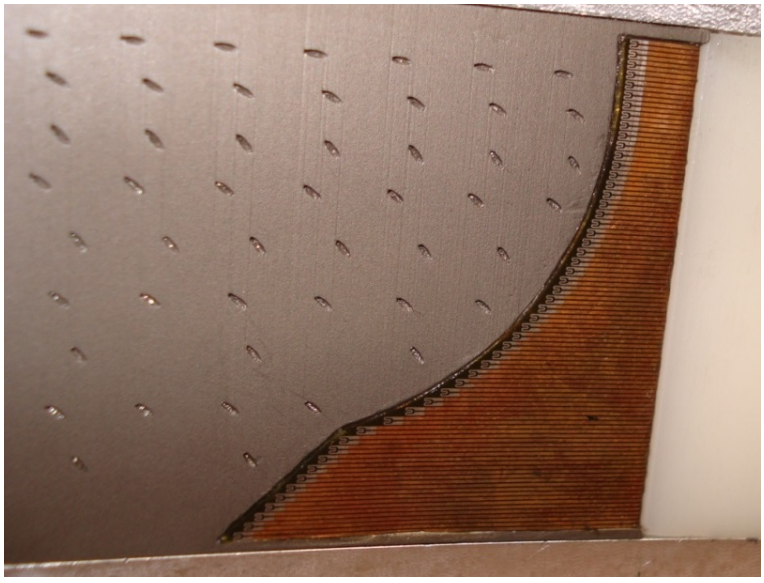

Figure 7.9. Instrumented cooling module for initial experimental tests.

These experiments make use of the original HTA2 amplifiers developed by Oldfield et al. (1978) and Oldfield et al (1984). TFHFGs are connected to a Heat Transfer Amplifier (HTA) which makes use of a transmission line analogue to convert the temperature signal from the gauge to a heat flux signal, Oldfield et al. (1978), Oldfield et al (1984). This heat flux signal is

recorded by a DAQ, which originally negated the need at the time for lengthy data processing techniques. The HTA2 assumes that the gauge is placed on a material that is thick enough to be assumed semi-infinite for the experiments duration. Advances in both computer power, and in particular the development of the impulse response processing technique Oldfield (2008), have substantially reduced the time required to compute the heat flux from the measured temperature signal.

In more recent years, it has become common to apply a reverse transformation of the recorded heat flux signal from the HTA using a semi-infinite 1D impulse response function to return the measured but not recorded temperature signal, for example Chana and Jones (2003). It is then possible to account for a non-semi-inifinite substrate using further impulse response processing Oldfield (2008).

In this initial study, the voltage and hence the surface temperature of each gauge was directly recorded and the heat flux calculated using the impulse response method. This was done as significant heating on the casing was observed during the spin up of the rotor before the run. The HTA2 box is unable to output both the heat flux analogue signal and DC temperature signal (the heat flux signal is essentially AC coupled), so only the temperature signal was recorded to measure the pre-run temperature rise.

7.4.5 Initial Experimental Results

Each run recorded the output from 52 TFHFGs along with mainstream flow parameters. The data presented in this section is taken from one clocked position relative to the vane, chosen to avoid the wake. The test matrix is given in table 7.3.

Table 7.3. Test matrix for initial experiments. Nominal $\dot{m}_c/\dot{m}_{12}$ = 0.44%.

Location	Inlet Conditions	$\dot{m}_c/\dot{m}_{12}$	Repeats
1 Clocked position	Uniform inlet	Nominal +30% +20% +10% -20% 0	x2
			12 Runs

Adiabatic wall temperature and heat transfer coefficient were computed using a linear regression of the recorded surface temperature history and the reconstructed heat flux signal obtained with the impulse response method of Oldfield (2008). At this stage the improved data processing techniques described in the uncooled heat transfer chapter had not been developed and so were not applied to this data set.

Results are plotted for three different coolant mass flow rates in fig. 7.10.

7.4.6 Initial Experimental Results Discussion

The results indicate a good agreement from gauge to gauge (gauges are measured and processed independently of each other) however there is a significant run to run variation between repeat runs, masking any quantifiable differences between the data sets. This uncertainty precludes further analysis of this data and instead further analysis focuses on areas of improvement for the revised experimental study.

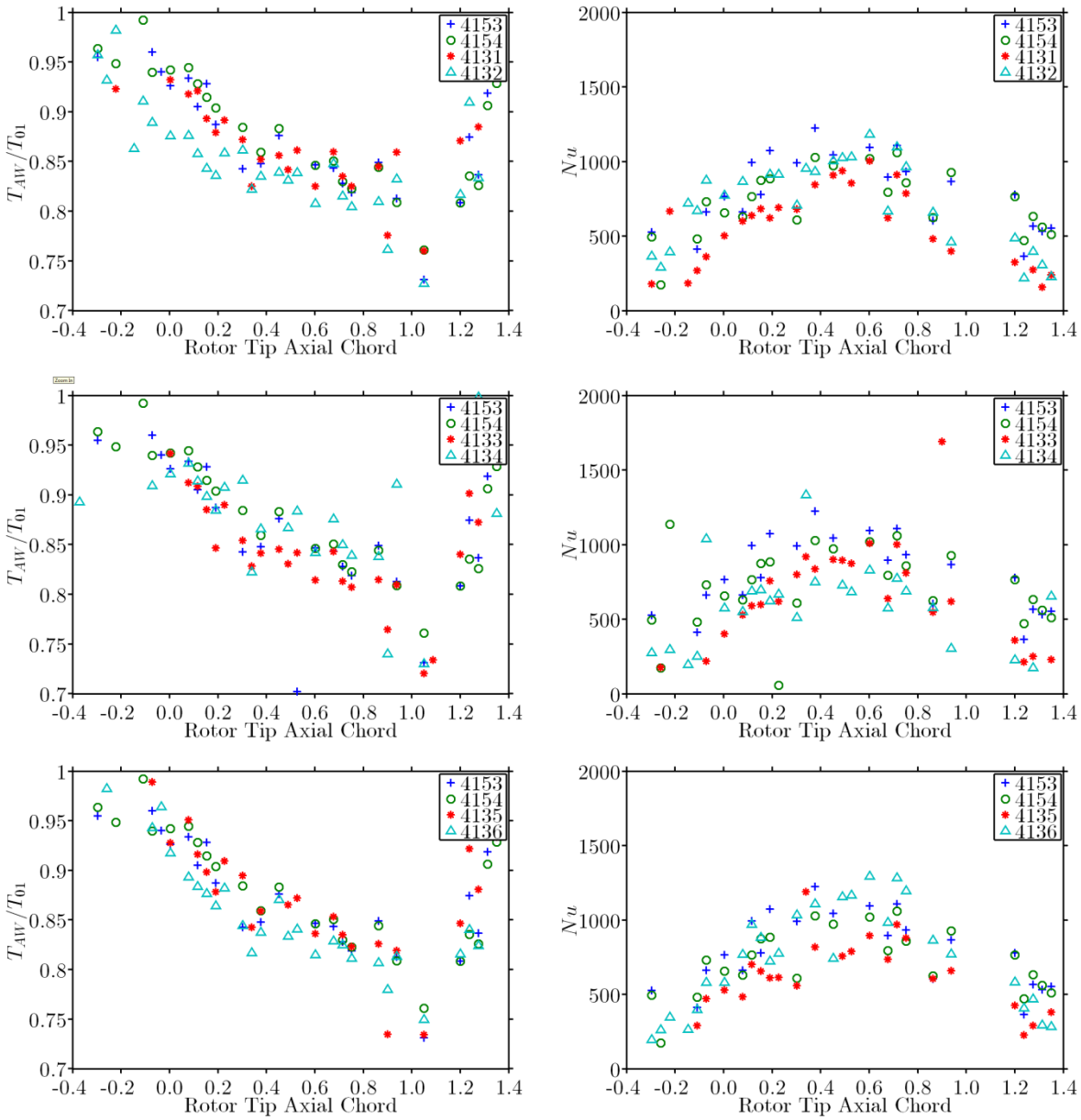

Figure 7.10. Initial experimental results of T_{AW} and Nu for $\dot{m}_C/\dot{m}_{12}$ =0.40 – 0.55%.

Table 7.4. Coolant mass flow rates for presented runs.

Run	$\dot{m}_C/\dot{m}_{12}$
4131	0.48%
4132	0.48%
4133	0.52%
4134	0.52%
4135	0.55%
4136	0.55%
4153	0%
4154	0%

7.4.7 Potential Failings of Initial Experiment

The run to run variations of the data and other problems with the OTRF prompted the initial study to be cut short. A number of possible problems were identified which were addressed in the design of the revised experimental study. The problems and solutions are outlined below

- The gauges were located immediately downstream of a change of material. This could result in an undeveloped thermal boundary layer at the gauge location. Though the instrumented polyimide region was flush with the titanium casing surface, there was a small step which may also alter the flow field.
    - The revised experimental design extends the instrumented region between the cooling holes.
- During the portion of the run corresponding to steady conditions and where data could be acquired, there was only a small change in measured wall temperature.
    - A method of pre-heating/cooling the wall was developed to enhance the range of measured wall temperature histories.
    - Improved data processing techniques developed to account for changes in the inlet total temperature during the run.
- Gauge locations are such that at the low coolant mass flow rates film cooling effectiveness values would be very small.
    - Increase the coolant mass flow rate of the system by increasing the hole density and moving gauges closer to the cooling holes.
- Connections for the TFHFGs were fragile and difficult to change.
    - Future experimental designs used break out patch panels of BNCs connections which were connected to the TFHFGs with 50-way D-Sub connectors.

7.5 Revised Experimental Study

Experience from the initial experimental study was used to redesign the experimental hardware to address the problems found. The solutions to the problems identified in section 7.4.7 are described in detail in the following section.

7.5.1 Experimental Hardware

Experimental hardware was incorporated into the same aluminium removable cassette in the over tip rotor casing of the OTRF, see fig. 7.11. This held a removable cooling module manufactured from titanium using laser sintering (fig. 7.12). This contained the cooling system fed by a series of small choked holes, instrumentation and a water heating/cooling loop used to control the initial wall temperature. The cooling module was located on rails and could be clocked relative to the upstream stators with the use of interchangeable spacer blocks.

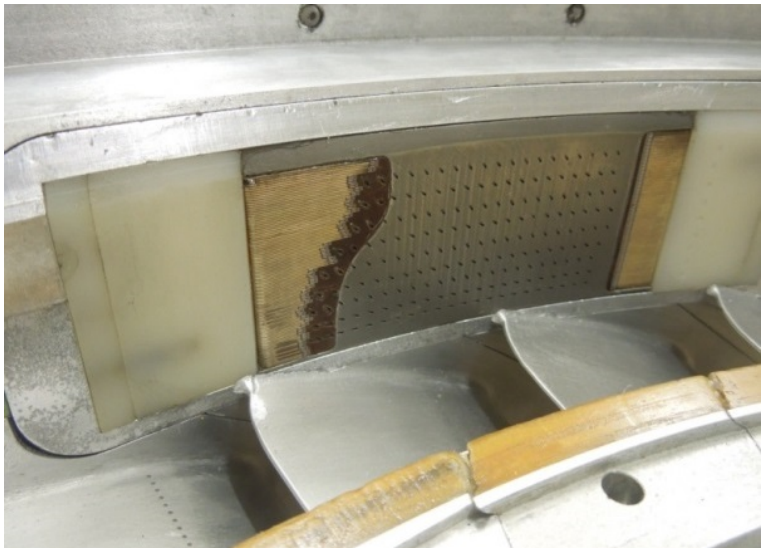

Figure 7.11. Installed cooling module located in aluminium cassette (rotor not present).

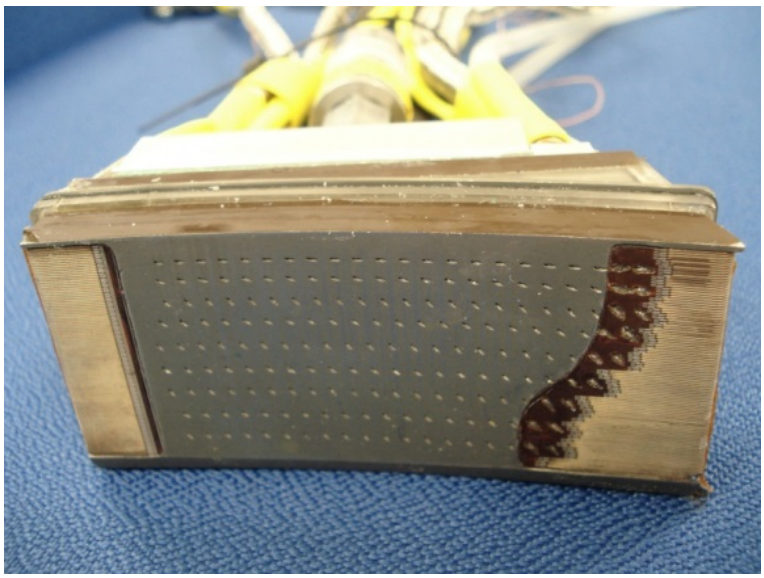

Figure 7.12. Instrumented cooling module.

7.5.2 Cooling System Geometry

The film cooling geometry investigated in this study was designed to cool a region between -35 – 110% C_{AX}, the measurable area on the casing over tip region of the OTRF. All cooling holes have a diameter of 0.4 mm and are inclined at 20° to the casing surface, with a circumferential hole spacing of 0.61° for all rows. This is similar to geometry B presented in the CFD chapter albeit with a slightly larger hole spacing and smaller diameter holes. There are nine rows of cooling holes in total fed from four plenums. Hole exit angles were the same as those in the initial experimental study.

7.5.3 Coolant Feed System

Particular attention was paid to the coolant feed system in terms of regulating the mass flow rates to each plenum and optimizing for transient operation.

Due to the short duration of the experiments, it is critical that any coolant system is able to respond sufficiently quickly to changes in feed and outlet pressure. At the start of a run, the plenums will pressurise as the working section is brought from vacuum to operating pressure. If we consider this process to be isentropic, the gas contained within the plenums will be heated. To mitigate this effect, the coolant plenum size was minimised as much as possible such that

the heated coolant will be mostly purged before heat transfer data is taken. The use of laser sintering enabled the plenums to be shrunk considerably as is visible in fig. 7.13.

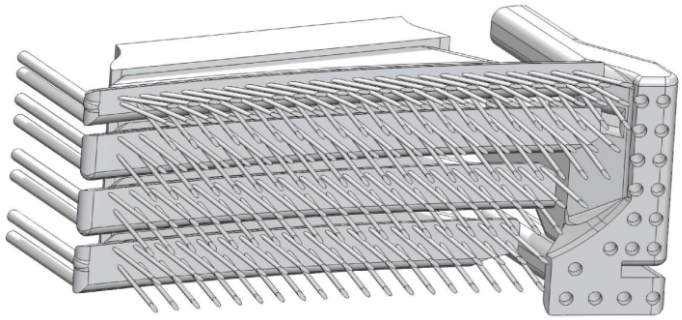

Figure 7.13. Cooling module internal volumes.

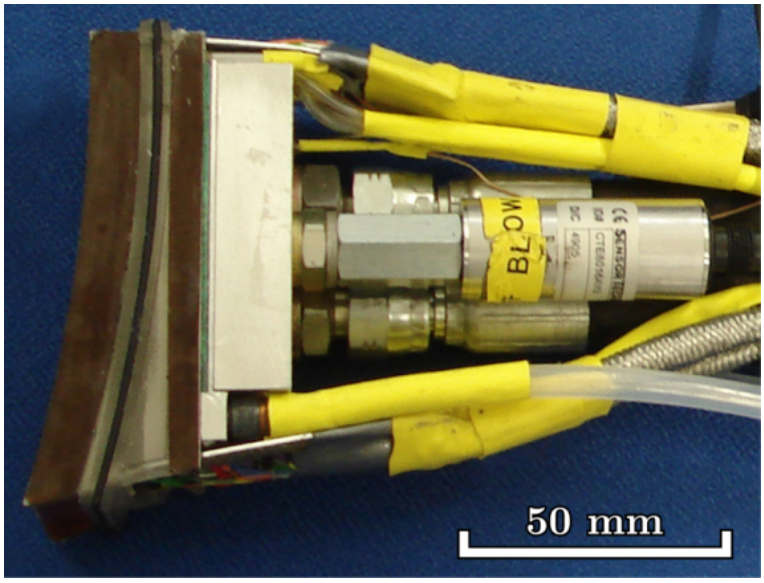

Figure 7.14. Cooling module incorporating coolant feed system, water cooling loop, 96 TFHFGS, 9 thermocouples, 4 pressure tappings and one pressure transducer.

To further reduce plenum size, each coolant plenum is fed from a common manifold attached to the coolant module through a plate containing a series of choked holes. This allows the relative mass flow rate into each plenum to be set, whilst the total mass flow rate can be altered by changing the common manifold total pressure. Each plenum incorporates a distribution plate to disperse the feed jets and equalize the feed pressures within the plenums. Thermocouples are placed in each plenum to measure the coolant total temperature and pressure tappings measure

the coolant total pressure. The entire cooling module including the coolant manifold and instrumentation measures only 100x40x44 mm and is shown in profile in fig. 7.14.

Mass Flow Calibration

The capacity characteristics of the manufactured cooling holes and feed holes for each plenum were measured using the flow calibration rig described in section 7.4.3 and shown in fig. 7.6. This allowed the mass flow rate into and out of each plenum to be calculated during the experiment using only measurements of the upstream and downstream pressures and temperatures. An unsteady flow model was created to check that the system behaved as expected during the experiments.

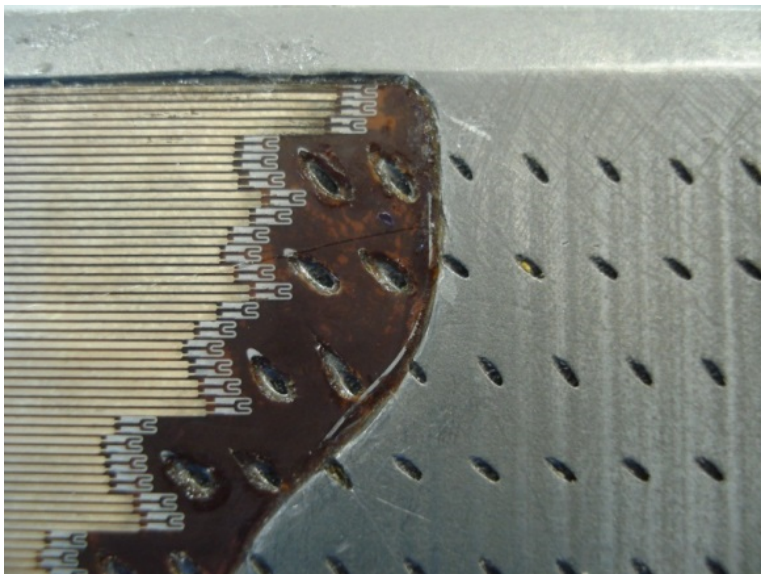

Figure 7.15. Instrumented casing region with 96 TFHFGS.

7.5.4 Instrumentation

The TFHFGs are similar in construction to those developed in Oxford by Jones (1995), with a thin film platinum sensing element deposited onto a polyimide substrate. The gauges used for this study are of an improved construction developed at Oxford and detailed in an earlier chapter. These TFHFGs utilise a new manufacturing process which makes use of a pre-laminated copper and polyimide substrate. This enables the thickness of the copper connecting

tracks to be increased from 0.5 μm to 18 μm. This allows the width of the connecting tracks to be shrunk considerably, which for this application offers a greater than fivefold improvement in lateral gauges density. The platinum sensor is also of a new serpentine design which increases the sensitivity for a given footprint. The result is a lateral gauge spacing of 0.8 mm vs. 4.4 mm used in similar previous studies Chana and Jones (2003).

Heat transfer instrumentation was located in two regions, one downstream and one upstream of the cooling system to record the uncooled casing heat transfer. The casing region is a very hostile environment for measuring film effectiveness as the coolant films are periodically perturbed and scraped off the casing by the passing of the rotor blade tip. TFHFGs were therefore placed as close to the cooling hole exits as possible, as seen in fig. 7.15. The polyimide substrate was also extended into the film cooled region to ensure that the thermal boundary layer had fully developed at the TFHFG measurement locations. This also ensured there were no surface discontinuities local to the gauges. The resulting instrumentation consisted of 48 TFHFGs in the cooled region and 48 TFHFGs in the uncooled region.

The TFHFGs were located on five layers of glue and polyimide corresponding to a composite thickness of 575 μm. This is less than the propagation distance of the thermal wave during the test duration, so a two-layered impulse response filter was used to calculate the heat flux from the temperature signal as described by Oldfield (2008).

Gauges were calibrated in the automated calibration facility described in the TFHFG chapter.

As described in the earlier uncooled experimental casing heat transfer chapter, the TFHFGs are connected to new Heat Transfer Amplifiers (HTAs) and a new Data Acquisition system (DAQ). This utilises a two break-point gain-shaping amplifier to boost the high frequency components of the temperature signal to avoid digitization errors at high frequencies caused by the reduced frequency response of thin film gauges at high frequencies, Anthony et al. (1999). The boosted

output from the new HTA is recorded by a high speed DAQ at a 2 MHz sampling frequency and then de-boosted in Matlab (which has much greater resolution than the DAQ) with an impulse response filter to recover the measured temperature signal. This can then be converted to heat-flux and processed using the impulse method as described by Oldfield (2008). This new HTA is able to resolve frequencies of 0 – 1 MHz vs. the previous HTA frequency range of 0 – 100 kHz, Oldfield et al. (1984). The new work process for measuring and processing heat transfer data is presented in fig. 7.16.

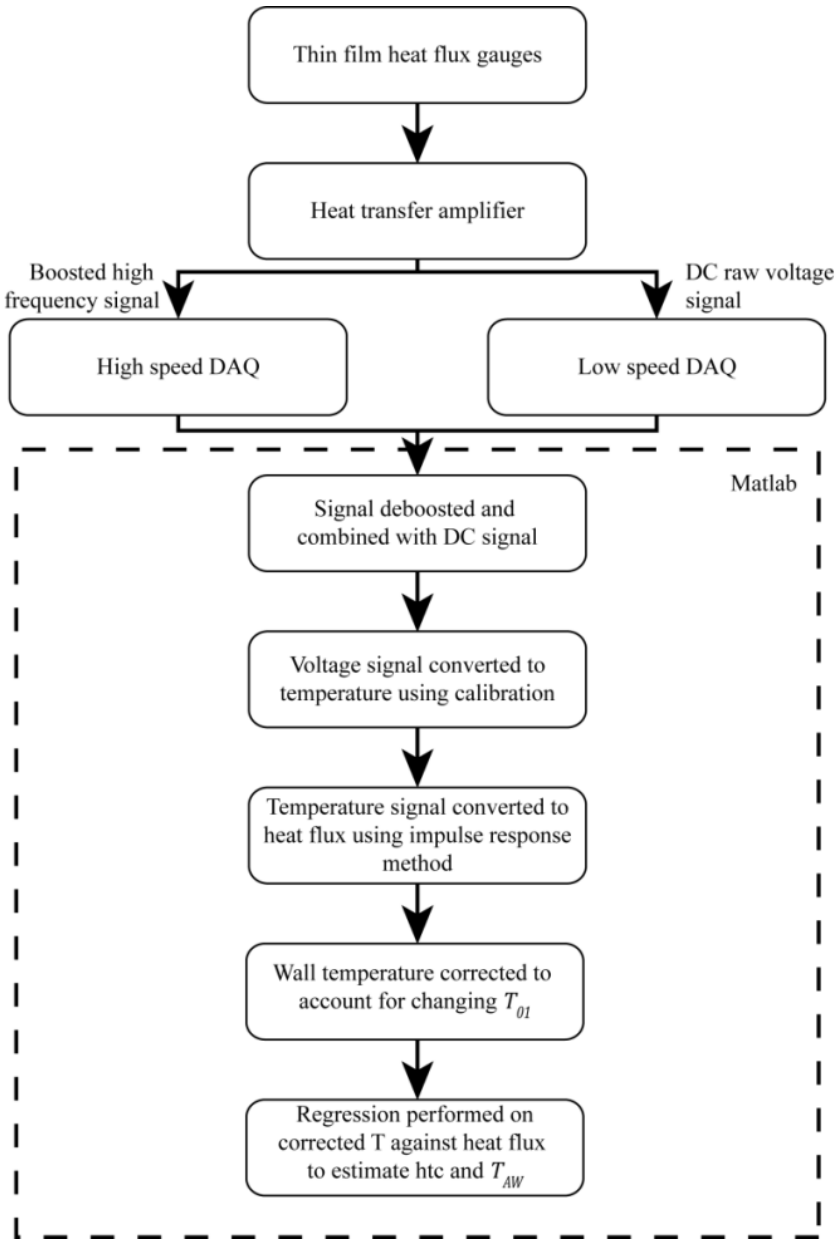

Figure 7.16. Work process for measuring, recording and processing heat transfer data using new HTA.

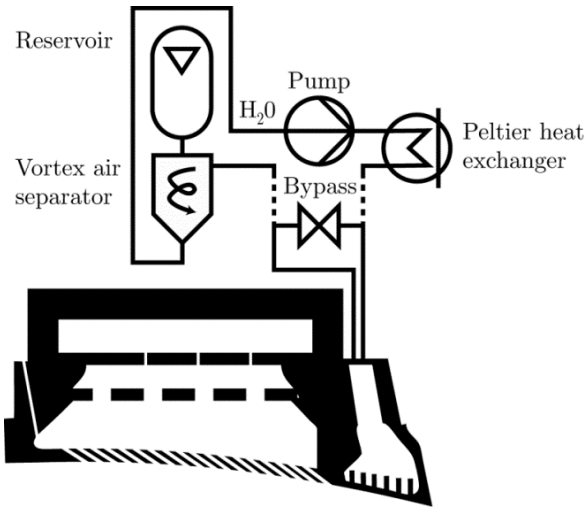

Figure 7.17. Schematic of wall heating/cooling hardware.

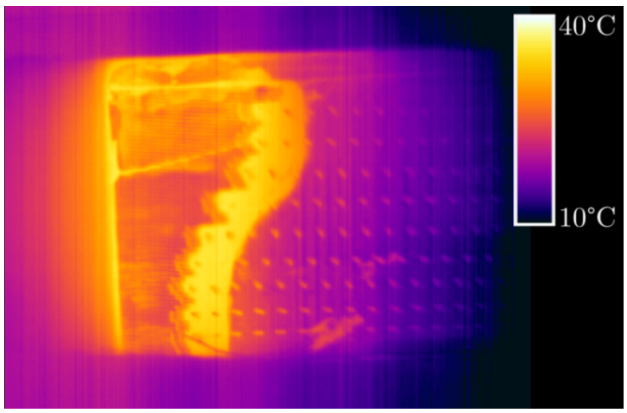

Figure 7.18. Infrared thermogram of instrumented pre-heated casing wall (image not corrected for different emissivity of instrumented region).

7.5.5 Wall temperature control

The initial wall temperature of the instrumented region is controlled using a water circuit, enabling measurements at a number of different gas/wall temperature ratios. A schematic of the custom built external hardware is illustrated in fig. 7.17. Heating or cooling is achieved by passing water through a heat exchanger connected to a number of thermostatically controlled peltier elements with a combined heating power of 250 W and cooling power of 72 W at room temperature. This water is pumped through a passage incorporating pin fins beneath the instrumented region, enabling the initial wall temperature to be set between 8 – 60 °C. An image acquired using infrared thermography of the casing surface during installation testing is shown in fig. 7.18, showing a pre-heated wall condition.

7.5.6 Experimental results

Each run recorded the output from 48 TFHFGs along with mainstream flow parameters. The data presented in this section is taken from one clocked position relative to the vane, chosen to avoid the wake. The coolant to mainstream mass flow rate was set to $\dot{m}_C/\dot{m}_{12}$ = 0.876%. A total of 3 different initial wall temperatures were set (14 °C, 24 °C and 43 °C) with a single repeat at each temperature, totalling 6 runs.

7.5.7 Cooling System Aerodynamic Performance

As already discussed, the cooling system was designed to rapidly respond to changes in the downstream pressure and mitigate the impacts of rapid pressurisation, due to the transient nature of the OTRF.

Figure 7.19 plots the recorded colant total pressures during a typical run. The coolant feed valve is opened approximately 1 s before the run start whilst the working section is at vacuum. In this state the cooling holes are choked due to the large pressure ratio and the plenum pressures are substantially lower than the design pressure. Upon the opening of the OTRF plug valve and the start of the run, the working section pressure rapidly rises, as do the plenum pressures. The run start location is defined as the point at which the working section pressure is stable. Figure 7.20 plots the time instantaneous pressure ratios across the holes. Casing static pressures are recorded using a modified spacer block with tappings at each of the cooling hole row exit axial locations. It is clear that the coolant feed system functions very well, with very stable pressure ratios across all rows of cooling holes. Figure 7.21 plots the coolant total temperature for three of the four plenums (one thermocouple was very noisy and omitted from the plot). The changes in coolant total temperautere are evidient at changes in plenum pressure. The magnitude of these changes is very small during the stable portion of the run, again showing the good performance of the coolant feed system.

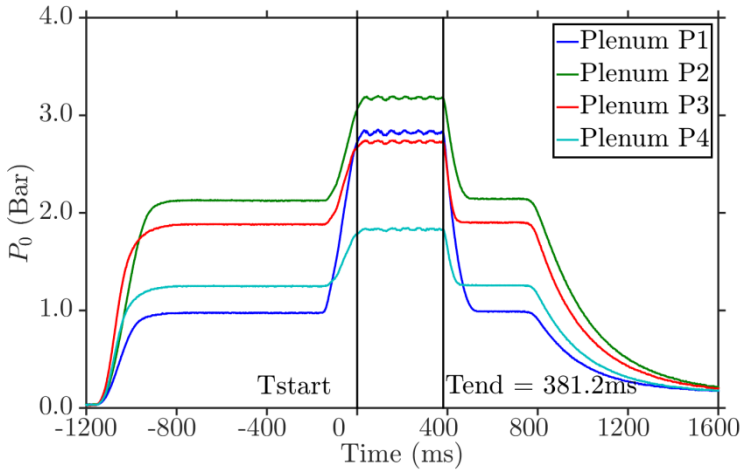

Figure 7.19. Plenum total pressures recorded during a typical run.

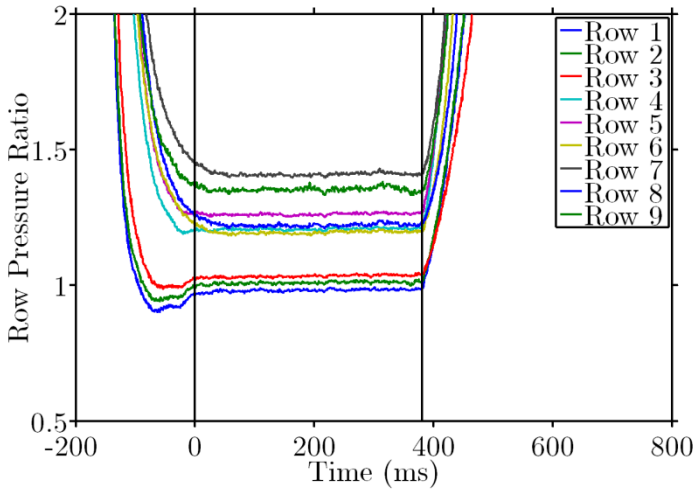

Figure 7.20. Recorded time instantaneous plenum pressure ratios.

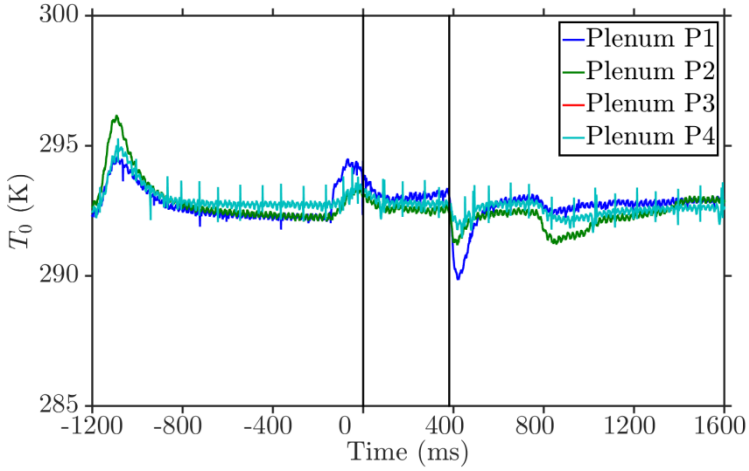

Figure 7.21. Coolant total temperatures recorded during a typical run.

7.5.8 Heat Transfer Data Processing

The data processing methodology for this study is described in the earlier uncooled casing experimental chapter. As per the previous study, the high speed boosted temperature history and low speed DC temperature are recorded during each run for the cooled gauges. The recorded high speed boosted signal is deboosted in Matlab using an impulse response filter and combined with the low speed DC signal as described by Oldfield (2008). The low speed DC temperature history is required to measure the initial wall temperature local to the gauges, as the spinning up of the OTRF in a near vacuum leads to localised heating. A set of zeroes data is measured on the low speed system when the instrumented block can be assumed to be iso-thermal. This is taken before the OTRF rotor is spun up and with the wall heating/cooling system circulating coolant through a bypass valve rather than the instrumented block. The initial wall temperature is measured by four thermocouples located under the TFHFGs. After this zeroes data is taken, the bypass valve is closed circulating pre-heated/cooled water through the block and the rig is spun up to speed.

Multiple runs with different initial wall temperatures were processed together, using the methods presented in the earlier chapter. A corrected wall temperature was used to correct for changes of the inlet total temperature T_{01} during the run.

$$T'_W = T_W - k(T_{01} - \overline{T_{01}}) \tag{7.1}$$

A linear regression can then be performed between T'_W andt $\dot{q}$ to solve the convective heat flux equation and derive the adiabatic wall temperature T'_{AW} and heat transfer coefficient. T'_{AW} is defined as $k\overline{T_{01}}$ and is given by the intercept with the corrected temperature axis, where $\overline{T_{01}}$ is defined as the time averaged inlet total temperature.

The value of k at each spatial and temporal (if performing a periodically unstable analysis) location is unknown so an iterative solution procedure must be undertaken. The updated value of k for each iteration is given by eqn. 7.2.

$$k_{(n)} = T'_{AW(n-1)}/\overline{T_{01}} \tag{7.2}$$

Effectiveness Regression

If the value of k_U (the uncooled $T_{AW}/k\overline{T_{01}}$) is known for an uncooled solution we can modify our regression to account for changes in coolant total temperature as well as for changes in inlet total temperature. We can define a local adiabatic film cooling effectiveness η' as

$$\eta' = \frac{k_U\overline{T_{01}} - T'_{AW}}{k_U\overline{T_{01}} - \overline{T_{0C}}} \tag{7.3}$$

Rearranging and combining with the convective heat flux equation to derive a corrected wall temperature

$$T''_W = T_W - (1-\eta')k_U(T_{01} - \overline{T_{01}}) + \eta'(T_{0C} - \overline{T_{0C}}) \tag{7.4}$$

In this case the local film cooling effectiveness η' is updated iteratively using eqn. 7.3. T'_{AW} is again defined as $k\overline{T_{01}}$ and is given by the intercept with the corrected temperature axis T''_W.

7.5.9 Time Averaged Processed Data

Time averaged values of T_{AW} and Nu obtained using the floating regression are plotted in fig. 7.22. Each data point represents an independent regression for an individual gauge with the T_{AW} and Nu values evaluated directly from the $\dot{q}$ vs. T'_W regression using the intercept and slope respectively.

The Nu results presented in fig. 7.22 are of a similar level to those presented in the uncooled casing heat transfer data presented in an earlier chapter. Some gauges indicate an enhanced Nu

but it is difficult to specify whether this is due to enhancement by the nearby film cooling holes or from experimental uncertainty.

Figure 7.23 plots η', evaluated using eqn. 7.3. In this case the effectiveness regression was not used as T_{0C} experienced very little variation during the run. The uncooled T_{AW} was taken from the measured uncooled casing results presented in the earlier uncooled casing chapter. η' results indicate that the film cooling scheme is most effective upstream of the blade tip. η' then decays linearly along the blade tip to approximately 0 at the trailing edge. Effectiveness values recover downstream of the rotor tip. It is important to note that each gauge measures at one location relative to the cooling holes. Thus the measured values are very dependent on gauge location and do not present a surface averaged value.

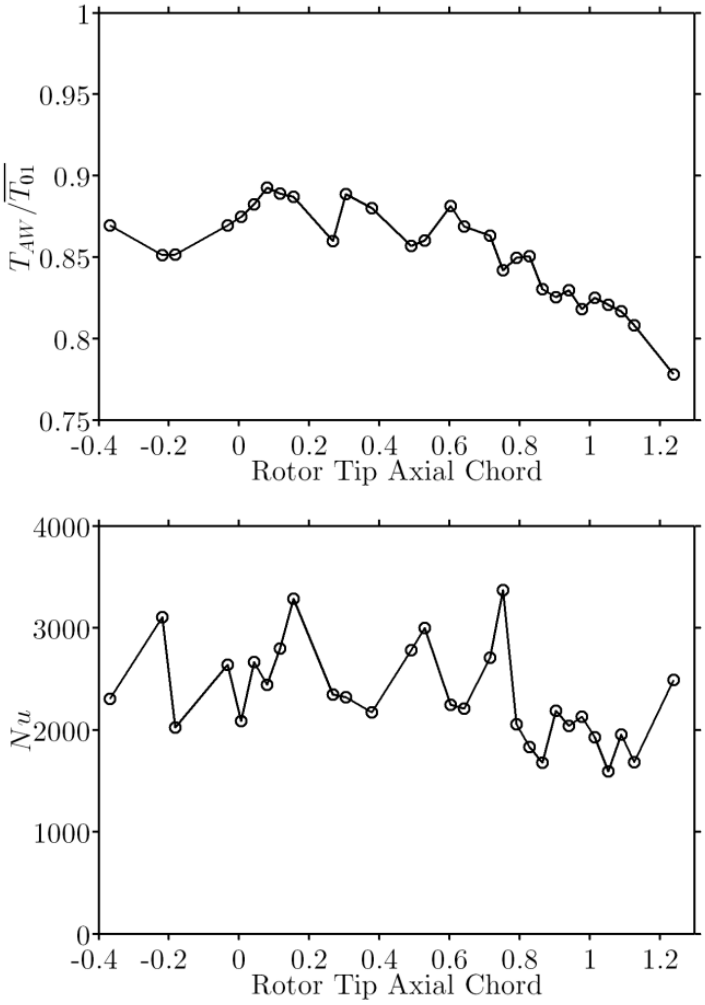

Figure 7.22. Time averaged plots of T_{AW} (top), Nu (bottom).

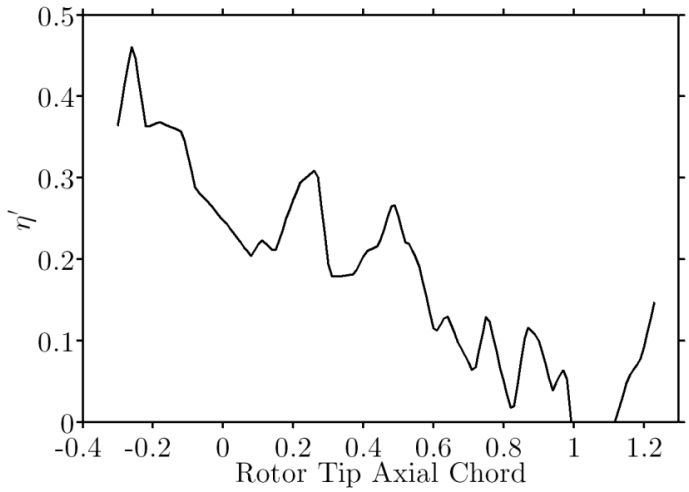

Figure 7.23. Time averaged plot of η' obtained by comparing with uncooled experimental results.

7.5.10 Time Resolved Processed Data

The large bandwidth (~ 150 kHz) of TFHFGs enables the measurement of high speed experimental data. Gauges located on the over-tip casing observe the passing of the rotor blade at the rotor passing frequency. It is therefore possible to measure the heat transfer in the rotor frame of reference by analysing the time-resolved periodic signal.

The time resolved data processing technique is described in the earlier uncooled casing experimental chapter and is summarised in fig. 7.24. The periodic signal is first phase locked using autocorrelation to group the passing events. A time history of the heat flux and surface temperature for a given rotor pitch can then be extracted for each gauge. Separate regressions are then conducted for a number of phase locked pitch points for each gauge.

This technique does not rely on time averaging the unsteady signal. To minimise the effects of experimental noise, each passing event was correlated against all others to identify the most statistically significant events. Only 70% of the best correlated events were used for the unsteady analysis.

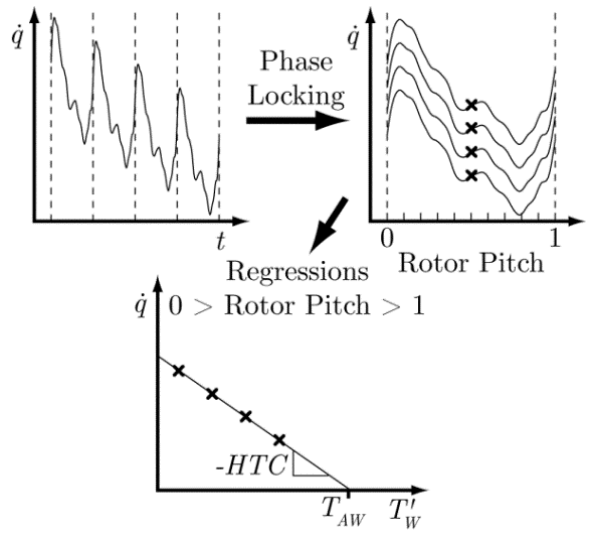

Figure 7.24. Schematic illustrating unsteady data processing to extract and T_{AW} and HTC as functions of rotor pitch.

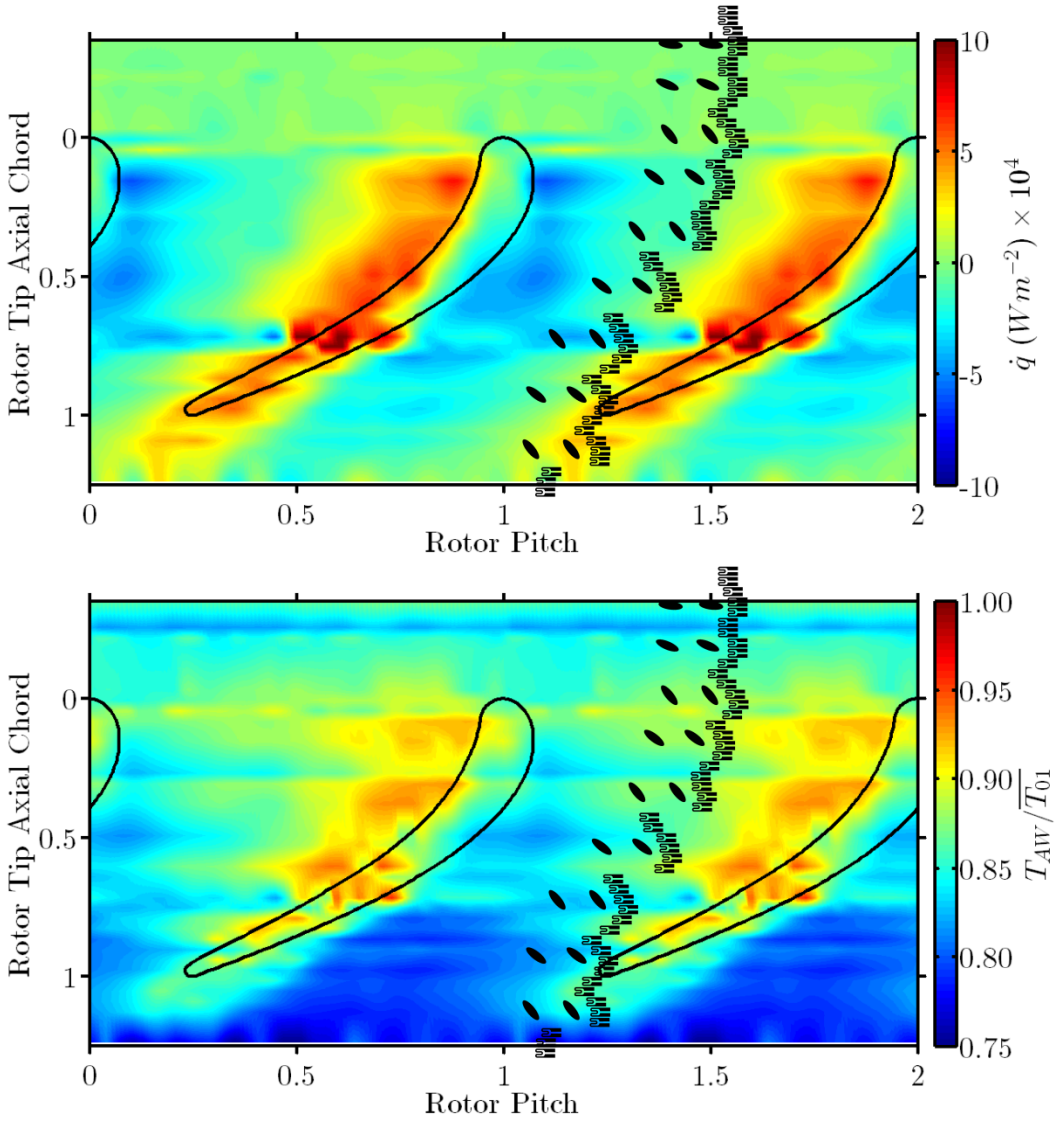

Figure 7.25. Time resolved experimental measurements of rotor casing unsteady heat flux (top) and T_{AW} (bottom) with gauge locations relative to cooling holes marked.

Processed unsteady results of high pass filtered unsteady heat flux and T_{AW} are presented in fig. 7.25. As with the time averaged data, T_{AW} is evaluated directly from the $\dot{q}$ vs. T'_W regression which is executed independently at 100 points per rotor passing event for each gauge. Twenty nine functional TFHFGs span the axial ordinate and with 100 time-resolved regressions per each rotor pitch, thus fig. 7.25 presents the data of 2900 independent regressions. The data is not subjected to any smoothing though there is interpolation in the axial ordinate to enable the plotting of a smooth surface.

The location of the rotor tip was inferred by cross correlating the heat flux signal at a number of gauge locations with a CFD solution.

Figure 7.26 plots the time resolved η' calculated using eqn. 7.3. The uncooled T_{AW} was taken from the time resolved measured uncooled casing T_{AW} presented in the earlier uncooled casing chapter.

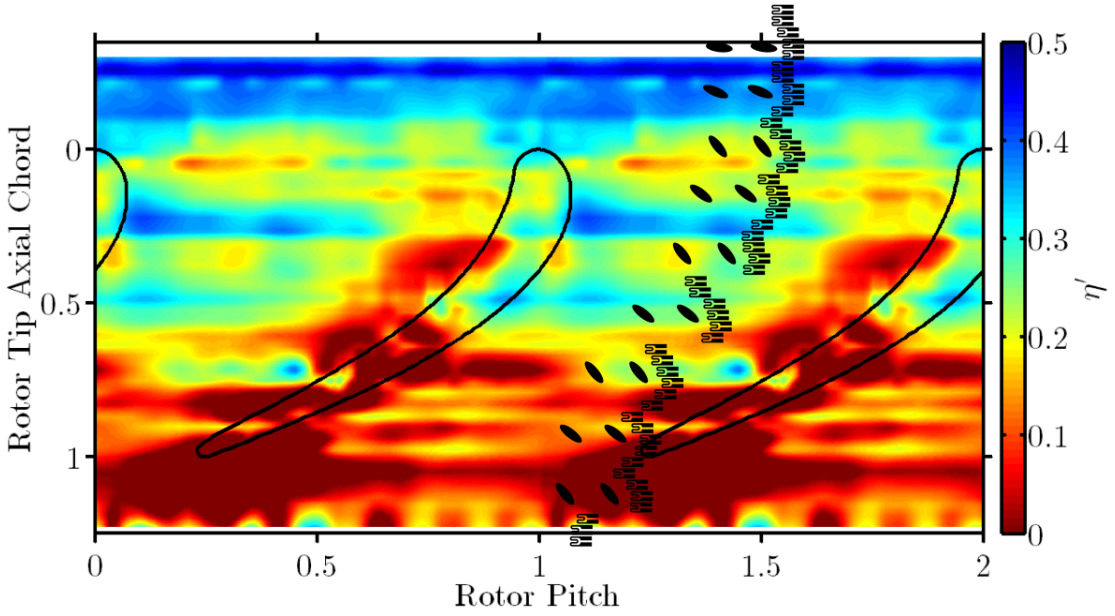

Figure 7.26. Time resolved experimental measurements of η′ with gauge locations relative to cooling holes marked.

7.5.11 Time Resolved Results Discussion

The cooled casing CFD chapter describes the interaction between coolant and the rotor passage. For brevity these will not be described again. Results are discussed with reference to the previous chapter on experimental uncooled casing heat transfer taken on the same facility.

- The magnitude of the unsteady heat flux signal is measured to be larger than on an uncooled casing. Study of T_{AW} and corresponding η' indicates that this results from a reduction in T_{AW} in much of the passage lowering the mean heat flux. The T_{AW} local to the pressure side corner is reduced to a lesser extent, manifesting itself in an increased unsteadiness of T_{AW} and subsequently heat flux in the passage.
- Time resolved η' is evident local to the film cooling holes. The magnitude and location of η' change with the passing of the rotor tip as a result of changes to the local flow direction and reestablishment of the cooling film after removal by the rotor tip. The mechanisms of coolant transportation in the casing relative environment are described fully in the cooled casing CFD chapter.
- Figure 7.26 indicates that there is little to no η' present in the regions corresponding to the tip leakage vortex. Indeed downstream of the rotor in the wake region the T_{AW} in the wake region is seen to be enhanced. Behr et al. (2008) measured an increase in the size of the tip passage vortex when coolant was introduced to the casing. This acted to displace the tip leakage vortex closer to the tip. It is perhaps this displacement of the tip leakage vortex, which consists mostly of higher temperature tip leakage fluid, which we observe in these results.
- Low values of η' are evident local to the pressure side corner. This reinforces the hypothesis that the flow entering the tip gap is mostly drawn from the passage and contains little coolant.
- In the over-tip casing, η' is witnessed to be relatively large upstream of 50% C_{AX}. This reinforces the conclusion in the cooled CFD chapter that some of the coolant film persists

after the passing of the suction side corner. Downstream of this region η' is low, suggesting that almost all the coolant film is removed by the tip leakage vortex which is present downstream of 50% C_{AX}.

7.6 Comparison with CFD Results

The experimental results present time resolved measurements from individual measurement points rather than results across the casing surface. To better compare the CFD from the earlier chapter to the experimental results, time resolved data was extracted from the CFD model at locations corresponding to the gauge locations in the experimental study.

The experimental geometry studied in this study closely resembles geometry B from the cooled CFD chapter. The as manufactured holes in this experimental study were smaller in diameter than those used in the CFD study (∅0.4 mm vs ∅0.5 mm) and the hole spacing was slightly increased (0.61° vs 0.5°). The resulting CFD coolant mass flow rates were approximately double those of the experimental study when the plenums were set to the same time mean pressure ratios. Individual plenum mass flow rates are detailed in table 7.5.

Table 7.5. CFD and experimental plenum coolant mass flow rates.

Plenum	CFD $\dot{m}_C/\dot{m}_{12}$	Experimental $\dot{m}_C/\dot{m}_{12}$
P1	0.351%	0.1984%
P2	0.490%	0.2855%
P3	0.576%	0.2438%
P4	0.309%	0.1479%

Time resolved results of T_{AW} and η', obtained from the CFD of geometry B detailed in the cooled CFD chapter, are presented in fig. 7.27. These are produced by extracting heat transfer data at each time step from superimposed experimental gauge locations.

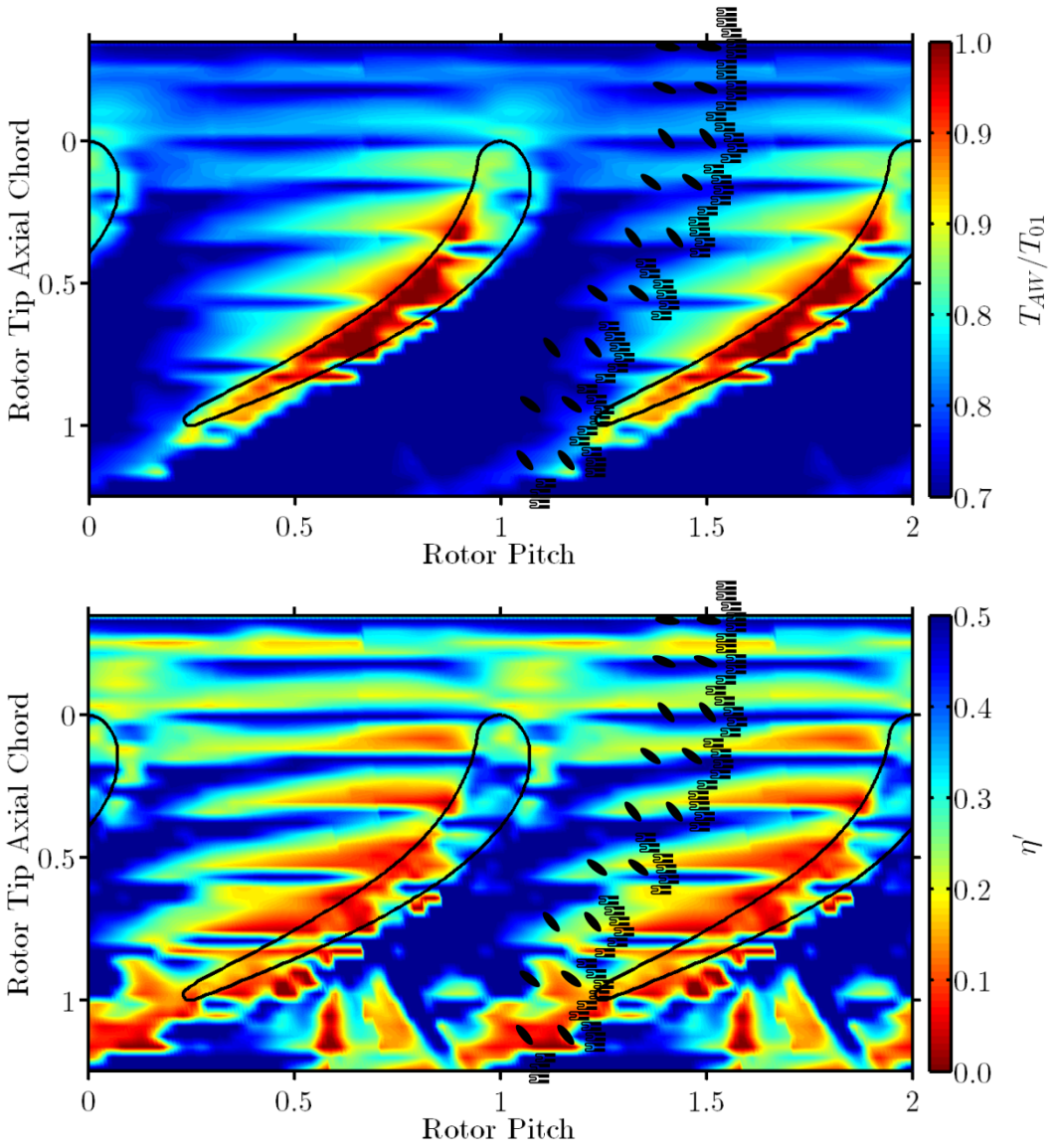

Figure 7.27. Time resolved T_{AW} (top) and η' (bottom) extracted from geometry B CFD model.

Due to the significant differences in coolant mass flow rate between the experimental and CFD results, quantitative comparison is not possible. Qualitatively, the general patterns of film cooling effectiveness are evident in both sets of results. Most significantly:

- The bands of film cooling effectiveness caused by the discrete locations of the gauges are evident in both plots at similar locations.
- The coolant film persists under the tip upstream of 50% C_{AX}, lowering the T_{AW}.
- Low values of η' are evident local to the pressure side corner and under the tip downstream of 50% C_{AX}.

These similarities support the mechanisms of the interactions between the coolant and rotor tip proposed in the CFD chapter.

7.7 Conclusions

Experimentally measured results of time resolved T_{AW} and η' have been presented for a film cooling scheme employed on the casing of an unshrouded rotor. To the author's knowledge these are the first time-resolved measurements of film cooling effectiveness presented. This has been made possible by significant improvements in TFHFGs and data processing routines.

A new data processing technique has been described which can account for variations in T_{01} and T_{0C} during an experimental run.

Experimental results have been compared with data from a CFD model presented in the earlier chapter. Qualitatively the experimental and CFD results agree well, supporting the conclusions drawn in that chapter.

7.8 Chapter Nomenclature

C	Rotor true chord (OTRF = 36.6 mm)
C_{AX}	Rotor tip axial chord (OTRF = 21.39 mm)
η'	Local film cooling effectiveness
k	T_{AW}/T_{01}
$\dot{m}$	Mass flow rate
M	Mach number
Nu	Nusselt number: $(htc \times C)/k_{01}$
p	Pressure
$\dot{q}$	Heat flux
Re	Reynolds number
t	Time
T	Temperature
T_{AW}	Adiabatic wall temperature
T_W	Wall temperature
T'_W	T_{01} corrected wall temperature
T''_W	T_{01} and T_{0C} corrected wall temperature
ω	Rotor disc speed

Subscripts

01	Rotor inlet total	c	Coolant
02	Rotor outlet total	rel	Rotor relative
12	Passage	U	Uncooled

Chapter 8: Summary and Conclusion

Computational and experimental investigations have been carried out into the feasibility and performance of a film cooling scheme employed on the casing of an unshrouded high pressure rotor. Significant advances have been made in the understanding of film cooling systems subjected to periodic pressure perturbation using both theoretical arguments and novel numerical investigations. The need to measure a highly unsteady and localised flow field has driven the development of much improved heat transfer instrumentation and data processing techniques. These have been applied to heat transfer measurements on the casing of an HP rotor to deliver perhaps some of the best heat transfer data obtained using thin film heat flux gauges yet presented. A summary of the important conclusions drawn in this thesis is provided below.

Acoustic Effects

A 2D CFD model has been used to model pressure wave reflections within cooling holes. These have a highly significant effect on the performance of film cooling holes in terms of ingestion characteristics, mean and temporal modulation of mass flux. All these factors are likely to have a strong bearing on the film cooling effectiveness of the system. It is necessary to be aware of these effects during the design stage, and to acoustically tune holes to achieve the optimum performance. New cooling hole shapes designed to make use of pressure wave reflections to benefit a film cooling scheme employed on the rotor casing have been designed.

It is believed this is the first time this important mechanism has been discussed in the literature of turbine cooling, and possibly is the first example of direct *exploitation* (through design) of unsteady effects to control how the film is beneficially modulated on a surface through temporal mass flow rate control (and therefore momentum flux ratio control).

This work was presented at the ASME turbomachinery conference 2014 and was published in the Journal of Engineering for Gas Turbines and Power in 2015. A patent has also been filed with the EU and US patent offices with regard to a number of new novel hole shapes which make best use of these acoustic effects.

Numerical Work

The use of a full 3D CFD model of a casing film cooling scheme has been used to study heat transfer on the casing of an HP rotor to understand the interaction of casing film cooling holes with an engine representative rotor. The model includes a sliding interface within the tip gap and to the author's knowledge is the first time such a model has been published. Analysis of a 3D CFD simulations incorporating cooling holes is used to explain the interaction of the injected coolant with the rotor tip. Most significantly, coolant films are scraped off the rotor casing by the tip leakage vortex and entrained into the tip passage vortex. The coolant injected in the tip gap induces a blocking effect which reduces the over-tip leakage mass flow rate (12% reduction for $\dot{m}_c/\dot{m}_{12}$= 1.73%). This has been shown, with the use of a number of cooled turbine efficiency models, to improve cooled rotor blade row efficiency for certain design configurations. A paper regarding the CFD modelling and loss analysis is currently pending submission.

Experimental Work

A new fabrication process for the manufacture of TFHFGs has been described and compared to previous methods. New gauge designs which improve the sensitivity for a given footprint are also introduced. The result is the ability to manufacture gauges which are both significantly smaller and more robust. Examples of TFHFGs which offer a 7 fold increase in gauge density are presented. A paper was published in the journal of Measurement Science and Technology in 2015.

Both time averaged and time resolved measurements of heat flux and the corresponding components of Nu number and T_{AW} have been measured on the casing of a high-speed fully scaled rotor casing. Significant improvements to data processing techniques are described and in conjunction with improved instrumentation has generated much improved measurements of time resolved Nu number and T_{AW} which are in good agreement with numerical predictions. The time resolved heat transfer results highlight important features which have not been previously observed in a rotating facility, though have been well documented in cascade tests. A paper on this work was presented at the ASME turbomachinery conference 2015 and has been recommended for publication in the ASME Journal of Turbomachinery.

Experimentally measured results of time resolved T_{AW} and η' have been presented for a film cooling scheme employed on the casing of an unshrouded rotor. To the author's knowledge these are the first time-resolved measurements of film cooling effectiveness presented. This has been made possible by significant improvements in TFHFGs and data processing routines. A paper is currently pending submission on this topic.

8.1 Applications of the Research and Future Work

This work has significantly expanded the knowledge and understanding of a film cooling scheme employed on a rotor casing. During the project, an engine test of a film cooled casing was undertaken on the Environmentally Friendly Engine (EFE) by Rolls-Royce. Results from this initial test correlated to the predicted mean effectiveness of the system derived from the CFD work documented in this thesis. The work of this project is now being applied to the design of an improved cooling scheme. The discovery that such a cooling scheme reduces the tip leakage losses has made the design far more attractive to the engine designer and it is hoped that a revised design will compete for implementation on an engine. Rolls-Royce are currently

funding a 6 month post-doctoral position for the author to conduct experimental loss measurements to support the numerical work in this thesis.

The work in this thesis has had a significant impact on the future of heat transfer measurements. The new miniature thin film heat flux gauges developed by the author offers an order of magnitude change in resolution, enabling much improved heat transfer measurements to be made. New gauges have already been used in other projects at the Osney Thermofluids laboratory and other institution. The new automated calibration facility has transformed the accuracy and time scales of gauge calibrations and is now widely used in the Osney laboratory.

Improvements in data processing are being applied to other work within the Osney laboratory. The data processing code included in the appendices has been used to derive meaningful measurements of heat transfer on IP vanes taken on the OTRF as published by Johansson et al. (2015). This is a challenging location for heat transfer measurements due to the small surface temperature rise during an experimental run. The processing routines allow multiple runs to be processed together using the floating regression technique, greatly improving the robustness of the regression to derive both the adiabatic wall temperature and heat transfer coefficient.

References

Ainsworth, R. W., Schultz, D. L., Davies, M. R. D, Forth, C. J. P., Hilditch, M.A., and Oldfield, M. L. G., 1988, ‘‘A transient flow facility for the study of the thermofluid-dynamics of a full stage turbine under engine representative conditions,’’ ASME Paper No. 88-GT-144.

Anderson, J.D., 2004, “Modern compressible flow: with historical perspective,” McGraw-Hill. ISBN 978-0071241366.

ANSYS® Fluent, Release 12.0, User’s Guide, ANSYS, Inc.

Anthony, R.J., Oldfield, M.L.G., Jones, T.V., LaGraff, J.E, 1999, “Development of high density arrays of thin film heat transfer gauges,” 5th ASME/JSME Thermal Engineering Joint Conference, San Diego, CA. AJTE 99-6159.

Beard, P. F, 2010, “On transient turbine efficiency measurements with engine representative inlet flows,” D.Phil Thesis, Department of Engineering Science, University of Oxford.

Beard, P. F., Smith, A. D., Povey, T., 2011, “Experimental and computational fluid dynamics investigation of the efficiency of an unshrouded transonic high pressure turbine,” Proceedings of the Institution of Mechanical Engineers, Part A: Journal of Power and Energy, 0957650911407979.

Behr, T., Kalfas, A. I., Abhari, R. S., 2007, “Unsteady flow physics and performance of a one-and-1/2-stage unshrouded high work turbine,” Journal of Turbomachinery, 129(2), pp. 348–359.

Behr, T., Kalfas, A. I., & Abhari, R. S., 2008, “Control of rotor tip leakage through cooling injection from the casing in a high-work turbine,” Journal of Turbomachinery, 130(3), 031014.

Bindon, J. P., 1989, “The measurement and formation of tip clearance loss,” Journal of Turbomachinery, 111(3), pp. 257-263.

Burghardt, M.D., 1993, “Engineering thermodynamics,” HarperCollins College, ISBN 0060410493.

Chana, K.S. Jones, T.V., 2003, “An investigation on turbine tip and shroud heat transfer,” ASME Paper No. GT2002-30554.

Chana, K.S., Haller, B., 2009a, “Novel turbine rotor shroud film-cooling design and validation, part 1,” ASME Paper No. GT2009-60242.

Chana, K.S., Haller, B., 2009b, “Novel turbine rotor shroud film-cooling design and validation, part 2,” ASME Paper No. GT2009-60246.

Chana, K., Cardwell, D., Jones, T., 2013, “A review of the Oxford turbine research facility,” ASME Paper No. GT2013-95687.

Chew, M., Soon, W.H., Su N., Liao E., Rao, V.S., Premachandran, C.S., Kumar R., Damaruganath P., 2009, “Development of negative profile of dry film resist for metal lift off process,” Electronics Packaging Technology Conference, 2009. EPTC '09. 11th , pp.884-888.

Collins, M. C. J, & Povey, T., 2015, “Exploitation of acoustic effects in film cooling,” Journal of Engineering for Gas Turbines and Power, 137, 102602-1.

Collins, M. C. J., Chana, K., & Povey, T., 2015, “New technique for the fabrication of miniature thin film heat flux gauges,” Measurement Science and Technology 26(2), 25303-25312.

Collins, M. C. J, Chana, K. S. & Povey, T., 2015, “Improved methodologies for time resolved heat transfer measurements, demonstrated on an unshrouded transonic turbine casing,” ASME Paper No. GT2015-43346.

Cumpstey, N. 1997, “Jet propulsion,” Cambridge University Press.

Courant, R., Friedrichs, K.O., 1948, “Supersonic flow and shock waves,” Interscience Publishers, New York.

Denton, J. D., 1993, “The 1993 IGTI scholar lecture: loss mechanisms in turbomachines,” Journal of Turbomachinery, 115(4), pp. 621-656.

Doorly, J.E., Oldfield, M.L.G., 1986, “The theory of advanced multi-layer thin film heat transfer gauges International Journal of Heat and Mass Transfer, 30(6), pp. 1159–1168.

El-Gabry, L.A., Ameri, A.A., 2010, “Comparison of steady and unsteady RANS heat transfer simulations of hub and endwall of a turbine blade passage,” Journal of Turbomachinery, 133(3), 031010.

Epstein, A. H., Guenette, G. R., Norton, R. J. G., & Yuzhang, C., 1986, “High-frequency response heat-flux gauge,” Review of Scientific Instruments, 57(4), pp. 639-649.

Friedrichs, S., 2008, "Turbine heat transfer," Cambridge Turbomachinery Course, Cambridge University. Vol. 1.

Gröber, H., and Erk S., 1961, "Fundamentals of heat transfer," McGraw-Hill.

Guenette, G. R., Epstein, A. H., Norton, R. J. G., & CAO, Y., 1985, "Time resolved measurements of a turbine rotor stationary tip casing pressure and heat transfer field," In AIAA, SAE, ASME, and ASEE, Joint Propulsion Conference, 21st, Monterey, CA.

Guo, S.M., Lai, C.C., Jones, T.V., Oldfield, M.L.G., Lock G.D., Rawlinson, A.J., 1998, "The application of thin-film technology to measure turbine-vane heat transfer and effectiveness in a film-cooled, engine-simulated environment," International Journal of Heat and Fluid Flow, 19(6), pp. 594–600.

Hartsel, J.E., 1972, "Prediction of Effects of Mass-Transfer Cooling on the Blade Row Efficiency of Turbine Aerofoils," AIAA-Paper No. 72-11.

Heyes, F. J. G., Dailey, G. M., & Hodson, H. P., 1992, "The effect of blade tip geometry on the tip leakage flow in axial turbine cascades," Journal of Turbomachinery, 114(3), pp. 643-651.

Hilditch, M. A., Fowler, A., Jones, T. V., Chana, K. S., Oldfield, M. L. G., Ainsworth, R. W., Hogg, S. I., Anderson, S. J., Smith, G. C., 1994, "Installation of a turbine stage in the Pyestock isentropic light piston facility," ASME Paper No. 94-GT-277.

Johansson M., Mårtensson J., Povey T., Chana K., Abrahamsson H., 2015, "Aerothermal measurements and predictions of an intermediate turbine duct turning vane," ASME Paper No. GT2015-43449.

Jones, T. V., 1988, "Gas turbine studies at Oxford 1969-1987," ASME Paper No. 88-GT-112.

Jones, T. V., 1995, "The thin film heat transfer gauges-a history and new developments," Invited lecture, 4th national UK heat transfer conference, IMechE conference transaction, Manchester p. 1-12.

Kentfield, J.A.C., 1993, "Nonsteady, one-dimensional, internal, compressible flows," Oxford University Press. ISBN 978-0195073584.

Köllen, O., and Koschel, W., 1985, "Effect of film cooling on the aerodynamic performance of a turbine cascade," AGARD CP-390.

Krishnababu, S. K., Newton, P. J., Dawes, W. N., Lock, G. D., Hodson, H. P., Hannis, J., & Whitney, C., (2009), "Aerothermal investigations of tip leakage flow in axial flow turbines—part 1: Effect of tip geometry and tip clearance gap," Journal of Turbomachinery, 131(1), 011006.

Lee, C.-P. & Durgin, G. A., 2001, "Preferentially cooled turbine shroud," US Patent US6196792.

Lee, C.-P., Robinson, G. D. & Orlando, J. P., 2012, "Duplex turbine shroud," US Patent US8104292.

Liotta, G. C. & Acquaviva, P. J., 1999, "Dual cooled shroud," US Patent US5993150.

Lowe, C. C., Powis, A. C., Clarke, J. P., 2003, "Turbine shroud asymmetrical cooling elements," US Patent US7147432.

Metzger, D. E., Dunn, M. G., & Hah, C., 1991, "Turbine tip and shroud heat transfer," Journal of Turbomachinery, 113(3), pp. 502–507.

Mischo, B., Burdet, A., Behr, T., & Abhari, R. S., 2007, "Control of Rotor Tip Leakage Through Cooling Injection From the Casing in a High-Work Turbine: Computational Investigation Using a Feature-Based Jet Model," ASME Paper No. GT2007-27669.

Mischo, B., Behr, T., & Abhari, R. S., 2008, "Flow physics and profiling of recessed blade tips: impact on performance and heat load," Journal of Turbomachinery, 130(2), 021008.

Moore, J. O. H. N., & Tilton, J. S., 1988, "Tip leakage flow in a linear turbine cascade," Journal of Turbomachinery, 110(1), pp. 18-26.

Neugebauer, C. A. and Webb, M. B., 1962 "Electrical conduction mechanism in ultrathin, evaporated metal films," Journal of Applied Physics, 33(1), pp. 74-82.

Oldfield, M. L. G., Burd, H. J., & Doe, N. G., 1984, "Design of wide-bandwidth analogue circuits for heat transfer instrumentation in transient tunnels," Heat and Mass Transfer in Rotating Machinery, 1, pp. 233-258.

Oldfield, M. L., 2008, "Impulse response processing of transient heat transfer gauge signals," Journal of Turbomachinery, 130(2), 021023.

Piccini, E., Guo, S. M., & Jones, T. V., 2000, "The development of a new direct-heat-flux gauge for heat-transfer facilities," Measurement Science and Technology, 11(4), 342.

Polanka, M. D., Hoying, D. A., Meininger, M., & MacArthur, C. D., 2003, "Turbine tip and shroud heat transfer and loading–part A: Parameter effects including Reynolds number, pressure ratio, and gas-to-metal temperature ratio," Journal of Turbomachinery, 125(1), pp. 97–106.

Qureshi, I., Beretta, A., Chana, K., Povey, T., 2011, "Effect of aggressive inlet swirl on heat transfer and aerodynamics in an unshrouded transonic HP turbine," ASME Paper No. GT2011-46038.

Qureshi, I., Smith, A. D., Chana, K. S., & Povey, T., 2012, "Effect of temperature nonuniformity on heat transfer in an unshrouded transonic HP turbine: an experimental and computational investigation," Journal of Turbomachinery, 134(1), 011005.

Rolls-Royce plc., 2015, "Trent 900 technology," http://www.rolls-royce.com/site-services/images/trent-900-poster.aspx, (accessed July 2015).

Saravanamuttoo, H. I. H., Rogers, G. F. C., & Cohen, H., 2001, "Gas turbine theory," Pearson Education.

Schultz, D.L, Jones, T.V., 1973, "Heat transfer measurements in short duration hypersonic facilities," AGARD 165.

Shapiro, J. D., 2007 "Counterflow film cooled wall," US Patent US7296967.

Sieverding, C. H., 1985, "Recent progress in the understanding of basic aspects of secondary flows in turbine blade passages," Journal of Engineering for Gas Turbines and Power, 107(2), pp.248-257.

Thorpe S.J., Yoshino S., Ainsworth R.W., Harvey N.W., 2004a, "An investigation of the heat transfer and static pressure on the over-tip casing wall of an axial turbine operating at engine representative flow conditions. (I). Time-mean results," International Journal of Heat and Fluid Flow, 25(6), pp. 933-944,

Thorpe, S.J., Yoshino, S., Ainsworth, R.W., Harvey, N.W., 2004b, "An investigation of the heat transfer and static pressure on the over-tip casing wall of an axial turbine operating at

engine representative flow conditions. (II). Time-resolved results," International Journal of Heat and Fluid Flow, 25(6), pp. 945-960.

Thorpe, S. J., Yoshino, S., Ainsworth, R. W., & Harvey, N. W., 2004, "Improved fast-response heat transfer instrumentation for short-duration wind tunnels," Measurement Science and Technology, 15(9), 1897.

Thorpe, S.J., Miller, R.J., Yoshino, S., Ainsworth, R.W., Harvey, N.W., 2007, "The effect of work processes on the casing heat transfer of a transonic turbine," Journal of Turbomachinery, 129(1), pp. 84-91.

Vidal, R.J., 1956, "Model instrumentation techniques for heat transfer and force measurements in a hypersonic shock tunnel," Cornell Aeronautical Laboratory, Rept AD-917-A-1.

Wang, H. P., Olson, S. J., Goldstein, R. J., & Eckert, E. R., 1997, "Flow visualization in a linear turbine cascade of high performance turbine blades," Journal of Turbomachinery, 119(1), pp. 1-8.

White, G. A. & Lee, C.-P., 2002, "Shroud cooling segment and assembly," US Patent US6354795.

Winterbone, D.E., Pearson, R.J., 2000, "Theory of engine manifold design: Wave action methods for IC engines," Wiley-Blackwell, ISBN 978-1860582097.

Yang, C. H., Lee, S. C., Wu, J. M., & Lin, T. C., 2005, "The properties of copper films deposited on polyimide by nitrogen and oxygen plasma pre-treatment," Applied surface science, 252(5), pp. 1818-1825.

Yaras, M. L., & Sjolander, S. A., 1991a, ''Effects of simulated rotation on tip leakage in a planar cascade of turbine blades. Part I: tip gap flow,'' ASME Paper No. 91-GT-127.

Yaras, M. I., & Sjolander, S. A., 1991b, ''Effects of simulated rotation on tip leakage in a planar cascade of turbine blades. Part II: downstream flow field and blade loading,'' ASME Paper No. 91-GT-128.

Yaras, M. I., & Sjolander, S. A., 1992, "Prediction of tip-leakage losses in axial turbines," Journal of Turbomachinery, 114(1), pp. 204-210.

Young, J. B., & Horlock, J. H., (2006), "Defining the efficiency of a cooled turbine," Journal of Turbomachinery, 128(4), pp. 658-667.

Appendix A

The Matlab code used for solving the heat transfer regressions was heavily refined during the course of this work and is included here for future reference. It implements the floating regression and multiple run processing techniques described in earlier chapters. The code has been optimised to run quickly, simultaneously processing multiple data sets.

Matlab Floating Regression Code

```
function
[Taw,HTC,TawCL,HTCCL,TDat,QDat]=QTMultiFit(TData,QData,T0Data,Fs,RunFlag,Ta
wGuess,HTCGuess,TawLimit,HTCLimit)

%QTMultiFit
%M. Collins 6/8/14
%Function to perform QT floating regression on multiple runs

%Inputs:
%TData: Time history of temperature data (K) (Can be a matrix) (for steady
%part of run)
%QData: Time history of heat flux data (W/m^2) (Can be a matrix)
%T0Data: Time history of T0 Data to correct using floating regression (Taw
will be a function of the time mean of this)
%Fs: Sample rate of Data (Hz)
%RunFlag: Series equal length to length of TData indicating which run data
%corresponds to ie [1;1;1;2;2;2;3;3;3;....]
%TawGuess: Initial guess for Taw (Function of T0Fit, TawGuess=TawGuess
(K)/mean(T0Fit)
%HTCGuess: Initial guess for HTC
%TawLimit: Vector with [upper lower] Taw limits
%HTCLimit: Vector with [upper lower] HTC limits

%Outputs
%Taw: Calculated adiabatic wall temperature as a function of T0Fit ie
%Taw=Taw (K) / mean(T0Fit)
%HTC: Calculated HTC
%TawCL: Vector of 95% Taw confidence limits
%HTCCL: Vector of 95% HTC confidence limits
%TDat: Fitting Data
%QDat: Fitting Data

%Example:
%              TDataHS=TGi(QCorrBestEvents,:);
%              QDataHS=QGi(QCorrBestEvents,:);
%              T0DataHS=T0FitHSi(QCorrBestEvents);
%              RunFlagHS=RunFlagi(QCorrBestEvents);
%              FsHS=9500;
%              TawGuess=0.9;
%              HTCGuess=2000;
%              TawLimit=[1.1 0.5];
%              HTCLimit=[5000 500];
%
%
[Taw(chan,:),HTC(chan,:),TawCLHStemp,HTCCLHStemp,TDatHS,QDatHS]=QTMultiFit(
```

```
TDataHS,QDataHS,T0DataHS,FsHS,RunFlagHS,TawGuess,HTCGuess,TawLimit,HTCLimit
);

%Initialise
InputWidth=size(TData,2);%Width of input matrices
htcguess=HTCGuess*ones(1,InputWidth);
TawEstimate=TawGuess*ones(1,InputWidth);
TawEstimate2=ones(size(TData,1),1)*TawEstimate;
TawError=ones(1,InputWidth);
T0Fit=T0Data*ones(1,InputWidth);
TDat=[];

%Create Filters
LPF2=500;%Low Pass Filter Frequency for filtering T
LPF=50;%Low Pass Filter Frequency for filtering normal to Tw-Taw
[b,a]=butter(3,2*LPF/Fs);
[b2,a2]=butter(3,2*LPF2/Fs);

%Set Fit Options
options=[];
options = fitoptions('poly1');
options.Lower=[-1/(HTCLimit(2)*mean(T0Data)) TawLimit(2)];%Set lower bound
on HTC
options.Upper=[-1/(HTCLimit(1)*mean(T0Data)) TawLimit(1)];%Set lower bound
on HTC

i=0;
QTFit=0;
while QTFit==0
i=i+1;
%Limit HTC using defined limits
htcguesslim=htcguess;
htcguesslim(htcguesslim>HTCLimit(1))=HTCLimit(1);
htcguesslim(htcguesslim<HTCLimit(2))=HTCLimit(1);
htcguesslim=smooth(htcguesslim,10)';%Smooth this : Only if doing unsteady
is this helpful
TawEstimate2=ones(size(TData,1),1)*TawEstimate;%k
TDat.Corrected=zeros(size(TData));
TDat.CorrectedAbsolute=zeros(size(TData));
TDat.ResampI=[];
QDat.ResampI=[];
TDat.RunFlagI=[];
            for r=1:(max(RunFlag))

                if length(TData(RunFlag==r,:))>200
                TDat.CorrectedRunAbsolute=TData(RunFlag==r,:)-
TawEstimate2(RunFlag==r,:).*T0Fit(RunFlag==r,:);
                TDat.CorrectedRun=(TData(RunFlag==r,:)-
TawEstimate2(RunFlag==r,:).*(T0Fit(RunFlag==r,:)-
(ones(size(TawEstimate2(RunFlag==r,:),1),1)*mean(T0Fit(RunFlag==r,:)))))./(
ones(size(TawEstimate2(RunFlag==r,:),1),1)*mean(T0Fit(RunFlag==r,:)));
                TDat.Corrected(RunFlag==r,:)=TDat.CorrectedRun;

TDat.CorrectedAbsolute(RunFlag==r,:)=TDat.CorrectedRunAbsolute;
                QDat.Run=QData(RunFlag==r,:);

                TDat.Resamp=[];
                QDat.Resamp=[];
                TDat.FilteredRun=filtfilt(b2,a2,TDat.CorrectedRun);%Filter
T & Q Signal
                QDat.FilteredRun=filtfilt(b2,a2,QDat.Run);%Filter T & Q
Signal
```

```
TDat.FilteredRunAbsolute=filtfilt(b2,a2,TDat.CorrectedRunAbsolute);%Filter
T & Q Signal

               %Filter normal to fitted regression with lower frequency

%QFitD3=(filtfilt(b,a,QFitD3./TDat.FilteredRun).*TDat.FilteredRun);   %Low
pass filter htc -THIS INTROUCES LARGE DIVIDE BY ZERO ERRORS NEAR ORIGIN!
                QDat.QErrRun=QDat.FilteredRun-
(ones(size(TDat.FilteredRunAbsolute,1),1)*htcguesslim).*(TDat.FilteredRunAb
solute);

QDat.FilteredRun=filtfilt(b,a,QDat.QErrRun)+(ones(size(TDat.FilteredRunAbso
lute,1),1)*htcguesslim).*TDat.FilteredRunAbsolute;

               %Fit a polynomial to temp rise to enable resampling
                if size(TDat.FilteredRun,1)>1
                   %Resample in T (fit a best fit poly to T vs time trace
and use that to resample)

x=[1:size(TDat.FilteredRun,1)]'*ones(1,size(TDat.FilteredRun,2));
                    y=TDat.FilteredRun;
                    n=2;
                    m = size(x,2);
                    Resamppfit = zeros(n+1,m);
                    for k = 1:m
                        M = repmat(x(:,k),1,n+1);
                        M = bsxfun(@power,M,0:n);
                        Resamppfit(:,k) = M\y(:,k);
                    end

                    ResamplePoints=[];
                    ResamplePointsTime=[];
                    for pitch=1:size(TDat.FilteredRun,2)

sampT=polyval(flipud(Resamppfit(:,pitch)),1:length(TDat.FilteredRun(:,1)));

ResamplePointsTemp=Resamppfit(3,pitch)*ResamplePoints.^2+Resamppfit(2,pitch
)*ResamplePoints+Resamppfit(1,pitch);

ResamplePointsTime=interp1(sampT,1:length(TDat.FilteredRun(:,1)),min(sampT)
:(max(sampT)-min(sampT))/500:max(sampT));

TDat.Resamp(:,pitch)=interp1(1:size(TDat.FilteredRun,1),TDat.FilteredRun(:,
pitch),ResamplePointsTime);

QDat.Resamp(:,pitch)=interp1(1:size(TDat.FilteredRun,1),QDat.FilteredRun(:,
pitch),ResamplePointsTime);
                    end
                else
                    TDat.Resamp=TDat.FilteredRun;
                    QDat.Resamp=QDat.FilteredRun;
                end
                TDat.ResampI=[TDat.ResampI; TDat.Resamp];
                QDat.ResampI=[QDat.ResampI; QDat.Resamp];
                TDat.RunFlagI=[TDat.RunFlagI;
ones(size(TDat.Resamp,1),1)*r];
                TDat.TFitMax(r,:)=max(TDat.Resamp);
                TDat.TFitMin(r,:)=min(TDat.Resamp);
                end
            end


if size(TDat.ResampI,1)>1
```

```
%Weight data such the overlapping data is less important

%Identify start and end temps for each run
 WeightingsT=[];
   for r=1:(max(RunFlag))

WeightTemp=(TDat.ResampI>=(ones(size(TDat.ResampI,1),1)*TDat.TFitMin(r,:)))
&(TDat.ResampI<=(ones(size(TDat.ResampI,1),1)*TDat.TFitMax(r,:)));
       if r==1
            WeightingsT=WeightTemp;
       else
            WeightingsT=WeightingsT+WeightTemp;
       end
   end

 WeightingsTFit=1./WeightingsT;

          %First do a fast fit using least squares
           ci=[];
          %%%%%%Fast Fit-0.03s
    if (max(abs(TawError))>0.01) && i<12
                x=QDat.ResampI;
                y=TDat.ResampI;
                w=sqrt(WeightingsTFit);
                n=1;
                m = size(x,2);
                V=[];
                p7=zeros(n+1,m);
                for k = 1:m
                   % Construct Vandermonde matrix.
                   %V(:,n+1) = ones(length(x(:,k)),1,class(x(:,k)));%If
normal least squares
                    V(:,2) =w(:,k);%Weighted least squares
                    V(:,1) = x(:,k).*V(:,2);
                   % Solve least squares problem.
                    [Q,R] = qr(V,0);
                   %p7(:,k)  = R\(Q'*y(:,k));   % Same as p = V\y;
                    p7(:,k)  = R\(Q'*(w(:,k).*y(:,k)));   %Weighted least
squares
                end

           TawError=TawEstimate-p7(2,:);
           TawEstimate=p7(2,:);
           htcguess=-1./(p7(1,:)*mean(T0Data));

          %If fits exceed limits (fit is slower)
           if min(htcguess)<HTCLimit(2) || max(htcguess)>HTCLimit(1)
          %Identify bad fits
           refittemp=(htcguess>HTCLimit(1))+(htcguess<HTCLimit(2));
                for pitch=1:size(TDat.FilteredRun,2)
                    options.weights= WeightingsTFit(:,pitch);
                    if refittemp(pitch)==1
                        p5 =
fit(QDat.ResampI(:,pitch),TDat.ResampI(:,pitch),'poly1',options);
                        ci(:,:,pitch) = confint(p5);
                        p2=p5.p1;
                        p2(2)=p5.p2;

                        TawError(pitch)=TawEstimate(pitch)-p2(2);
                        TawEstimate(pitch)=p2(2);
                        htcguess(pitch)=-1/(p2(1)*mean(T0Data));
                    end
                end
```

```
            end

              else
            %%%%%%THIS PART SLOW! : 2.1s Needed to compute confidence
            %%%%%%intervals
             for pitch=1:size(TDat.FilteredRun,2)
                  options.weights= WeightingsTFit(:,pitch);
                  p5 =
fit(QDat.ResampI(:,pitch),TDat.ResampI(:,pitch),'poly1',options);
                  ci(:,:,pitch) = confint(p5);
                  p2=p5.p1;
                  p2(2)=p5.p2;
                  TawError(pitch)=TawEstimate(pitch)-p2(2);
                  TawEstimate(pitch)=p2(2);
                  htcguess(pitch)=-1/(p2(1)*mean(T0Data));
                  QTFit=1;
             end
    end
else
   %No data to fit! Initialise variable to blanks.
                  TawEstimate=0;
                  htcguess=0;
                  TawCL=[0; 0];
                  HTCCL=[0; 0];
                  TDat.CorrectedRunAbsolute=[];
                  TDat.CorrectedRun=[];
                  TDat.FilteredRunAbsolute=[];
                  TDat.RunFlagI=[];
                  TDat.ResampI=[];
                  TDat.Resamp=[];
                  TDat.FilteredRun=[];
                  TDat.TFitMax=[];
                  TDat.TFitMin=[];
                  QDat.Run=[];
                  QDat.ResampI=[];
                  QDat.FilteredRun=[];
                  QDat.Resamp=[];
                  QDat.QErrRun=[];
                  QTFit=1;
end
end
Taw=TawEstimate;
HTC=htcguess;
if size(TDat.ResampI,1)>1
    for pitch=1:size(TDat.FilteredRun,2)
        TawCL(1,pitch)=ci(2,2,pitch);
        TawCL(2,pitch)=ci(1,2,pitch);
        HTCCL(1,pitch)=-mean(T0Data)/ci(2,1,pitch);
        HTCCL(2,pitch)=-mean(T0Data)/ci(1,1,pitch);
    end
end
end
```